



HAL
open science

Electrically driven fluorescence of single molecule junctions

Michael Chong

► **To cite this version:**

Michael Chong. Electrically driven fluorescence of single molecule junctions. Physics [physics]. Université de Strasbourg, 2016. English. NNT : 2016STRAE022 . tel-01468663

HAL Id: tel-01468663

<https://theses.hal.science/tel-01468663>

Submitted on 15 Feb 2017

HAL is a multi-disciplinary open access archive for the deposit and dissemination of scientific research documents, whether they are published or not. The documents may come from teaching and research institutions in France or abroad, or from public or private research centers.

L'archive ouverte pluridisciplinaire **HAL**, est destinée au dépôt et à la diffusion de documents scientifiques de niveau recherche, publiés ou non, émanant des établissements d'enseignement et de recherche français ou étrangers, des laboratoires publics ou privés.

ÉCOLE DOCTORALE Physique Chimie-Physique (ED 182)

Institut de Physique et Chimie des Matériaux de Strasbourg

THÈSE présentée par :

Michael CHONG

soutenue le : 01 Décembre 2016

pour obtenir le grade de : **Docteur de l'université de Strasbourg**

Discipline/ Spécialité : Physique

**Electrically driven fluorescence of single
molecule junctions**

RAPPORTEURS :

Mr BOUHELIER Alexandre
Mme FRANKE Katharina

Directeur de Recherche, ICB, Dijon
Professor, Freie Universität Berlin

AUTRES MEMBRES DU JURY :

Mr GENET Cyriaque
Mr ORRIT Michel
Mr RUFFIEUX Pascal
Mr SCHULL Guillaume

Directeur de Recherche, ISIS, Strasbourg
Professor, Leiden Institute of Physics, Leiden
Group Leader, EMPA, Dübendorf
Directeur de thèse, IPCMS, Strasbourg

Acknowledgements

This manuscript is the result of three long years of work. The first time I came to Strasbourg to visit the place that would become the place where I spent most of my time in the following years, I was not convinced to do a PhD. I remember wandering the halls of IPCMS, the institute where my lab is, feeling a bit lost and confused. I remember speaking with Guillaume Schull, my future supervisor, in a lab that appeared rather simple, with one big machine and few other things around. I remember telling him, during our first face to face conversation, that I was not convinced that science was made for me. Then I went home and in an email I also told him I was not convinced about Strasbourg as a city, that looked rather small for what I was used to.

Despite my doubts, Guillaume, with his amazing ability to mix a motivational speech with a genuine human empathy, managed to convince me to start a doctoral project with him. With these premises, it is easy to imagine that the years spent in the lab were not always easy for me, I lost motivation several times, often due to my impatience towards getting results, sometime because I suffered being surrounded by really smart students and colleagues. However, thanks to the great human support I received in the time I spent in Strasbourg, I always found a way to go ahead, and I happily reached the end.

For these three years, for this manuscript, for the science we did and for how much I have grown as a person (and hopefully as a scientist), I have to acknowledge several people.

First of all I want to thank Dr. Alexandre Bouhelier and Prof. Katharina Franke, for accepting to examine and review my manuscript. I deeply appreciate the time and effort they put into it. Also, I want to thank the other members of my doctoral jury, who animated my defense with their interesting questions and remarks: Dr. Cyriaque Genet, Prof. Michel Orrit and Dr. Pascal Ruffieux.

I already mentioned Guillaume Schull, who has been an incredible supervisor. He provided advices, both technical and human, gave me insights and taught me how to do science, almost from A to Z. I was lucky to learn from a person with such a vision and intuition. But I was even more lucky to find a great human being. For these reasons I would like to thank him.

A great, great role was played by Fabrice Scheurer, who almost acted as a second supervisor to me. Fabrice is one of the sharpest and most rigorous minds I have had

the chance to meet. He is also tireless, unselfish and extremely kind. He taught me tons of technical aspects, he helped me understanding science and reviewing my works. I owe him the world.

It is easy to work well when the group you work in is made of nice people. And the STM group of IPCMS is a great example of this. Together with Guillaume and Fabrice, Laurent Limot was a great source of laughter, advices and support. Virginie Speisser made my adaptation to the French bureaucracy as smooth as silk. She also was a day to day help for everything concerning vacuum, preparations and unexpected problems. And, most importantly, she did all this with a smile on her face. Michelangelo Romeo provided an amazing support for all the computer-experiment interfaces, together with the worst possible jokes. Thank you all for being a great group of people to work with. The young, non-permanent, members of the team were also extremely important. First of all Gael, the PhD student of the group at the time I joined it. Not only he taught me how to use an STM, and introduced me to several people in the institute, but he also became a real friend. Working with him was an extreme pleasure. Sam, who spent some months with us as a master student, and left for a more rewarding life. Nasima, who spent a year as a postdoc, who me impressed for her kindness. Benjamin Doppagne, who came as a Master student and is now going on as a PhD candidate. You have a bright future in front of you. How not to mention the members of the "spin" part of the group. Nicolas, *el chiquito*, with whom I had the (bad) luck of sharing the office: thanks for the chocolate, the cookies and for always being available for helping. Benjamin Verlhac, *le monsieur mechant*, for helping me in making fun of Nicolas.

Last in this list, but far from the least: Maider. The list of thing I am grateful you for does not fit in this space. You were the best possible office colleague, a friend, a shoulder, a support, someone to lean on and someone to laugh with. It is impossible to describe the importance you had in making me reach the end of this work, thank you so much.

My work was also possible thanks to several collaborations. I would like to acknowledge Fabrice Mathevet and Lydia Sosa-Vargas from the Institut Parisien de Chimie Moléculaire, who synthesised many molecules that were fundamental for the experiments. Also, Delphine Felder-Flesch from IPCMS, for synthesising Zn-DPP.

I spent a lot of time discussing with, and desperately seeking help from Alex Boeglin and Hervé Bulou, who performed most of the theoretical calculations reported in this manuscript: for their time, their patience and their kindness, I would like to thank them. For the fruitful collaboration on the topic of GNR, thanks to Deborah Prezzi, Andrea Ferretti and Claudia Cardoso, from CNR Nano in Modena. For the scientific discussions and for participating in the jury of my mid-term presentation, I would also like to thanks Stephane Berciaud and Guillaume Weick.

For the technical support in the laboratory, for the reparations and the conception of new parts I would like to acknowledge the work of Jean-Georges Faullumel, Bernard

Muller, Arnaud Boulard and Maxime Valentin from the *atelier mécanique*. For the support in all aspects of electronics, the credit goes to Emmanuel Sternitzky. Also, my gratitude to Jacques Faerber for sharing his knowledge about vacuum technology and for providing SEM images of samples and tips.

Three years in the institute and in Strasbourg gave me the chance to meet a good deal of people, who helped me going through the struggles of a PhD and provided good fun. Without any particular order, I would like to thank the members of *place du café* and other friends from IPCMS: Dominik, Dimitra, Celine, Francois, Florian, Manu, Christian, Tindara, Guillaume, Ondrej, Silvia Kerstin, Olga, Vadym, Peter, Etienne, Olivia, Marco, Ferdaous and Irene. Also, some people from the *normal* world: Serena, Marisa, Davide, Ingrid, Magda and Teo. A special mention goes to Edoardo, that maybe is the real responsible for my choice of coming to Strasbourg, and who have been my best friend in the last three years.

Some friends showed their important support even from other countries, and for this reason I would like to thank them: Francesco, Barbe, Eugenio, Emilio, Piero, Andrea, Fabio, Barto, Annalisa and Bobo.

The most important at the end: the family. Thank you mom, and thank you my beautiful sisters, Linda and Nicole. Your support meant the world to me. Finally thank you, little Anna, for bringing a spark of life when I needed it the most.

Contents

List of Figures	ix
List of abbreviations	xii
Resumé	xiii
1 General introduction	1
2 Scanning Tunneling Microscopy and STM-induced light emission	5
2.1 Scanning Tunneling Microscopy	5
2.1.1 Scanning Tunneling Spectroscopy	10
2.1.2 Experimental setup	11
2.1.3 Light collection system	13
2.1.4 Software	17
2.2 STM-induced light emission	18
2.2.1 Basic principles	18
2.2.2 Experiments on metals	21
2.2.3 STM-LE from molecules adsorbed on metallic surfaces	23
2.2.4 Decoupling from the electrodes	24
2.2.5 Light emission mechanisms from decoupled molecules	28
2.3 Conclusions and outline	34
3 Narrow line emission of light from a molecular junction	37
3.1 Sample preparation	38
3.1.1 Concept of the experiment and basic methodology	38
3.1.2 Preliminary study	40
3.1.3 Synthesis of the co-polymers	42
3.2 Manipulation of the co-polymers by STM	44
3.3 Light emission	48
3.3.1 Experimental details	48
3.3.2 First experimental evidence	48
3.3.3 Effect of the coupling with the surface	50
3.3.4 Control of the emission energy by chemical engineering	55
3.3.5 Analysis of the vibronic peaks of the R-band	59
3.3.6 Towards a plasmon excitation mechanism: voltage bias dependency of the emission	66

3.3.7	Surface plasmons dependency of the emission intensity	70
3.3.8	Peak shape	72
3.3.9	Analysis of the B-band: observation of molecular hot electrolu- minescence	77
3.4	Vibrational spectroscopy on double DPP and on fused-ZnDPP	80
3.5	Summary and conclusions	85
4	STM-LE from graphene nanoribbons	89
4.1	Introduction	89
4.2	Synthesis of 7-AGNRs	92
4.3	Electronic and mechanical properties of 7-AGNRs	94
4.3.1	Manipulation of GNRs	94
4.3.2	Differential conductance	98
4.3.3	Tamm state	100
4.3.4	Conclusion	102
4.4	Light emission from 7-AGNR	103
4.4.1	Generation of C-terminated ribbons	104
4.4.2	Effect of the terminus on the light emission properties	105
4.4.3	STM-LE from C-terminated GNRs	107
4.4.4	Quantum yield of the emission	109
4.4.5	Shift of the spectral features with voltage	111
4.4.6	Negative bias	115
4.4.7	Dependency of the emission energy with z	116
4.4.8	STS on C-terminated GNRs	118
4.5	Origin of the light emission	120
4.6	Summary and conclusions	124
5	Conclusion and perspectives	127
	Appendices	131
A	Voltage threshold in the electron injection luminescence mechanism	133
B	Cyclo-dehydrogenation of porphyrins	137
C	Interaction between thiophene and fused-DPP	141
D	Scanning tunneling spectroscopy of suspended fused-DPP	145
	Bibliography	149
	List of publications	165

List of Figures

2.1	Energy diagrams of an STM junction.	7
2.2	Principle of functioning of the imaging modes of an STM.	9
2.3	Scheme of the STM.	12
2.4	Light collection system.	14
2.5	Light emission spectra and mechanism of STM-induced light emission.	18
2.6	Principle of the surface plasmons.	19
2.7	Light emission from a metallic surface.	22
2.8	Emission from molecules adsorbed on a metallic surface.	24
2.9	Decoupling methods.	25
2.10	Comparison of light emission mechanisms.	28
2.11	Single and double barrier tunneling junctions.	29
2.12	Electron injection mechanism.	31
2.13	Plasmon mediated mechanism.	32
2.14	Light emission from molecules on the shaft of an STM tip.	33
3.1	Experimental concept of an emitter in a molecular junction.	38
3.2	On-surface polymerization procedure.	39
3.3	Building blocks: DBrTT and Br ₂ -DPPH ₂	40
3.4	Cyclodehydrogenation of DPPH ₂	41
3.5	Synthesis of copolymers of fused-DPP and oligothiophene.	43
3.6	Manipulation of the copolymers of fused-DPP and oligothiophene.	45
3.7	First light emission spectra of fused-DPP.	49
3.8	Impact of the tip-sample separation on the width of the main peak in the light emission spectra.	51
3.9	Sketch of the lifting of the co-polymer.	52
3.10	Details of the light emission from fused-DPP.	53
3.11	Synthesis of co-polymers containing fused-MPP or fused-DNP.	56
3.12	Energy dependency of the main peak with the chromophore.	58
3.13	R-band of fused-DPP.	60
3.14	Models of vibronic transitions. Harmonics of a single mode and spectroscopy of different modes.	62
3.15	Comparison of experimental spectrum of the R-band with calculated optically active Raman modes.	63

3.16	Comparison of the R-band of fused-MPP, fused-DPP and fused-DNP.	65
3.17	Comparison of light emission mechanisms.	66
3.18	Onset of the emission and dependency with voltage.	67
3.19	Polarity dependence of the light emission.	69
3.20	Impact of the plasmon on the R-band.	71
3.21	Asymmetric shape of the 0-0 transition of fused-DPP.	73
3.22	Normalized electroluminescence spectra presenting three different behaviours at the 0-0 resonance and corresponding Fano fits.	74
3.23	Simulated spectra of lorentzian emission (red lines) and absorption (blue lines).	75
3.24	Details and origin of the B-band.	78
3.25	Synthesis of double fused-DPP and of fused-ZnDPP.	81
3.26	Optical spectra from double fused-DPP and from fused-ZnDPP.	82
3.27	Emission from the thermalised excited state. Emission from the non-thermalised excited state.	83
4.1	Structure of GNRs.	90
4.2	Synthesis of 7-AGNRs.	93
4.3	Lifting of 7-AGNRs.	95
4.4	Comparison of $G(z)$ for lifted 7-AGNRs and other molecular polymers.	95
4.5	Modulations of the conductance $G(z)$.	96
4.6	Lateral sliding and vertical lifting.	97
4.7	Differential conductance as a function of the applied bias (dI/dV) for H-terminated ribbons.	99
4.8	Differential conductance as a function of the tip-sample separation for H-terminated ribbons.	100
4.9	Tamm states of H-terminated ribbons.	101
4.10	Tamm states H-terminated ribbons in the lifted configuration.	102
4.11	First evidence of STM-LE from GNRs.	103
4.12	Controlled generation of C-terminated ribbons.	104
4.13	Controlled transformation of a ribbon terminus and impact on its optical spectrum.	106
4.14	Optical spectra of lifted C-terminated GNRs.	108
4.15	Optical spectra from lifted GNRs and from bare metallic surface.	109
4.16	Comparison of the emission intensity for C-terminated GNRs and fused-DPP.	111
4.17	Dependency of the light emission with the voltage bias.	112
4.18	Optical spectra from GNR at positive and negative polarities.	115
4.19	Dependency of the light emission with the tip-sample separation.	116
4.20	dI/dV spectra of C-terminated GNRs.	119
4.21	Tip-GNR interaction.	121

4.22	Example of light emission mechanisms involving relative shift of GNR states.	123
A.1	Impact of the voltage drop in the electron injection mechanism.	134
B.1	Porhyrins and their fused counterparts after dehydrogenation.	138
C.1	DFT calculation of the relaxed structure of a co-polymer of fused-DPP and oligothiophene.	142
C.2	Synthesis and characterization of co-polymers based on 5,15-(dibromo - diphenyl)-porphyrin. and DBrTT.	143
D.1	Extreme variability of the STS spectra for a single suspended co-polymer of oligothiophene and fused-DPP.	146

List of abbreviations

AFM atomic force microscopy. 5

AGNR graphene nanoribbon with armchair edges. 89

Br₂-DNPH₂ 5,15-(dinaphthalene)-10,20-(dibromo)-porphyrin. 57

Br₂-DPPH₂ 5,15-(diphenyl)-10,20-(dibromo)porphyrin. 39

Br₂-MPPH₂ 5-(phenyl)-10,20-(dibromo)-porphyrin. 55

DBrTT 5,5''-Dibromo-2,20:5',2''-terthiophene. 39

DFT density functional theory. 42

DPPH₂ 5,15-(diphenyl)-porphyrin. 40

fused-DNP fused-dinaphthalene porphyrin. 57

fused-DPP fused-diphenyl porphyrin. 41

fused-MPP fused-monophenyl porphyrin. 57

FWHM full width at half maximum. 17

GNR graphene nanoribbon. 89

LSP localised surface plasmon. 19

NCP nano-cavity plasmon. 20

- RDS** reflectance difference spectroscopy. 92
- SEM** scanning electron microscope. 22
- SPP** surface plasmon polariton. 20
- STM** scanning tunneling microscope. 5
- STM-LE** STM-induced light emission. 5
- STS** scanning tunneling spectroscopy. 10
- TD-DFT** time-dependent density functional theory. 42
- TERS** tip-enhanced Raman scattering. 20
- UHV** ultra high vacuum. 11
- ZGNR** graphene nanoribbon with zigzag edges. 89

Resumé

Introduction

La détection des molécules uniques et la possibilité de caractériser leurs propriétés optiques sont devenues réalité à la fin des années 1980 [1, 2, 3]. L'un des intérêts dans l'étude des molécules uniques est dans la possibilité de découvrir des comportements et des interactions qui peuvent être cachés lors de la réalisation de mesures d'ensemble. En outre, il est plus facile de modéliser des molécules uniques que des systèmes plus complexes, rendant ainsi une comparaison entre les expériences et la théorie plus fiable. Dans des expériences à molécule unique, on utilise des sondes optiques non invasives qui permettent de étudier des molécules uniques situées dans des matrices solides. Les méthodes les plus courantes sont basées sur la mesure d'un signal de fluorescence qui fournit des informations détaillées sur les molécules uniques ainsi que sur leur environnement [4, 5, 6]. Cependant, dans ces approches tout-optiques, la résolution spatiale de l'excitation est limitée par diffraction, et il n'y a pas de possibilité de contrôler directement l'environnement à l'échelle nanométrique des molécules.

Une alternative consiste à utiliser des électrons plutôt que des photons pour étudier les propriétés optiques des molécules. L'avantage principal des électrons est qu'ils peuvent être confinés à des chemins d'échelle atomique. Pour la première fois en 2003 [7], il a été démontré que la luminescence d'une seule molécule peut en effet être excitée par le courant tunnel d'un microscope à effet tunnel (*scanning tunneling microscope* - STM). La réponse optique de la molécule a même pu être sondée en fonction des variations sous-moléculaires de la position de la pointe du STM, suggérant que ce type de spectroscopie optique pourrait atteindre une sensibilité à l'échelle atomique [8]. Un autre avantage de cette méthode est que l'environnement nanométrique de la molécule émettrice est connu et est potentiellement contrôlable en utilisant la pointe de la STM [9, 10, 11]. Enfin, cette approche d'excitation électronique est également pertinente pour les futures applications optoélectroniques qui reposent sur la combinaison des circuits électriques et photoniques/plasmoniques. Dans de tels dispositifs hybrides, des éléments optiquement actifs seraient intégrés dans des circuits électroniques usuels. Dans ce contexte, nous sommes intéressés à démontrer que des jonctions à une seule molécule (c'est-à-dire une molécule unique reliant directement deux électrodes) peuvent être utilisées pour convertir une stimulation électrique en un signal optique bien

contrôlé.

Après avoir décrit certains des avantages potentiels d'utiliser un STM pour exciter électriquement les propriétés optiques d'une molécule unique, on introduit son principal inconvénient: la nécessité absolue d'utiliser des électrodes pour injecter et collecter le courant électrique. Le contact direct avec un substrat métallique est connu pour altérer les orbitales moléculaires et provoque l'extinction (*quenching*) de la luminescence moléculaire, c'est à dire l'absence de transitions intramoléculaires radiatives [12]. Il a fallu dix ans après la première expérience d'émission de lumière des molécules induite par STM [13] pour trouver une solution à ce problème. En utilisant une couche mince d'oxyde (d'une à deux atomes d'épaisseur) pour découpler des molécules uniques à partir d'un substrat métallique, Qiu *et al.* ont montré que la luminescence des porphyrines peut être excitée par les électrons qui peuvent *tunnelier* de la pointe STM au substrat métallique sous-jacent [7]. Il est surprenant que, dans les dix années qui ont suivi ce travail séminal, seules quelques expériences ont utilisé le STM pour étudier les propriétés optiques des molécules uniques et ont toutes utilisé une stratégie de découplage similaire [14, 8, 15]. Une problématique courante de ces expériences réside dans la difficulté à déterminer les transitions électroniques à l'origine de l'électroluminescence. En effet, dans ces exemples, les énergies d'émission observées ne sont pas compatibles avec la fluorescence attendue des molécules sondées. Cette question, comme nous le verrons dans le manuscrit, soulève également des questions fondamentales concernant le mécanisme d'électroluminescence, qui supposait une recombinaison radiative d'électrons et de trous injectés dans la molécule à partir des électrodes [7].

Outre que ces considérations fondamentales, l'approche de Qiu *et al.* est également limitée en ce qui concerne les applications futures, où un contact direct entre la molécule et l'électrode est obligatoire. La configuration dans laquelle une seule molécule relie directement deux électrodes est largement étudiée dans la communauté de jonction de rupture [16, 17] car elle peut être formée dans de nombreuses conditions expérimentales (y compris la température ambiante et dans le liquide) mais aussi parce qu'elle constitue l'étape ultime de miniaturisation d'un dispositif électronique organique. Fournir un tel dispositif à échelle moléculaire avec des fonctionnalités optiques apparaît comme une perspective naturelle et passionnante. En effet, comme avec tout dispositif électronique, les composants moléculaires ont une bande passante limitée à la bande GHz [18]. Les dispositifs qui combinent des éléments électroniques et photoniques ou plasmoniques peuvent permettre d'étendre la bande passante par plusieurs ordres de grandeur [19, 20, 21]. Cependant, dans cette configuration *orientée dispositif*, on s'attend que le contact direct avec les électrodes métalliques altère les propriétés de la molécule et étanche son émission. Pour contourner cette impasse conceptuelle, Reecht *et al.*, ont proposé une stratégie consistant à suspendre des fils moléculaires longs entre la pointe et l'échantillon du STM. Dans ce cas, alors que les extrémités du fil - un oligothiophène conjugué de 4 à 5 nanomètres longs - sont en contact direct avec les électrodes, la partie centrale du fil est suffisamment découplée pour qu'un pic de luminescence, attribué à une transition intramoléculaire, soit observée [22]. Bien

que cela constitue un exemple intéressant d'un dispositif émetteur de lumière à une seule molécule, la largeur de l'émission (≈ 300 mV) ne permet pas une analyse spectroscopique détaillée et empêche une analyse plus détaillée des mécanismes impliqués. En outre, ce système ne comporte pas certains degrés de liberté qui permettraient à l'expérimentateur de régler ses paramètres d'émission tels que l'intensité, la couleur ou la largeur de la ligne.

Par conséquent, l'objectif de ce manuscrit est double. Il vise à mieux comprendre le mécanisme à l'origine de la luminescence des molécules uniques excitées par les électrons et à répondre à certains des défis qui peuvent transformer les dispositifs optoélectroniques à échelle moléculaire plus proches de la réalité.

Ce manuscrit est composé de trois parties.

Le **chapitre 2** est une introduction technique à l'instrumentation, à l'STM et à l'émission de lumière par STM.

Le **chapitre 3** est consacré à l'observation d'une ligne étroite d'émission de lumière à partir d'une jonction moléculaire spécifiquement conçue.

Le **chapitre 4** est consacré aux propriétés optoélectroniques de nano-rubans de graphène (*graphene nanoribbons*, GNR) uniques.

Dans la suite nous procédons à resumer le contenu de trois chapitres.

Chapitre 2: Microscope à effet tunnel et émission de lumière induite par STM

Dans ce chapitre, nous présentons d'abord les principales techniques et instruments utilisés dans le cadre de cette recherche, puis décrivons l'état de l'art des sujets qui seront discutés au cours de ce document. Le principal instrument que nous avons utilisé est le microscope à effet tunnel (STM). Il a été inventé en 1981 par Gerber, Binnig et Rohrer [23, 24, 25] qui ont reçu le prix Nobel pour son développement en 1986. La première partie du chapitre est consacrée à la fonction de la STM, à l'explication de ses différents modes de fonctionnement et à la description de notre installation expérimentale. Cela nous amènera à la spécificité de l'instrument que nous utilisons: un système de collection de lumière qui permet d'effectuer des mesures d'émission de lumière induite par la STM (STM-LE), coeur de la plupart des résultats présentés dans ce manuscrit.

L'invention du STM a été précédée par la conception du *topographiner* au début des années 1970 [26, 27], un instrument qui contenait la plupart des éléments que l'on pourrait trouver dans un microscope à effet tunnel. Cependant, c'est cette dernière qui a le plus affecté le domaine de la science de surfaces.

L'invention du STM a ouvert l'ère de la microscopie à sonde de balayage, un type de microscopie où une sonde est utilisée pour balayer une surface pour produire des images topographiques de la surface elle-même et des objets nanoscopiques déposés sur elle. Différentes techniques de sonde de balayage ont été inventées depuis, y compris la microscopie à force atomique (AFM) [28], la microscopie à force magnétique [29] et la sonde Kelvin microscopie de force [30], pour en mentionner quelques-uns. Le STM et le AFM offrent, encore aujourd'hui, la meilleure façon de produire des images *réels* avec une résolution au delà de l'ångström.

Éffet tunnel

Nous allons d'abord présenter les concepts de base de la microscopie à effet tunnel. La spécificité de la STM réside dans l'utilisation de l'effet de tunnel quantique qui donne son nom à cet outil. Lorsque deux électrodes sont rapprochées les unes des autres à une distance de quelques angströms, et qu'une tension V est appliquée entre eux, des électrons de faible énergie (quelques eV) peuvent circuler d'une électrode à l'autre. Ces électrons traversent la barrière de potentiel de vide en raison de l'effet tunnel. Le processus de *tunneling* est décrit par l'équation de Schrödinger pour les électrons:

$$\frac{-\hbar}{2m} \nabla^2 \psi(\vec{r}) + [V(r) - E]\psi(\vec{r}) = 0, \quad (1)$$

où \hbar est la constante de Planck réduite, m et E sont la masse et l'énergie de l'électron, $\psi(r)$ est la fonction d'onde à la position r , et $V(r)$ la barrière de potentiel à la position r . La probabilité de trouver un électron à une certaine position r est proportionnelle au carré de la fonction d'onde à cette position. En résolvant l'équation de Schrodinger, nous pouvons connaître la probabilité de trouver l'électron d'un côté ou de l'autre de la barrière, ou même à l'intérieur de la barrière. Dans une dimension, z , pour une barrière de potentiel constante ($V = V_0$), la solution de l'équation est:

$$\psi(z) \propto e^{\pm kz}, \quad (2)$$

où la constante de décroissance est

$$k = \frac{\sqrt{2m(V_0 - E)}}{\hbar}. \quad (3)$$

Dans le STM le rôle des électrodes est joué par une surface plane et par une pointe métallique. En raison de la dépendance exponentielle avec la distance, les électrons circulant depuis les derniers atomes de la pointe dominant le signal. Pour cette raison, l'extension spatiale du flux d'électrons peut être considérée comme la plus localisée au sein de ces atomes. Ceci explique la résolution latérale sous-nanométrique de la STM.

Emission de lumière induite par STM

Le STM peut être utilisé pour exciter localement la luminescence (émission de lumière induite par STM ou STM-LE) à partir d'un échantillon métallique ou semiconducteur [31, 32, 33]. En utilisant un système de détection approprié (*c.f.* section 2.1.3), il est possible de mesurer des spectres d'émission lumineuse comme celui présenté dans la figure 2.5(a), où le nombre de photons est tracé en fonction de leur énergie.

Nous pouvons expliquer le mécanisme d'émission de lumière induit par STM comme le produit de deux facteurs: les électrons tunnel inélastiques et les plasmons de surface localisés (*c.f.* section 2.2.1). Cela peut être exprimé en termes d'une règle d'or de Fermi [34], où le taux d'émission à la fréquence ν est

$$\Gamma(\nu) = \frac{2\pi}{\hbar^2} |\langle i | \hat{d} | f \rangle|^2 \rho(\nu) E_Z(M)^2, \quad (4)$$

où $|\langle i | \hat{d} | f \rangle|$ est le moment dipolaire de transition entre un état initial $|i\rangle$ et un état final (après la transition) $|f\rangle$ et $\rho(\nu) E_Z(M)^2$ sont la densité spectrale (à une fréquence ν) et la densité spatiale (à une position M) du champ électromagnétique. En d'autres termes, le premier est le terme décrivant la transition électronique entre les états occupés d'une électrode et les états inoccupés de l'autre électrode, représentant ainsi le courant inélastique, tandis que le second terme décrit la contribution plasmonique.

La suite du chapitre 2 est dédié à l'état de l'art, au début de mon doctorat, sur le thème de l'émission de lumière induite par STM (*c.f.* section 2.2.2), avec un focus sur les systèmes de molécules et les molécules uniques (*c.f.* section 2.2.3 et 2.2.4), et une section sur les mécanismes d'excitation des molécules (section 2.2.5).

Conclusions

La résolution spatiale extrême d'un STM permet d'étudier les propriétés des molécules uniques, une caractéristique qui a un énorme potentiel pour la compréhension des propriétés fondamentales de ces objets. Cependant, les études STM-LE de molécules uniques rapportées jusqu'à présent, ne parviennent pas à exploiter pleinement ce potentiel.

Un exemple est l'origine de l'émission lumineuse: des spectres optiques montrant des pics avec une énergie bien définie (et une émission de largeur de bande étroite) ont été rapportés dans plusieurs expériences [7, 14, 8, 15]. Cependant, l'affectation de ces pics à une transition optique bien définie n'est pas simple.

Un autre exemple concerne les pics vibrationnels dans les spectres optiques. Bien que ces caractéristiques aient été observées dans certaines expériences [7, 14, 8], elles découlent d'une progression harmonique d'un seul mode, ne fournissant ainsi pas d'empreinte chimique de l'émetteur comme celle obtenue par spectroscopie Raman.

De plus, même si les sources de photon unique dans une expérience STM-LE ont été observées récemment [35], ce sont des grappes de molécules qui rendent impossible la localisation de l'émetteur spécifique.

Enfin, dans toutes les expériences sur des molécules uniques, une excitation électronique de l'émetteur à travers le courant tunnel a été suggérée. Cependant, l'existence du mécanisme d'excitation à médiation plasmon [36, 37], qui a été prouvée pour les multicouches de molécules, laisse une question ouverte sur la possibilité que ce mécanisme puisse aussi jouer un rôle dans le STM-LE des molécules simples.

Si l'on se tourne vers les aspects applicatifs et qu'on souhaite intégrer une composante moléculaire dans un circuit électronique, le contact direct de la molécule avec les électrodes devient essentiel. Cependant, dans cette configuration, l'interaction avec la pointe métallique et l'échantillon éteint la plus grande partie de la fluorescence. Le travail récent de Reecht *et. al* a prouvé que, en utilisant des molécules allongées, il est possible de observer la fluorescence d'une jonction moléculaire [22]. Cependant, le couplage résiduel avec les électrodes a entraîné un élargissement du pic d'émission à une largeur de ≈ 250 meV, comparable à celui d'une émission purement plasmique.

La possibilité de générer une émission de lumière de ligne étroite (FWHM dans la gamme meV) à partir d'un système moléculaire en contact avec les électrodes est donc encore manquante. La construction d'un tel système serait utile pour la conception de dispositifs qui interagissent des circuits électroniques avec des circuits optiques et plasmoniques.

Certaines caractéristiques spécifiques seraient souhaitables dans un tel dispositif. Tout d'abord, l'énergie d'émission doit être bien définie et prévisible. Un contrôle sur les propriétés de la lumière émise, comme la couleur et la cohérence, serait souhaitable. Selon l'utilisation spécifique, il peut être utile d'avoir soit des photons à la demande (source à photon unique) soit une luminosité élevée. Pour obtenir une luminosité élevée, un rendement quantique élevé et / ou la possibilité de commander la composante à courant élevé sont nécessaires. Dans une étape ultérieure, il serait important d'obtenir une résistance mécanique et une consistance élevées (présentant les mêmes propriétés à chaque fois).

Les chapitres 3 et 4 sont donc dédiés à fournir des solutions à certains questions qu'on vient de ouvrir.

Chapitre 3: Émission de lumière étroite d'une jonction moléculaire

Dans ce chapitre, nous présentons un rapport sur la synthèse et la caractérisation de systèmes à molécules simples qui permettent une émission de ligne étroite tout

en conservant une configuration de dispositif. Le système se compose d'un émetteur intégré dans un fil moléculaire qui relie les électrodes. Ce système est une version nanométrique échelle organique d'un point quantique intégré dans un nanofil [38].

Synthese

Ces dispositifs ont été fabriqués par une technique de co-polymérisation [39] de surface entre des molécules chromophores et de chaînes de oligothiophènes (*c.f.* section 3.1). Les oligothiophènes sont des molécules conjuguées- π qui peuvent former de longs fils et dont les propriétés électroniques, mécaniques et optiques ont été étudiées au niveau d'une molécule unique [40, 22, 41]. Les fils sont stables et permettent l'utilisation de courants assez élevés lorsqu'ils sont suspendus entre la pointe et l'échantillon ($I < 5$ nA). Les dérivés de porphyrine ont été choisis comme émetteurs moléculaires. Les molécules de la famille des porphyrines montrent généralement une absorption et une émission dans le visible du fait de la conjugaison étendue du macrocycle composant le noyau de la molécule de base, la porphyrine. C'est donc l'une des familles de colorants les plus étudiées, avec les phtalocyanines. De plus, ces molécules jouent un rôle important dans de nombreux processus biologiques, y compris la photosynthèse. L'étude de leurs propriétés optiques jusqu'au niveau d'une molécule unique est donc pertinente pour obtenir une compréhension atomique de ces phénomènes. Lors de la réalisation des co-polymères, on remarque que la porphyrine se transforme en une version dit *fused* (fused-DPP), ce qui change ses propriétés optiques.

Tirage

Une fois les copolymères synthétisés, l'objectif est de les soulever de la surface. C'est une étape clé pour obtenir une configuration dans laquelle la porphyrine est suspendue entre la pointe et l'échantillon de notre STM, et potentiellement découplée des électrodes par les chaînes oligothiophène.

La procédure pour soulever le fil est similaire à celle introduite par Lafferentz *et al.* sur le polyfluorène [42] et plus tard utilisée pour lever d'autres fils moléculaires, y compris les nano-rubans de graphène [43], oligothiophène [22] et d'autres [44, 45].

Nous appliquons cette procédure à des fils terminés par une porphyrine fusé qui sera utilisé comme unité d'ancrage pour le levage. Le détails de la procédure sont décrit en section 3.2.

Émission de lumière

Une fois que le copolymère est suspendu dans la jonction, nous procédons à la mesure de son émission lumineuse. Nous avons observé que quand on commence à tirer le fil moléculaire, la raie de l'émission lumineuse est large. En soulevant plus le co-polymères, de que on découple une porphyrine de la surface, on peut mesurer une émission de ligne étroite ($\text{FWHM} \leq 3 \text{ meV}$).

Source de l'émission. Le pic d'émission est centrée à 817 nm, correspondant à une énergie de 1,52 eV. Selon l'échantillon étudié, l'énergie varie légèrement entre 1,47 et 1,55 eV. Ces valeurs concordent parfaitement avec le gap optique théorique du fused-DPP (1,51 eV) calculé par TD-DFT. Ceci est une forte indication que l'émission lumineuse provient de la transition $S1 \rightarrow S0$ d'une porphyrine *fused*.

L'attribution de l'émission à la porphyrine fusionnée est confirmée par le changement du chromophore utilisé pour construire le copolymère. En utilisant une molécule avec une longueur de conjugaison plus grande, il est possible de déplacer de manière prévisible le pic de l'émission à une énergie plus faible, tandis qu'en utilisant une plus petite longueur de conjugaison le pic se déplace à des énergies plus élevées (*c.f.* section 3.3.4).

Quelques autres résultats obtenus sur ce système sont:

Empreinte chimique. Outre la ligne principale (0-0), les spectres d'émission lumineuse présentent deux bandes de pics de vibrations: l'une à énergie inférieure (la bande R) et l'autre à énergie plus élevée (la bande B). Nous avons analysé le premier et prouvé qu'il provient des transitions du niveau fondamental vibrationnel de $S1$ aux états vibrationnels excités de $S0$, chacun appartenant à un mode différent (transitions 0-1). Les énergies de ces pics sont bien reproduites par des modes Raman optiquement actifs calculés. C'est la première fois que ce type d'empreinte spectroscopique est observé sans l'utilisation d'une source lumineuse externe. En d'autres termes, notre expérience ajoute une résolution chimique à une expérience STM, sans la nécessité d'un laser.

Mécanisme de excitation. Nous avons démontré que le mécanisme d'excitation est de type *mediée par les plasmon* plutôt que due à l'injection d'électrons et de trues des électrodes. L'interaction avec le plasmon de nanocavité est cependant assez complexe, comme illustré par l'intensité relative des pics vibratoires et par la forme asymétrique de la ligne d'émission principale. L'observation d'une forme de ligne de Fano est une indication d'une interaction avec le plasmon qui est responsable d'une large émission de fond.

Une conséquence de l'interaction avec les plasmons de surface localisés est une réduction drastique de la durée de vie de la fluorescence. Il en résulte l'observation des pics vibratoires de la bande B, qui sont interprétés en termes d'émission d'un état exci-

tonique non-thermalisé, phénomène connu sous le nom de *dehot-luminescence*. Pour que la hot-luminescence soit mesurable, le processus d'émission de lumière doit être en compétition avec la relaxation vibrationnelle à l'intérieur de l'état S1, phénomène qui est typiquement des ordres de grandeur plus rapides en l'absence des plasmons.

Nous avons observé la luminescence des excitons non-thermalisés en deux configurations.

Pour le MPP *fused* et le DNP *fused* (c.f. section 3.3.9), l'état fondamental S0 et l'état excité S1 sont *alignés dans l'espace*. Il en résulte une quasi-symétrie entre la bande B et la bande R. Pour le DPP double et le ZnDPP (c.f. section 3.4), les états S0 et S1 sont décalés et présentent une progression harmonique des pics associés à un seul mode vibratoire. Dans ce cas, la majeure partie de l'émission provient des états non thermalisés de S1.

Ces observations ont permis d'estimer la durée de vie de la fluorescence en présence des plasmons de surface localisés dans la plage de 0.3 à 10 ps. Une façon de déterminer précisément la durée de vie serait de mesurer la corrélation de temps entre les photons émis. Ce type d'expérience, réalisée à l'aide d'un interféromètre Hanbury Brown-Twiss, permettrait également de prouver si l'émetteur est une source de photons uniques, comme cela a été récemment fait dans une expérience STM-LE pour des multi-couches de molécules par Merino *et al.* [35].

Une configuration orientée dispositif. Une des motivations de notre concept expérimental était la nécessité d'un contact direct du système moléculaire avec les électrodes, afin de permettre la conception future de dispositifs optoélectroniques à l'échelle moléculaire. Non seulement nous avons prouvé qu'il est possible d'avoir une émission avec un pic fin dans cette configuration, mais nous avons également montré que nous pouvons contrôler certaines de ses propriétés.

Tout d'abord, nous avons montré que nous pouvons contrôler la largeur de ligne de cette émission en accordant le couplage avec la surface de l'échantillon (c.f. section 3.3.3). Cela permet de régler continuellement à partir d'une émission *large* (FWHM ≥ 100 meV) à une très étroite (FWHM ≈ 2 meV).

Deuxièmement, nous avons présenté la possibilité de générer des spectres d'émission lumineuse semblables, presque monochromatiques, à différentes énergies. Cela a été fait en adaptant la nature chimique de l'émetteur. Nous atteignons de cette manière une émission à 1.28 eV, à 1.51 eV et à 1.68 eV selon l'émetteur utilisé. Ces valeurs correspondent aux gaps optiques calculés par TD-DFT. Cela implique qu'on a une manière prédictive de choisir la molécule à utiliser, selon la couleur nécessaire pour chaque application.

Ces deux exemples illustrent l'intérêt de cette installation pour l'intégration de circuits opto-électroniques à l'échelle moléculaire. Une autre expérience intéressante serait l'étude de l'impact d'un émetteur dans une configuration comme celle que nous avons proposée, sur les polaritons de plasmon de surface propagateurs [46, 47, 48, 49, 50].

La découverte d'une empreinte du chromophore, éventuellement sous forme d'un *true* dans l'émission des plasmons de surface, montrerait la possibilité d'intégrer des circuits électroniques et plasmoniques à l'échelle moléculaire.

Chapitre 4: STM-LE de nano-rubans de graphène.

Le graphène est perçu comme le matériau de l'avenir dans de nombreuses applications de la nanoélectronique, de la conservation de l'énergie, de la médecine, des télécommunications, etc. Malgré ses nombreuses propriétés impressionnantes et son caractère 2D, l'absence d'un gap électronique dans la structure de bande de graphène limite ses applications en optoélectronique et en photonique.

Si on plie ou si on découpe une feuille de graphène on obtient des matériaux avec un gap optique (*i.e.*, les nanotubes de carbone [51, 52] et les nano-rubans de graphène [53, 54]). Dans ces matériaux, la plupart des propriétés mécaniques, de transport et chimiques du graphène sont préservées, tandis que la présence d'un gap optique ouvre de nouvelles possibilités pour la réalisation de dispositifs tels que les transistors à effet de champ et les composants optoélectroniques [53, 55, 56].

Ce chapitre est consacré à l'étude des nano-rubans de graphène (GNR) qui présentent un gap optique. Dans ces structures 1-D, le gap dépend de la largeur exacte du GNR et de la structure atomique de ses bords [54, 57].

Les rubans de taille finie peuvent présenter des bords en zigzag et en fauteuil (*Armchair*). Le nom donné à un ruban contient des informations relatives à la symétrie de ses bords dans l'axe long (A pour *Armchair*, Z pour *Zigzag*) et le nombre d'atomes de carbone dans leur axe court.

Les deux types de GNR (zigzag et *armchair*) présentent des propriétés intéressantes. Les ZGNR, par exemple, devraient avoir des états de bord polarisés par spin qui ressemblent à des isolants topologiques 2D, qui peuvent trouver des applications pour la spintronique à base de graphène [58, 59].

Les rubans de type *armchair* offrent, au contraire, un gap de bande qui dépend fortement de la largeur atomique du ruban [54]. Les AGNRs peuvent être divisés en trois familles: les rubans de $3m$ ou $3m+1$ carbones (avec un nombre entier déterminant la largeur du ruban) se comportent comme des semi-conducteurs tandis que les GNR de $3m+2$ carbones ont un petit gap et se comportent presque comme des métaux. Pour les trois familles, l'écart diminue lorsque m augmente.

Des mesures directes des propriétés optiques des GNR sont compliquées, en particulier au niveau d'un ruban unique. Récemment, des mesures de *reflectance difference spectroscopy* sur des 7-AGNRs atomiquement précis adsorbés sur un substrat métallique cite Denk2014 a démontré l'impact des effets excitoniques dans la réponse optique. Le rôle des effets excitoniques et bi-excitoniques a été mis en évidence par des expériences de

pompe-sonde sur GNR en solution cite Soavi2016. Ces études sont appuyées par des calculs théoriques approfondis et des résultats cohérents, soulignant à la fois le niveau élevé de compréhension de ces systèmes et l'intérêt qu'ils génèrent. Cependant, il s'agit principalement de mesures de σ en ensemble. Une étude des propriétés optiques au niveau du GNR unique est toujours manquante.

STM-LE fournit un moyen d'étudier les propriétés optiques de nano-rubans individuels suspendus entre la pointe et l'échantillon. Ce chapitre présente une étude détaillée de ces propriétés.

Synthese

Nous avons synthétisé des nano-rubans de graphène de 7 atomes de carbone de largeur (7-AGNR) sur un substrat Au (111). La synthèse suit la procédure décrite dans [60]. Un monomère précurseur (10,10'-dibromo-9,9'-bianthryl) est sublimé sur un substrat Au(111) maintenu à la température ambiante. Lors du recuit thermique, il se produit une dé-halogénéation et le couplage C-C conduit à la formation de polymères linéaires. Le recuit à une température plus élevée active une réaction de cyclo-déshydrogénation qui conduit à la formation de GNR entièrement aromatiques. Les deux réactions ont été réalisées en une seule étape de recuit à une température de 670 K.

Les GNR produits peuvent présenter des terminus différents, un comportement qui a été précédemment rapporté dans [43, 61] et analysé en détail dans [62]. Sur la base d'une comparaison avec des images STM simulées, la nature des différentes extrémités a été déterminée. Il est montré qu'ils dépendent essentiellement du numéro de coordination de l'atome de carbone central de l'arête court 7-AGNR et de la nature chimique de l'atome auquel il est lié. Lorsque cet atome C est laissé avec un électron non apparié (terminé en C), il apparaît plus sombre dans la partie centrale du bord. La plupart du temps, le carbone est passivé par un atome de hydrogène (terminé en H), ce qui donne une structure à trois points. Un second hydrogène peut se lier avec le même carbone (terminé en 2H), ce qui donne une structure stable qui apparaît sans caractéristiques dans les topographies.

Manipulation

Dans un premier temps, nous avons levé un nano-ruban suivant la procédure décrite au chapitre ref Manipulation. Il est instructif de comparer la courbe $G(z)$ du tirage de GNRs avec celle du polyfluorène, ou de l'oligothiophène. Alors que les oscillations périodiques de la conductance avec z sont observées pour les deux polymères, elles sont absentes pour la GNR.

Dans le cas du polyfluorène, les oscillations peu profondes ont été attribuées à la

flexion locale de la chaîne moléculaire [42]. Pour l'oligothiophène, les changements de conductance sont plus brusques. Leur périodicité a été attribuée au détachement de monomères de thiophène de la surface [41]. La composante abrupte est liée à une modification de la conjugaison du fil. Une augmentation de la contrainte mécanique se produit avant le détachement d'un monomère de la surface, en réduisant la conjugaison et par conséquent la conductance. La contrainte est libérée après le détachement du monomère, ce qui entraîne une conjugaison et une conductance accrues.

L'absence de telles caractéristiques sur le spectre GNR pourrait être le signe d'une interaction plus faible avec la surface, ce qui entraînerait un glissement plus facile des GNR sur l'or. Des expériences récentes de microscopie à force atomique ont en effet montré que les GNR se déplacent presque sans friction sur Au(111) [63]. Dans une première approximation, nos mesures sont en accord avec cette hypothèse.

Transport électronique

Une fois que le GNR est surlevé dans la jonction, nous procédons à la mesure de ses propriétés de transport. Les spectres dI/dV dans la géométrie soulevée ressemblent à celui des 7-AGNR posés à plat sur la surface de l'échantillon. Cette observation est expliquée par la chute de tension principalement à l'interface pointe-GNR. Ceci est encore étayé par le faible impact de la séparation de l'échantillon de pointe dans la configuration soulevée sur l'énergie des états.

L'effet principal du contact pointe-GNR est observé dans la largeur des résonances, qui est réduit ($\text{FWHM} \approx 50 \text{ meV}$) par rapport à la configuration à plat. Ceci suggère que les GNRs soulevés sont partiellement découplés des électrodes. Toutes les autres caractéristiques des rubans sont préservées dans cette configuration, y compris la taille de l'espace et la présence de l'état Tamm. Nous disposons maintenant des informations essentielles pour l'étude des propriétés optiques des jonctions GNR.

Émission de lumière

Les GNR en suspension montrent deux types différents de spectres d'émission lumineuse, selon la nature de l'extrémité d'où ils sont soulevés. Les GNR terminés en H montrent une émission large et sans caractéristiques, alors que les rubans terminés en C montrent une émission avec un pic étroit. On se focalise donc sur l'émission des rubans de-hydrogénés (terminé en C).

Nous avons trouvé une résonance principale à une énergie de 1,61 eV dans le spectre d'émission lumineuse des nanorubans de graphène à terminaison C. Nous avons remarqué avec surprise que la largeur du pic principal est presque un ordre de grandeur plus petite que dans le cas des rubans de H-terminated. Il est en effet inattendu de mesurer une caractéristique d'émission de lumière aussi forte que 40 meV avec un

système en contact direct avec les électrodes [22]. La largeur étroite du pic et la reproductibilité de son point d'énergie vers une origine intra-ruban de l'émission. Cependant, la largeur du pic principal est un ordre de grandeur plus grand que celui observé dans le chapitre 3 pour les porphyrines fusionnées. Cela suggère que le système n'est pas aussi bien découplé.

Pics vibrationnelles. Deux caractéristiques de faible énergie ont également été détectées, ce qui révèle une dispersion énergétique proche de linéaire. En raison de leur faible intensité et du fait qu'ils n'apparaissent pas si la ligne d'émission principale n'est pas excitée nous les assignons provisoirement à la progression vibronique d'un seul mode. Leur changement d'énergie est en bon accord avec le pic Raman D du graphène ($1340 \text{ cm}^{-1} \approx 0.166 \text{ eV}$) [64] et des matériaux à base de carbone sp^2 en général, ce qui est associés aux modes de respiration des anneaux à six atomes. Il est intéressant de noter, que pour être observable, ces modes nécessitent un certain désordre ou la présence de défauts [65]. Le pic D a été précédemment mesuré et calculé pour des mesures Raman sur des GNR dans différentes configurations [60, 66].

Rendement quantique. Une analyse de l'intensité de l'émission des GNR montre qu'ils sont plus efficaces que les jonctions d'or pour générer une émission de lumière à basse tension. Des rendements similaires ont été observés dans le cas de l'émission de porphyrines que nous avons présentée au chapitre 3. Cependant, les GNR offrent la possibilité d'utiliser des courants beaucoup plus grands, ce qui entraîne une plus grande intensité absolue de l'émission

Origine de l'émission. De plus, la transition optique montre un changement d'énergie linéaire avec la tension appliquée, ainsi qu'avec la séparation échantillon-pointe. Ceci est probablement dû à un effet Stark induit par le champ électrostatique dans la jonction STM, ou à un déplacement relatif des niveaux moléculaires impliqués dans la transition optique, induite par la tension appliquée. En extrapolant l'énergie du pic principal à un biais nul, on déduit que la transition optique, dans le système non perturbé, a une valeur de 1.15 eV. Cette valeur est incompatible avec l'écart optique attendu de 7-AGNR (1.9-2.3 eV). Ces observations ont motivé l'hypothèse que l'émission lumineuse provient d'une transition entre un état Tamm des rubans et un état délocalisé.

Conclusion

Dans ce manuscrit, nous avons étudié les propriétés optoélectroniques des jonctions moléculaires réalisées avec un microscope à effet tunnel (STM). La thèse est basée sur deux chapitres expérimentaux. Le chapitre 3 est consacré à la synthèse et à la caractérisation optoélectronique du co-polymère moléculaire composé d'une molécule émettrice incorporée dans un fil moléculaire. Le chapitre 4 est une étude des propriétés

de transport et d'émission lumineuse des nanoribbons de graphène (GNR).

Les aspects communs de ces deux études sont dans la méthode de synthèse et dans la configuration expérimentale utilisée pour réaliser les études d'émission lumineuse. La synthèse des co-polymères et des GNR est réalisée en utilisant une technique de polymérisation sur surface suivie d'une réaction de cyclo-déshydrogénation. Dans les deux cas, le système moléculaire est soulevé entre la pointe et l'échantillon du STM pour fournir un découplage des électrodes métalliques.

D'un point de vue fondamental, la limite principale de la configuration soulevée est la perte de capacité d'imagerie de la STM. De plus, une fois qu'un fil est suspendu dans la jonction, nous ne pouvons plus mesurer la variation de l'émission de lumière avec la position de pointe, ni avons la possibilité de déplacer des objets ou des molécules proches.

Certaines expériences récentes de STM-LE à partir de phtalocyanines interagissant sur NaCl/Ag [67, 68] mettent en évidence l'intérêt d'utiliser une configuration où les molécules reposent à plat sur une surface. Dans ces expériences, grâce à l'excitation spatialement résolue, l'interaction entre des molécules voisines peut être observée dans les spectres optiques, montrant des variations dans *l'espace réel*.

Les expériences STM-LE dans la configuration soulevée restent d'une grande importance pour étudier les futurs dispositifs moléculaires. Dans cette perspective, nous avons déjà discuté du grand contrôle qui peut être obtenu en incorporant un émetteur dans un fil moléculaire suspendu (chapitre 3). Cependant, ce système a également révélé certaines limites en termes de stabilité, de reproductibilité et de luminosité. Ces problèmes ont été partiellement résolus en utilisant des GNR comme source d'émission de lumière. De plus, grâce aux courants élevés qui peuvent être utilisés avec les rubans, et grâce à une efficacité quantique comparable à celle du plasmonique à des tensions similaires (10^{-5} photons/électrons), le GNR s'est révélé intéressant Pour l'intensité absolue de leur émission lumineuse. Deux perspectives peuvent être envisagées pour ce type de jonctions moléculaires. (1) La combinaison des deux systèmes que nous avons explorés dans cette thèse, par exemple en incorporant un chromophore à l'intérieur d'un GNR. De cette façon on pourrait espérer garder la stabilité des rubans et introduire la flexibilité d'un émetteur dédié. (2) Combinaison de jonctions moléculaires avec des guides plasmoniques pour les polaritons plasmoniques de surface (SPP). Notre appareil fonctionnerait alors comme une source pour les SPP monochromatiques. De cette manière, on combinerait efficacement un circuit électronique et un photonique, la jonction moléculaire agissant comme transducteur.

CHAPTER 1

General introduction

The detection of single molecules and the possibility to characterize their optical properties became reality in the late 1980s [1, 2, 3]. One of the interests in studying single molecules lies in the possibility to discover behaviours and interactions that may be hidden when performing ensemble measurements. Moreover, it is easier to handle single molecules in theory than more complex systems, making thus a comparison between experiments and theory more reliable.

In single molecule experiments, non-invasive optical probes are used, which allow to investigate single molecules hosted in solids. The most common methods are based on the measurement of a fluorescence signal that provides detailed information on single molecules as well as on their host environment [4, 5, 6]. However, in these all-optical approaches, the spatial resolution of the excitation is limited by diffraction, and there is no possibility to directly control the nanometer scale environment of the molecules.

An alternative consists in using electrons rather than photons to address the optical properties of single molecules. The main advantage of electrons is that they can be confined to atomic-scale pathways. For the first time in 2003 [7], it has been shown that the luminescence of a single-molecule can indeed be excited by the tunnelling current of a scanning tunnelling microscope (STM). The optical response of the molecule could even be probed as a function of sub-molecular variations of the STM tip position, suggesting that optical spectroscopy could reach atomic-scale sensitivity [8]. Another advantage of this method is that the nanometer-scale environment of the emitting molecule is known and is potentially controllable by using the tip of the STM [9, 10, 11]. Last but not least, this electronic excitation approach is also relevant for future optoelectronic applications that rely on the combination of electrical and photonic/plasmonic circuits. In such hybrid devices, optically active elements would be integrated in usual electronic circuitry. In this context, we are interested to demonstrate that single-molecule junctions (*i.e.* a single molecule directly bridging two electrodes) may be used to convert an electrical stimulation into a well controlled

optical signal.

Having described some of the potential advantages of using an STM to electrically excite the optical properties of a single molecule, it is fair to discuss its principal drawback: the absolute necessity of using electrodes to inject and collect the electrical current. The direct contact with a metallic substrate is known to alter the molecular orbitals and results in the quenching of the molecular luminescence that is the absence of a radiative intramolecular transitions [12]. It took ten years since the first STM-induced light emission experiment with molecules [13] to find a solution to this issue. By using a thin oxide layer (one to two atom thick) to decouple single molecules from a metallic substrate, Qiu *et al.* shown that the luminescence of porphyrins can be excited by the few electrons that can tunnel from the STM tip to the underlying metallic substrate [7].

Surprisingly, in the ten years that followed this seminal work, only few experiments used STM to study the optical properties of single molecules, and all used a similar decoupling strategy [14, 8, 15]. A common issue of these experiments lies in the difficulty to determine the electronic transitions at the origin of the electroluminescence. Indeed, the observed emission energies were not compatible with the expected fluorescence of the probed molecules. This issue, as we shall see in the manuscript, also raises fundamental questions regarding the detailed electroluminescence mechanism which, so far, assumed a radiative recombination of electrons and holes injected in the molecule from the electrodes [7].

Besides these fundamental considerations, the approach of Qiu *et al.* is also limited regarding future applications where a direct contact between the molecule and the electrode is mandatory. The configuration where a single molecule directly bridges two electrodes is widely studied in the break junction community [16, 17] because it can be formed in many experimental conditions (including room temperature and in liquid) but also because it constitutes the ultimate miniaturisation step of an organic electronic device. Providing such molecular-scale device with optical functionalities appears as a natural and exciting perspective. Indeed, as with any electronic device, molecular components have a bandwidth limited to the GHz range [18]. Devices that combine electronic and photonic or plasmonic elements may allow extending the bandwidth by several orders of magnitude [19, 20, 21]. However, in this device-oriented configuration, the direct contact to the metallic electrodes is expected to alter the properties of the molecule and to quench its emission. To circumvent this conceptual dead-end, Reecht *et al.*, proposed a strategy that consists in suspending long molecular wires between the tip and the sample of the STM. In this case, while the extremities of the wire – a 4-5 nanometer long π -conjugated oligothiophene – are in direct contact to the electrodes, the central part of the wire is sufficiently decoupled so that a broad luminescence peak, attributed to an intramolecular transition, is observed [22]. While this constitutes an interesting example of a single-molecule light emitting device, the broadness of the emission (≈ 300 meV) did not allow a detailed spectroscopic investigation and

prevented a more detailed analysis of the involved mechanisms. Moreover, this system lacks some degrees of liberty that would allow the experimentalist to tune its emission parameters such as the intensity, the colour or the linewidth.

Therefore, the objective of this manuscript is double. It aims at getting a better understanding of the mechanism at the origin of the luminescence of single-molecule excited by electrons and to address some of the challenges that may turn optoelectronic molecular-scale devices closer to reality.

The manuscript is divided in three chapters:

Chapter 2 is divided in two. First, the basic functioning of the STM, as well as the principles of scanning tunnelling spectroscopy are introduced. Then, the experimental setup, including the light collection system is described. Eventually, the basic methods used to clean and prepare samples and tip are described.

The second part of the chapter is devoted to the description of the principles of STM-induced light emission from metals and from molecules. A particular attention is paid to the decoupling strategies that allow studying the luminescence of single molecules. The chapter is concluded by the description of the light emission mechanisms reported in the literature.

Chapter 3 is devoted to the observation of a narrow line emission of light from specifically designed molecular junctions.

The chapter is divided in three parts. In the first one, the experimental concept is described. Essentially, it is based on a molecular emitter suspended between the sample and the tip of the STM by organic linkers. The synthesis of this complex molecular architecture is then presented.

The second part, that constitutes the core of the chapter, is dedicated to the optical properties of this system. We first report on the narrowest spectral feature ever reported in an STM-induced light emission (STM-LE) experiment. This allows us to explore several aspects of the emission, including the interactions between the molecular emitter, the substrate, and with surface plasmons localized at the tip-sample junction. Here, we also present a method to tune the emission linewidth over nearly two orders of magnitude. Moreover, we determine with certainty the electronic transition at the origin of the emission and we show that a proper design of the chemical structure of the emitter allows one controlling the colour of the emitted light.

In the last part of the chapter, an emission mechanism that is different from the generally accepted one, for single molecules, is proposed. This model explains more subtle aspects of the optical spectra, in particular the presence of blue-shifted vibronic peaks that are eventually interpreted in terms of non-thermalised excitonic emission.

The works reported in this chapter resulted in the publication of two articles [69, 70].

Chapter 4 is devoted to the study of the optoelectronic properties of individual graphene nanoribbons (GNR).

Here, we first describe how GNRs can be synthesised with atomic precision, and how they can be manipulated to create a molecular junction. In this configuration, both the electronic transport and the light emission properties are explored. For a specific type of GNRs, this study reveals a sharp emission peak that can be linked to an intra-ribbon optical transition. The energy of the emitted light however, is smaller than the expected optical gap of the considered ribbon. This leads us to suggest a mechanism involving an electronic transition between an edge state localised at the ribbon termini (also known as Tamm state) and a state delocalized on the ribbons. We also report on the possibility to tune the emission energy of the suspended ribbons by changing the voltage or the tip sample distance. Therefore, this study does not only provide a method to study the optical properties of a system, a GNR, that is difficult to address otherwise, but also constitutes an example of a highly stable, bright and tunable single-molecule light emitting device.

CHAPTER 2

Scanning Tunneling Microscopy and STM-induced light emission

In this chapter we first introduce the main techniques and instruments used in the course of this research, then describe the state of the art of the topics that will be discussed in the course of this document.

The main instrument that we used is the **scanning tunneling microscope (STM)**. It was invented in 1981 by that Gerber, Binnig et Rohrer [23, 24, 25] who received the Nobel prize for its development in 1986. The first part of the chapter is dedicated to the function of the STM, to the explanation of its different functioning modes and to the description of our experimental setup. This will bring us to the specificity of the instrument that we use: a light collection system that allows to perform **STM-induced light emission (STM-LE)** measurements, the heart of most of the results presented in this manuscript.

2.1 Scanning Tunneling Microscopy

The invention of the STM was preceded by the conception of the topographiner in the early 1970s [26, 27], an instrument that contained most of the elements that would be later found in a scanning tunneling microscope. However it was the latter that most impacted the domain of surface science. The invention of the STM opened the era of scanning probe microscopy, a type of microscopy where a probe is used to scan a surface to produce topographic images of the surface itself and of nanoscopic objects deposited on it. Different scanning probe techniques have been invented since, including **atomic force microscopy (AFM)** [28], magnetic force microscopy [29] and Kelvin probe force microscopy [30], to mention some. STM and AFM still offer, nowadays, the closest to

a *real* image of objects with sub-ångström resolution.

We will first introduce the basic concepts of scanning tunneling microscopy. The specificity of the STM lies in the use of the quantum tunneling effect that gives its name to this tool. When two electrodes are approached one to another at a distance of few ångströms and a voltage bias V is applied between them, low energy electrons (few eV) can flow from one electrode to the other. These electrons flow through the vacuum potential barrier due to the tunneling effect. The tunneling process is described by the Schrödinger equation for the electrons:

$$\frac{-\hbar}{2m} \nabla^2 \psi(\vec{r}) + [V(r) - E]\psi(\vec{r}) = 0, \quad (2.1)$$

where \hbar is the reduced Planck constant, m and E are the mass and energy of the electron, $\psi(\vec{r})$ is the wave function at the position \vec{r} , and $V(\vec{r})$ the position dependent potential barrier. The probability to find an electron at a certain position r is proportional to the square of the wave function at that position. By solving the Schrödinger equation we can know the probability to find the electron on one side or the other of the barrier, or even inside of the barrier. In one dimension, z , for a constant potential barrier ($V = V_0$) the solution of the equation is :

$$\psi(z) \propto e^{\pm kz}, \quad (2.2)$$

where the decay constant is

$$k = \frac{\sqrt{2m(V_0 - E)}}{\hbar}. \quad (2.3)$$

This solution, where the \pm sign refers to the propagation in the $+z$ or $-z$ direction, shows that even inside of the vacuum barrier the probability of finding an electron, $|\psi(z)|^2$, is non zero. $\psi(z)$ and its first derivative are required to be continuous functions and this results in a set of boundary conditions between regions where the exponential is real or imaginary (inside or outside of the barrier). When a potential bias is applied, the Fermi levels of the electrodes shift one from the other. This results in a net flow of electrons in one direction. This current is proportional to the square of the wave function that corresponds to the dominating direction ($-z$ for instance):

$$I \propto |A|e^{-2kz}. \quad (2.4)$$

The magnitude of the tunneling current generated this way depends exponentially on the size of the barrier and the distance that separates the electrodes. So even a small variation of the distance between the electrodes leads to a large change in the tunneling current. A precise detection of this current allows for the detection of small variations of the distance between the electrodes.

The tunneling current in an STM junction

In the STM the role of the electrodes is played by a flat surface and by a sharp metallic tip. Due to the exponential dependency with the distance the electrons flowing from

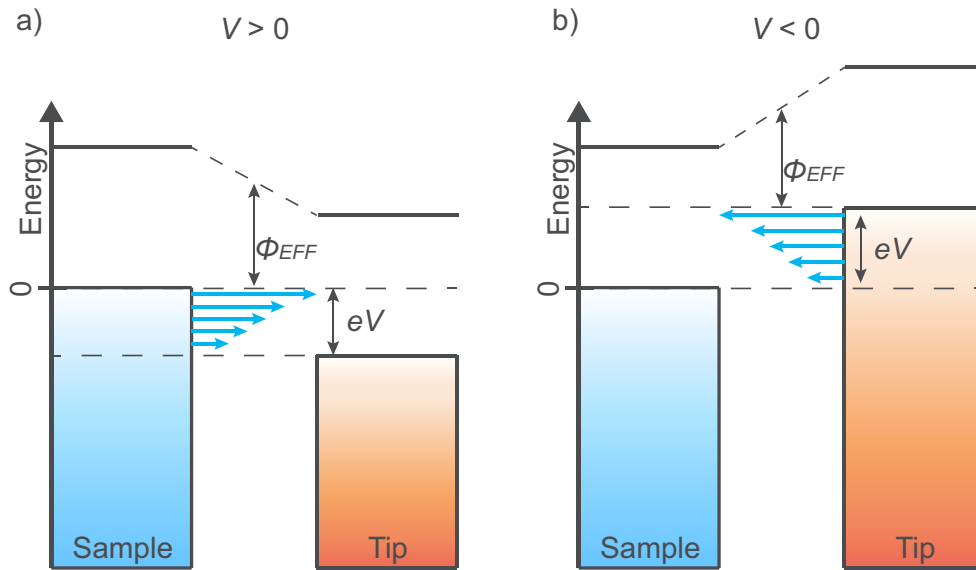


Figure 2.1 – Energy diagrams of an STM junction. Positive (a) and negative (b) voltage bias. The bias potential reference is the Fermi level of the sample. The blue rectangle represents the filled levels of the sample, while the orange rectangle refers to the tip. The number 0 represents the original position of the Fermi level of the system without bias. Φ_{EFF} is the average of the work functions of the electrodes and represents the effective tunneling barrier. With positive (negative) bias, tunneling electrons flow from the occupied levels of sample (tip) to the unoccupied levels of the tip (sample). The tunneling electrons are represented by light blue arrows.

the last few atoms of the tip dominate the signal. For this reason the spatial extension of the electron flow can be considered as mostly localized within those atoms. This explains the sub-nanometric lateral resolution of the STM.

In the following we present the expression of the tunneling current for the specific case of the STM .

We often refer to the system made of surface, tip and a (vacuum) barrier in between as to an STM junction. In figure 2.1 the energy diagram of such a junction is presented with a voltage bias applied to the tip, the sample potential being used as a reference. In (a) $V > 0$ and in (b) $V < 0$. The tunneling electrons are represented as light blue arrows. They flow through the junction from occupied states of the sample (tip) to unoccupied states of the tip (sample) when the bias is positive (negative). Briefly after the invention of the STM, Tersoff and Hamann derived an expression for the tunneling current in the approximation of small voltage and assuming that the relevant wave functions of the tip have a spherical form (s-wave tip model) [71, 72]:

$$I(z, V) \propto \int_0^{eV} \rho_t(E - eV) \rho_s(E) [f_t(E - eV) - f_s(E)] T(E, eV, z) dE, \quad (2.5)$$

where z is the tip-sample distance, V is the applied bias, $\rho_t(E)$ (respectively $\rho_s(E)$) is the density of states of the tip (sample) at the energy E , $f_t(E - eV)$ and $f_s(E)$ are the Fermi distribution of the electron of tip and sample, and $T(E, eV, z)$ is the probability of transmission of an electron through the barrier. The transmission term depends on the specific shape of the tunneling barrier. For a trapezoidal barrier it can be expressed, using the Wentzel-Brillouin-Kramer approximation, as:

$$T(E, eV, z) \propto \exp\left(-2z\sqrt{\frac{m}{\hbar^2}(2\phi_{Eff} + eV - 2E)}\right), \quad (2.6)$$

where Φ_{Eff} is the average of the work functions of the metals composing tip and sample and represents the average barrier height as we can see from figure 2.1. We remark that the transmission term is energy dependent: highly energetic electrons have a higher transmission probability. This is illustrated by the size of the blue arrows in figure 2.1.

When working at cryogenic temperatures the thermal excitation becomes negligible ($k_B T \ll eV$) and we can approximate the Fermi distribution by Heaviside step functions. As a consequence $f_t(E - eV) - f_s(E) \approx 1$. Moreover for gold and silver tips, as the ones we used, the density of state can be considered as constant [72]. Overall, these approximations allow reducing the tunneling current expression to:

$$I(z, V) \propto \int_0^{eV} \rho_s(E) T(E, eV, z) dE, \quad (2.7)$$

where the tunneling current depends only on the density of states of the sample and on the transmission term. We then recover an expression equivalent to the one of equation 2.4 for the tunneling current, that shows the exponential dependency on the tip-sample separation. The constant part of the exponential is

$$k = 2\sqrt{\frac{m}{\hbar^2} 2\phi_{Eff}}. \quad (2.8)$$

Typically, for silver and gold, $\phi_{Eff} \approx 5$ eV and $k = 11.5$ nm⁻¹. This means that for a variation in z of 0.1 nm the current changes by $e^{-2kz} = 0.1$. This exponential behavior confers high z sensitivity to the STM. As an example, the step height for a Au(111) surface is 2.36 Å of height. Such a distance corresponds to more than two orders of magnitude in variations of current. Moreover, if we consider that the typical diameter of an atom is ≈ 0.3 nm, we understand why the tunneling current is dominated by the last atoms of the tip.

The lateral resolution of the STM can be defined as size of the region that contributes to the tunneling current up to a value of $\approx e^{-2}$ of the maximum contribution, the one given by the apex of the tip. In the limit of a tip with a radius R larger than the tip-sample separation z_0 , where effects due to non-parallel tunneling can be neglected, the lateral current distribution of the current can be written as

$$I(\Delta x) \propto e^{-2k\frac{\Delta x^2}{2R}}. \quad (2.9)$$

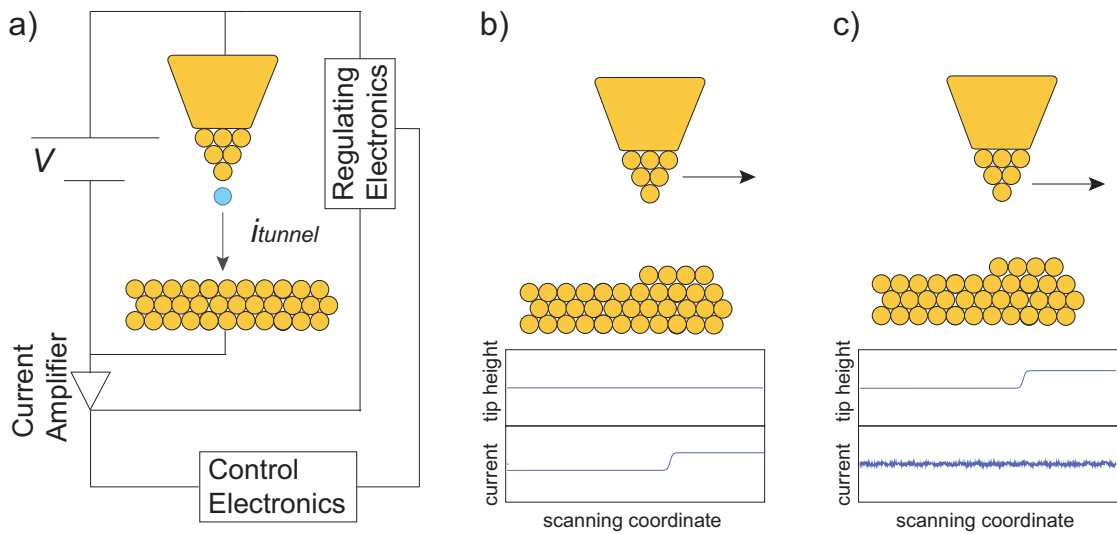


Figure 2.2 – Principle of functioning of the imaging modes of an STM. (a) Scheme of an STM circuit. (b) Constant height imaging mode. (c) Constant current imaging mode.

The term $\frac{\Delta x^2}{2R}$ represents the variation in tip-sample distance Δz at a distance Δx from the apex of the tip. For a curvature of the tip of 1 nm we thus obtain a relevant contribution to the current from a region of radius 0.7 Å. With sharper tip terminations better resolutions are obtained.

How to make an STM image

In figure 2.2(a) an illustration representing the surface and the tip as well as the basic electronic setup is shown. In order to obtain images, the STM tip needs to be moved precisely in the three directions. The tip is mounted on piezoelectric ceramic tube. By applying a voltage bias to it the piezo-tube expands or contracts in a controlled way, resulting in a movement of the tip. The position of the tip is controlled by two different electronics, a regulation and a control one. The bias is applied to the tip while keeping the sample as a reference. The tunneling current needs to be amplified due to its tiny magnitude (pA- μ A range) before being sent to the electronics that regulates the current and the one that controls position of the piezoelectric ceramic.

Two main imaging modes can be used with an STM. In figure 2.2(b) the simplest one is presented: the z coordinate of the tip is kept constant while the surface is scanned and the tunneling current is recorded. In this mode, known as *constant height* mode or *current image* mode, the current varies locally as a function of the asperity of the sample and of the local density of states. The image is then obtained from the

value of the current at each pixel of the x,y grid. More often, the *constant current* or *topographic* mode is used. In this mode, presented in figure 2.2(c), the current is regulated at a constant value thanks to a feedback loop (regulating electronics) that permanently adjusts the tip height. This results for instance in the tip retracting when there is a protrusion on the surface. The image is then reconstructed from the z coordinate of the tip at each (x,y) pair of coordinates.

2.1.1 Scanning Tunneling Spectroscopy

In the simplified expression of the tunneling current (equation 2.7) we observe a dependency on the local density of states of the surface. This dependency is at the heart of the **scanning tunneling spectroscopy (STS)**.

If we differentiate the expression of the tunneling current with respect to the voltage bias we obtain [73]:

$$\frac{dI}{dV}(V) \propto \rho_s(eV)T(E_F + eV, eV, z) + \int_0^{eV} \rho_s(E) \frac{dT(E, eV, z)}{dV} dE. \quad (2.10)$$

For small values of V the variation of T is small so we can drop the second term. The *differential conductance* $dI/dV(V)$ is then linearly proportional to the local density of state of the surface and to the probability of transmission. The latter depends monotonically on the bias V. Consequently, in a $dI/dV(V)$ spectrum at constant z, the presence of a resonance (that appears as a peak) can be associated with a feature in the density of state $\rho(eV)$. The energy of the peaks becomes an information about the electronic density of states of the surface or of molecules or thin layers of materials laying on the surface. Since the sample is used as a reference for the potential, when positive (negative) bias is applied the occupied (unoccupied) states of the surface are probed.

In practice, the tunneling current $I(V)$ is measured while sweeping the voltage bias at constant z (feedback loop open). A time dependent sinusoidal modulation of the voltage bias is added to the voltage ramp: $\Delta V(t) = V_m \cos(\omega_m t)$. If the amplitude of the modulation V_m is small with respect to the bias V, we can express the resulting current with its Taylor expansion:

$$\begin{aligned} I(V + \Delta V) &= I(V) + \frac{dI}{dV} \Delta V + \frac{1}{2} \frac{d^2 I}{dV^2} \Delta V^2 + \dots \\ &= I(V) + \frac{dI}{dV} V_m \cos(\omega_m t) + \frac{1}{2} \frac{d^2 I}{dV^2} (V_m \cos(\omega_m t))^2 + \dots \end{aligned} \quad (2.11)$$

The modulation is generated by a lock-in amplifier that is then fed with the $I(V + \Delta V)$ signal. The lock-in filters only the signal with the same frequency as the modulation. The filtering is obtained by integrating the signal over a small period of time. The

orthogonality of sinusoidal functions allows to strongly reduce any out-of-phase signal and to amplify the in-phase ones when integrating. Consequently the $\frac{dI}{dV}$ term can be separated from the other ones and registered.

The amplitude of the modulations we used is in the range of the mV. The modulation period is in the range of the ms, corresponding to frequencies in the range of the kHz. The exact frequency is selected in order to be compatible with the bandwidth of the current-voltage amplifier. Both parameters as well as the integration time are adjustable to optimize the detection of the signal.

2.1.2 Experimental setup

We use a commercial low temperature STM produced by *Omicron* (figure 2.3). The cryogenic system is composed of two cryostats. The inner one is a bath cryostat that can be filled with liquid helium (LHe) or liquid nitrogen (LN₂). The external cryostat is concentric with the inner one and can be filled with LN₂. When measuring at low temperature conditions the inner cryostat is filled with LHe and the external one with LN₂. The role of the external cryostat is to protect the inner one from radiation in order to minimize the boiling rate of LHe. The standing time of the LHe in the inner cryostat is of 25 hours.

The STM head (tip and sample) are in thermal contact with the inner cryostat and reach a working temperature of 4.7° K.

The STM chamber is kept under **ultra high vacuum (UHV)** thanks to the use of an ionic pump. With the additional cryogenic pumping provided by the cryostats the base pressure is $P \approx 5 \times 10^{-11}$ mbar. This pressure results in very small contamination of the sample that can be used for several weeks without re-preparation.

The STM head can be decoupled from the chamber and be left freely suspended by means of three metallic springs. This is the first and local stage of vibration damping used to reduce the mechanical noise. A second damping stage is located at the level of the whole STM chamber, which is placed on a pneumatic system that decouples it from the ground. The combination of the two damping stages allows a minimal vibrational noise of 3 pm (peak to peak) as measured with the tip in tunneling conditions.

We prepare samples in a preparation chamber that is kept under UHV conditions and decoupled from the STM chamber by a valve. The preparation chamber has a base pressure of 1×10^{-10} mbar. The preparation chamber is equipped with an argon ion gun used for sputtering the samples, with a water-cooled Knudsen cell evaporator to sublimate molecules and with a local heating stage that is used for thermal annealing. The preparation chamber is connected to a load-lock. We can insert samples, tips and crucibles in the load lock and make a preliminary vacuum ($P \approx 1 \times 10^{-8}$ mbar) before entering them in the preparation chamber. This heavily reduces contamination of the preparation chamber and avoids breaking the UHV.

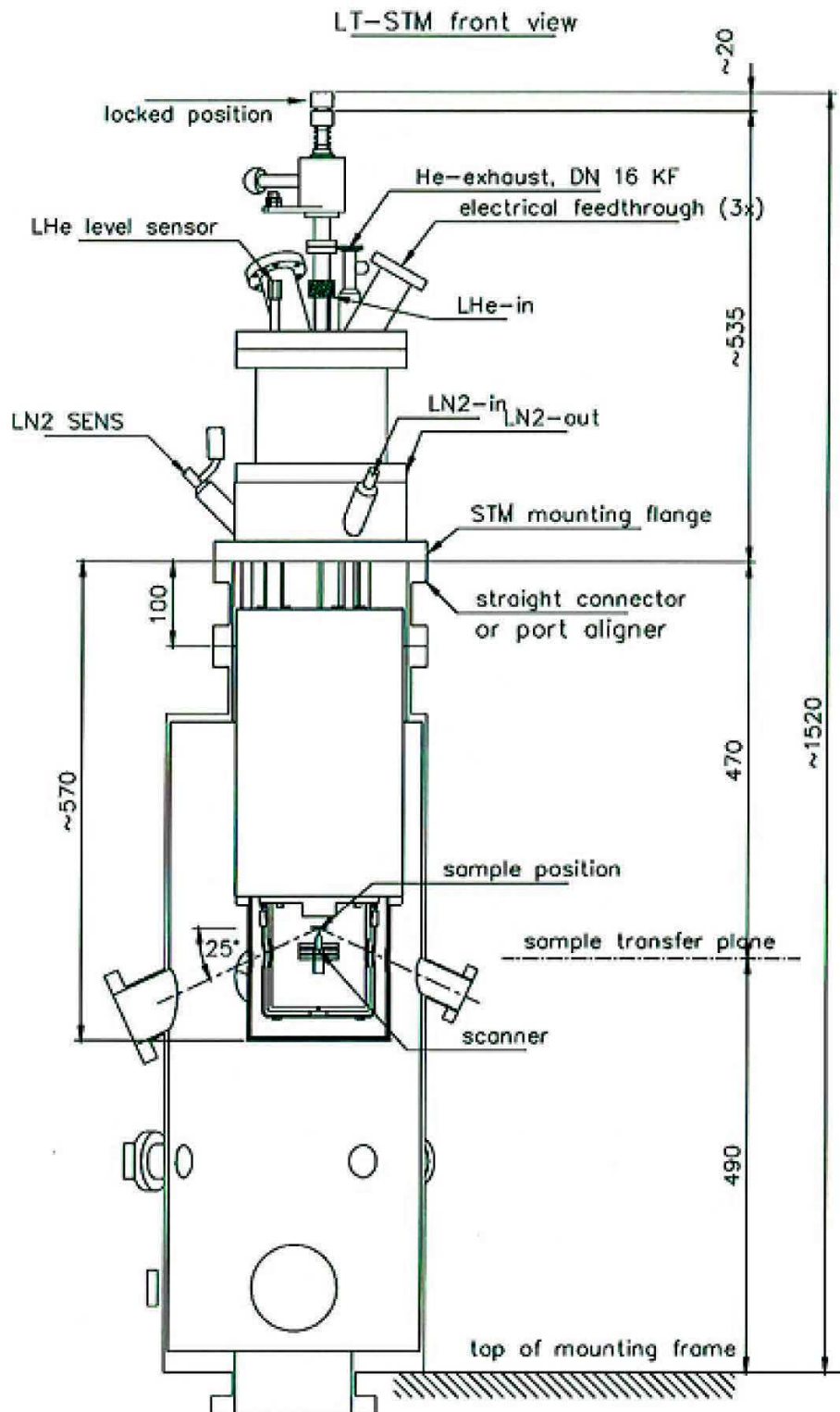


Figure 2.3 – Scheme of the STM. Distances are indicated in mm. Source Omicron GmbH.

The STM chamber is also equipped with an evaporator that allows a direct deposition of molecules. This evaporator is used when the sample needs to be at cryogenic temperature during the deposition.

Sample preparation

The experiments reported in this manuscript are performed on gold substrates. Two different types of gold samples were used indistinctly: mono crystalline Au(111)¹ or epitaxial Au(111) thin film grown on mica substrate²

Samples were repeatedly treated with cycles of sputtering and annealing before any further use. Sputtering consists in bombarding the sample with high energy (≥ 1200 keV) Ar⁺ ions in order to remove the dirt layers on top of the crystal. Therefore the sample is annealed at temperatures between 600 K and 800 K for several minutes in order to reconstruct flat areas on the surface.

Tip preparation

For the work presented in this manuscript we used only tungsten tips. The tips were obtained from W wires of 0.25 mm of diameter. The wires were electrochemically etched using a solution of NaOH to obtain a sharp tip [74]. The tips were then inserted into the vacuum chamber where they were thermally annealed and then argon-sputtered. This procedure serves the double role of cleaning the tip from any oxide layer formed on the W wire and to further sharpen the edge of the tip [75].

The tips were then entered in the STM head and indented by several nanometers in the surface of the metallic sample (Ag/Au). This procedure allows to cover the tip with several layers of silver or gold. For tips used in light emission measurements this last procedure was repeated several times in order to optimize the light emission signal from the pristine junction [76, 77]. Small indentations (≤ 2 nm) were used in combination with voltage pulses to optimize the imaging quality or the spectroscopic resolution in STS measurements, while preserving the plasmonic signal.

2.1.3 Light collection system

The application of a voltage bias to the STM junction may result in an emission of light that originates from the junction itself. We will discuss the emission mechanism

¹Commercial from *SPL* and from *MaTeck*

²Both commercial from *Phasis* and homemade.

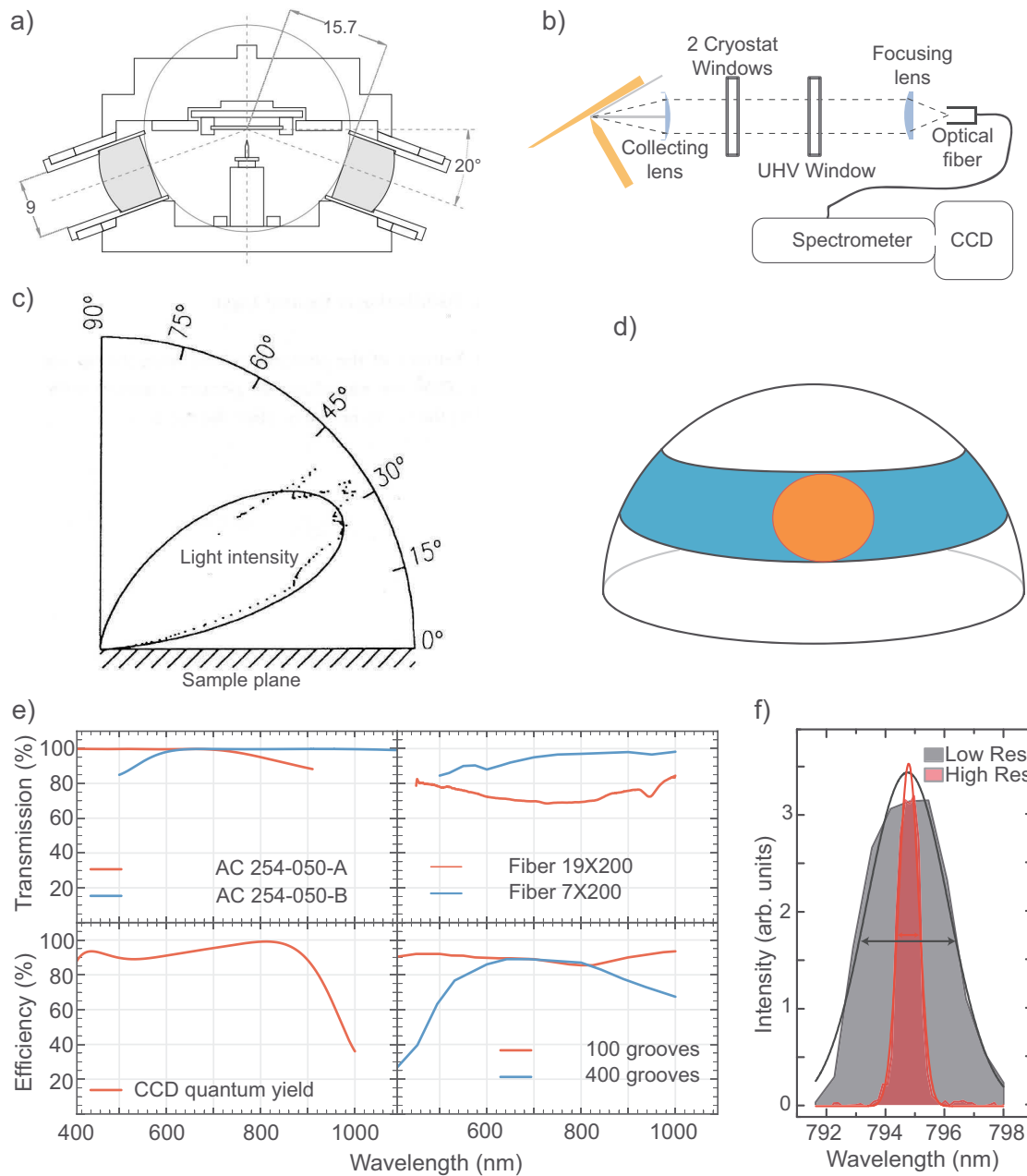


Figure 2.4 – Light collection system. (a) Scheme of the inside of the STM head (adapted from [78]. Note that the angle is of 25° in our setup, instead of the 20° indicated in the figure). (b) Scheme of the full optical detection system. (c) Calculated angular distribution of photon emission for photons with $\lambda = 500 \text{ nm}$ (adapted from [79]) (d) Scheme representing the hemisphere above the sample surface and an anisotropic emission (blue sector) like the one of (c). The lens is represented by an orange circle. (e) Optical response of the main components of the detection system: focusing lenses (top left), optical fibers (top right), CCD sensor (bottom left) and spectrometer gratings (bottom right). (f) Spectra of the 794.818 nm line of a Ne/Ar lamp obtained with the low (gray) and high (red) resolution grating.

in detail in section 2.2. In order to measure the emission, a light collection system is installed on the STM. The base system was developed by Keizer *et al.* [78] and commercialized by Scienta Omicron.

Due to the low efficiency of the emission process (1 photon per 10^4 tunneling electrons), and to the use of currents in the nA range, it is important to optimize the collection of photons. For this reason the detection system is composed of two parts. The first one is inside the STM head and consists of a lens used to collect the light emitted at the junction. The second part is situated outside of the vacuum chamber.

In-situ collection system. The in-situ collection system (figure 2.4(a)) consists in a lens (diameter of 9 mm, $f = 15.0$ mm, numerical aperture = 0.543), mounted near the tip-sample junction, tilted with an angle of 25° with respect to the sample surface³. The choice of the lens and its position is made in order to transform the light emitted from the junction into a parallel beam of collimated light directed outwards. The tilt angle of the lens is a critical parameter. Let's understand why through two extreme examples.

- **Isotropic emission from the junction.** The amount of light that is collected in this case depends on the solid angle covered by the lens, and on its distance from the junction. The angular collection efficiency can then be estimated to be $\approx 6\%$ of the emitted light. This value provides then an estimate of the lower limit of the collection efficiency.
- **Directional emission from the junction.** This hypothesis is motivated by the presence of the metallic surface, that is expected to impact the angular distribution of the emission. Theoretical calculations and experimental measurements performed by Berndt in [79] indicate that the intensity of the emission has a maximum at an angle of 30° with respect of the sample plane (figure 2.4(c)). In order to estimate the maximum collection efficiency, we make the extreme hypothesis that *all* the light is emitted in a spherical segment at an angle of 30° , with height equal to the lens diameter (figure 2.4(d)). Under these conditions, the percentage of collected light is the ratio between the surface of the lens (in orange in figure 2.4(d)) and the surface of the spherical segment (in blue in figure 2.4(d)), and can be estimated to be $\approx 10\%$.

By positioning the lens at an angle of 25° we are in between the two extreme values we presented (6-10%). We thus have an upper and a lower bound for the collection efficiency of our system.

³This value differs from the original value proposed in [78] where it is of 20° .

Ex-situ collection system. The collimated beam of light from the in-situ lens follows the path sketched in figure 2.4(b) to reach the camera. First, the beam passes through two cryostat windows (BK7 glass) and through a UHV window (MgF_2). Then it reaches a focusing lens that is coupled to an optical fiber. At the other end, the fiber is coupled to a spectrometer. Eventually, the detection is made by a liquid nitrogen cooled CCD camera.

We now discuss the efficiency of each component of the ex-situ system.

- The transmission of the BK7 and of the UHV windows, in the visible and near infra red range, is close to 90%.
- As focusing lens, we used one of two different achromatic doublets from Thorlabs (AC254-050-A, AC254-050-B, $f = 50$ mm, $d = 1$ inch) depending on the measurement. These lenses have reduced chromatic aberration in the 400-700 nm and 650-1050 nm range respectively. Their optical transmission is reported in figure 2.4(e) (top left).
- As optical fiber we used, interchangeably, two different fiber bundles. The bundles are composed of 19 or 7 silicate fibers of respectively 100 and 200 μm of diameter.

On one side, the bundles are disposed in a circle to increase the coupling with the light focused by the lens. The coupling can be maximized manually: indeed, the focusing lens and the fiber are mounted on a support that offers three translational degrees of freedom and 2 rotational ones. Moreover the fiber entry has two translational degrees of freedom with respect to the lens (the plane perpendicular to the entrance of the fiber) for a fine adjustment of the coupling. The transmission between the lens and the fibers can reach 90% when the coupling is optimized [80].

The wavelength dependent optical transmission inside of the fibers is presented in 2.4(e) (top right).

Spectrometer and CCD camera As a spectrometer we used an Acton SP2300 from Princeton Instruments. The spectrometer is equipped with two different gratings. The first one, used for low resolution measurements, has 100 grooves per mm and is blazed at 780 nm. The second one, used for higher resolution measurements, has 400 grooves per mm and is blazed at 850 nm. Their efficiency, for a focal distance of $f_s = 300$ mm, is presented in 2.4(e) (bottom right). The spectrometer is necessary to disperse the light depending on the wavelength. The dispersed light is then sent towards the CCD camera. We used a Pylon Excelon 100BR from Princeton Instruments whose detection efficiency is presented in 2.4(e) (bottom left). The rectangular sensor of the camera has a size of 100×1340 pixels. When used to perform spectroscopy, the vertical dimension of the sensor is binned. The association of each channel to a

wavelength is obtained by calibrating the spectrometer using a Ne/Ar lamp, whose peaks are at well defined wavelengths.

To illustrate the resolution of the system, a measurement of the 794.818 nm line of a Ne/Ar lamp, obtained using the two gratings is presented in figure 2.4f). The 100 grooves/mm grating yields the low resolution measurement (in grey) with a **full width at half maximum (FWHM)** of 3.5 nm. The use of the 400 grooves/mm one results in the high resolution measurement (red) with a FWHM of 0.8 nm. Since the size of the CCD sensor is fixed ($W = 26.8$ mm), the use of a higher resolution grating results in a smaller measurement range $\Delta\lambda$. We can evaluate the range as

$$\Delta\lambda = Wd, \quad (2.12)$$

where d is the dispersion of the grating. The dispersion of the grating is calculated as

$$d = \frac{1}{f_s r_d}, \quad (2.13)$$

with $f_s = 300$ mm being the focal length of the spectrometer and r_d being the number of grooves per millimeter of the chosen grating. This results in $\Delta\lambda \approx 900$ nm for the low-resolution grating and ≈ 225 nm for the high-resolution one.

One grating offers high resolution on a small range of wavelength, the other offers a lower resolution on a large range of wavelength. It is possible to switch from one to the other during an experiment.

In conclusion the efficiency of the system depends on the specific combination of lens, grating and fiber used and, most importantly, on the optimization of the light-fiber coupling. In optimal conditions we can estimate that an average of 50% of the light collected by the internal lens will be measured at a wavelength of 800 nm.

Considering both the *in situ* and the *ex situ* part of the system we can estimate the overall efficiency to be in the range 2% to 5%.

2.1.4 Software

The STM data were acquired using MATRIX Control System and its related software, produced by Omicron. Light emission data were acquired using the Winspec spectroscopic software from Princeton Instruments.

The data treatment and analysis was done using different softwares. For image analysis we used WsXM [81]. For spectroscopic data a combination of Vernissage by Omicron, Origin by ©OriginLab and custom written python scripts were used. For light emission data we used a combination of custom Scilab scripts and custom python scripts.

2.2 STM-induced light emission

The STM can be used to locally excite the luminescence (STM-induced light emission or STM-LE) from a metallic or semiconducting sample [31, 32, 33]. Using the detection system described in section 2.1.3 it is possible to measure light emission spectra like the one presented in figure 2.5(a), where the number of photons is plotted as a function of their energy. In the following we describe the basic principles of STM-LE.

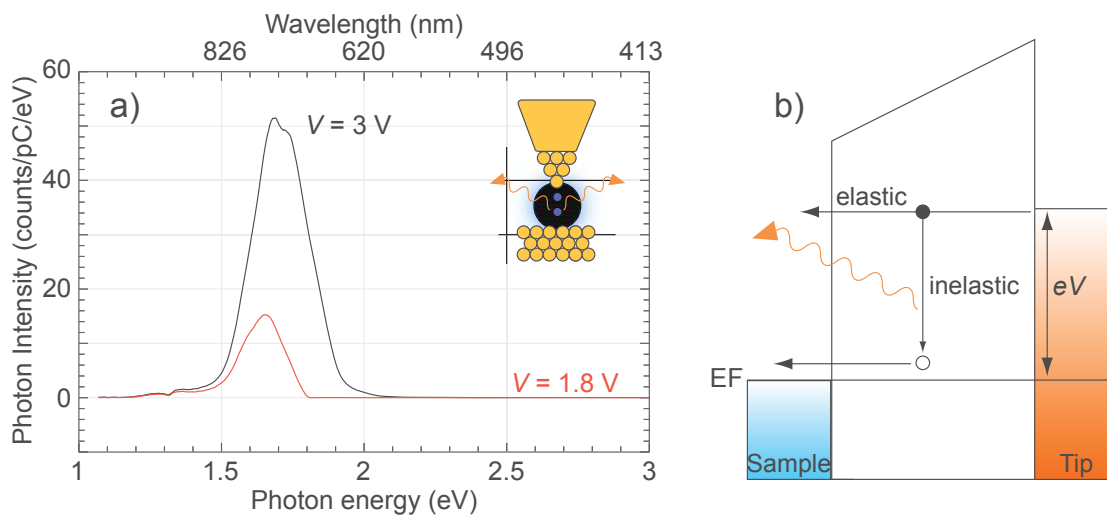


Figure 2.5 – Light emission spectra and mechanism of STM-induced light emission. (a) STM-induced light emission spectra from a pristine junction (sketch in inset) at $V = 3\text{ V}$ (black curve) and $V = 1.8\text{ V}$ (red curve), $I = 10\text{ nA}$. (b) Energy diagram of the biased junction illustrating the basic light emission mechanism.

2.2.1 Basic principles

In order to understand the mechanism of STM-LE two curves are presented in figure 2.5(a). The black curve represents the number of photons as a function of their wavelength when a voltage bias $V = 3\text{ V}$ is applied to the junction. The spectrum is obtained with a gold tip on a gold sample in tunneling conditions (as sketched in the inset), with a current of $I = 10\text{ nA}$. The red curve is measured on the same junction when a bias $V = 1.8\text{ V}$ is applied. Here, no photons are emitted at wavelengths smaller than $\approx 690\text{ nm}$. This value corresponds to a photon energy $h\nu = 1.8\text{ eV}$.

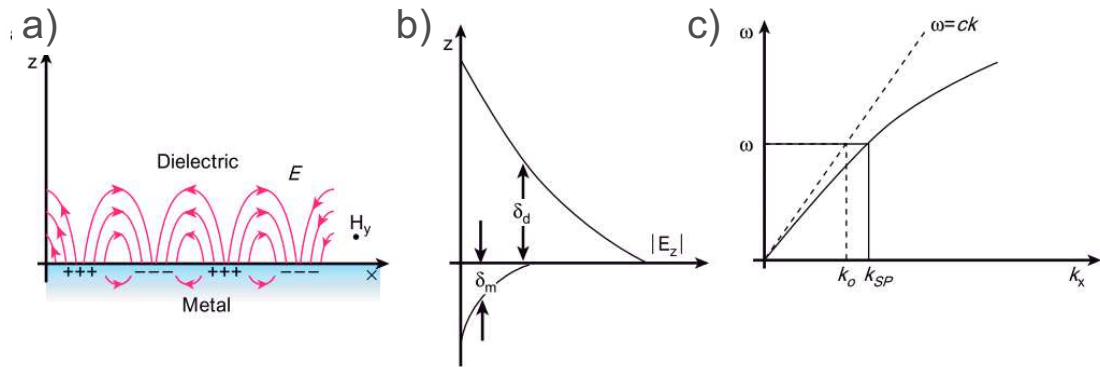


Figure 2.6 – Principle of the surface plasmons. (a) Schematic representation of a surface plasmon polariton. (b) Evanescence of the electric field in the direction normal to the interface. (c) Dispersion relation of surface plasmons (full line) and free space photons (dashed line). Adapted from [82].

The role of the tunneling current. The spectra of figure 2.5(a) illustrate the role of the voltage bias and, indirectly, of the tunneling electrons in the emission of light from an STM junction. Figure 2.5(b) presents an energy diagram of the junction, in a configuration where a bias V is applied. Tunneling electrons of energy $E \leq eV$ flow through the vacuum barrier. For most of the electrons the tunneling process is elastic: they reach the other electrode without losing energy. Their energy is then dissipated in the metal. However, a small fraction ($\approx 0.1\%$ for a bias of 3 V) lose some energy in an inelastic process that is at the origin of the photon emission. This explains the quantum cutoff of the photons $h\nu \leq eV$ observed in the red curve: if we exclude processes involving multiple electrons, the energy of a photon cannot exceed the energy of the electron that generated it.

We can estimate the orders of magnitude involved in this process. For a current $I = 1$ nA there are $\approx 10^{10}$ e^-/s flowing through the junction. Consequently there are around 10^7 inelastic electrons per second that can generate the emission of a photon.

The role of surface plasmons The black curve of figure 2.5(a) shows that no signal is observed at wavelength lower than 590 nm. This value, corresponding to 2.1 eV cannot be explained only by the quantum cutoff relation, since the applied bias is 3 V. This example illustrates that the energy of the inelastic electrons is not the only parameter influencing the light emission spectra in STM-LE.

The other element that defines the shape of an optical spectrum, are the **localised surface plasmon (LSP)** modes, induced by the presence of the tip close to the surface [83, 84, 75, 47].

Surface plasmon polaritons. Before describing the nature of LSPs, we give a more general description of surface plasmons.

In general terms, surface plasmons are collective oscillations of conduction electrons in metals at the interface with a dielectric, in our case the vacuum. These oscillations of charge propagate in the metal and give rise to an electromagnetic field in the dielectric. Altogether we speak of a **surface plasmon polariton (SPP)** (see figure 2.6(a)). The electromagnetic field in the dielectric is evanescent in the direction normal to the interface, as illustrated in figure 2.6(b).

By solving the Maxwell equations at the interface between the metal and the dielectric it is possible to obtain the dispersion relation for SPPs. The dispersion curve is shown in 2.6(c) (solid line) as compared to the one of free propagating photons (dashed line). We see that SPPs have a larger momentum than free space photons of the same energy. This mismatch makes the SPP non-radiative by nature. The presence of a roughness on the surface or the use of a prism can help matching the momentum of plasmons and photons, allowing a conversion of one into the other [46, 47, 49, 48].

Localized surface plasmons. In the STM however, the presence of the tip in the proximity of the surface creates tip-induced localized plasmon modes that strongly interact with inelastic tunneling electrons. LSPs are localized at the tip apex and the sample below. For a spherical approximation of the tip (see figure 2.7(b)) the lowest LSP modes correspond to a dipole oscillating perpendicularly to the surface [83, 85]. The frequency of the LSP modes depends both on the bulk plasmonic mode of the metal (hence on the material) and on the radius of the tip. The STM junction is sort of a nano-cavity and the LSP correspond to its normal modes. For this reason we sometimes call them **nano-cavity plasmon (NCP)**. LSP couple rather efficiently with radiative electromagnetic modes.

One way to describe the STM-LE process is that inelastic tunneling electrons excite the LSP that can decay by sending out light [86]. In this picture, the light emission spectra of figure 2.5(a) provide information on the density of the plasmonic modes of the nano-cavity, and are often referred to as the spectra of the plasmon. By changing the structure of the tip the plasmonic modes change and this results in different shapes of the spectra. Localized surface plasmons can also decay in a non radiative way, for instance by exciting SPPs [47], by creating electron hole pairs in the bulk of the metal or through ohmic losses. In the model of Persson and Baratoff, where electrons tunnel from the s-orbital of a tip to a metallic sphere, only one tenth of the relaxation of surface plasmons is radiative [86]. This value, combined with a ratio of inelastic electrons over total number of tunneling electrons of $\approx 10^{-3}$, gives a first estimate of one photon each $\approx 10^4$ tunneling electrons.

We point out that LSP modes can be excited also by incoming light, for instance a laser. In this case the LSP strongly amplifies the electromagnetic field locally. This phenomenon is exploited for example in the case of **tip-enhanced Raman scattering (TERS)** [87, 88].

Fermi golden rule description of STM-LE. We can summarize the STM-induced light emission mechanism as the product of two factors: inelastic tunneling electrons and localized surface plasmons. This can be expressed in terms of a Fermi golden rule [34], where the rate of emission at the frequency ν is:

$$\Gamma(\nu) = \frac{2\pi}{\hbar^2} |\langle i | \hat{d} | f \rangle|^2 \rho(\nu) E_Z(M)^2, \quad (2.14)$$

where $|\langle i | \hat{d} | f \rangle|$ is the transition dipole moment between an initial state $|i\rangle$ and a final state (after the transition) $|f\rangle$ and $\rho(\nu) E_Z(M)^2$ are the spectral density (at a frequency ν) and the spatial density (at a position M) of the electromagnetic field. In other words, the first one is the term describing the electronic transition between the occupied states of one electrode and the unoccupied states of the other electrode, hence representing the inelastic current, while the second term describes the plasmonic contribution.

2.2.2 Experiments on metals

In this section we briefly review some key results obtained from STM-LE that will clarify the role of the tip in the luminescence mechanism. All the results reported in this section are obtained with a metallic tip on a metallic surface in tunneling conditions (sketch in figure 2.7(a)).

The first model used to calculate LSP modes by Rendell *et al.* is shown in figure 2.7(b). This model has been then adapted by Johansson *et al.* to calculate light emission stimulated by tunneling electrons in the STM [84].

In figure 2.7(c) a set of spectra obtained with a Ir tip on a silver sample at varying voltage bias is presented. The voltage spans from 2.0 V in the bottommost curve to 5.8 V in the topmost. This data, obtained by Gimzewski *et al.* in one of the first papers on STM-LE [33], illustrates two phenomena. First, we observe the shift of the cutoff in the light emission as the bias is increased. Second, we note that, given a high enough bias, the position of the peak at 2.4 eV does not shift. This is an example of a common feature of plasmonic spectra: as soon as the energy of the electrons is sufficiently high, the position of the resonances is insensitive to the bias. This is true also for a change of polarity in the bias, indicating the plasmonic modes are polarity independent.

In figure 2.7(d) the results obtained by Berndt *et al.* using W tips on different substrates (Ag(111), Au(110) and Cu(111)) are presented [75, 89]. The measurement in tunneling regime (top row) are compared with success to calculations based on the model of Johansson *et al.* (bottom row). The spectra illustrate that different materials have the plasmonic resonance at different energies. This is understood by the fact that the LSP modes depend on the dielectric function of the material [75].

In figure 2.7(e) an hyperbolic model for the tip is shown. This model by Aizpurua

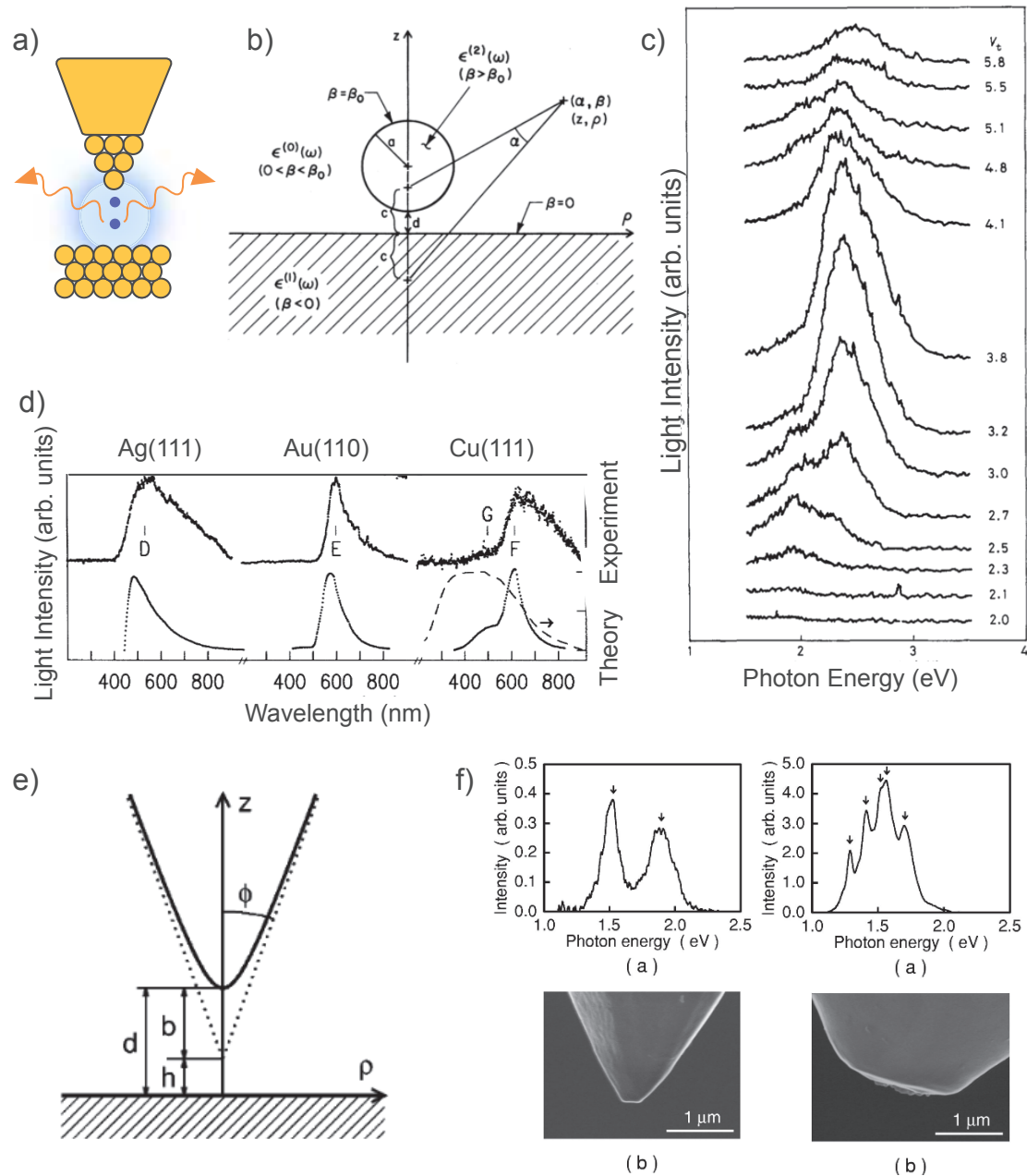


Figure 2.7 – Light emission from a metallic surface. (a) Sketch of the experimental plasmonic junction. (b) Spherical model for the tip as proposed by Rendel *et al.* Adapted from [83]. (c) Optical spectra obtained for an Ir tip over a silver sample. Constant I and variable voltage bias. Adapted from [33]. (d) Optical emission spectra from Ag(111), Au(110) and Cu(111) surfaces. Bottom row: calculated spectra based on Johansson’s model [84]. Top row: experimental light emission in tunneling regime. Adapted from [75]. (e) Hyperbolic model [76] of the tip to calculate the impact of higher plasmonic modes. Adapted from [77]. (f) Plasmon spectra of two different Au tips on Au(111) sample (top row). Corresponding scanning electron microscope (SEM) images of the tips (bottom row). Adapted from [77].

et al. [76] is an extension of the spherical one. Based on this model the energy of the plasmonic resonance has a maximum when the curvature $\phi = 45^\circ$ and decreases for sharper tips and for really broad ones. Moreover when the tip has an irregular shape, multiple plasmonic resonances in the same energy range can emerge. This was experimentally demonstrated by Meguro *et al.* and is illustrated in figure 2.7(e). Here two plasmonic spectra showing multiple resonances are presented. The SEM image of the corresponding tip is presented below the spectra. It should be clear that the influence of the tip on the optical spectra is huge. In particular there are two different scales influencing the plasmonic emission. The curvature of the tip on a larger scale influences the energy of the resonance. Simultaneously, the fine structure of the tip edge may be responsible for substructures and the presence of multiple plasmonic modes. For this reason it is crucial to measure the plasmonic response of the tip, by acquiring a light emission spectrum of the tip in front of the bare metallic sample surface, before performing any experiment. Moreover this explains why small indentations of the tip in the sample's surface can be used to optimize its optical response

2.2.3 STM-LE from molecules adsorbed on metallic surfaces

STM-induced light emission from molecules on metallic surfaces has been investigated since the early 1990s. In these experiments, the molecules are evaporated on a sample in small quantities in order to form sub-monolayer covering of the surface.

The tip is positioned above an area covered with molecules and, upon the application of a voltage bias, light is emitted (sketch in figure 2.8(a)). The optical spectrum measured in this way is then compared with the one obtained with the same tip above the metallic surface. This allows to determine the impact of the molecules on the emission.

Over the last 25 years this experiment was done using C60 [13, 90, 91], porphyrins [92, 93], pthalocyanines [94], PTCDA [95] and other molecules [96, 97] on different noble metals. In these experiments, the STM-induced light emission from the adsorbed molecules often differ in intensity and/or in energy, from the one on the bare metallic surface. Nonetheless, the emission remains of plasmonic nature. To understand the modification on the energy of the emission, the energy diagram of the pristine STM junction is presented in figure 2.8(b) and compared to the one where the molecules are on the surface (c). In the latter case the presence of molecular levels (blue curve in (c)) offer new channels for radiative decays of inelastic electrons. These inelastic transitions are favoured, and this results in a shift of the energy of the emission. Moreover, the increased distance between the tip and the sample results in a modification of the NCP, whose modes shift to a lower energy [79].

We point out that in these experiments the emitted light never arise from *intramolecular* transitions, and phenomena like molecular fluorescence and phosphorescence are not observed in these conditions. We rather speak of a modification of the plasmonic

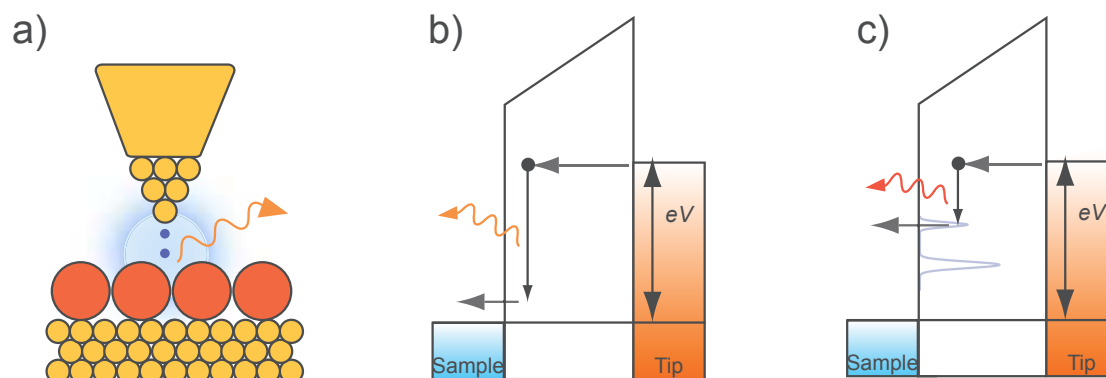


Figure 2.8 – Emission from molecules adsorbed on a metallic surface.

- (a) Sketch of the light emission from molecules adsorbed on a metallic surface. (b) Energy diagram of the tunneling junction illustrating the light emission mechanism. (c) Energy diagram illustrating the role of molecular levels on the light emission of the system.

emission due to the presence of the molecular states [93, 98, 99]. This is not a phenomenon exclusively related to molecules. It was for instance observed by placing silver chains on a NiAl sample [100, 101] or thanks to the modification of the density of surface states of Au(111) due to standing waves near step edges and in triangular islands [102].

The absence of radiative intramolecular transitions is typical from experiments where the molecules are in direct contact with the electrodes. It is due to the coupling between the molecular and the metal states. This provides a fast charge transfer channel from the molecule to the electrodes that dominates over the slower luminescence mechanisms [12]. This short distance (≈ 1 nm) effect is similar to energy transfer of the Dexter type [103]. We speak then of quenching of the fluorescence. Something similar occurs for the photoluminescence of molecules in the presence of metals. Here, both Dexter type, and the longer range Förster energy transfer [104], which is due to dipolar coupling, result in the quenching of the radiative emission [105, 106].

2.2.4 Decoupling from the electrodes

Decoupling the molecules from the metallic substrate has been shown to reduce the quenching of the fluorescence.

We can classify the decoupling methods into three main families, as illustrated in figure 2.9. The first one, in (a), uses a multilayer of molecules as an organic spacer [107, 108, 95, 36, 37, 35].

The second way, in (b), consists in the use of a thin insulating layer as a support for the

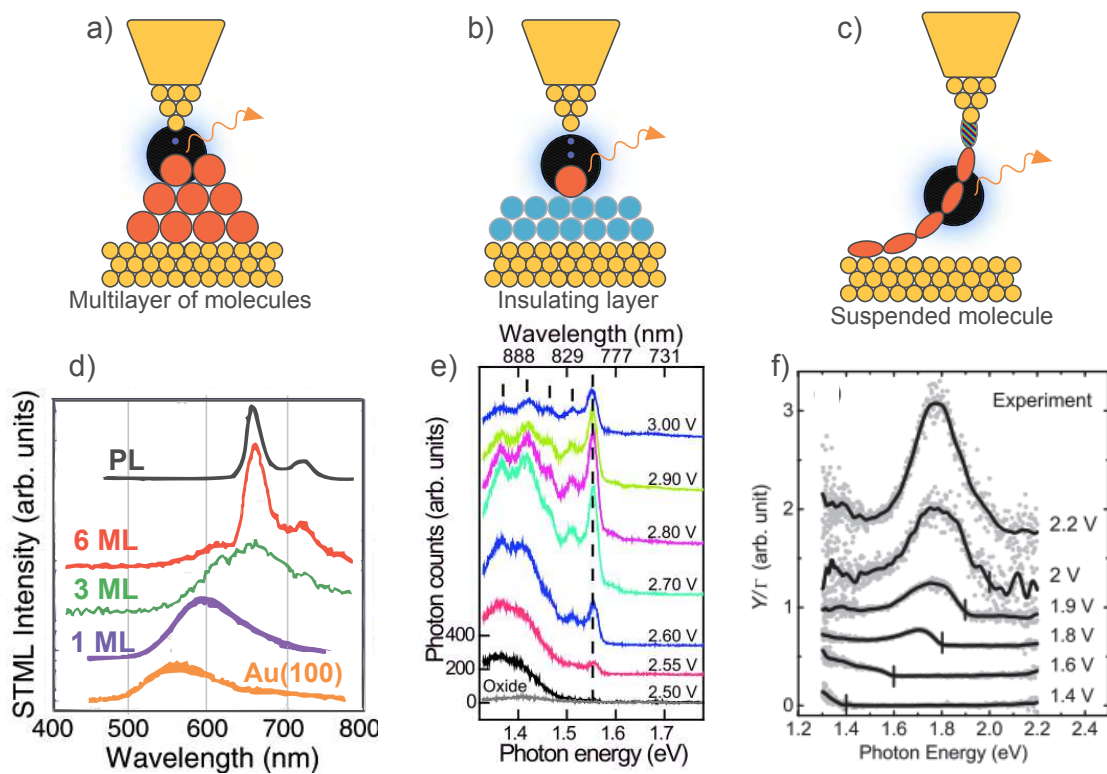


Figure 2.9 – Decoupling methods. (a)-(c) Schemes of different decoupling methods. (d)-(f) Corresponding light emission spectra. Adapted from [107, 14, 22]

molecules. This has been demonstrated using oxides [7, 14, 8, 15], salt [67, 109] and organic support [110]. It is also possible to combine an insulating layer and molecular crystals [111, 112, 113].

Lastly, a more device oriented approach has been demonstrated: (c) the use of elongated π -conjugated molecules suspended between tip and sample of the STM [22].

These methods share the capability of slowing down the non-radiative charge/energy transfer towards the electrodes sufficiently to allow intramolecular processes to occur. In the following sections we describe these three approaches through some examples.

Multilayer of molecules

In figure 2.9(d) the results of a STM-LE experiment on a multilayer of *Meso*-tetrakis(3,5-di-tertiarybutyl-phenyl)porphyrin on Au(100) are reported [107]. The light emission spectra illustrate the effect of an increased number of molecular layers on the decoupling. While for one to three layers of molecules the luminescence resembles the plasmonic emission on the bare sample, for six layers (red curve) the spectrum closely resembles the fluorescence spectrum acquired on a crystal of the same molecule (black curve).

When working on clusters of molecules, either a multilayer or a molecular crystal, it is important to determine what and where is the source of the emission. It is generally accepted that the emission comes from the superficial layers of the cluster, while the lower ones prevent the luminescence quenching. Moreover, the experiment allows the localization of the tip on a precise molecule of the top layer. As a consequence, it has been first claimed that the light emission was generated by this specific molecule. However, experiments by Rossel *et al.* using mixed crystals of C60 and C70 pointed to the fact that the emission does not originate from an individually selected molecule [85]. They came to this conclusion by observing an optical spectrum of C70 type even when a C60 molecule was located under the tip. This suggests that the excitation generated at the tip-molecule interface may be transferred, by charge or energy exchange, between molecules of the cluster. The emitting center is therefore not the molecule directly addressed by the STM tip. One may even wonder if one or several molecules contribute to the optical spectrum. Merino *et al.* recently answered this question by studying the photon statistics through time correlation measurements performed using a Hanbury Brown-Twiss interferometer [35]. Their experimental observation of photon *antibunching*, the first ever reported in an STM-LE experiment, indicates the presence of single photon sources. However, the source of the emission was assigned to specific emitting centers due to the presence of spatially localized charge traps, and not directly to a single molecule.

Insulating layer

The use of insulating layers made of oxides or nitrides, allows getting rid of the ambiguity about the origin of the emission by studying isolated molecules (figure 2.9(b)). This was demonstrated first by W. Ho and collaborators by studying Zn(II)-etioporphyrin I (ZnEtiol) adsorbed on a thin Al_2O_3 film [7]. The same group performed also similar studies with magnesium porphyrin (MgP) [14, 8]. A set of optical spectra on an isolated MgP is reported in figure 2.9(e) as a function of the bias. These spectra show a narrow-line emission at 1.56 eV ($\text{FWHM} \leq 5$ meV) whose position is independent on the emission bias, a strong indication of intramolecular transitions. Moreover, on the low energy side of this emission a broader emission is detected (associated to plasmonic emission), together with a series of low intensity peaks, corresponding to the harmonic progression of a vibrational mode of the porphyrin.

It is interesting to remark that in these experiments, as well as in the more recent ones by Lee *et al.* on a similar system [15], the electroluminescence cannot be assigned to optical transitions of the molecule (*i.e.* the energy of the emission does not match the fluorescence of the molecule).

While the absence of neighboring molecules allows to assign the luminescence to the specific molecule on top of which the tip is located, the subnanometric resolution of the STM allows going one step further. Indeed, depending on the precise location of the tip on different parts of the molecule, the light emission spectra can have different intensity or shape. Recently, the high resolution of the STM was used by Zhang *et al.* to probe the influence of the environment on the emission of Zinc phthalocyanine (ZnPC) on a thin NaCl layer [67]. In this experiment, they studied the emission from a single ZnPC and compared it to the emission when a second molecule is approached. They evidenced the dipolar coupling between the two molecules from the splitting of the emission line. They also acquired photon maps at the energies corresponding to different peaks, reconstructing a “real space image” of the dipolar coupling.

Suspended molecule

The study of the STM-LE of single molecules decoupled by thin insulating layers is of great interest from a fundamental point of view. However, if we envision to exploit the light emission properties of single molecules in a device, the presence of an insulating layer may be a limitation. One of the reasons is the limited current that can flow through the junction (≤ 1 nA) in presence of the insulator. To face this issue a contact with the electrodes seems mandatory. STM-LE experiments where molecules simultaneously contact both tip and sample were first performed by Schneider *et al.* [114]. While they revealed a connection of the emitted light with the shot noise in the current at the molecular contact (something already known for metallic contacts

[115]), the coupling with the metal resulted in the quenching of any intramolecular transitions.

In order to combine direct contact with the metal and intrinsic luminescence, Reecht *et al.* suspended an elongated π -conjugated polythiophene molecule (see figure 2.9(c)) between the sample and the tip of the STM [22]. In the previous methods the decoupling was provided either by the first molecular layers or by the insulator. In this case, the lifting procedure leaves a part of the molecule free from contact with the electrodes. When the suspended part is long enough, an intramolecular transition becomes possible. The result of their experiment is presented in figure 2.9(f) for a wire lifted by $3 \leq z \leq 5$ nm, and for different applied bias. We observe the presence of a broad resonance (FWHM ≈ 200 meV) at 1.8 eV whose position is independent from the applied bias.

This experiment was a successful proof of concept: it is possible to measure fluorescence from a molecule in a circuit-like configuration. However, the large width of the resonance indicates that this system is still partially coupled to the electrodes and the molecular orbitals involved in the transitions are broadened due to this coupling. As a consequence, it is impossible to observe low energy features like vibrational modes that, if present, are hidden by the broad nature of the emission. This makes it also non obvious to distinguish the emitted light from the purely plasmonic one. Moreover, for fundamental reasons, having a well defined emission line would be an asset. It would indeed allow the coding of information in the energy of the emission, something possible only when the energy is well defined.

2.2.5 Light emission mechanisms from decoupled molecules

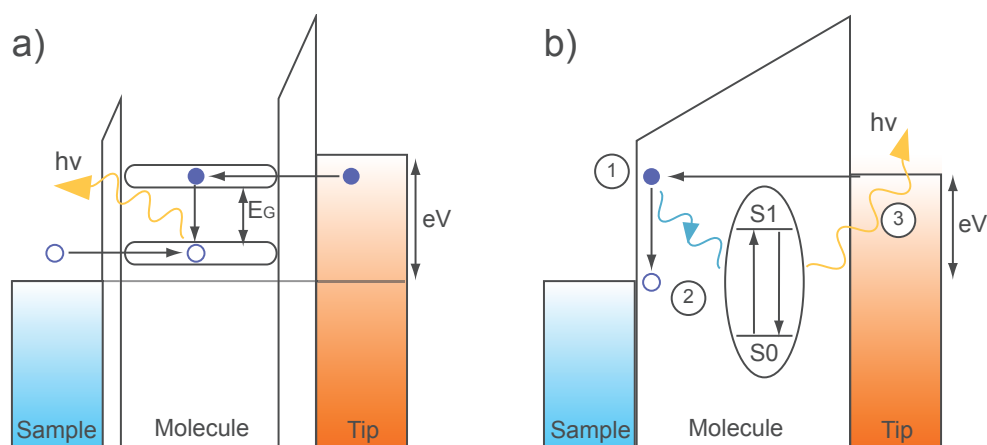


Figure 2.10 – Comparison of light emission mechanisms. (a) Scheme of the electron injection mechanism. (b) Scheme of the plasmon mediated mechanism.

There are two fundamentally different models used to explain the STM-LE from molecule. They are sketched in figure 2.10. The first one, (a), is the injection of

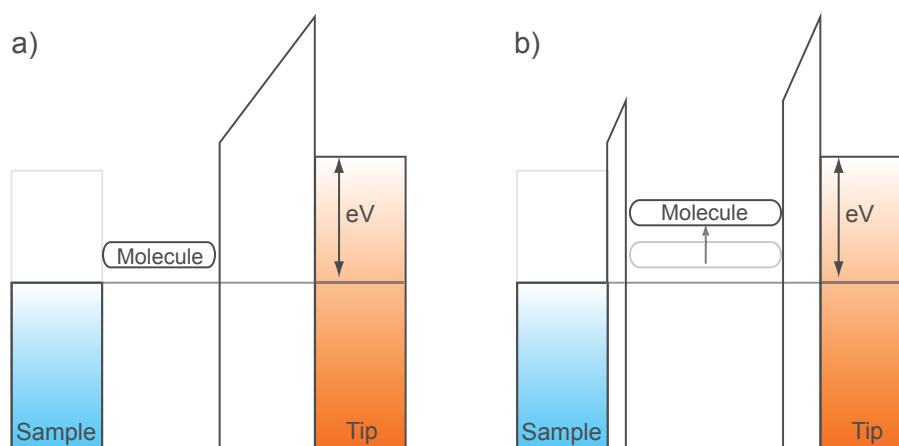


Figure 2.11 – Single and double barrier tunneling junctions. (a) Scheme of a single barrier junction. The molecular level is “pinned” to the sample. (b) Scheme of a double barrier tunneling junction. The voltage drops partially on the two sides of the molecule. The molecular level shifts with the applied bias.

charges in the molecule, followed by a radiative recombination. In the second one, (b), the excitation occurs through an energy transfer from the tunneling electrons to the molecule, mediated by localized plasmons. Before turning to the description of the two models, it is important to discuss how the voltage drops in a tunneling junction for two different cases: the single barrier tunneling junction and the double barrier tunneling junction.

Single barrier tunneling junction. When the molecule is on the metallic sample the vacuum barrier between the tip and the molecule offers the highest impedance in the system. For this reason we consider that the voltage drops exclusively between the tip and the molecule. In this case, the molecular levels are “pinned” to those of the sample. This is illustrated in the single tunneling barrier model (figure 2.11(a)).

Double barrier tunneling junction. In the case of decoupled molecules the situation is more complex. The insulating layer, or the first layers of molecules, plays the role of a barrier. The junction behaves now as a voltage divider. When a bias is applied, the voltage drops partially between the sample and the molecule and partially between the molecule and the tip (dbtj: double barrier tunnel junction, figure 2.11(b)). This results in a shift of the molecular levels with respect to both electrodes: the molecular levels are no longer “pinned” to the sample. We will explain why this is a key point for the emission mechanism.

The case of the suspended molecule is peculiar. Here, there is a direct contact with both tip and sample. This means that no vacuum barrier is present. However, there

are two contact resistances at the interfaces between the molecule and the metallic tip and sample. In such a junction, it is often considered that all the voltage drops at these interfaces. In the case of thiophene the resistance is of the same order of magnitude, albeit not identical, on the two sides. This results again in a double barrier model for the voltage.

We can now turn to the description and comparison of the two models of STM-LE from molecules.

Electron injection model

The charge injection mechanism consists in the injection of a tunneling electron into a high energy electronic level of the molecule followed by an internal radiative decay to a lower energy level. The mechanism, presented in figure 2.10, can also be understood as a simultaneous injection of an electron in the high energy level and of a hole in the low energy one. Their recombination results in the emission of a photon. The emitted photon has energy $h\nu$ corresponding to the gap between the two levels involved in the transition E_G .

The prerequisite for this mechanism is to have two (partially) empty electronic states between the Fermi levels of the electrodes, these are generally the HOMO and the LUMO of the molecule [107, 111, 8, 22, 67], but sometimes transitions between LUMO+1 and LUMO were proposed [7, 14].

As a consequence, the voltage bias V required to stimulate the luminescence of the molecules is generally higher than the energy gap between the levels E_G , or, equivalently, of the energy of the radiative transition: $eV > E_G = h\nu$. This is illustrated in figure 2.12, where the energy diagram of a double barrier tunneling junction is presented for three different bias voltages. In (a) the system at zero bias is presented, defining the initial positions of the molecular levels with respect to the Fermi levels of the electrodes. In (b) a bias V corresponding to the HOMO-LUMO gap, E_G , is applied to the tip. We observe that, due to the repartition of the voltage drop at the two barriers, the molecular levels are shifted with respect to (a). For this reason only the HOMO is in the energy window between the Fermi levels of the electrodes, and molecular luminescence cannot occur. Finally, in (c), the threshold bias is reached and the two molecular levels are available simultaneously for injection of electrons and holes. A decay of an electron from the HOMO to the LUMO results in the emission of a photon. A more detailed version of this example is presented in appendix A.

A second important characteristic arises from the asymmetry of the position of the molecular levels, and from the asymmetry of the voltage drop: the voltage threshold for the onset of the luminescence is different for positive and negative polarity.

A third important specificity of this model is that, since the tunneling electrons are the source of the excitation, there is a direct link between the $dI/dV(v)$ spectra and

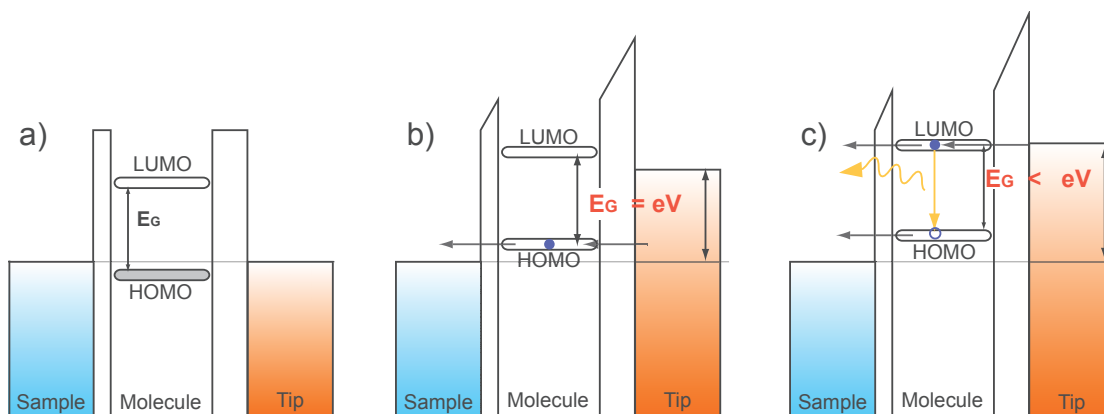


Figure 2.12 – Electron injection mechanism. Energy diagram of a double barrier tunneling junction for zero applied bias (a), a voltage bias equal to the molecular gap (b) and the threshold voltage bias for luminescence (c). The dashed arrow in (c) represents an elastic (non-radiative) tunneling from the molecule to the sample.

the optical one. This allows the indirect measurement of the voltage drop repartition across the junction [7, 22]. Moreover, since the two molecular levels involved in the optical transition need to be located between the Fermi level of the electrodes, their resonances should be detected in the STS spectra at the same polarity [22].

Finally we describe the role of the localized surface plasmon. Once the electron is in the high energy level of the molecule, it can still tunnel out elastically (dashed arrow in figure 2.12(c)) or decay to the lower level in a non-radiative way. Normally in STM experiments, elastic tunneling dominates and the molecule can be considered a bad emitter. This means that the radiative rate Γ_{rad} is small when compared with the overall rate Γ of de-excitation of the molecule: $\Gamma_{rad}/\Gamma \ll 1$.

A plasmonic resonance at the energy of the molecular transition offers new decay paths that can be radiative and non-radiative, a mechanism known as Purcell effect [116]. The number of inelastic electrons thus increases at resonance with the plasmons. The net result, for a bad emitter, is an increase of the radiative rate.

Plasmon mediated excitation

The second excitation mechanism was first proposed in two experimental papers [36, 37] and discussed from a theory point of view in [117, 118]. This mechanism involves the excitation of the emitter by the localized plasmons, as sketched in figure 2.13. The process consists in three steps: (1) an inelastic tunneling electron loses its energy to a LSP. (2) The localized plasmon transfers its energy to the molecule. In this way, an electron from a molecular level is promoted to a higher energy level, leaving a hole

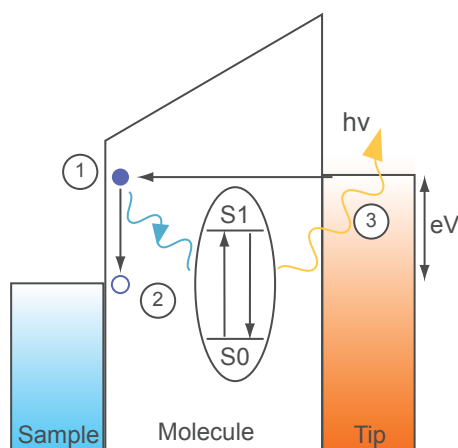


Figure 2.13 – Plasmon mediated mechanism. Energy diagram illustrating the plasmon mediated excitation mechanism.

behind. The molecule goes from the ground state S_0 to the first excited state S_1 . Finally, in step (3) the molecule decays to its ground state emitting a photon.

Let us make some observations about this mechanism. The molecule still needs to be decoupled from the metal, to avoid the quenching of the fluorescence. However, the voltage drop is not a critical issue anymore since electrons and holes are not injected in the molecule from the electrodes. Rather, an exciton is created thanks to the energy transferred by the plasmon. Therefore, the two molecular levels do not need to be in between the Fermi levels of the electrodes. Consequently, no direct relation between the STS spectrum and the optical one is expected.

In this mechanism, an inelastic electron of energy eV equal to the molecular gap E_G is sufficient to excite the emitter. Moreover, this mechanism is bipolar, meaning that the onset of the luminescence is expected for the same voltage at positive and negative bias. Nonetheless, different yields can be expected for the two polarities: the presence of molecular states can modify the plasmonic intensity at opposite polarities, thus influencing the transfer of energy to the molecule.

A specificity of this mechanism is the possibility to excite the emitter “at distance”. This was first demonstrated by Schneider *et al.* by measuring the luminescence of porphyrins adsorbed on an STM tip [37]. To perform the experiment, STM tips with the shaft covered by multilayer of adsorbed TPP molecules and a clean tip end were prepared (*m*-tips, sketched in figure 2.14(a)). The luminescence spectrum obtained using an *m*-tip on a clean Ag(111) surface (figure 2.14(b), top spectrum) was compared with the spectrum obtained with a normal Ag tip on a molecular cluster of TPP (figure 2.14(b), bottom spectrum), showing that the emission features of the molecules can be found in both. However, with an *m*-tip, tunneling current do not flow through the molecules, therefore an electronic excitation of the molecules on the shaft is excluded. This (1) proves the validity of the plasmon excitation model and (2) illustrates the possibility to excite molecules not directly located under the STM tip.

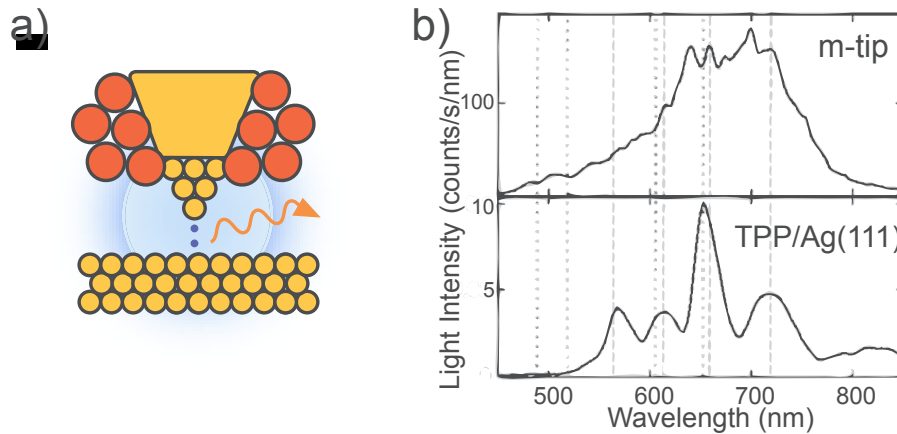


Figure 2.14 – Light emission from molecules on the shaft of an STM tip.

(a) Schematic representation of an *m*-tip. The shaft is covered with molecules while the tip end is clean. (b) Light emission spectra of (top) an *m*-tip on a clean Ag(111) sample, (bottom) a clean Ag tip on a molecular cluster of TPP on Ag(111). Adapted from [37].

Finally let us stress that, in this mechanism, the plasmon is crucial to excite the molecule, but it also affects the de-excitation through the Purcell effect. Therefore the dependency of the emission with the LSP is non-trivial. This aspect is further discussed in sections 3.3.6 and 3.3.7.

Comparison of the mechanisms

In general terms we can express the emission rate of the molecule as

$$\gamma_{em} = \gamma_{ex} \frac{\Gamma_{rad}}{\Gamma}, \quad (2.15)$$

where γ_{ex} represents the excitation rate and $\frac{\Gamma_{rad}}{\Gamma}$ is the photon emission probability. The two proposed mechanisms differ in the excitation term. In one mechanism the excitation is due to the injection of electrons (electronic excitation), while in the other the LSP mediates the energy transfer to the molecule (plasmon mediated excitation). For both, the emission probability term is influenced by the presence of the plasmonic resonance [119, 120]. With this in mind, in table 2.1 we can compare the two excitation mechanisms.

Table 2.1 – Comparison of the excitation mechanisms

	Electron injection	Plasmon mediated
Threshold	$eV > E_G = h\nu$	$eV = E_G = h\nu$
Threshold is polarity	Dependent	Independent
Link with $dI/dV(V)$	Yes	Not necessary
Remote excitation	No	nm range

We observe that two entries in the table are related to the threshold on the voltage bias, that is indeed a key point in distinguishing between the two mechanisms. In particular, a molecular fluorescence appearing as soon as the electrons have energy eV corresponding to the molecular gap E_G (and, consequently, to the frequency of the emitted photons $h\nu$) is a strong indication of a plasmonic excitation.

2.3 Conclusions and outline

In this chapter we introduced the basic techniques and instruments used during my Ph.D. Moreover, we detailed the STM-induced light emission mechanism and discussed some important results on molecular fluorescence excited with an STM.

The extreme spatial resolution of an STM allows investigating the properties of single molecules, a feature that has an enormous potential for the understanding of fundamental properties of these objects. However, STM-LE studies of single molecules reported until now, somehow fail to fully exploit this potential.

One example is the origin of the light emission: optical spectra showing peaks with a well defined energy (and narrow linewidth emission), have been reported in several experiments [7, 14, 8, 15]. However, the assignment of these peaks to a well defined optical transition is not straightforward.

Another example concerns vibrational peaks in optical spectra. Although these features have been observed in some experiments [7, 14, 8], they arise from a harmonic progression of a single mode, thus failing to provide a chemical fingerprint of the emitter like the one that can be obtained through Raman spectroscopy.

Moreover, even if single photon sources in an STM-LE experiment were recently observed [35], it was from clusters of molecules, thus making impossible to localize the specific emitter.

Last, in all the experiments on single molecules, an electronic excitation of the emitter through the tunneling current has been suggested. However, the existence of the plasmon mediated excitation mechanism [36, 37], that has been proved for multilayers of molecules, leaves an open question on the possibility that this mechanism might play a role in the STM-LE of single molecules as well.

If we turn to the applicative aspects, and we wish to integrate a molecular component in an electronic circuit, the direct contact of the molecule with the electrodes becomes essential. However, in this configuration, the interaction with the metallic tip and sample quenches most of the fluorescence.

The recent work of Reecht *et. al* proved that, by using elongated molecules, it is possible to recover the fluorescence from a molecular junction [22]. However, the residual coupling with the electrodes resulted in a broadening of the emission peak to a width of ≈ 250 meV, comparable to the one of a purely plasmonic emission.

The possibility to drive a narrow line light emission (FWHM in the meV range) from a molecular system in contact with the electrodes is thus still missing. Building such a system would be useful for the conception of devices that interface electronic circuits with optical and plasmonic ones.

Some specific features would be desirable in such a device. First of all, the emission energy should be well defined and predictable. A control over the properties of the emitted light, like the color and the coherence, would be desirable. Depending on the specific use it may be useful to have either on-demand photons (single-photon source) or a high luminosity. To achieve high luminosity, a high quantum yield and/or the possibility to drive the component with elevated current is required. In a later stage, it would be important to achieve high mechanical resistance, and consistency (showing the same properties every time).

In order to address some of these challenges, we propose the realization of systems composed of a molecular wire and an emitting unit, a chromophore, in a similar way to what has been done by Marquardt *et al.* with carbon nanotubes [121]. The hypothesis is that, by lifting such a system with the STM tip, the molecular wires will provide the contact with the electrodes, while the chromophore will be decoupled from them.

In principle this system offers the possibility to adapt the molecular wire and the emitting unit, in order to find the combination that has the desired opto-electronic properties.

The next chapter is dedicated to the realization of this system and to the study of its optical properties. This study will provide several insights into the fundamental aspects of STM-induced light emission from single molecules.

CHAPTER 3

Narrow line emission of light from a molecular junction

We saw in chapter 2.2.5 that STM-induced light emission (STM-LE) from molecules interacting with a plasmonic environment has been studied since the beginning of the 1990s [13]. A key result is that a direct contact of the molecule with the metallic electrodes results in the quenching of any intrinsic luminescence [114] as it happens in standard photoluminescence experiments [106]. This problem has been solved by decoupling the molecules from the electrodes with thin insulating layers of oxide [7, 14, 15] or salt [67, 109, 68] or by using self-decoupled molecules [110]. While these approaches can be extremely insightful for a fundamental understanding of STM-LE, they lack an efficient transport capability due to the presence of the insulating layer and of a vacuum gap between tip and molecule, thus making it non suitable for integration in future electronic circuits. In 2014, Reecht *et al.* [22] reported on the intrinsic electroluminescence of a single π -conjugated molecular chain suspended between the tip and the substrate of an STM. In this device-oriented configuration, long molecular chains were exploited to reduce the coupling with the electrodes, in a similar manner to what has been done by Marquardt *et al.* [121] with carbon nanotube electrodes. In this experiment, using oligothiophene, the wire was however not fully decoupled from the electrodes, and a broad emission line of some hundreds of meV was observed. This prevented to gain further information from the light emission spectra.

In this chapter we report on the synthesis and the characterization of single molecule systems that allow narrow line emission while conserving a device configuration. The system consists of an emitter embedded in a molecular wire that bridges the electrodes. This system is a nanometer scale organic version of a quantum dot embedded in a nanowire [38].

These devices were made by on-surface co-polymerization of chromophore molecules and oligothiophene chains. Oligothiophenes are π -conjugated molecules which can

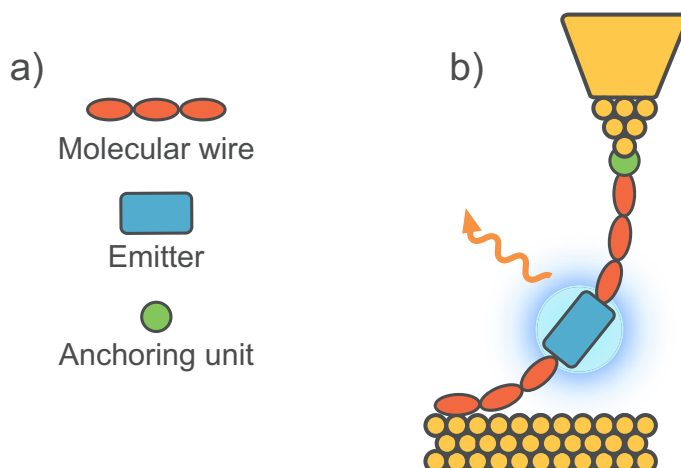


Figure 3.1 – Experimental concept of an emitter in a molecular junction.
(a) Components. (b) Lifted configuration for measurement.

form long wires, and whose electronic, mechanical and optical properties have been studied at the single molecule level [40, 22, 41]. The wires are stable and allow for the use of fairly high currents when suspended between tip and sample ($I < 5$ nA). Porphyrin derivatives were chosen as molecular emitters. Molecules from the porphyrin family generally show absorption and emission in the visible range due to the extended conjugation of the macrocycle composing the core of the base molecule, porphyrin. It is therefore one of the widely studied family of dyes, together with phthalocyanines. Moreover, these molecules play an important role in many biological processes, including photosynthesis. Studying their optical properties down to the single molecule level is therefore relevant to get atomic-scale understanding of these phenomena.

3.1 Sample preparation

This section is divided in three parts. First we describe the concept of the experiment. Then we report on the synthesis of the co-polymer. In the final part we show how it is possible to manipulate the molecule in order to suspend it between the sample and the tip of the STM.

3.1.1 Concept of the experiment and basic methodology

The experimental concept is illustrated in figure 3.1. In (a) the three components of the molecular systems are presented: a molecular wire for transport of the current and for decoupling a chromophore acting as the emitter, and an anchoring that ensures a

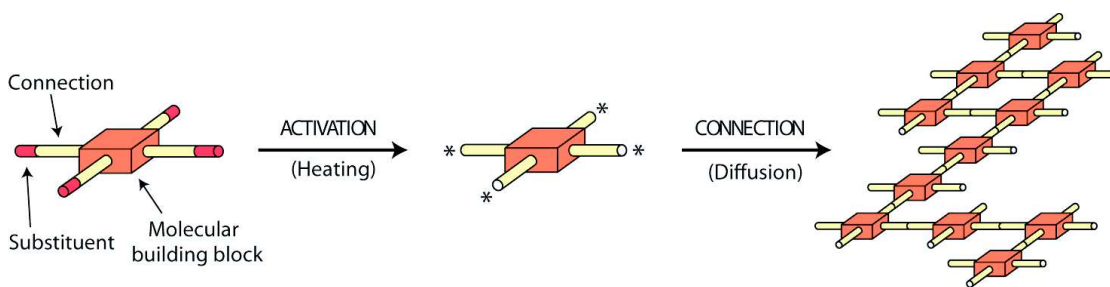


Figure 3.2 – On-surface polymerization procedure. The on-surface polymerization procedure consists in three steps: First, the deposition of a building block with a connection and a substituent unit. Second, the activation by heating of the surface; this removes the substituents and leaves free radicals in the desired positions. Third, the connection due to the diffusion of activated molecules on the surface. Adapted from [39]

good connection between the molecule and the STM tip. The final configuration is sketched in (b), where the molecular device is suspended between the sample and the tip of the STM.

In order to build such a system we realized an on-surface polymerization of the different elements. In 2007, Grill *et al.* established a method to covalently bond molecular building blocks on a metallic surface [39]. The method is depicted in Fig 3.2. It requires molecular building blocks with halogen radicals (typically Br or I) at their extremities. The halogens act as substituent units in the functionalized molecule. First, the building blocks are evaporated on a metallic surface. The activation consists in providing thermal energy to the molecules in order to dissociate the halogens from the base units. The molecules are then left with a free radical in the position once occupied by the halogen. Depending on the chosen halogen and on the nature of the metallic substrate the activation temperature can change. Thermal energy can be also used to induce the third step where molecules diffuse on the surface until a connection is made between two free radicals.

Since its conception, this method has been used to build several unidimensional systems like porphyrin wires [122], polyfluorene chains [42], polythiophene chains [40, 22], phenyl based structures [123] or atomically precise graphene nanoribbons [60, 124, 125]. This method is also highly promising for the production of two dimensional covalent organic networks, a kind of 2D polymers having fascinating electronic and optical properties [126].

In our experiment we used 5,5'-Dibromo-2,20:5',2''-terthiophene (DBrTT) purchased from Sigma-Aldrich as a basis for the molecular wire (see figure 3.3(a)). For the chromophore we used a derivative of porphyrin: 5,15-(diphenyl)-10,20-(dibromo)porphyrin ($\text{Br}_2\text{-DPPH}_2$), purchased from Frontier Scientific (see figure 3.3(b)). As we will see in the following, $\text{Br}_2\text{-DPPH}_2$ acts also as the anchoring unit. In this way we need to build

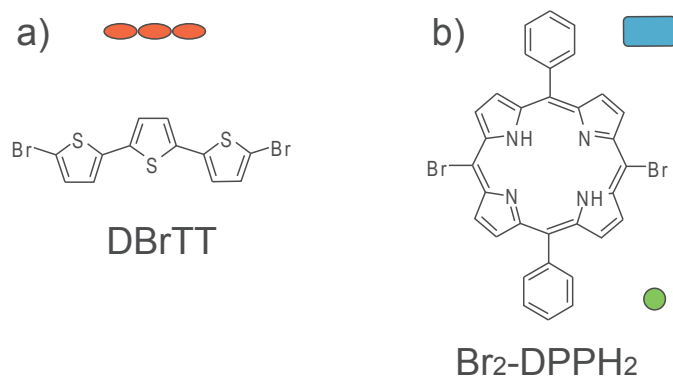


Figure 3.3 – Building blocks: DBrTT and Br₂-DPPH₂. (a) Chemical structure of dibromo-terthiophene (DBrTT) which will form the molecular wire, and (b) dibromo-diphenyl-H₂-Porphyrin (Br₂-DPPH₂) that is used both as emitter and as anchoring unit.

co-polymers of only two different elements. The two types of base units are functionalized with bromine atoms to make the on-surface polymerization through Ullmann de-halogenation reaction possible.

3.1.2 Preliminary study

The activation and the diffusion of the molecules on the surface require some thermal energy that is provided by annealing the sample. One has to know the effects of the annealing on the basic components before trying to build the co-polymers. DBrTT has been previously studied and is known to produce flexible wire-like structures on the Au(111) surface [40, 22]. On the other hand some porphyrins on metallic surface are known to undergo transformations like self-metalation [127] and dehydrogenation reactions [128, 129] among others [130]. For this reason, we decided to perform a preliminary study of porphyrin alone. We first used 5,15-(diphenyl)-porphyrin (DPPH₂) (sketch in figure 3.4(a), the same molecule that will be used to build the polymers, but without the bromine atoms.

We sublimated DPPH₂ from a Knudsen cell on the Au(111) sample. The sample is kept at 5 K during the evaporation in order to minimize any possible spontaneous reaction. The molecule sublimates at ≈ 500 K. A STM image of the deposited species is provided in figure 3.4(b). In this image we first recognize the core of the porphyrin that appears as a square with a hollow center. The two bright spots on the side are also visible, and may be associated to the extended phenyl rings, twisted with respect to the porphyrin core due to steric hindrance. This out-of-plane configuration of the rings yields an increased contrast in the topographies.

The following step consists in annealing the sample at a temperature of 480 K, the

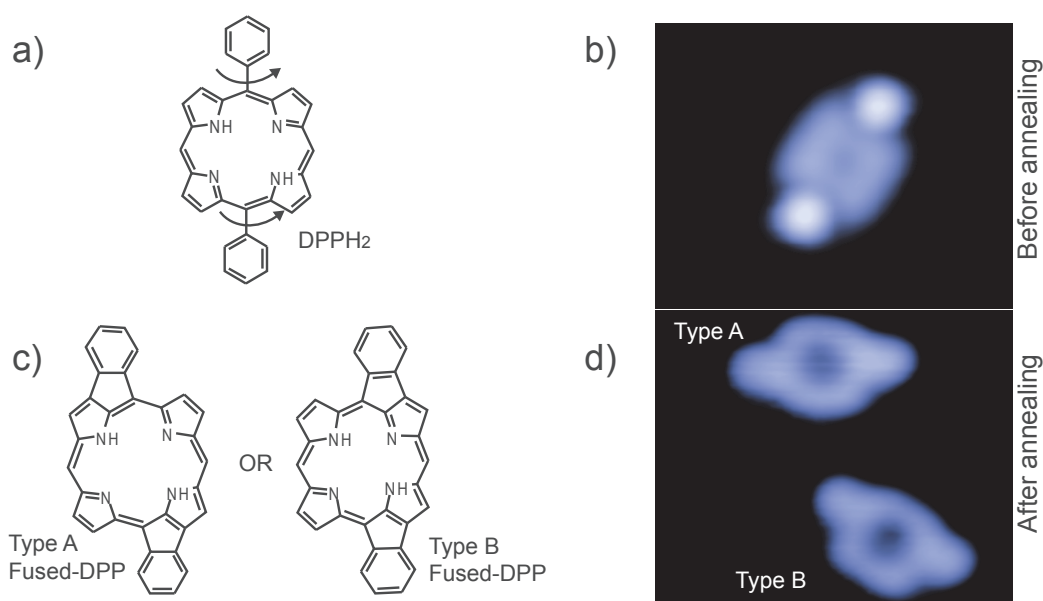


Figure 3.4 – Cyclodehydrogenation of DPPH₂ (a) Sketch of diphenyl-H₂-Porphyrin (DPPH₂). (b) STM topography of DPPH₂ on Au(111) ($3.5 \times 2.8 \text{ nm}^2$, $V = -0.1 \text{ V}$, $I = 0.1 \text{ nA}$). (c) Sketch of the two fused-DPP isomers. (d) STM topography of the two fused-DPP isomers ($3.5 \times 2.9 \text{ nm}^2$, $V = -0.1 \text{ V}$, $I = 0.1 \text{ nA}$).

same temperature used to form the thiophene polymers [40]. After this procedure, the STM images (figure 3.4(d)) change drastically. The porphyrins appear now in two different conformers. For both of them the intensity of the phenyl ring in the STM image is now the same than on the core of the molecule. This suggests that the rings are now in-plane with the rest of the molecule. Based on the structure of the DPPH₂ the presence of the two isomers is hard to explain. However, the high temperature might have induced some intramolecular transformation. It is known that a similar molecule, free-base tetraphenylporphyrin (2H-TPP) can undergo a surface assisted thermally activated cyclo-dehydrogenation on Ag(111) [128, 129]. In this process, a ring closing reaction occurs. Surface assisted cyclo-dehydrogenations are known to occur also on Au(111) and Cu(111) for different molecules: they are a key ingredient for the bottom-up synthesis of different graphene nanostructures [60, 131].

Based on these examples, we can interpret the presence of the two isomers on the surface as a result of cyclo-dehydrogenation reactions. This leads to a configuration where the two phenyl rings are fused to the core of the molecule. Note that each of them can either fuse *on the right* or *on the left*, resulting in the two isomers sketched in figure 3.4(c). In the isomer of type A the phenyl rings are fused in a *trans* configuration with respect to the core. In type B they are in a *cis* configuration. We will refer to these two isomers, indistinctly, as **fused-diphenyl porphyrin (fused-DPP)** in the rest of the manuscript.

This cyclo-dehydrogenation has some practical consequences. The first is the fact that the fused-DPP has a planar structure. This might play a role when trying to make co-polymers with DBrTT. The second one is related to their optical properties. The absorption energy of DPPH₂ is essentially determined by the porphyrin core of the molecule. In the fused-DPP the conjugation length is extended by the presence of the now fused rings. This should reduce the optical gap of the molecule. This is actually confirmed by calculations made by **time-dependent density functional theory (TD-DFT)**¹. The energy gap between the first excited state (S1) and the ground state (S0) decreases from 2.19 eV, for DPPH₂, to 1.51 eV for fused-DPP.

Note that annealing the sample above 600 K leads to the desorption of most of the molecules from the surface.

3.1.3 Synthesis of the co-polymers

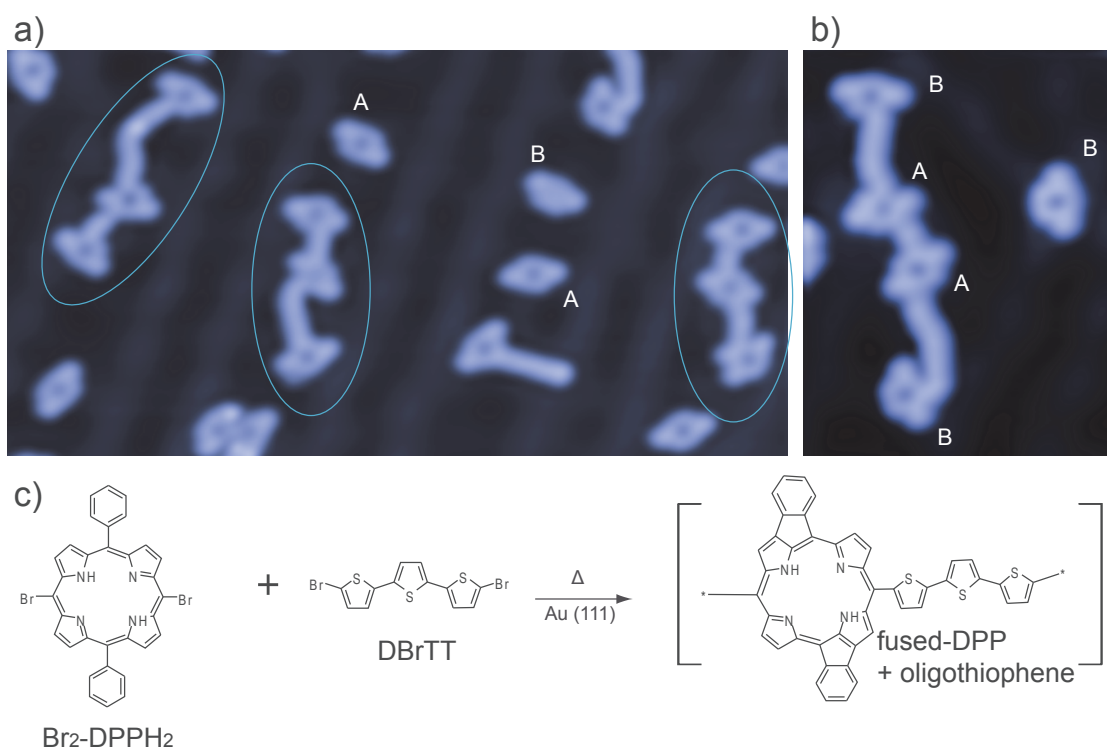
The deposition of the molecules is done in two consecutive steps : first the DBrTT is evaporated on the gold substrate, then the Br₂-DPPH₂ is added on the same sample.

- DBrTT spontaneously sublimates at room temperature, at a base pressure of $5 \cdot 10^{-10}$ mbar [40]. We use a Ta crucible kept at some millimeters of distance from the sample at room temperature to evaporate it. The covering rate depends linearly on the deposition time.
- Br₂-DPPH₂ were sublimated from a Knudsen cell, on the sample kept at room temperature. The evaporation rate was monitored with a quartz crystal micro balance.

The samples with the adsorbed molecules were annealed to a temperature of $T = 480$ K for 15 minutes. At this temperature both the de-halogenation and the diffusion processes occur. In figure 3.5(a) a topography obtained after the annealing is presented. We observe several isolated porphyrins as well as wire-like structures made of alternating porphyrin and oligothiophene units. We observe that the porphyrins appear in their fused form, indicating that the cyclo-dehydrogenation reaction occurs also on bromine-functionalized molecules. It is sometimes possible to find a de-halogenated but non fused porphyrin on the surface. This suggests that the cyclo-dehydrogenation occurs at a slightly higher temperature than the de-halogenation.

Amongst the different combinations we are interested in co-polymers that are terminated with a porphyrin, like the ones highlighted in figure 3.5(a). In these systems the porphyrin terminating the wire can be used as an anchoring unit to lift the polymer.

¹Calculations were performed using the Gaussian 09 software. The geometries of the molecules were optimized using the B3LYP functional and the 6-31G(d,p) basis set.



In (b) a more resolved image of such a co-polymer is presented. We observe that the porphyrins are also fused in the co-polymer. This image also shows that two porphyrins can be separated by thiophene units of different lengths. In the example of (b) both terthiophene and sexithiophene units are present. Examples with longer thiophene wires are seldom found. We point out that, even if well defined wires containing pairs of consecutive porphyrins are obtained, such configurations are not so frequent. More complex and less well defined polymeric structures are also observed.

Overall, we can summarize the sample preparation by the co-occurrence of two reactions: a double cyclodehydrogenation of DPPH₂ and a thermally activated polymerization through the Ullmann-type reaction. The overall reaction is sketched in figure 3.5(c).

In this section we demonstrated a method to synthesize, on the Au(111) surface, well-defined molecular architectures composed of a chromophore unit (fused-DPP) integrated in a current carrying wire (oligothiophene) terminated by anchoring units (the extremal porphyrin molecules). We are now ready to manipulate the wires in order to lift them and create a molecular junction like the one sketched in figure 3.1(b).

3.2 Manipulation of the co-polymers by STM

Once the co-polymers have been synthesized the objective is to lift them from the surface. This is a key step in order to obtain a configuration in which the porphyrin is suspended between the tip and sample of our STM, and potentially decoupled from the electrodes by the oligothiophene chains.

The procedure to lift the wire is similar to the one introduced by Lafferentz *et al.* on polyfluorene [42] and later used to lift other molecular wires including graphene nano ribbons [43], oligothiophene [22] and others [44, 45].

We apply this procedure to wires terminated by a fused-DPP that will be used as anchoring unit for the lifting². As a first step, the STM tip is located over the extremity of a co-polymer, position 1 in figure 3.6(a). Then the tip is approached in a controlled way³ until a contact is made with the molecule. During the procedure the tunneling current is measured. In figure 3.6(b) we represent the normalized conductance G/G_0 (here $G = I/V$ and $G_0 = \frac{2e^2}{h}$ is the quantum of conductance) recorded during this procedure. The red curve corresponds to the approach of the tip to the molecule. At large tip-sample separation there is an exponential increase of the conductance as the tip approaches the surface in the tunneling regime. A jump in the conductance signals

²Oligothiophene-terminated wires were also tested, but the tip-thiophene bond appeared to be less strong, and the wire generally detached from the tip before spectroscopic measurement were done.

³During the manipulation of a wire the feedback loop is turned off, giving full control on the tip position to the experimenter.

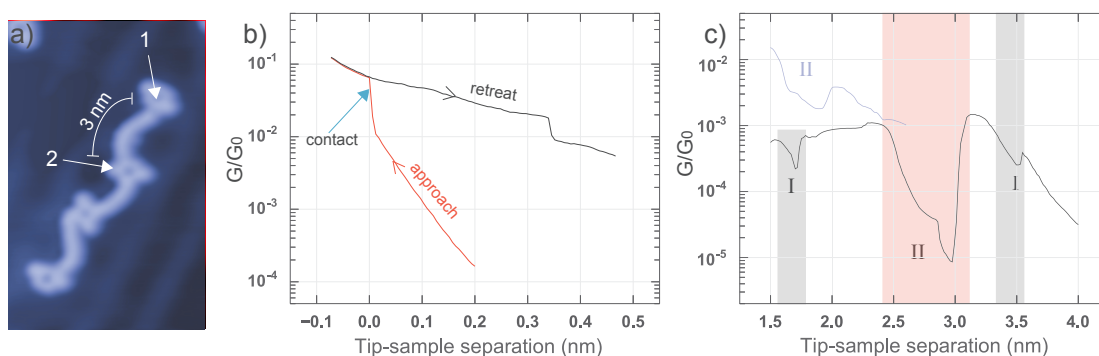


Figure 3.6 – Manipulation of copolymers of fused-DPP and oligothiophene. (a) STM topography of a molecular wire composed of fused-DPP and oligothiophene ($9 \times 14 \text{ nm}^2$, $V = -0.1 \text{ V}$, $I = 0.1 \text{ nA}$). Position 1 is where the wire was attached to the tip. Position 2 is the porphyrin whose detachment is represented in (c). (b) Normalized conductance as a function of the tip sample separation ($V = -0.1 \text{ V}$, logarithmic scale) during the first lifting of the wire. The red curve represents the approach of the bare tip towards the molecule. The black curve is the retraction of the tip. (c) Tip sample separation ($V = -0.3 \text{ V}$, logarithmic scale) during the detachment of the porphyrin number 2 of (a) (black curve). Features 'I' are related to the detachment of a thiophene basis. 'II' is the typical signature of the macro-cycle detaching from the surface. The pale blue curve ($V = 1.6 \text{ V}$, a feature of type II) was obtained on a different co-polymer, where the porphyrin is separated from the lifting point by a shorter unit (terthiophene) with respect to the black curve (sexithiophene).

the contact with the molecule, that is followed by a regime where the conductance rises more slowly. The black curve corresponds to the retraction of the tip with the wire attached to it. The behaviour is again an exponential decreasing with the distance. We remark that the slope of the retreat curve is milder than the slope recorded during the approach. Consequently, the conductance differs by several orders of magnitude after only a few ångströms of retraction. This is a signature of the molecule being connected to the tip.

Once the “anchoring” porphyrin is attached to the tip it is possible to lift the rest of the wire with relative ease. The lifting of oligothiophene wires with an STM tip has been studied in detail in [41]. The conductance as a function of the tip-sample separation overall decreases exponentially with a slope that depends on the bias. These curves also exhibit abrupt conductance jumps which are due to a variation of the mechanic of the wire during the pulling procedure. The stress directly impacts the electronic conjugation and, consequently, the conductance of the junction. Typical conductance jumps related to the detachment of the thiophene units are identified in the $G(z)$ curve of figure 3.6(c) (features I, black line).

Another type of behavior (feature II) is also observable in this curve. It corresponds to a massive decrease of the conductance (two orders of magnitude in the example) followed by an abrupt recover to values close to the starting one ($10^{-3}G_0$ in this case). Features of type 'II' have a spatial extension (≈ 1 nm, marked by the pale red area in figure 3.6(c)) that is larger than the features of type 'I' (pale gray area in the same figure). This suggests that they relate to larger structures compared to the thiophene basis. The tip-sample separation at which the type 'II' features occur in the black curve of figure 3.6(c), is centered around 3 nm. This value approximately corresponds to the distance separating the porphyrin labelled as 2 from the lifting point in figure 3.6(a). This strongly hints that this type of feature is related to the detachment of a porphyrin from the surface. A detailed modelling of this phenomena goes beyond the scope of this manuscript.

An important remark is that the distance separating two porphyrin units depends on the length of the oligothiophene linking them. In the presented case, the two porphyrins are separated by an oligothiophene composed of six thiophene bases (sexithiophene); situations where a terthiophene separates them are also possible. This influences the tip-sample separation at which the signature of the detaching of a porphyrin occurs. An example for a wire where a terthiophene unit is present, is shown as a pale blue curve in figure 3.6(c). There, a feature of type II is centered at a tip-sample separation of 1.7 nm.

Finally, it is important to point out that the system does not appear to be rigid. Oligothiophene is known for its flexibility [40] and to stretch under mechanical constraint [41]. As a consequence, the tip-sample separation required for a detachment of a porphyrin slightly changes from a molecule to the other.

The ability of the STM to manipulate a lifted wire with atomic scale precision, together with the real time monitoring of the conductance, provide a relatively high degree of

control on the junction parameters. This will prove to be especially important to determine, with relatively good precision, the distance between the lifted porphyrin and the surface.

3.3 Light emission

In this section we describe the electroluminescence of the suspended molecular architectures described in the previous sections.

3.3.1 Experimental details

The light emission measurements were realized with an open feedback loop. In this configuration, small variations of the current, that are due to instabilities of the suspended junctions, may occur during the optical spectra acquisition. In such situations the average of the current during the acquisition is considered. The bias is kept constant during the acquisition of the optical spectra. Typical values of the current are in the range of 0.1 nA to 20 nA. Considering the efficiency of the light collection system (around 5%) and a typical yield that does not exceed 10^{-4} photons/electron, the acquisition time was in between 1 minute and 10 minutes for each spectrum.

3.3.2 First experimental evidence

In figure 3.7 (a) and (b) two luminescence spectra obtained on a co-polymer made of oligothiophene and fused-DPP (Fig 3.7(c)) suspended in the junction are presented. Both spectra were obtained for a bias voltage of 1.6 V with an acquisition time of 60 s. The first remark is that in both spectra there is no measurable light for wavelengths below 775 nm (dark arrow in the figure). This wavelength is equivalent to 1.6 eV, corresponding to the bias applied to the junction. This is expected since the photons should not have an energy exceeding the one of the tunneling electrons (quantum cutoff condition $h\nu \leq eV$, cf. chapter 2.2). The spectrum of Fig 3.7(a) was acquired at a tip-surface separation of 1.2 nm; the tunneling current measured during the acquisition is $I = 8.9$ nA. It appears as a smooth and broad (FWHM = 70 nm) peak centered around 840 nm. The spectrum of Fig 3.7(b) was obtained with the tip at a distance of 2.3 nm from the surface. The current measured during the acquisition is of $I = 0.6$ nA. In this spectrum we see a sharp (FWHM ≤ 5 nm) asymmetric peak centered at 817 nm. First, these two spectra prove that it is possible to measure the light emitted from a co-polymer suspended between the STM tip and the sample. They also show two clearly different behaviours for the same wire: a broad emission (a) and a narrow-line one (b). As we will see in the next section it is not a coincidence that the tip-sample separation in the two spectra corresponds to values well below and well above the distance between the lifting point (white arrow in Fig 3.7(c)) and the following fused-DPP.

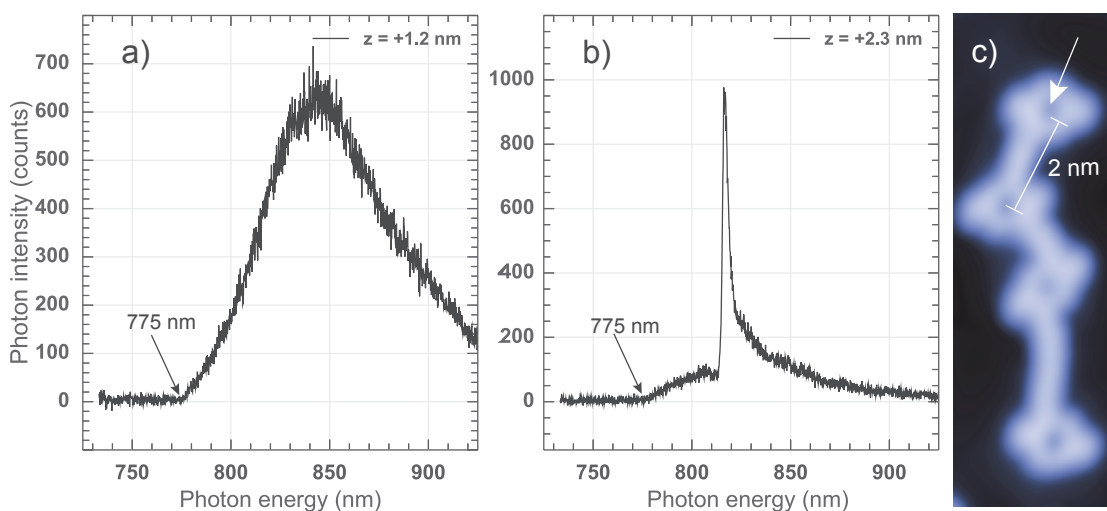


Figure 3.7 – First light emission spectra of fused-DPP. (a),(b) Electroluminescence spectra acquired on the molecular co-polymer of oligothiophene and fused-DPP represented in c) in a lifted configuration. The spectra were acquired at constant voltage (1.6 V) at two different tip-sample separations: (a) $z = 1.2$ nm, acquisition time $t = 60$ s, current $I = 8.9$ nA. (b) tip-sample separation $z = 2.3$ nm, $t = 60$ s, $I = 0.6$ nA/ (c) STM topography of the co-polymer before lifting (10.4×3.5 nm², $I = 0.1$ nA, $V = -0.1$ V). The arrow represents the anchoring position with the tip. The distance between the anchoring porphyrin and following one is ≈ 2 nm.

3.3.3 Effect of the coupling with the surface

We describe here the role of the tip-sample separation in the transition between the two regimes presented in figure 3.7. To do this, five light emission spectra obtained with the same co-polymer suspended in the junction at intermediate z values were acquired and are presented in figure 3.8(a). The voltage bias is of 1.6 V for the five spectra. We observe that the spectra have different intensities. Since we are working with a constant bias but with different tip-sample separations, the current flowing through the junction is not the same for the five spectra. Even if, in a first approximation, the current decreases in an exponential manner as the wire is lifted, we saw in section 3.2 that during the detachment of the thiophene basis and of the porphyrin units the current can vary by several orders of magnitude.

To correct for this effect, the spectra were normalized by the duration of the acquisition and by the current flowing through the junction (figure 3.8(b))⁴.

The picture then changes drastically. First of all, we remark that the intensities of the emitted light (shifted vertically for sake of clarity) are now comparable in all the spectra. What is remarkable is that the peak centered at 817 nm seems to appear and narrow down with increasing tip-sample separation. To further characterize the continuous narrowing of the peak with z , the spectra are shown as a function of the energy in eV in figure 3.8(c); the spectrum of the plasmonic response of the tip-sample junction (as measured with the tip on the bare surface), is also presented (black curve). In the same figure the values of the width of the peak are given, showing that there is more than one order of magnitude of difference in FWHM from the spectrum acquired with a tip-sample separation of 1.2 nm and the one at 2.3 nm.

Source of the emission. First, a pure plasmonic origin of the emission (as observed for molecules on metals) can be excluded from the width of the peak. This narrow-line emission indicates an intramolecular optical transition. We want here to identify the source of the emission. In practice, we have two fused-DPPs in the junction and thiophene wires may also be optically active in the visible range (fluorescence at $h\nu \approx 1.8$ eV [22]). Eventually, the different sub-units may also interact with each other, and more complex emission mechanisms could be envisaged. To discriminate between these different processes two elements should be considered:

- the position of the peak: the emission line is centered at 817 nm, corresponding to an energy of 1.52 eV. Depending on the specimen studied, the energy slightly varies between 1.47 and 1.55 eV. These values are in excellent agreement with the theoretical optical gap of the fused-DPP (1.51 eV) as we reported in section 3.1.2. This is a strong indication that the light emission comes from the $S1 \rightarrow S0$ transition of a fused-DPP.

⁴Here we assume a linear dependency of the light emission with the current.

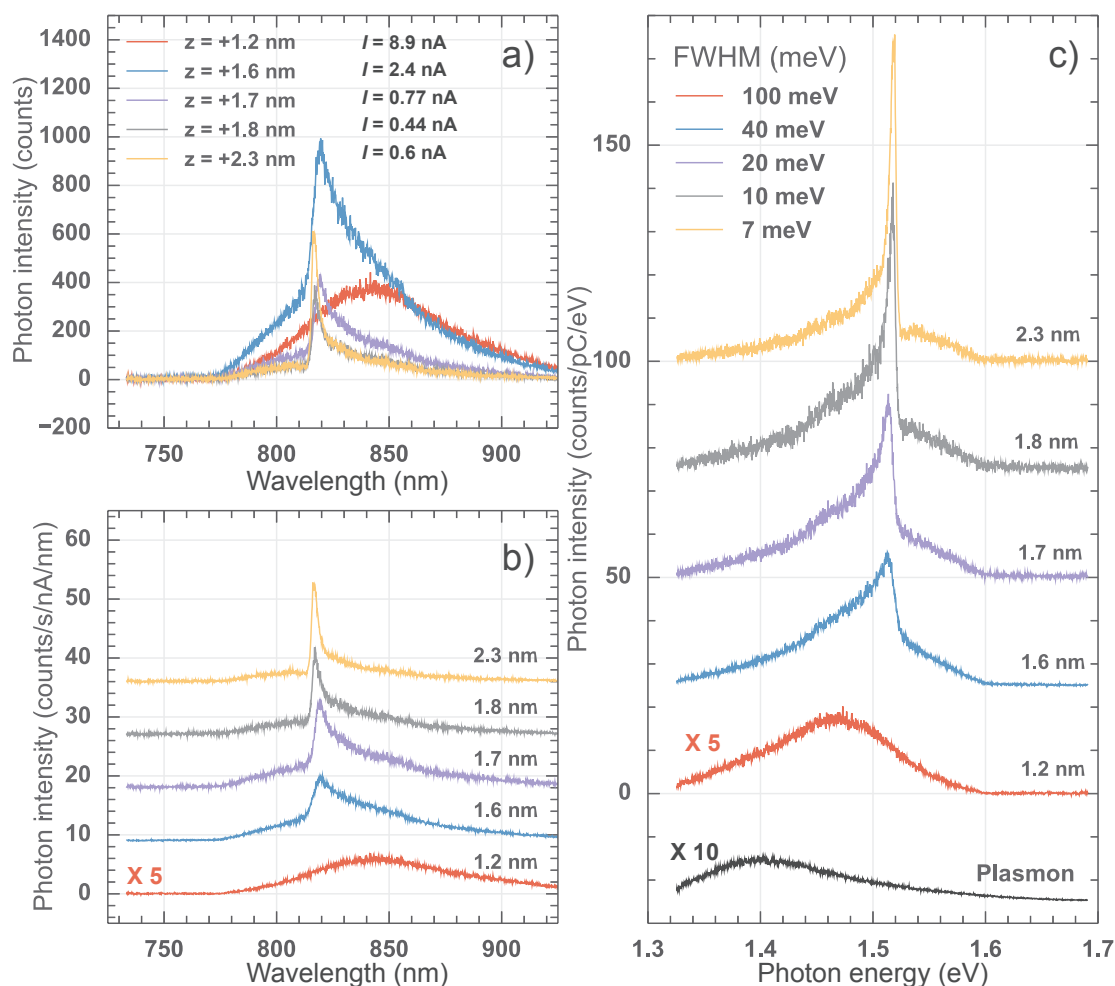


Figure 3.8 – Impact of the tip-sample separation on the width of the main peak in the light emission spectra. Light emission spectra acquired on a molecular junction composed of oligothiophene and fused-DPP for different tip sample separations ($V = 1.6$ V, $t = 60$ s). (a) Raw spectra of light intensity as a function of the wavelength. (b) Same spectra normalized by the acquisition time and by the current. (c) Normalized spectra as a function of the photon energy in eV. The black curve is a measure of the plasmon obtained with the same tip on the bare surface. The “plasmon curve” was acquired with $V = -3$ V, $I = 90$ nA, $t = 60$ s. Spectra in (b) and in (c) have been shifted vertically for sake of clarity.

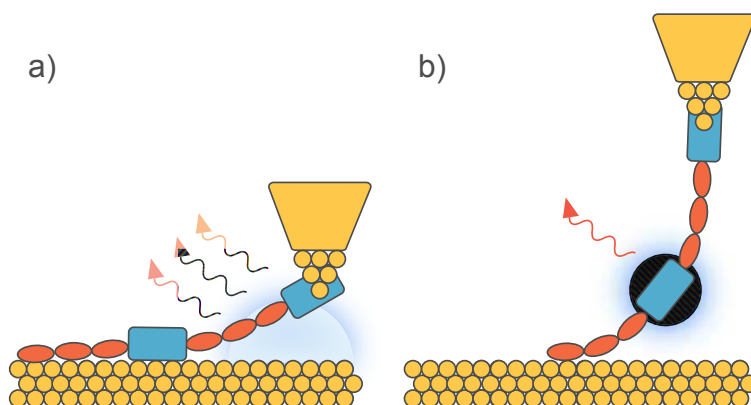


Figure 3.9 – Sketch of the lifting of the co-polymer. Sketch of the light emission from the lifted wire with (a) the emitter on the surface and (b) with the emitter suspended in the junction.

- The fused-DPP used to anchor the wire is in strong contact with the tip, and we expect its luminescence to be quenched (*c.f.* chapter 2.2). The spectrum at 1.2 nm (red curve in figure 3.8), is obtained in a situation resembling the one sketched in figure 3.9(a), where only the anchoring fused-DPP is lifted from the surface. This shows that the narrow line is not generated by the fused-porphyrin at the terminus of the wire.

The first spectrum presenting a clear peak is at a tip-sample separation of 1.6 nm; starting from there, the peak gets narrower the more the polymer is lifted. This tip-sample separation is compatible with the second porphyrin detached from the surface, which indicates that the source of the narrow-line emission is the fused-DPP suspended in the junction (figure 3.9(b)).

Width of the emission line. The series of spectra in figure 3.8 thus illustrates the progressive decoupling of the emitter from the surface, with the linewidth getting narrower as the interaction with the substrate reduces. The narrowing of the peak reflects an increase of the lifetime of the emitter. The width of the emission line, ΔE , and the lifetime of the excited state, Δt , are linked by a Heisenberg relation:

$$\Delta E \Delta t \geq \hbar/2. \quad (3.1)$$

For small z values, the coupling with the metallic substrate provides an efficient de-excitation channel for the emitter, reducing its excited state lifetime. By decreasing the interaction with the surface we can tune the impact of this channel until the emitter is fully detached and no longer affected by the presence of the electrodes. When this configuration is reached, the peak width is limited by other factors, for instance the interaction with phonons and with the plasmons. We can then use equation 3.1 to estimate a *lower bound* for the lifetime of the excited state of the molecule when it is

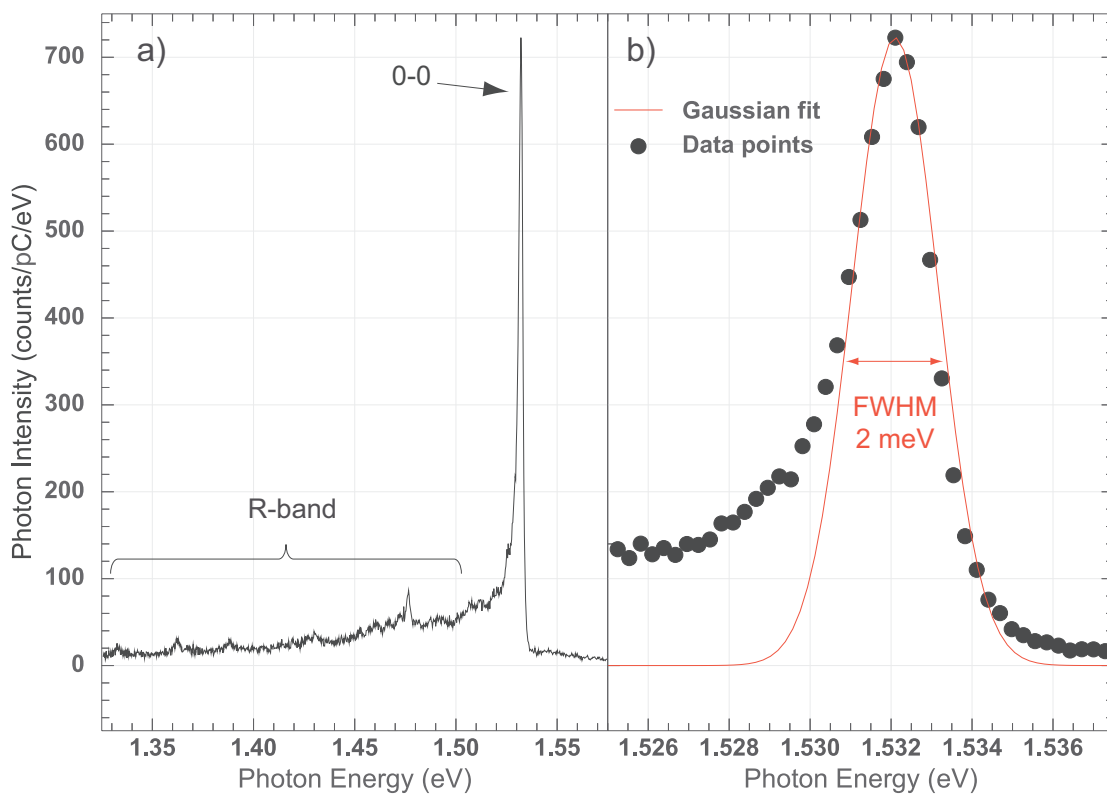


Figure 3.10 – Details of the light emission from fused-DPP. (a) Highly resolved light spectrum of a molecular junction ($V = 1.6$ V, $I = 0.66$ nA, $z = 1.8$ nm, $t = 60$ s, high resolution grating). The main peak is labelled 0-0. On the low energy side of the spectrum, a series of low intensity peaks is labelled R-band. (b) Enlarged view of the 0-0 line (black filled circles) and Gaussian fit to the peak (red line).

decoupled. The extreme case, presented in figure 3.10, shows a linewidth of 2 meV (as deduced from the FWHM of a Gaussian fit). This corresponds to a lifetime ≥ 0.163 ps. We have to keep in mind that due to all the environmental factors the actual fluorescence lifetime can be orders of magnitude longer. These aspects will be further discussed in section 3.3.9.

We point out that this is the narrowest linewidth ever reported in a STM-induced light emission experiment. This shows that a single-emitter can be very efficiently decoupled by organic linkers, and validates our experimental concept. Moreover, this approach provides a way to control the degree of coupling of the emitter with the electrodes, something that is impossible for a molecule deposited on a spacer [7, 14, 8, 15].

Interestingly, the thiophene chains do not seem to affect the energy of the emission, which fits with the optical gap of the isolated fused-DPP calculated with a TD-DFT approach. This is confirmed by performing similar calculations on the fused-DPP connected to two ter-thiophene units: the value of the $S1 \rightarrow S0$ transition is barely affected, decreasing to 1.48 eV. This value is still in good agreement with the measured emission. The picture that emerges is that the narrow line emission of the light is generated by the fused-DPP that acts as an optically active unit. Oligothiophene chains enable charge transport through the co-polymer and simultaneously decouple the central unit. A more detailed discussion about the role of the oligothiophene and its interaction with fused-DPP is reported in appendix C.

Some other aspects are worth noticing in the spectra of figure 3.8 and 3.10:

- We can observe that even in the presence of the sharp peak, a broad background is detected. This background is associated to a plasmonic emission that occurs simultaneously to the emission of the molecule.
- We already remarked that the main emission line is asymmetric, with a sharp edge on the high energy end and a shallow tail on the low energy side. This shape is reminiscent of a Fano line [132]. Its origin will be discussed in section 3.3.8.
- On the low energy side of the spectra we also observe low intensity features named *R-band* in figure 3.10. They will be discussed in detail in section 3.3.5, but we anticipate their vibronic origin. In contrast, the main emission line is a zero-phonon line, not involving any vibrationally excited state. For this reason we sometimes refer to it as the 0-0 line.

A final comment should be made on the emission yield of the system, which corresponds to the number of photons generated per electron flowing in the junction. The highest measured yield, was of $(1.0 \pm 0.3)10E - 5$ photons/electron. In this case, the photons were integrated over all the spectral range which encompasses both molecular

and plasmonic emission. On the same data, one can limit the photon integration range to the 0-0 line⁵. In this case, a yield of $(0.3 \pm 0.01)10E - 5$ photon per electron is found, which represents one third of the overall emission. In other words, the sharp 0-0 line dominates the signal and, considering its width and intensity, the emission can be considered as *almost monochromatic* [133, p. 20].

We stress that these cases represent the highest measured yield. However, the yield is observed to vary by orders of magnitude from one co-polymer to the other. This variability is probably related to the specific configuration of the polymer in the junction, which may vary during the lifting and from a specimen to the other. Also, the connection to the tip may vary from a molecule to the other, resulting in effects that are not controllable.

Conclusions. In this section we have shown how the linewidth of the emission narrows down when we lift the co-polymer from the surface. This phenomenon is readily interpreted in terms of decoupling of the chromophore from the metallic substrate. This, in combination with the energy of the peak, allowed us to assign the source of the narrow line emission: the suspended fused-DPP. The agreement with the optical gap of this molecule also confirms the cyclodehydrogenation of the porphyrin during the preparation of the sample (*c.f.* section 3.1.2). The presence of the fused phenyl rings thus changes the optical properties of the molecule in a measurable way. This opens a way to manipulate the optical gap of the emitter. In section 3.3.4 we will explore this aspect to prove the high flexibility of this system and the possibility to select the energy of the emission.

3.3.4 Control of the emission energy by chemical engineering

We saw in section 3.3.3 that the energy of the emission line corresponds to the optical gap of the fused chromophore. Here, we will show that the energy of the emission can be controlled by changing the detailed chemical structure of the porphyrin, while preserving the other characteristics of the emission.

We used two porphyrin derivatives that differ from DPPH₂ by their side groups (figure 3.11). The idea behind this experiment is that different side groups will produce different fused-porphyrins, with different conjugation lengths. The new molecular wires were obtained by evaporating the molecules together with DBrTT and following the same co-polymerization and cyclo-dehydrogenation procedures used in section 3.1. One wire was prepared using 5-(phenyl)-10,20-(dibromo)-porphyrin (Br₂-MPPH₂, shown on the left in the scheme of figure 3.11(a), and in the topography in (b)). The reaction

⁵The integration is performed considering photons in an energy window of 20 meV around the energy of the main peak.

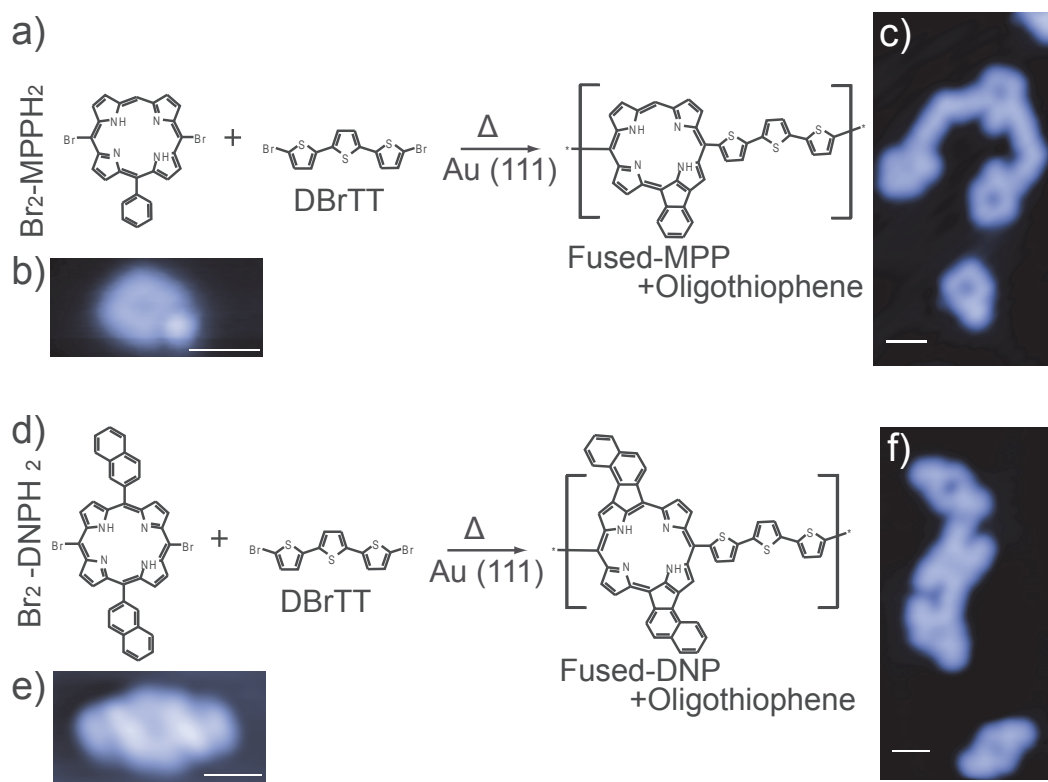


Figure 3.11 – Synthesis of co-polymers containing fused-MPP or fused-DNP. On-surface synthesis of the co-polymers. (a) Sketch of the chemical reaction that produces fused-MPP and oligothiophene polymers. (b) STM topography of $\text{Br}_2\text{-MPPH}_2$ on Au(111). (c) STM topography of a co-polymer of fused-MPP and oligothiophene. (d) Sketch of the chemical reaction to produce fused-DNP and oligothiophene polymers. (e) STM topography of $\text{Br}_2\text{-DNPH}_2$ on Au(111). (f) STM topography of a co-polymer of fused-DNP and oligothiophene. In (b),(c),(e) and (f) the white bar represents 1 nm. The topographies were obtained at $V = -0.1$ V and $I = 0.1$ nA.

is schematized in figure 3.11(a) and the topography of the final product is presented in (c). We observe that $\text{Br}_2\text{-MPPH}_2$ undergoes a cyclo-dehydrogenation and forms a fused-MPP. This molecule was designed so that its fused version has a shorter conjugation length than fused-DPP. The product of the reaction is a co-polymer alternating fused-MPP and oligothiophene units. In the topography in (c) we also observe an isolated fused-MPP.

The other emitter was obtained using 5,15-(dinaphthalene)-10,20-(dibromo)-porphyrin ($\text{Br}_2\text{-DNPH}_2$, on the left in the scheme of figure 3.11(d), and in the topography in (e)). The use of naphthalene side units allows, through cyclo-dehydrogenation, to obtain fused-DNP, a molecule with a longer conjugation length. The reaction is presented in figure 3.11(d). In (e) the topography of the product is presented, showing a co-polymer of fused-DNP and oligothiophene. In the same figure an isolated fused-DNP is observed. We remark that, *a priori*, $\text{Br}_2\text{-DNPH}_2$ may have up to six possible fused isomers. Experimentally only two were observed, with a strong prevalence (about 95% of the molecules on the surface) for the one presented in figure 3.11(d). More details on this aspects are presented in appendix B.

The next step consists in probing the electroluminescence properties of these new molecular emitters suspended in the STM junction.

In figure 3.12(a), a typical electroluminescence spectrum for each co-polymer is presented. In all cases, the spectra were obtained when the tip-sample separation was large enough to fully decouple the emitter from the sample surface.

All spectra are characterized by an intense and remarkably narrow ($\text{FWHM} \leq 10$ meV) emission line (0-0 line in figure 3.12(a)) and a series of low intensity peaks at higher and/or lower energies (R-band, B-band). The overall shape of the spectrum is similar in the three cases but the energy of the main peak is shifted depending on the chromophore. The experimental distribution of the energy of the 0-0 line, obtained from successive measurements on different wires, is represented as a green Gaussian in each plot. Once again, we assign this spread in the experimental distribution to variations in the configuration of the polymers in the junction and to the connection to the tip, that may vary from one specimen to the other.

In figure 3.12(b) the time-dependent density functional theory (TD-DFT) calculations of the optical gap ($S_1 \rightarrow S_0$ transition) of the isolated fused-porphyrins are presented. As expected, the fusion of the different peripheral units to the core results in different optical gaps for the molecules.

In table 3.1 we summarize the experimental and calculated optical gaps for both the isolated fused-porphyrins and for the porphyrins in presence of two ter-thiophene units (btT) on the side.

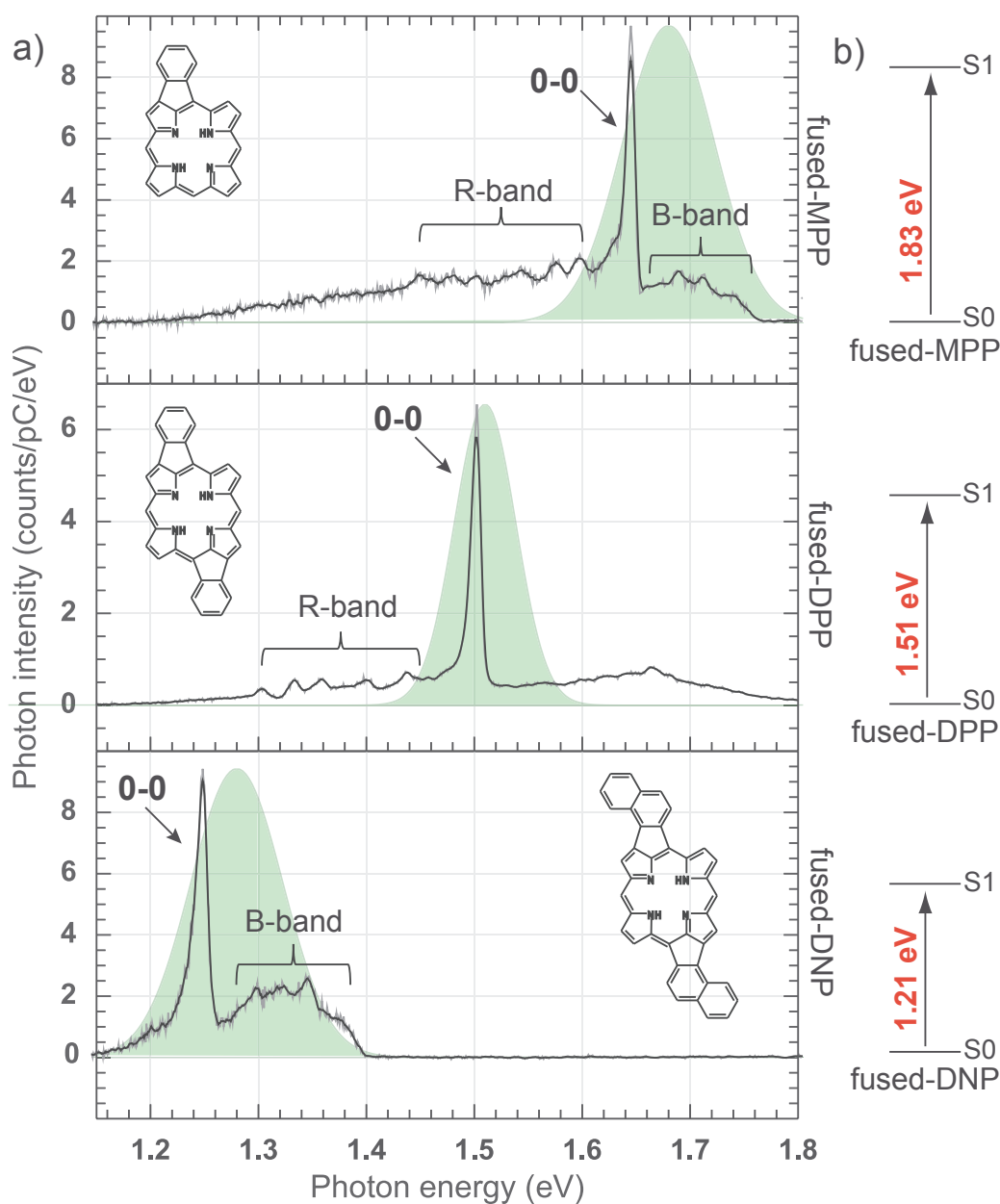


Figure 3.12 – Energy dependency of the main peak with the chromophore.

(a) Electroluminescence spectra of fused-MPP, fused-DPP and fused DNP. Low intensity vibrational bands on the low energy side (R-band) and/or on the high energy side (B-band) are observed. The green areas represent the experimental dispersion of the energy of the main emission line for the three systems. The raw (smoothed) data appear in gray (black). (b) Optical gaps of different porphyrins calculated using time-dependent density functional theory (TD-DFT).

Table 3.1 – TD-TFT of optical gap - Experimental values

Molecule	TD-DFT (eV) emitter	TD-DFT (eV) emitter+btT	Experimental
Fused-MPP	1.83	1.75	1.68 ± 0.06
Fused-DPP	1.51	1.48	1.51 ± 0.04
Fused-DNP	1.21	1.21	1.28 ± 0.06

We observe a good agreement between the calculated and the experimental values for the three molecules⁶. The presence of the oligothiophene units has a limited effect on the calculated optical gap of the co-polymers, which confirms the previously established picture.

The absence of a measurable R-band in fused-DNP is probably due to the low detection efficiency of the optical setup at low energy (see chapter 2.1.3).

Overall, the good agreement between the experimental and the calculated values of the optical gaps confirms that the emission can be assigned to each of the fused-porphyrins. The energy of the 0-0 line varies with the nature of the selected porphyrin; the rule of thumb is, the bigger the conjugation length the lower the emission energy. This not only confirms the picture we drew in section 3.3.3, but also demonstrates that a proper design of the chromophore provides control over the emission energy. We therefore obtained a molecular-scale light emitting device that presents an almost monochromatic emission and whose color can be controlled by chemical engineering. This is unreported in STM experiments and is of potential interest for hybrid electronic-photonic devices of molecular scale.

3.3.5 Analysis of the vibronic peaks of the R-band

We now turn to the description of the vibrational features of the R-band that we find in the electroluminescence spectra of fused-DPP and fused-MPP. These contributions appear as low intensity peaks on the low energy side of the main peak.

In figure 3.13 a set of five electroluminescence spectra obtained on different specimens of fused-DPP are presented. The spectra are presented as a function of the shift from the 0-0 line chosen as origin of the energy scale. The first observation is that most of the vibrational peaks are identified in all spectra. These peaks are highlighted with vertical dotted lines. Their shift from the 0-0 peak is reported in figure 3.13(f), and plotted in 3.13(g) as a function of the peak number. While all the vibrational peaks of the R-band have comparable magnitudes, their relative intensity vary slightly from

⁶The experimental values and incertitudes are defined as the mean and the standard deviation of the values obtained on different specimen.

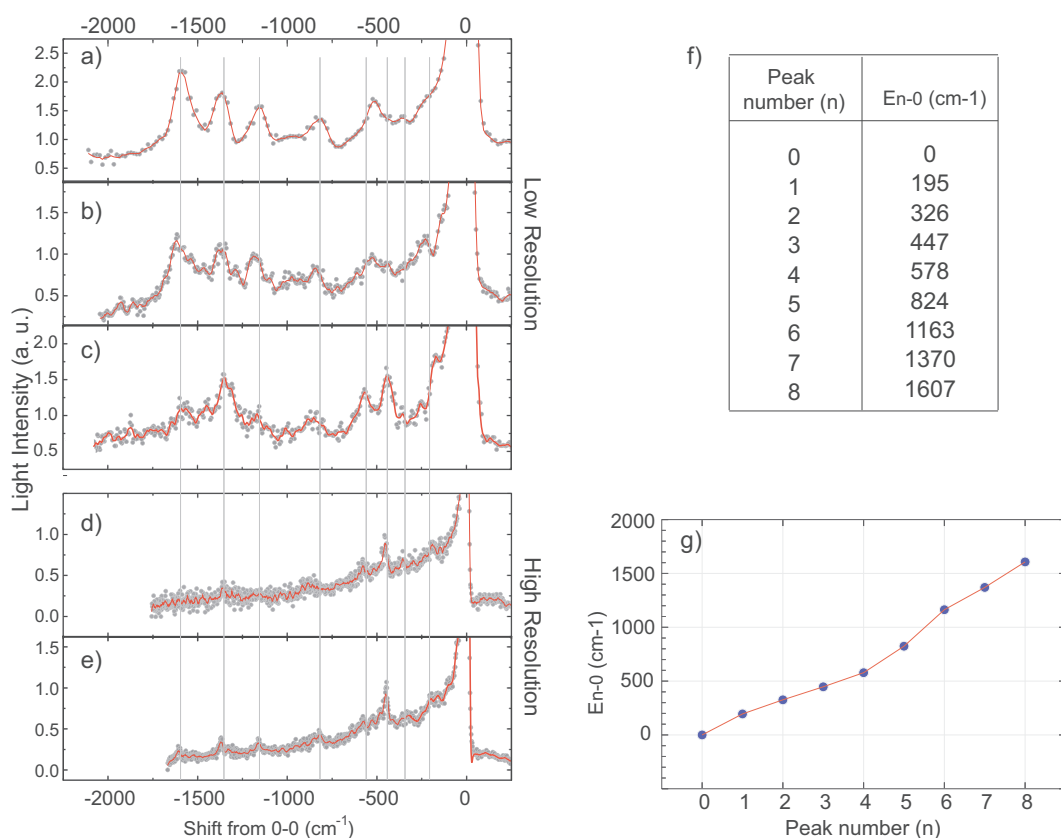


Figure 3.13 – R-band of fused-DPP. Electroluminescence spectra of different specimen of fused-DPP as a function of the shift (in cm⁻¹) from the 0-0 line . (a),(b) and (c) are measured with the low resolution grating of the spectrometer. (d) and (e) are obtained with the high resolution grating. Vertical dotted lines are a guide for the eye to localize the peaks that are more frequently detected. (f) Table with the energy distribution (in cm⁻¹) of the vibrational peaks as a function of the peak number. The number of the peaks are assigned starting from the 0-0 line ($n = 0$). (g) Plot of the energy distribution of the peaks presented in (f).

one spectrum to the other. In some cases, the intensity is so low that the presence of the peak cannot be ascertained (in (d) for example). Also, the peaks at -500 cm^{-1} in the spectra (a) and (b) sometimes appear split as we observe in (c) and (e).

Two points may be directly noticed: (1) No peak is detected with a shift larger than 1610 cm^{-1} . (2) The energy distribution of the peak is not linear.

Nature of the peaks. Vibrational features were previously reported in some STM-induced luminescence from single molecules [7, 14, 8, 15]. In those cases the low intensity peaks were associated to the harmonic progression of a single vibrational mode. This can be understood from the sketch of figure 3.14(a), where the transitions from the ground vibrational level of an excited electronic state to different harmonics of a vibrational mode of the ground state are represented. The probability of each transition is proportional to the square of the integral of the overlap between the wave functions of the two states involved in the transition. This leads to a highly characteristic spectrum, as the one presented in figure 3.14(b). While the relative intensity of the peaks depends on the so-called Franck and Condon factors, their dispersion depends on the shape of the potential of the vibrational mode. In the harmonic approximation the dispersion is then linear.

In contrast to this picture, our spectra reveal a series of extremely weak vibronic peaks and an intense 0-0 line. This behavior suggests an alignment of the two electronic states in the plot of figure 3.14(a), and indicates that the geometry of the molecule is essentially the same in the ground and in the excited state. In this case, each line corresponds to a given vibrational mode of the emitter, similarly to what is observed in fluorescence line-narrowing spectroscopy, a technique used to obtain high-resolution optical spectra of molecules or atomic ions embedded in amorphous solids [134, 135, 136]. The nature of the red-shifted peaks is also reminiscent of the Stokes peaks observed in Raman spectroscopy. The mechanism is schematically represented in figure 3.14(c) where several transitions from an excited electronic level to different vibrational states of the ground electronic level are presented. Here, only the transition to the first harmonic of each mode is intense enough to be detected. This results in an irregular peak distribution, like the one presented in figure 3.14(d), and as we observe experimentally. We therefore conclude that we observe the first harmonic of different vibrational modes.

Comparison with calculated Raman-active modes. The presence of peaks belonging to different modes provide in principle a fingerprint of the molecular emitter. Since we know that the 0-0 line corresponds to the $S1 \rightarrow S0$ transition of the fused-DPP, the vibronic features should belong to modes that are optically active in a transition of strong π to π^* character, namely in-plane and symmetric (Raman-active) modes. It is possible to calculate⁷ these modes for both the fused-DPP and the non-

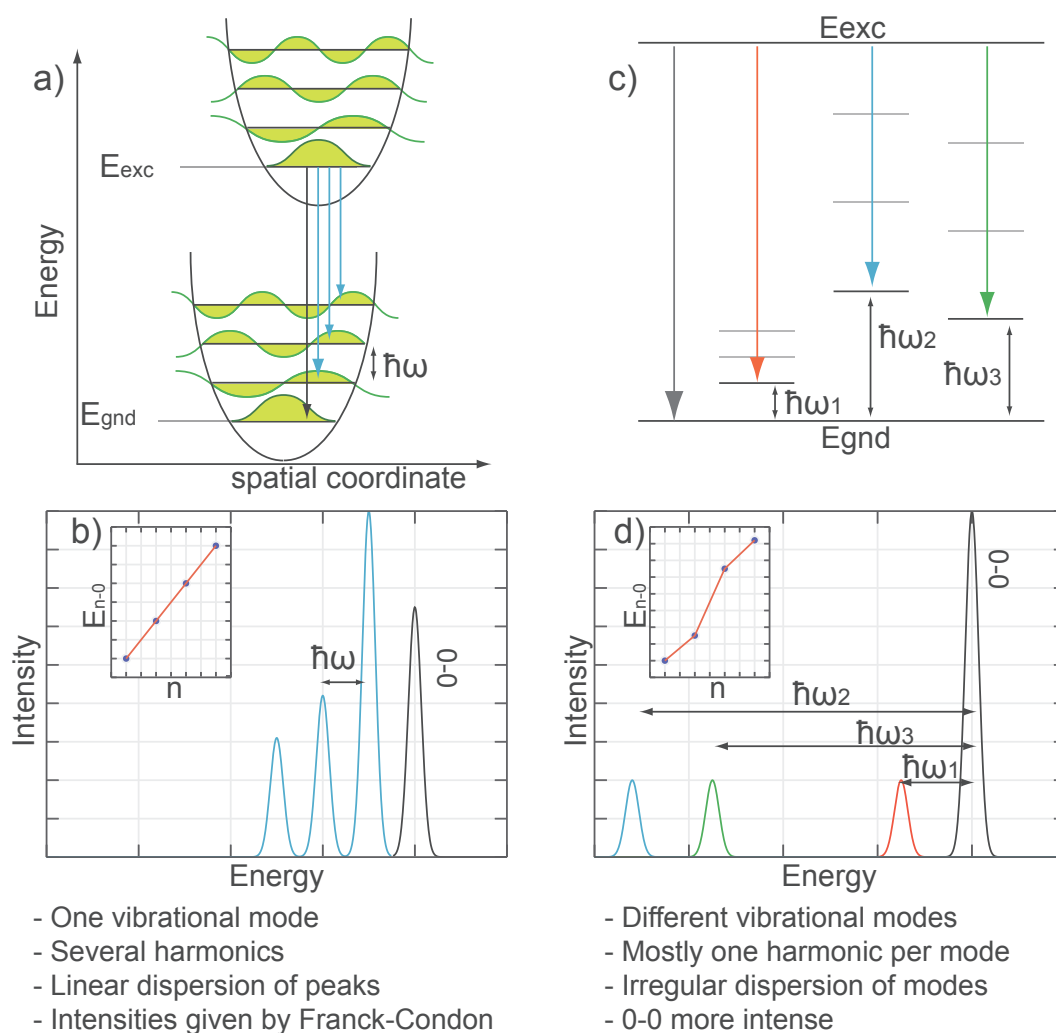


Figure 3.14 – Models of vibronic transitions. Harmonics of a single mode and spectroscopy of different modes.

a) Energy diagram of an electronic transition coupled with a vibrational transition. The arrows represent the emission from the ground vibrational state of the excited level to different harmonics of a vibrational mode of the ground state. The black arrow represents the transition without changes in the vibrational level (0-0). The width of the arrows mimics the different probabilities for the transitions resulting in the Franck and Condon factors. b) Typical peak dispersion resulting from the energy diagram of (a). In inset the energy distribution of the peaks with respect to the 0-0. c) Energy diagram of an electronic transition coupled with different vibrational modes. Three vibrational modes (energy = $\hbar\omega_1$, $\hbar\omega_2$ and $\hbar\omega_3$) are shown. For each mode the transition to the fundamental harmonic is highlighted with a colored arrow. The overall 0-0 transition results from the 0-0 transition of each mode and is thus the most probable (black arrow). d) Possible peak dispersion resulting from the energy diagram in (c). In inset the energy distribution of the peaks with respect to the 0-0.

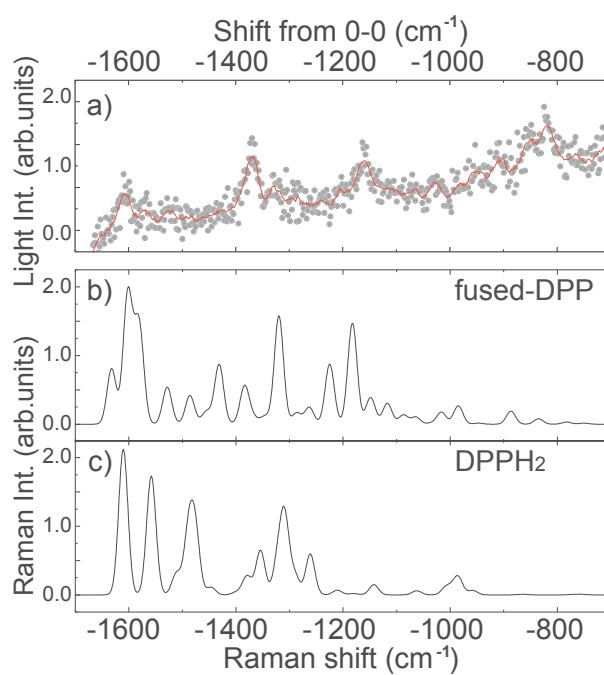


Figure 3.15 – Comparison of experimental spectrum of the R-band of fused-DPP with calculated optically active Raman modes of fused-DPP and DPPH₂. (a) Electroluminescence intensity of a co-polymer made of oligothiophene and fused-DPP as a function of the energy shift from the 0-0 line. Calculated optically active Raman modes of (b) fused-DPP and (c) DPPH₂.

fused DPPH₂ and compare them with the experimental data. In figure 3.15 such a comparison is presented for energy shifts between⁸ -700 cm⁻¹ and -1600 cm⁻¹, which corresponds to the so-called *fingerprint region*. Indeed, those highly shifted modes are more localized on the macro-cycle of the porphyrin. For this reason the influence of external factors (for instance the presence of the oligothiophene chains) is less significant in this region. The comparison of the experimental data with the calculated spectra of the fused-DPP (3.15(b)) and of DPPH₂ (3.15(c)) reveals a better agreement with the fused molecule, especially for highly shifted peaks. This further confirms that we are probing the fused-porphyrin isomer. It also highlights the importance of the vibronic spectrum, that provides a chemical signature of the molecule.

The peaks above 1000 cm⁻¹ are especially well reproduced and correspond to in-plane C-C stretching modes. Eventually, we note that both in the theoretical and in the experimental spectra, there is no vibrational peak shifted more than 1700 cm⁻¹. This value corresponds to the higher limit of the C-C stretching modes. This definitively confirms the nature of the low intensity feature in the spectra. We emphasize that it is the first time that such an interpretation is proposed for STM-induced fluorescence of single molecules.

Comparison of fused-porphyrins. In figure 3.16 the R-bands of the different fused porphyrins are represented as a shift from the 0-0 transition (in cm⁻¹). In this plot the 0-0 transition of the different molecules are aligned, allowing for an easier comparison of the lower intensity features. Although the R-band in the spectrum of fused-DNP is almost non-measurable because of the low sensitivity of the CCD in the infra-red region (*c.f.* chapter 2.1.3), one extremely weak peak is detected at ≈ 400 cm⁻¹. More importantly, the spectra of figure 3.16 reveal that the vibrational peaks belonging to the R-band are roughly aligned for the three molecules.

The strong similarity between these spectra is not surprising. The molecules have almost identical structures and, therefore, most of the vibrations that are involved in the optical transitions for one moiety, are also contributing to the spectra of the others.

Conclusions. The vibrational peaks of the R-band provide a spectroscopic fingerprint of the molecular species by mapping the vibrational modes of the S₀ level. Together with the energy of the 0-0 transition, they allowed to unambiguously assign the nature of the emitter. Such vibrational fingerprints are generally obtained with Raman spectroscopy. While Raman spectroscopy is usually performed on crystals containing a huge number of molecules, recent experiments show that this technique can reach

⁷The computations have been performed by Alex Boeglin using the PBE exchange and correlation functionals with the 6-31G (d,p) basis set.

⁸At low shift the modes are not easily reproduced by theory which may be due to a strong coupling to the environment of these modes.

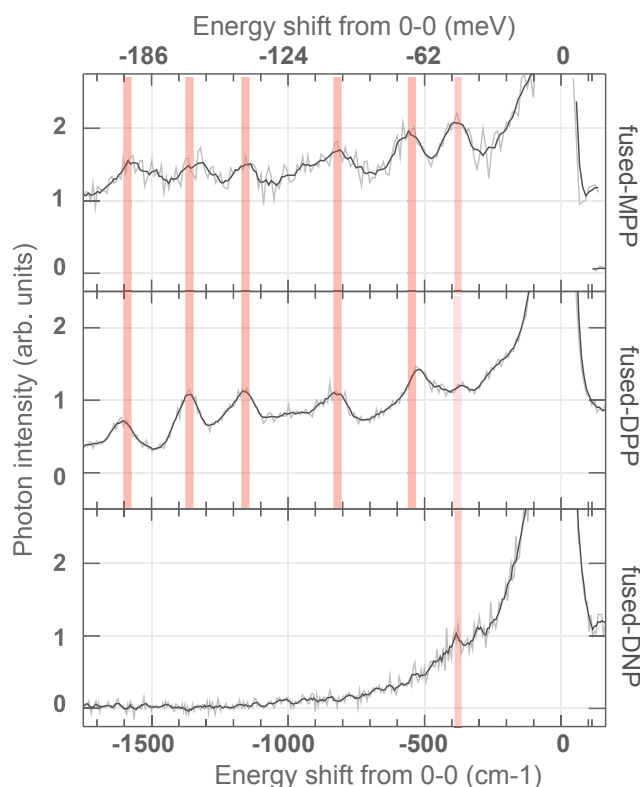


Figure 3.16 – Comparison of the R-band of fused-MPP, fused-DPP and fused-DNP. Light emission spectra of fused-MPP, fused-DPP and fused-DNP plotted as a function of the energy shift from the 0-0 lines. The red lines are meant to guide the eyes on the vibrational peaks of the R-band.

single-molecule sensitivity by taking advantage of plasmon resonances localized at the apex of a metallic tip [88, 137]. Here, we obtain a similar level of spectroscopic and spatial resolution as in tip-enhanced Raman spectroscopy *without* the need of an external laser source.

It would have been interesting to compare our experimental data with experimental Raman spectra acquired on bulk assemblies of fused-porphyrin. Unfortunately fused-porphyrins are not commercially available. We tried to perform Raman measurements on a sample covered by a monolayer of fused-DPP but the emission was dominated by the response of the Au(111) substrate and the Raman signal from the molecules could not be detected.

In section 3.3.4, we also noticed the presence of vibronic features on the blue side of the 0-0 line. The nature of this B-band will be discussed after introducing the detailed luminescence mechanism, that is necessary for a full understanding of its origin.

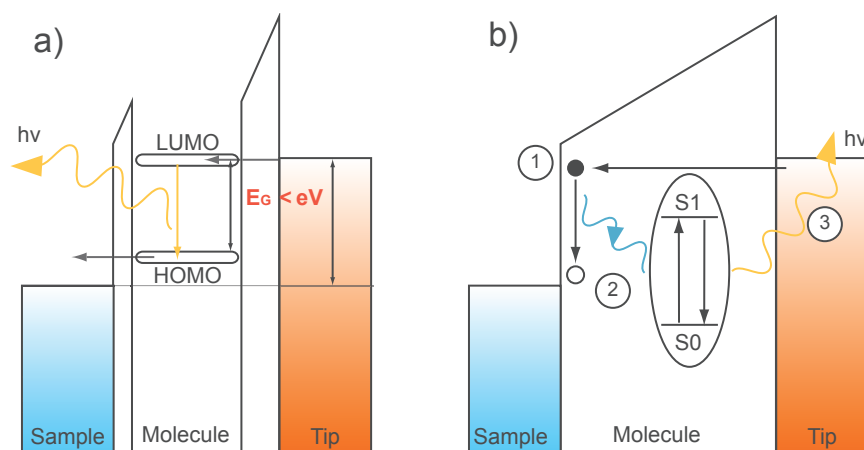


Figure 3.17 – Comparison of light emission mechanisms. (a) Electron injection mechanism. (b) Plasmon mediated mechanism.

3.3.6 Towards a plasmon excitation mechanism: voltage bias dependency of the emission

In this section we study the voltage dependence of the light emission. In particular, we are interested in the study of the onset of the emission, a feature that provides important information regarding the luminescence mechanism.

In previous STM-induced luminescence experiments on molecules, two different excitation mechanisms were proposed. We detailed them in chapter 2.2.5. The first one, presented in figure 3.17(a), involves the simultaneous injection of an electron and a hole in two molecular states. The injection is then followed by a recombination that generates a photon of energy $h\nu = E_G$. In this mechanism, the required bias V must generally be higher than the gap E_G to obtain the molecular luminescence (*c.f.* chapter 2.2.5).

The second mechanism, illustrated in figure 3.17(b), is a plasmon mediated energy transfer from inelastic tunneling electrons to the molecule. It follows three successive steps: (1) an inelastic electron of energy eV loses its energy in the junction and transfers it to the nanocavity plasmon. (2) The NCP transfers its energy to the molecule that promotes an electron from the ground state S_0 to the excited state S_1 . (3) The molecule relaxes to the ground state producing a photon of energy $h\nu = eV$. An important difference with the previous mechanism, is the onset of the emission: as soon as the tunneling electrons have an energy $eV = E_G$ the intramolecular emission becomes possible.

By studying the threshold of the narrow line emission as a function of the bias we can hope to discriminate between the two mechanisms.

In figure 3.18(a) a set of four electroluminescence spectra obtained with a suspended fused-DPP at a fixed tip-sample separation is shown. For this set the voltage bias is progressively increased from 1.54 V (blue spectrum) to 1.6 V (black spectrum). The

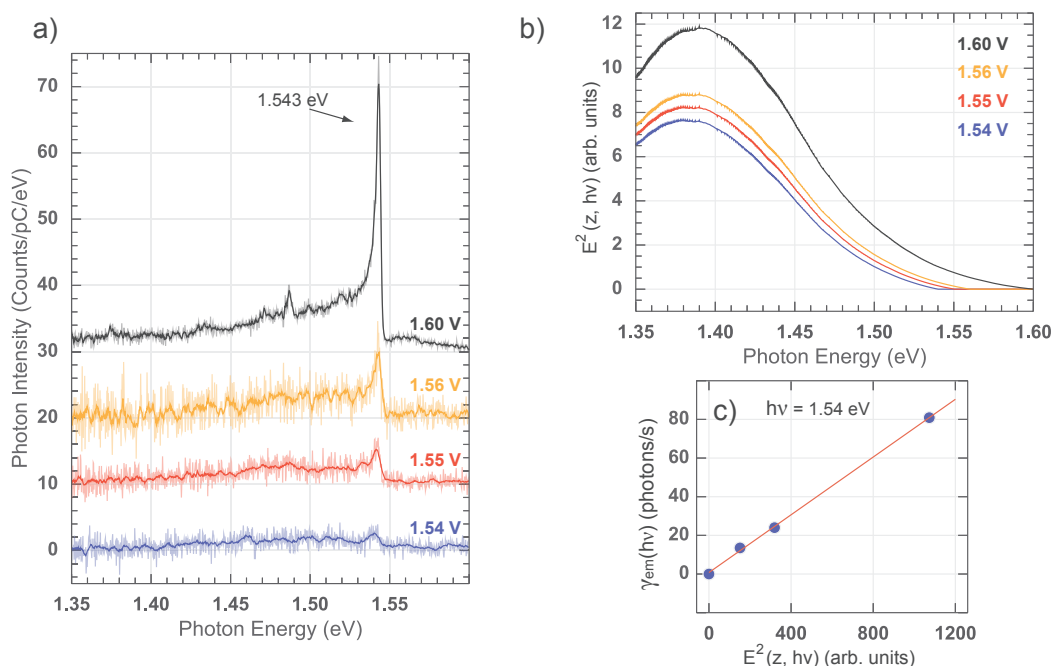


Figure 3.18 – Onset of the emission and dependency with voltage. (a) Electroluminescence spectra obtained at various applied bias on a fused-DPP (measured using a high resolution grating). The molecule is a co-polymer of oligothiophene and fused-DPP lifted at a tip-sample separation of $z = 2.1$ nm. The spectra are meant to evidence the onset of the emission, and are vertically shifted for clarity. (b) Squared local electromagnetic field intensity as a function of the energy as estimated from a pure plasmonic emission measured with the same tip on the bare surface. (c) Intensity of the 0-0 line (counts/s) as a function of the squared electromagnetic field at $h\nu = 1.54$ eV. The red line is a linear regression.

0-0 line appears at $h\nu_{0-0} = 1.543$ eV. This plot reveals that the voltage onset (V) of the main emission peak corresponds to the energy of the 0-0 line. In other words, light is emitted as soon as $eV = h\nu_{0-0}$. We remark that the energy of the main emission line does not shift as we increase the bias, providing a further indication of an intramolecular emission. This is confirmed by measurements on other specimens of the same molecule which do not show any shift of the main emission line for a voltage bias up to 2.2 V. Higher voltages damage the suspended wire and bleach its fluorescence. The observation of an intramolecular emission with a voltage threshold corresponding to the energy of the emission is at odds with a recombination of electrons and holes injected from the tip and the sample [7, 14, 110, 22, 15, 67]. On the other hand, it fits with a plasmon mediated excitation model, which is expected to have such a threshold.

Detail of the excitation term. If we assume a plasmonic mediated excitation of the emitter, it may be useful to determine the intensity of the electromagnetic field in the nano-cavity. Indeed, we can make an analogy with experiments on single molecules excited by a laser, in presence of plasmonic gold nanostructures [120]. In that case, the fluorescence rate follows:

$$\gamma_{em} = \gamma_{ex}Q, \quad (3.2)$$

where γ_{ex} is the excitation rate and Q is the photon emission probability. There, $\gamma_{ex} \propto E^2(z, h\nu)$, where $E(z, h\nu)$ is the electromagnetic field intensity at the position of the molecule z and at the energy of the emission $h\nu$. In their example, the E^2 term depends on the laser intensity and on electromagnetic density of states ($\rho(h\nu)$), which directly depends on the presence of plasmonic modes.

In our system the excitation source is the tunneling current and the electromagnetic field is determined using

$$E^2(z, h\nu, V) \propto I \rho(h\nu)(eV - h\nu), \quad (3.3)$$

where I is the measured tunneling current, $\rho(h\nu)$ the electromagnetic density of states of the pristine junction, and where $(eV - h\nu)$ (with $h\nu \leq eV$) takes into account the number of accessible transitions (eq.3.3 assumes flat electronic densities of states in the tip and sample). In a first step, $\rho(h\nu)$ is determined from the experimental spectrum of the pristine junction recorded at $V = -3$ V, which is proportional to $E^2(z, h\nu, -3)$, using eq: 3.3.

In a second step, knowing $\rho(h\nu)$, the electromagnetic field intensity as a function of $h\nu$ is recalculated by eq.3.3 for different voltages. The result is plotted in figure 3.18(b).

Figure 3.18(c) shows the photon intensity of the 0-0 line (obtained by integration over a window of 20 meV around $h\nu = 1.54$ eV) for the different bias voltages (figure 3.18(a)), plotted as a function of the corresponding square electromagnetic field deduced by integrating over the same window the spectra in figure 3.18(b). Note that the spectrum at $h\nu = 1.54$ eV (blue curve) was not used because of the noise level; the (0,0) point

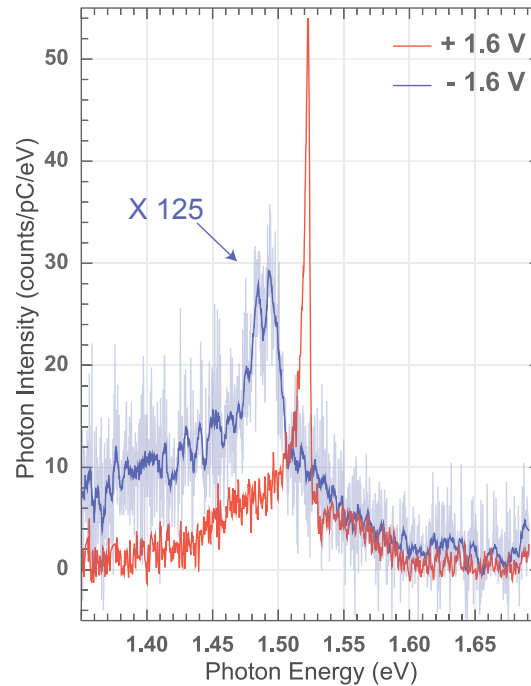


Figure 3.19 – Polarity dependence of the light emission. Electroluminescence spectra of the fused-DPP. For the red curve $V = +1.6$ V, $I = 0.31$ nA, $t = 60$ s, $z = 2.6$ nm. For the blue curve $V = -1.6$ V, $I = 18.2$ nA, $t = 60$ s, $z = 2.6$ nm.

has been added as the reference. Note that we assume here that the presence of the molecular wire does not affect significantly the electromagnetic field.

This figure shows that the emission rate γ_{em} is proportional to $E(z, h\nu)^2$. Actually, the emission probability Q is affected by the plasmons: the density of the plasmonic field may either strongly enhance Q , or quench the emission probability (see discussion in section 3.3.7). Here however, since we work at constant z , the plasmonic cavity remains the same and Q is therefore unchanged for the series of spectra presented in figure 3.18(a) Hence, we conclude that $\gamma_{ex} \propto E(h\nu)^2$, validating the plasmon mediated model.

Polarity dependence of the light emission

All spectra that we presented until now were acquired with a positive sample voltage. The main reason for this is the larger current flowing through the wire for the opposite polarity (see caption of figure 3.19) most of the time, which often causes damages to the polymer or leads to a release of the wire from the tip.

In figure 3.19 two light emission spectra obtained on the same specimen of oligoth-

iophene and fused-DPP at opposite polarities are presented. The two spectra were obtained one after the other, with the co-polymer lifted at the same tip-sample separation ($z = 2.6$ nm). We observe that the spectrum acquired at negative bias is 125 times less intense than the spectrum at positive bias, which indicates a less efficient emission process. Moreover, the 0-0 line is shifted to slightly lower energy for the negative bias. This may be a signature of a Stark shift induced by the electric field. Also, we observe that the peak is broadened. This is likely due to electron-phonon interactions occurring at large currents. The spectra of figure 3.19 show a bipolar emission, which is extremely unlikely for electron-hole injection induced light emission [22, 67], while it is expected for a plasmon mediated excitation (*c.f.* chapter 2.2.5). The extremely different photons/electron yield for the two polarities remains to be explained.

In the following sections we will discuss the influence of the local density of electromagnetic modes on the emission probability, Q , of the emitter.

3.3.7 Surface plasmons dependency of the emission intensity

In section 3.3.6 we demonstrated that the intensity of the 0-0 line depends on the intensity of electromagnetic field generated by the plasmons, themselves excited by the tunneling electrons. We associated this to the effect of the NCP on the excitation term γ_{ex} term. In this section we turn to the effect of the plasmonic resonance on the photon emission probability $Q = \gamma_{rad}/\gamma$, where γ_{rad} represents the radiative emission rate and γ is the overall de-excitation rate.

To study the effect of the plasmon on Q we need to get rid of the influence of the plasmon on the excitation term. This is not possible in practice. However, we can study the effect of the plasmon on the relative intensity of the 0-0 line and the peaks belonging to the R-band. As illustrated in figure 3.20(a), the 0-0 and the vibronic peaks correspond to transitions that start from the same level: the ground vibrational level of S1. For this reason their *relative* intensities do not depend on the excitation term γ_{ex} .

In figure 3.20(b) and (c) two optical spectra of fused-DPP and the corresponding NCP spectra are presented. The two plasmons show different spectral shapes: the one in (b) is centered at high energy and presents a small difference in intensity at the energy corresponding to the R-band and at the 0-0 line. In contrast, the plasmon in (c) is centered on the R-band, where the intensity is roughly three times higher than on the 0-0 line. We observe that in (b), the R-band appears less intense than the 0-0 line by a factor ≈ 10 . In contrast, in (c) the vibrational features are far less intense when compared to the main emission peak (by a factor ≈ 50).

This qualitative example illustrates that the photon emission probability Q is reduced in presence of a stronger plasmonic resonance.

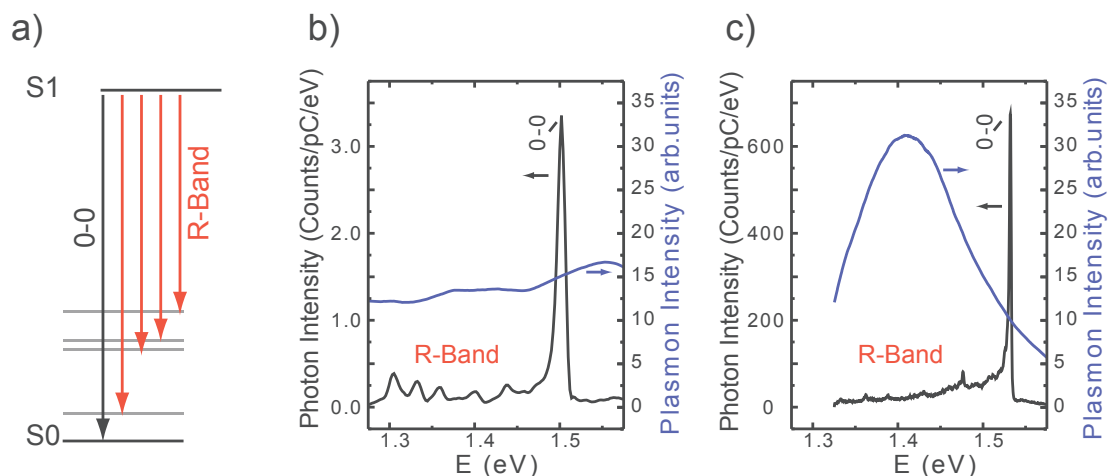


Figure 3.20 – Impact of the plasmon on the R-band. (a) Schematic representation of the transitions generating the R-band. (b)(c) Spectra of different copolymer junctions with their respective plasmon spectra (the blue line) recorded with the metal tip in front of the bare Au(111) prior to the formation of the molecular junction.

Discussion. This conclusion may appear surprising at a first glance, plasmonic nanostructures being known to enhance the fluorescence rate of molecules in their environment. Indeed, the first effect of the plasmonic structure is to enhance the excitation rate of the molecule, as we observed and discussed in the previous section.

The role of the plasmons on the photon emission probability Q is less trivial as was discussed in [120], and depends on the value of Q in the absence of plasmonic structure.

If the molecule is intrinsically a bad emitter ($\gamma_{rad}/\gamma \ll 1$), the presence of a plasmonic particle in the environment will increase (by Purcell effect) the rate of radiative transitions over the non-radiative channel and Q will rise. Such a configuration would lead to an enhancement of the optical transitions that experience an intense density of electromagnetic states⁹, which is not what the data in figure 3.20(b) reveals.

Conversely, in the case of an intrinsically good emitter ($\gamma_{rad}/\gamma \approx 1$), the effect of the plasmonic structure is different. In this case, the presence of the plasmon cannot increase the emission probability further. In contrast, this plasmonic entity provides new non-radiative decay paths for the emitter. In this case, the transitions that experience a weak density of electromagnetic field would be favoured. This is exactly what we observe in figure 3.20(b).

It should be noted here, that the influence of other parameters on the relative intensity

⁹Which is proportional to the measured plasmon intensity.

of the vibronic peaks compared to the 0-0 line in figure 3.20(b) cannot be excluded. Among them, the geometry of the tip-molecule contact, that may vary from one experiment to the other, are certainly the most important.

In an ideal situation, out of reach with our setup, we would probe the same emitter and vary the energy of the plasmonic resonance in a controlled way.

3.3.8 Peak shape

Until now we essentially focused our attention on the energy of the 0-0 peak, but we did not describe its shape. In figure 3.21 (and in most other spectra) we see that the shape of the 0-0 line is asymmetric with a sharp edge on the high energy side and a shallow tail on the low energy one.

The spectrum of the plasmon, as measured on the pristine junction (black curve), is also displayed in the figure. The plasmonic curve was scaled so that the low energy tail of the two spectra are aligned. This suggests, as we previously remarked, that there is a plasmonic contribution in the spectrum of the molecule. In the energy range of the 0-0 transition ($1.5 \leq h\nu \leq 1.6$ eV), the spectrum acquired on the fused-DPP shows the asymmetric peak feature, which is directly followed by a small dip. In this range, the plasmon curve is still more intense. The dip is observed in most of the spectra, but with variable intensity and width. It is generally more pronounced when the plasmonic contribution is more intense at the energy of the 0-0 line (see for instance the spectrum for fused-DNP in figure 3.12, where an intense plasmonic background is observed together with the emission from the molecule).

Finally, above 1.6 eV, the molecular emission is limited by the cut-off ($V = 1.6$ V), which is not the case for the plasmonic curve (acquired at $V = 3$ V).

Figure 3.22 shows spectra obtained for different emitters, that reveal three different shapes for the 0-0 transition. In (a) the most common shape is presented. (b) and (c) show less common characteristics. In particular the spectrum in (c) presents an intense plasmonic background and almost no peak. In contrast the dip is more pronounced. (b) represents an intermediate situation between (a) and (c); here the intensity of the peak is of the same order of magnitude as the depth of the dip. While obtained on different molecular species (fused-DPP for (a), fused-MPP for (b) and fused-DNP for (c)) we observed the first two behaviours for the three types of molecules. The situation depicted in (c) was only obtained on fused-DNP.

Below we discuss the possible origin of these lineshapes.

Interaction with low energy phonons. Similar lineshapes were reported, for instance, in photoluminescence experiments of single emitters embedded in carbon nan-

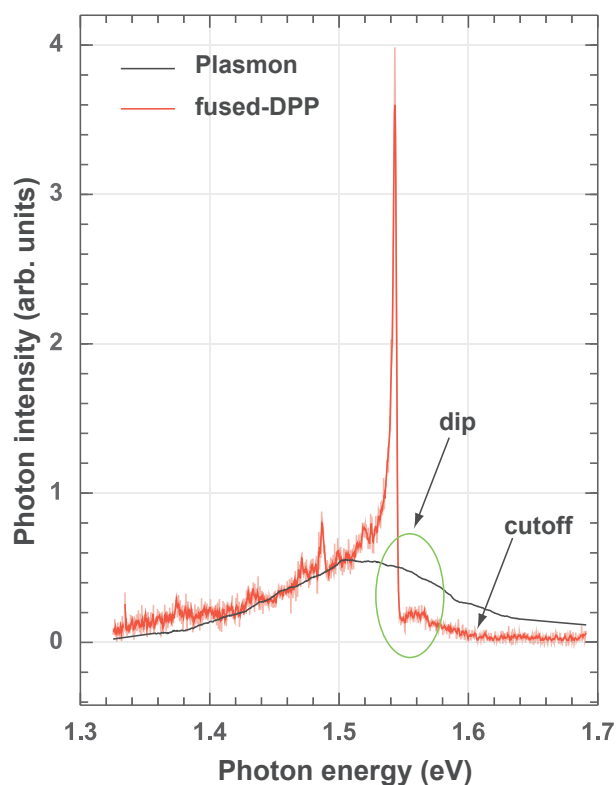


Figure 3.21 – Asymmetric shape of the 0-0 transition of fused-DPP.

Electroluminescence spectrum for co-polymer containing fused-DPP (red curve) and corresponding plasmon as measured on the pristine junction at $V = 3V$. The two spectra have been normalized so that the low energy tail of the two spectra are aligned. The cutoff at 1.6 V for the molecular spectrum is marked. An apparent dip on the high energy side of the 0-0 transition is evidenced by a green oval. Parameters for the STM-LE of the molecule: $V = 1.6 V$, $t = 300 s$, $I = 0.5 nA$, $z = 1.9 nm$.

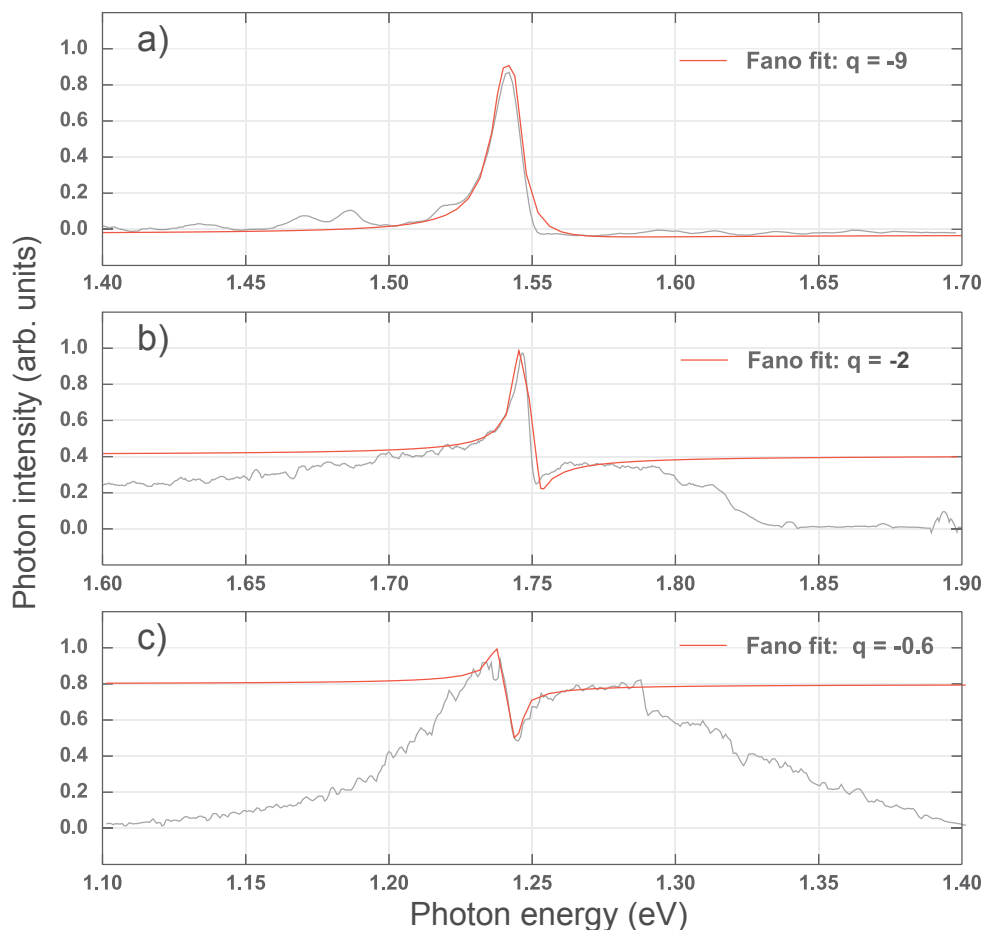


Figure 3.22 – Normalized electroluminescence spectra presenting three different behaviours at the 0-0 resonance and corresponding Fano fits. (a) Most common lineshape. Measured on a fused-DPP. (b) Intermediate situation. Measured on a fused-MPP. (c) Extreme case showing only a dip. Obtained on a fused-DNP.

The spectra were obtained on different specimens of different molecular species (fused-DPP, fused-MPP and fused-DNP respectively for (a),(b) and (c)). The spectra were normalized to highlight the aspects related to the peak shape. The q values for the Fano fits (red lines) are reported.

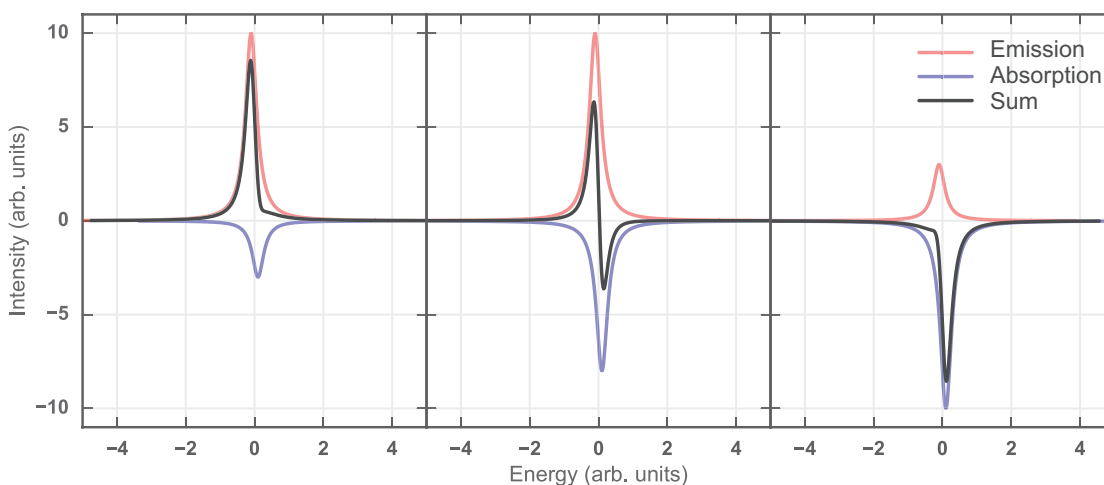


Figure 3.23 – Simulated spectra of Lorentzian emission (red lines) and absorption (blue lines). The respective intensity varies and their sum (black lines) produces an asymmetric lineshape dominated either by one process or the other.

otubes [138]. In this case, an asymmetric peak is observed with a sharp edge at high energy and a shallow tail at low energy. This shape is due to the coupling of a localized exciton with phonon modes of the 1D nanotube. In analogy, we could imagine that the fused-DPP emitter couples with low energy phonon modes of the oligothiophene chain.

While this explanation would reasonably explain the asymmetric shape of the peak, it is not clear how it would explain the presence of a dip on the high energy side of the emission. In particular, extreme situations like the one in figure 3.22(c) would be impossible to explain on the basis of this mechanism only.

Emission and absorption. A possible explanation of the asymmetric lineshape that would explain the presence of the dip, is a co-existence of a narrow-line emission and of a narrow line absorption. The peak would then correspond to the emission of the fused-porphyrin, while the dip would be linked to a reduced plasmon emission at the absorption energy of the molecule. Such a behavior was previously reported in the optical spectra of a molecular aggregate adsorbed on the shaft of an STM tip [114], that we discussed in figure 2.14.

In figure 3.23, spectra illustrating this process are shown. If the absorption (blue line) happens at a slightly higher energy than the emission (red line), and both of them have a Lorentzian line shape, their combination (black line) is really similar to what is observed in the experiments (figure 3.22).

In this interpretation the final shape is determined by the relative amplitude of the function representing the absorption and the emission. This model is based on the

assumption that the molecule absorbs energy from the plasmon, as expected from a plasmon mediated mechanism. The plasmon can normally de-excite in both radiative and non-radiative ways, with a calculated ratio of one to ten between the two paths [86]. The presence of the molecule offers a de-excitation path for the plasmon, whose emission probability is reduced at the absorption energy of the emitter. Of course, the dip in the spectrum can only be observed if the emission due to the plasmon is measurable in the spectrum of the lifted molecule. This may explain why the dip is absent in the spectrum of figure 3.22(a) and intense in the one of figure 3.22(c). Note that this interpretation also assumes a small shift between the absorption and emission energy of the emitter.

Interference with plasmons: Fano lineshape. The last interpretation we suggest is motivated by the strong resemblance of the peaks in figure 3.22 with Fano lineshapes [132]. Fano resonances arise from the interference of a continuum of states and a discrete level system. In experiments at the nanoscale, we can find them in many experiments involving a resonant scattering effect [139, 140]. Recently, Fano resonance were also observed in experiments involving molecules at the interface with metals, where Raman spectroscopy [141] and STM-LE measurements [15] were performed. The simplest relation that models a Fano resonance is

$$\sigma = \frac{(\epsilon + q)^2}{\epsilon^2 + 1}, \quad (3.4)$$

where, originally, σ represents a scattering section and ϵ is a reduced energy. The relevant term however is q , which is the shape parameter. It defines the asymmetry of the resulting curve and represents the balance between the influence of the discrete states and the continuum of states.

The Fano fits that are shown in figure 3.22 describe well the three situations and the q parameter decreases in magnitude from situation (a), no dip, $q = -9$, to situation (c), almost only dip, $q = -0.6$, with the intermediate situation having an intermediate q value.

In our STM-LE model the continuum of states would correspond to the LSP and the two level system to the molecular emitter.

Conclusions We observed different peak shapes for which we do not have a definite interpretation. The spectra show the simultaneous presence of plasmonic and molecular emission, possibly with interference between the two. Recently, the interplay between plasmons and molecular emission was discussed by Imada *et al.*, who observed asymmetric lineshapes in the STM-LE from pthalocyanine molecules on NaCl [109, 68]. In their case the lineshape was assigned to the quantum interference between the successive absorption and re-emission of energy between the molecule and the LSP [142, 143].

This discussion on the interaction between LSP and molecule will be further illustrated in the following section, where we discuss the origin of the vibrational feature on the high energy side of the 0-0 (B-band).

3.3.9 Analysis of the B-band: observation of molecular hot electroluminescence

We have underlined the importance of the localized surface plasmons in our system. They are part of the excitation mechanism of the molecule and impact the emission, both in its intensity and lineshape. In this section we discuss the nature of the B-band, a family of low intensity peaks that appear blue-shifted as compared to the 0-0 line. We will see how their origin further clarifies the strong impact of the plasmons on the emitter properties. In figure 3.24(a) the optical spectra of fused-MPP and fused-DNP are presented as a function of the shift from the 0-0 lines. We observe that the position of the peaks of the B-band, highlighted by blue vertical lines, is the same for the two molecules.

Because the peaks of the B-band appear at higher energy than the 0-0 line, they cannot originate from transitions starting from the ground vibrational level of S1. Moreover, these peaks appear as soon as the bias corresponding to their energy is applied, proving that they are not the R-band of a different electronic level of higher energy (e.g. S2). Based on these two considerations we deduce that the peaks of the B-band are generated by transitions between excited vibrational levels of S1 and the ground vibrational level of S0.

Before discussing the consequences of this fact we summarize the full excitation and emission path in figure 3.24(c) and (d). In (c), a tunneling electron excites a LSP (1) whose energy is transferred to the suspended molecular emitter (2). Eventually, the molecule relaxes by emitting a photon (3). Step (2) and (3) are detailed in (d). The molecule starts in the ground vibrational state of S0¹⁰. From there, we first consider the case where an energy transfer from the plasmon drives the molecule to the ground vibrational level of S1 (upward arrows in process I and II). From this level, a decay to S0, either to the ground vibrational level (process I, green downwards arrow, yields the 0-0 line) or to an excited vibrational level (process II, red downward arrows, yielding the R-band) leads to the emission of a photon.

If the plasmon has sufficient energy, transitions to vibrationally excited states of S1 are also possible (upward arrow in III). Here, according to Kasha's rule (see discussion below) the system should relax to the ground vibrational state of S1 before decaying to S0 either through path I or path II [144]. Our data rather suggest a direct transition from these excited vibrational levels, to S0, as illustrated by the downward arrows in

¹⁰The experiment are performed at 4.7 K, therefore the molecule cannot be in an excited vibrational level of S0.

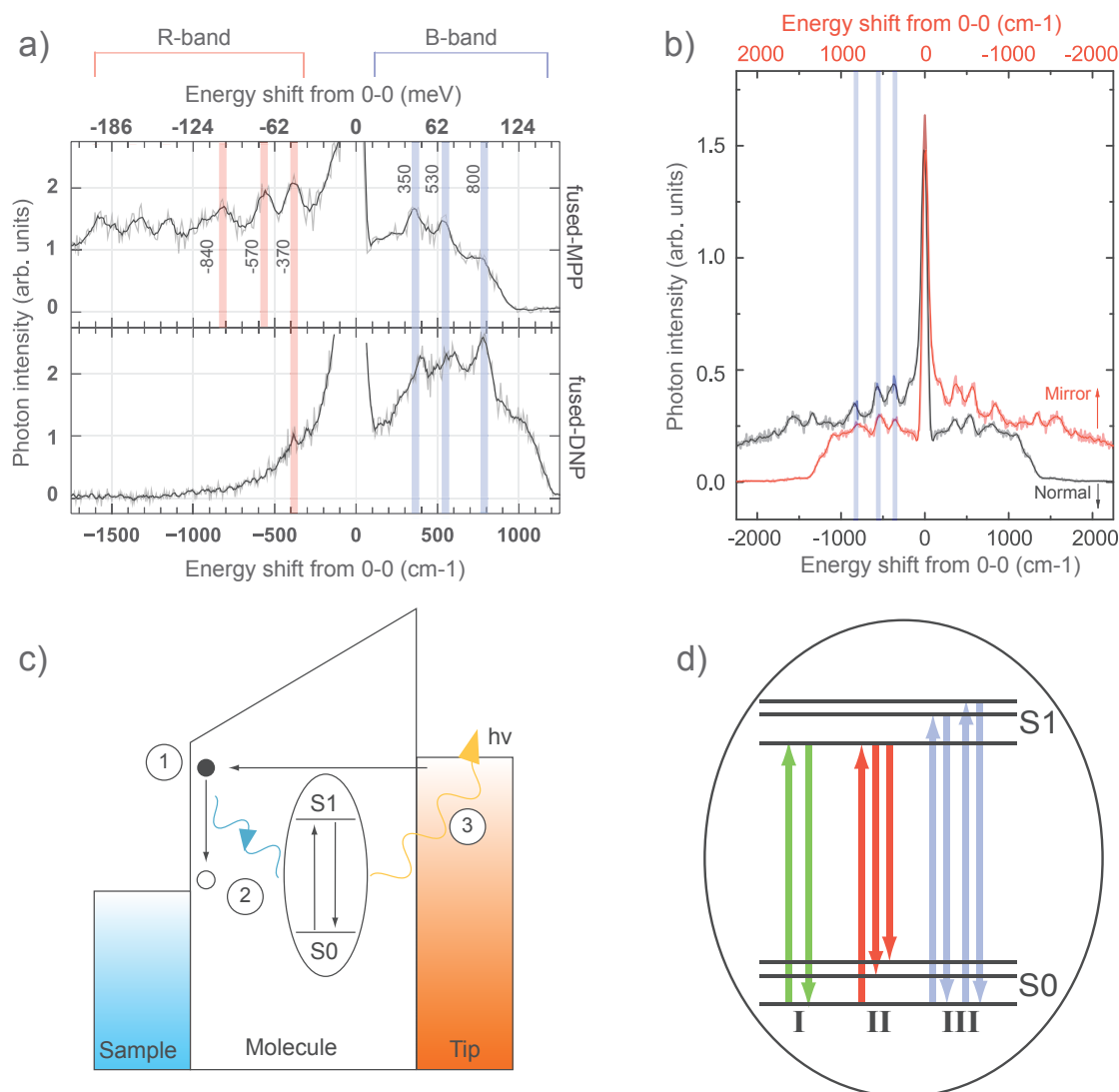


Figure 3.24 – Details and origin of the B-band. (a) Light emission spectra of fused-MPP and fused-DNP plotted as a function of the energy shift from the 0-0 lines. The raw (smoothed) data appear in gray (black). The blue vertical lines highlight the position of the B-band peaks. The red vertical lines highlight the position of the symmetric peaks in the R-band. (b) Mirror symmetry between R- and B-bands: light emission spectrum of a suspended fused-MPP (in black) and its mirror image (in red) with respect to the 0-0 line ($V = 1.8$ V). The blue vertical lines highlight the strong resemblance between the energy dispersion of the vibronic peaks on both side of the 0-0 line. (c) Schematic representation of the plasmon mediated excitation mechanism. (d) Details of the excitation and de-excitation process. Three possible paths are described: The green arrows characterize the most efficient path leading to the 00 emission line. It corresponds to a molecule excited to the vibrational ground level of S1 relaxing to the vibrational ground level of S0. The red and blue arrows characterize much less efficient paths. In path II the molecule is also excited to the vibrational ground level of S1 but decays to vibrational excited levels of S0 (R-band). Path III corresponds to a molecule excited to vibrational excited levels of S1 which relaxes to the vibrational ground level of S0 (B-band).

path III. These are the transitions that yield the B-band.

In this interpretation, the energy distribution of the blue-shifted peaks thus provides a map of the vibrational modes of the excited state of the molecule. For this reason the peaks in the R-band and in the B-band provide two distinct information, the first mapping the vibrations of S0 and the second mapping the vibrations of S1.

Considerations regarding the excited lifetime of the emitter. The vibrational relaxation time inside an electronic level is typically in the 1-100 ps range, while fluorescence is in the 1-10 ns range for usual chromophores [145, 146]. In this situation Kasha's rule applies: there is no luminescence from non-thermalised molecular excitons [144].

In our case, the observation of the B-band means that at least part of the emission is due to non-thermalized excitons, a phenomenon known as hot-luminescence [147]. This suggests that the fluorescence lifetime is strongly reduced compared to the usual case where the molecules are in solution. Reduced fluorescence lifetime is also reported for emitters with plasmonic nanostructures in their environment (cite), and it is known as Purcell effect. If the lifetime reduction is strong enough, hot-luminescence may be observed, as was reported for multi-layers of molecules in STM-LE experiments [36]. No experimental evidence of this phenomenon was reported so far at the single-molecule level.

A theoretical modelization of hot-electroluminescence in STM experiments on molecules was reported in [142, 143], and implied that the plasmon may act as a coherent excitation source of the chromophore. While such an interpretation may apply in our case as well, confirming this hypothesis would require a more detailed theoretical treatment, which is beyond the scope of this work.

We remark that, from the observation of the peaks alone, it is hard to estimate exactly which fraction of the non-thermalized exciton is directly re-emitted, instead of relaxing to the ground state of S1. This means that we do not know which dominates between the relaxation and the radiative rate.

Symmetry of S0 and S1. In the same spectra of figure 3.24(a), three peaks of the R-band are highlighted with red lines. We observe that the distribution of the peaks in the R-band is nearly the same as in the B-band. The only difference is a slightly larger shift of the R-band peaks. This near symmetry between R-band and B-band is further illustrated in figure 3.24(b), where a spectrum of fused-MPP is plotted (black curve) together with its mirror image with respect to the 0-0 line (red curve). Here, we observe that the positions of the peaks of the two mirror spectra overlap almost perfectly. This observation indicates that the vibrational modes of S0 and S1 are almost identical. While *a priori* there is no reason for such a symmetry, this behavior is expected for large and rigid molecule like porphyrins, where the geometry of the S0 and S1 states are similar [148]. In this configuration, the slightly larger shift of

the R-band peaks is also expected [148]. This is also in agreement with an emission spectrum dominated by an intense 0-0 line.

Final remarks. In this section we discussed the nature of the B-band, and demonstrated that it originates from hot-luminescence from vibrationally excited states of S1. The B-band therefore provides crucial information related to the vibrational modes of the electronically excited state. This information is thus complementary to the one provided by the R-band, that maps the modes of S0. For this reason the R-band corresponds to the fluorescence spectrum of the emitter, while the B-band is similar to its absorption spectrum.

3.4 Vibrational spectroscopy on double DPP and on fused-ZnDPP

So far we demonstrated that by passing current through a single emitter suspended by organic linkers between the tip and the sample of the STM, a narrow light emission can be induced.

In this section we present preliminary studies made on two new emitters. We will see how they provide new information on the emission mechanism, essentially through the analysis of their vibronic features.

The two systems are presented in figure 3.25: in (a) we see a pair of fused-DPP within the usual co-polymer architecture, while in (b) it is a co-polymer containing fused-ZnDPP.

Synthesis. Co-polymers containing double fused-DPP units are obtained in a small amount when preparing the usual samples with the fused-DPP. By increasing the ratio of Br₂-DPPH₂ over DBrTT during the evaporation phase (*c.f.* 3.1.3), it is possible to increase the number of co-polymers containing consecutive pairs of fused-DPP.

Molecular wires containing fused-ZnDPP are obtained by co-polymerizing DBrTT with dibromo-diphenyl-Zn-Porphyrin (Br₂-DPPZn) (3.25(c)). Its structure is identical to the one of fused-DPP, except for the presence of a Zinc atom in the core of the macrocycle. Like the metal-free counterpart, it can yield two fused isomers: the *cis* and the *trans* forms, as can be observed in the topography (b).

Light emission spectra. The luminescence spectrum obtained from the wire of figure 3.25(a), once the two porphyrins were detached from the surface, is presented in

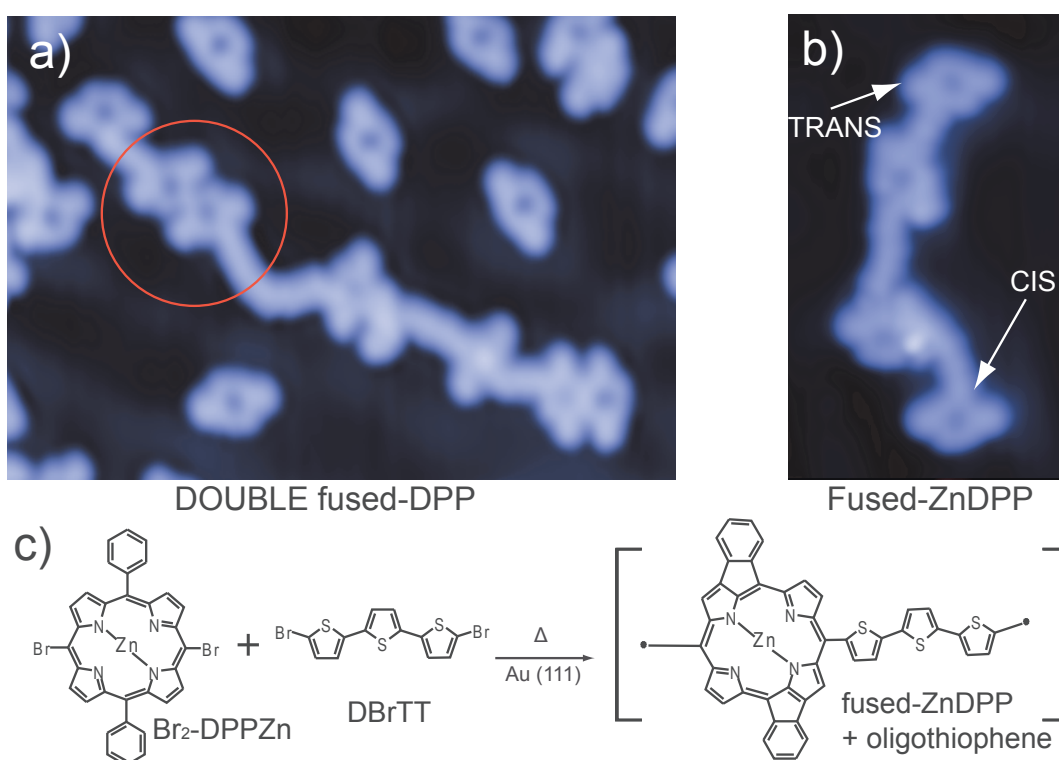


Figure 3.25 – Synthesis of double fused-DPP and of fused-ZnDPP. (a) STM topography of fused-DPP/oligothiophene co-polymer showing two fused-DPP directly linked (inside of the red circle). $14.9 \times 10.3 \text{ nm}^2$, $V = -0.1 \text{ V}$, $I = 0.1 \text{ nA}$. (b) STM topography of fused-ZnDPP/oligothiophene co-polymer. $5.7 \times 9.4 \text{ nm}^2$, $V = -0.1 \text{ V}$, $I = 0.1 \text{ nA}$. (c) Sketch of the synthesis of the co-polymers containing fused-ZnDPP.

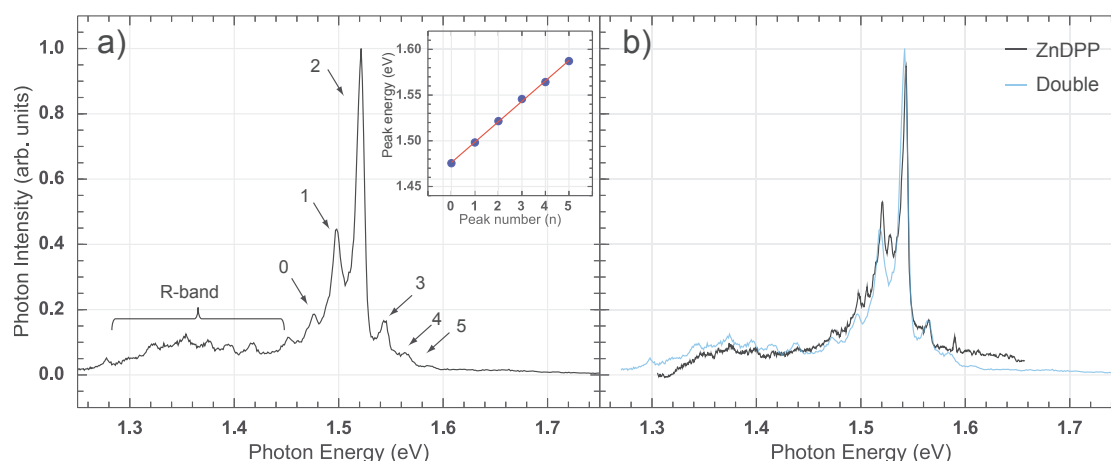


Figure 3.26 – Optical spectra from double fused-DPP and from fused-ZnDPP.(a) STM-LE of a co-polymer containing a double fused-DPP ($z = 2.3\text{nm}$, $I = 4.55\text{ nA}$, $t = 60\text{ s}$, $V = 1.7\text{ V}$). The R-band is highlighted. The peaks indicated with a number belong to the harmonic progression of a single mode. Their linear energy dispersion is plotted in the inset. (b) Normalized spectrum from fused-ZnDPP (black curve) ($z = 1.7\text{nm}$, $I = 4.8\text{ nA}$, $t = 600\text{ s}$, $V = 2.1\text{ V}$). The spectra of double fused-DPP (light blue line) is added and shifted horizontally to align the most intense peaks of the two spectra.

figure 3.26(a). The low energy side of the spectrum shows vibrational peaks, characteristic of the R-band. In the energy range where we usually found the 0-0 emission line, we find instead a set of peaks (indicated by numbers from 0 to 6). The relative intensity of these peaks resembles the harmonic progression of a same mode, whose probabilities are determined by the Frank and Condon principle. This is supported by the inset in figure 3.26(a) which shows a linear energy distribution of these peaks with a vibrational mode energy $\hbar\omega = 22\text{ meV}$ (*c.f.* section 3.3.5).

In the case of fused-ZnDPP, two types of optical spectra were observed. The first type, presented in figure 3.26(b) (black curve), we observe a striking similarity with the one of double fused-DPP, shown in figure 3.25(a) and superimposed as a light blue line in (b). Instead, the second type of spectrum is almost identical to the one of fused-DPP that was discussed in the previous sections and, therefore, we will not analyse it further.

Nature of the peaks. In the following we assume that the spectra of figure 3.26(a) and (b) are identical.

The linear dispersion of the vibronic peaks in figure 3.26(b), and their respective intensities are clear indications that the equilibrium geometry of the emitter is different in the excited state S_1 and in the ground state S_0 . It shows as well that one vibronic mode (of energy $\hbar\omega = 22\text{ meV}$), couples preferentially with the optical transition.

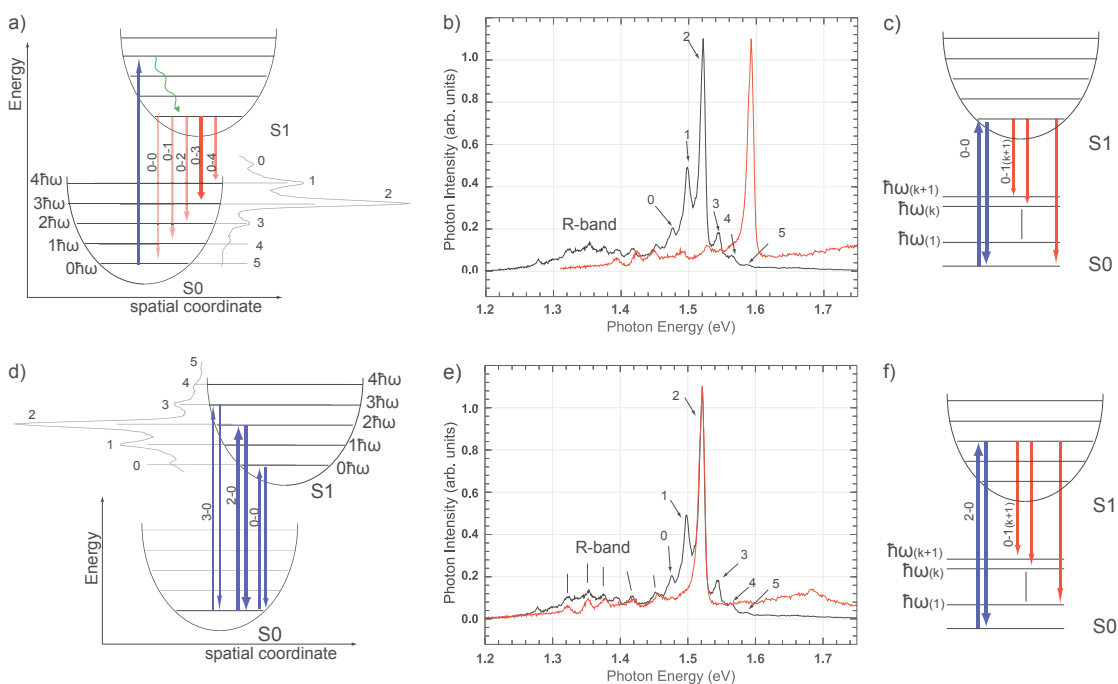


Figure 3.27 – (a)(b)(c) Emission from the thermalised excited state. (a)

Energy scheme of the transitions yielding a harmonic succession of vibrational peaks of one mode of S0. Excitation from S0 to S1 (blue arrow). Internal relaxation to the ground state of S1 (green arrows). Radiative transition yielding an harmonics succession of peaks (0-n transitions) of the mode of S0 of energy $\hbar\omega$ (red arrows). (b) Optical spectra of the double fused-DPP and the fused-DPP. The spectra were horizontally shifted to superpose the 0-0 line of the fused-DPP to peak number 5 of the double fused-DPP (corresponding to its 0-0 line in this model). (c) Transitions yielding the R-band. The emission occurs from the ground state of S1 to different vibrational modes of S0 (0-1_k transitions. *k* refers to the different vibrational modes of S0.)

(d)(e)(f) **Emission from the non-thermalised excited state.** (d) Energy scheme of the transitions yielding a harmonic succession of vibrational peaks of one mode of S1. Excitation from S0 to different harmonics of a mode of energy $\hbar\omega$ of S1 (upward arrows), followed by an immediate re-emission (downward arrow; n-0 transitions). (e) Optical spectra of the double fused-DPP and the fused-DPP. The spectra were horizontally shifted to superpose the 0-0 line of the fused-DPP to the most intense line of the double fused-DPP. (corresponding to the line number 2). (f) Transitions yielding the R-band. The emission occurs from a the non-thermalised excited state, to different vibrational modes of S0 (n-1_k transitions. *k* refers to the different vibrational modes of S0.).

In the following we try to understand to which transition these features effectively correspond. We start by discussing the most common model used to describe such a behavior.

In figure 3.27(a) only the harmonics of one dominant vibrational mode are presented for both S0 and S1. To account for the varying equilibrium geometry, the S1 and S0 parabolas are shifted on the “spatial coordinate” axis. The system is excited to S1 from the ground state of S0 (blue arrow). Because of Kasha’s rules, the system relaxes to the ground state of S1 (green arrow).

The radiative transitions start from this level and reach different harmonics of the mode of energy $\hbar\omega$ in S0 (red arrows). These are 0-n transitions and their emission probabilities are determined by the Franck and Condon factors. In this model, the 0-0 transition would correspond to the peak number 5 in the spectrum in (b). All other transitions are at lower energies.

However, does this model also explain the presence of the vibronic peaks belonging to the R-band? If the 0-0 transition is the peak labelled 5 in the spectrum of double fused-DPP, the shift of the R-band peaks is much larger than usual, as is observed in figure 3.27(b). Here, a spectrum of fused-DPP (red curve) is aligned to the one of double fused-DPP (black curve) in order to make the 0-0 line correspond. Based on this observation, this model should be discarded and an alternative model should be found.

In section 3.3.9, the emission from non-thermalized molecular exciton was evidenced. Assuming such a mechanism, we propose the model of figure 3.27(d). Here, excitations from the ground level of S0 to different harmonics of a vibrational mode of S1 are shown. These are followed by a direct radiative transition to the initial ground state of S0. This implies that hot-luminescence dominates the emission, and that Kasha’s rule does not apply. In this scenario, the 0-0 transition yields the peak labelled 0 in the spectrum of double fused-DPP (figure 3.27(e)). The most intense line would correspond to the 2-0 transition. The Franck and Condon factors this time characterize the absorption probability of each harmonic of the vibrational mode of S1 (of energy $\hbar\omega = 22$ meV).

This second picture is supported by the comparison presented in figure 3.27(e), where the spectra of fused-DPP (in red) and of double fused-DPP (in black) have been shifted to align the most intense lines. These lines correspond to the 0-0 transition of the former, and to the 2-0 transition (of the dominant mode of energy $\hbar\omega$) of the latter. We observe now a good alignment between the R-bands of the two systems. Figure 3.27(f) shows that, in this model, the R-band corresponds to transitions starting from the second harmonic of the mode of energy $\hbar\omega$ of S1, and arriving in different vibrational modes, k , of energy $\hbar\omega_k$ of S0: we are observing 2-1 transitions.

A close inspection of the spectra in (e) shows that double fused-DPP has more peaks in the R-band. These peaks are probably generated by transitions from the other relevant harmonics to the different vibrational modes of S0: n-1 transitions.

The model of figure 3.27(d)(e)(f) therefore explains both the presence of the vibronic

progression close to 1.5 eV, and the R-band.

Final remarks We reported on the light emission spectra of suspended fused-ZnDPP and double fused-DPP. These spectra present simultaneously an R-band and a series of peaks close to the transition energy that follow an harmonic progression. We proposed an interpretation that implies that most of the emission comes from non-relaxed vibrational states of S1. Interestingly, the R-band provides a map of the vibrational modes of S0, while the Franck and Condon features map the absorption of a vibrational mode of S1. These observations suggest that the equilibrium “coordinates” of the molecule are different for S1 and S0, which contrasts with what was observed for fused-DPP. This behavior must be linked to the presence of a dimer of fused-porphyrins in one case, and to the presence of the zinc atom in the other. However, the detailed effect of these modifications of the emitters are yet unclear.

These conclusions imply that the fluorescence, thanks to the plasmonic amplification, is here a much faster process than vibronic relaxations in the emitter. This provides a good indication of the lifetime of the excited state of the molecule in our configuration. Indeed, in section 3.3.3 we used the width of the main emission line to give a lower limit to the lifetime in the order of some hundreds of fs. From the competition with the vibrational relaxations, which occurs generally in the ps range [145, 146], we can deduce that the radiative lifetime of our emitter is in the $0.1 \text{ ps} \leq \tau_{rad} \leq 1\text{-}10 \text{ ps}$. This value is a factor ≈ 1000 lower than the typical fluorescence lifetime of porphyrin molecules [145, 146], indicating that the tip-sample junction acts as a very effective plasmonic cavity.

We stress that these are preliminary results. Further experimental studies and a systematic theoretical modelling of this phenomenon will be needed to confirm our interpretation.

3.5 Summary and conclusions

In this chapter we presented a STM-LE investigation of the optoelectronic properties of porphyrin molecules suspended by organic linkers between two metallic electrodes. We proved for the first time that it is possible to excite an intramolecular radiative transition with a very narrow emission line ($\text{FWHM} \leq 10 \text{ meV}$) from a molecular device bridging two electrodes.

We demonstrated that on-surface co-polymerization can be used to produce complex molecular architectures with the desired opto-electronic properties. We also showed that the thermal annealing used for the synthesis, results in a transformation of the emitter, yielding a new family of molecules: fused-porphyrins. These organic systems can be manipulated and lifted with the STM tip, decoupling a porphyrin from the

surface. A narrow line emission of light is excited by tunneling electrons crossing the junction. The energy of the light emission corresponds to the fluorescence of the emitter, thus validating the experimental concept.

Below we list some of the important conclusions that result from our experiment.

Fingerprint. Besides the main line (0-0), the light emission spectra present two vibrational sidebands: one at lower energy (the R-band), and one at higher energy (the B-band). We analysed the former and proved that it arises from transitions from the ground vibrational level of S_1 to excited vibrational states of S_0 , each belonging to a different mode (0-1 transitions). The energies of these peaks are well reproduced by calculated optically active Raman modes. This is the first time that this type of spectroscopic fingerprint is observed without the use of an external light source. In other words, our experiment adds a chemical resolution to an STM experiment, without the need of a laser. We remark however that, in this lifted configuration, the spatial resolution provided by the STM is lost since the tip is used to suspend the molecule.

Mechanisms. We demonstrated that the excitation mechanism is plasmon mediated rather than due to electrons and holes injection from the electrodes. The interaction with the nanocavity plasmon is however rather complex, as illustrated by the relative intensity of the vibrational peaks and by the asymmetric peak shape of the main emission line. The observation of a Fano line shape is an indication of an interaction with the plasmon that is responsible for a broad background emission.

One consequence of the interaction with the localised surface plasmons is a drastic reduction of the fluorescence lifetime. This results in the observation of the vibrational peaks of the B-band, which are interpreted in terms of emission from a non-thermalised excitonic state, a phenomenon known as hot-luminescence. For the hot-luminescence to be measurable, the light emission process have to compete with the vibrational relaxation inside of the S_1 state, a phenomenon that is typically orders of magnitude faster in the absence of the plasmons.

We observed hot-luminescence in two configurations.

For fused-MPP and fused-DNP, the ground state S_0 and the excited state S_1 are "spatially aligned". This results in the near symmetry between the B-band and the R-band that appear both with extremely low intensity when compared to the 0-0 line. For double fused-DPP and fused-ZnDPP, the S_0 and S_1 states are shifted, and present an harmonic progression of peaks associated to a single vibrational mode. In this case, most of the emission comes from non-relaxed states of S_1 .

These observations allowed to estimate the fluorescence lifetime in the presence of the localised surface plasmons to be in the 0.3-10 ps range. One way to determine

the lifetime precisely would be by measuring the time correlation between emitted photons. This kind of experiment, done using a Hanbury Brown-Twiss interferometer, would also allow to prove if the emitter is a source of single photons, similarly to what has been recently done in a STM-LE experiment for clusters of molecules by Merino *et al.* [35].

A device oriented configuration. One of the motivations of our experimental concept was the need of a direct contact of the molecular system with the electrodes, in order to allow the future conception of devices. Not only we proved that it is possible to have a narrow line emission in this configuration, we also showed that we can control some of its properties.

First, we showed that we can control the linewidth of this emission by tuning the coupling with the sample surface. This allows to continuously tune from a broad emission ($\text{FWHM} \geq 100$ meV) to an extremely narrow one ($\text{FWHM} \approx 2$ meV).

Second, we presented the possibility to generate similar, almost monochromatic, light emission spectra at different energies. This was done by chemically engineering the nature of the emitter. We reached this way an emission at 1.28 eV, at 1.51 eV and at 1.68 eV. These values fit with TD-DFT calculations of the optical gap of the porphyrins, that thus provide a predictive method for choosing the molecule to use for each specific need.

These two examples illustrate the interest of this setup for the integration of optoelectronic circuits at the molecular scale.

Another interesting experiment, would be the study of the impact of an emitter in a configuration like the one we proposed, on propagative surface plasmon polaritons [46, 47, 48, 49, 50]. Finding an imprint of the chromophore, possibly in the form of a dip, on the emission from SPPs would show the possibility to integrate electronic and plasmonic circuits at the molecular scale.

Perspectives. Some limits can be found in this molecular system, mainly due to the extreme variability in the quantum yield, that does not allow to predict if the emission from a molecule would be even measurable.

Moreover, the lifted co-polymers are unstable: high currents, or movements of the tip can easily result in accidentally dropping the wire from the tip or in a destruction of the polymer itself.

These issues points to the need of a more stable system, that possibly stands higher currents and that still has some of the flexibility of the co-polymers of fused-porphyrins and oligothiophene. For this reason, we turn in the next chapter to the study of graphene nano ribbons, an organic structure known both for its optical properties and its extreme robustness.

CHAPTER 4

STM-LE from graphene nanoribbons

4.1 Introduction

Graphene is perceived as the material of the future in numerous applications in nanoelectronics, energy conservation, medicine, telecommunications, sensing [149, 150, 151, 152, 153, 154]. Despite its many impressive properties and its 2D character, the absence of an electronic gap in the graphene band structure limits its applications in optoelectronics and photonics. “Wrapping” and “cutting” a graphene sheet (*i.e.*, carbon nanotubes [51, 52] and **graphene nanoribbon (GNR)** [53, 54]) lead to a gap opening. In these materials, most of the relevant mechanical, transport and chemical properties of graphene are preserved, while the presence of an optical gap opens new possibilities for the realization of devices such as field-effect transistors and optoelectronic components [53, 55, 56].

This chapter is dedicated to the study of graphene nanoribbons (GNR) that present an optical gap. In these 1-D structures, the gap depends on the exact width of the GNR, and on the atomic structure of its edges [54, 57]. The scheme in figure 4.1(a) presents the different ribbon families that can be obtained by cutting a graphene sheet. Depending on the direction of the cut, the GNR can have *zigzag* (delimited by blue lines in the figure) or *armchair* edges (red lines)¹.

Finite size ribbons may present both zigzag and armchair edges (figure 4.1(a)). The name given to a ribbon contains information relative to the symmetry of its edges in the long axis (A for Armchair; Z for Zigzag) and the number of carbon atoms in their short axis. For instance, we refer to the finite ribbon of figure 4.1(a) as a 7 armchair

¹More complex edges can be obviously obtained.

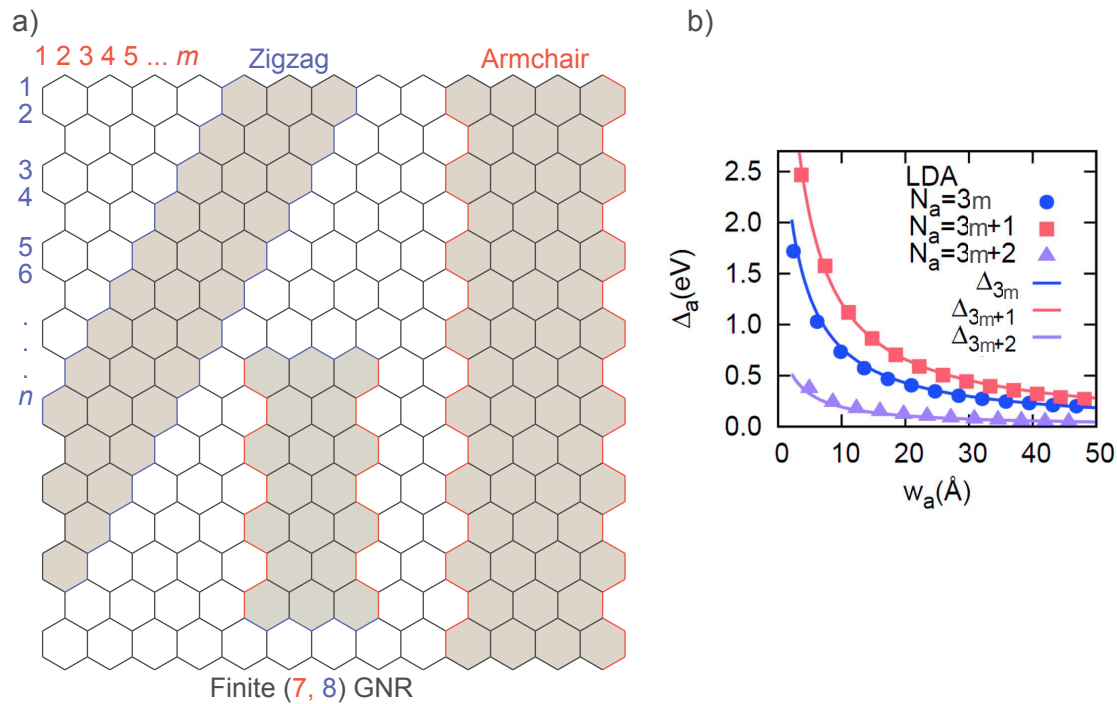


Figure 4.1 – Structure of GNRs. (a) Different types of GNR obtainable from an infinite graphene sheet. An infinite Zigzag edged with $m = 7$. An infinite Armchair edged with $m = 9$. A finite GNR with $m = 7$ and $n = 8$. For finite GNR we give the name based on the type of the longest edge. The one in figure is a 7-AGNR (of length 8). Adapted from [155]. (b) LDA calculations of the band gap of AGNRs as a function of their width. The three curves show the existence of three families of ribbons, depending on the number of carbons of the short edge ($3m$, $3m+1$, $3m+2$ where m is an integer). (Adapted from [54]).

GNR, or 7-AGNR (of length 8).

Both GNRs types (zigzag and armchair edges), show interesting properties.

ZGNRs, for instance, are expected to have spin-polarized edge states reminiscent of 2D topological insulators, that may find applications for graphene based spintronics [58, 59].

Ribbons with armchair edges offer, instead, a band gap that strongly depends on the atomic width of the ribbon [54]. This is illustrated in figure 4.1(b), where first principle calculations of the band gap for increasing width is reported. We observe that AGNRs can be divided into three families: ribbons with $3m$ or $3m+1$ carbons (with m an integer determining the width of ribbon) behave like semiconductor while GNRs with $3m+2$ carbons have a narrow gap and behave almost like metals. For the three families the gap decreases as m is increased.

State of the art. The existence of these three families makes AGNRs particularly interesting: this offers, in principle, the possibility to have radically different optical properties by changing the width of the ribbon by just one atom. However, this requires an extreme degree of control in the synthesis of such structures. In the following, we describe the state of the art of the methods used to synthesise GNRs and of the studies of their optical properties.

In 2007, the first experimental studies of the transport properties of GNRs appeared for structures obtained by lithography [55, 156]. In 2008, a chemical route to produce narrow GNRs in solution was proposed [157] and, in 2009, a fabrication method based on the unzipping of carbon nanotubes by plasma etching was invented [158]. These methods allowed for a high production yield of narrow width GNRs (10-20 nm). However, they lack control over the atomic scale geometry of the edges.

In 2010, a method that revolutionized the study of this material was published: Cai *et al.* showed the possibility to synthesize atomically precise GNRs by on-surface polymerization and subsequent cyclo-dehydrogenation of a molecular precursor [60]. This paper opened the way to the controlled production of different types of GNRs with a width below 10 nm with atomic scale control of the edge geometries.

Following similar procedures and using different precursors, atomically precise GNRs with various sizes and edge types were synthesized, including type 3,5,7,9 and 13-AGNR [124, 125, 60, 159]. ZGNRs types were also synthesized by this method [160, 161].

Thanks to this synthetic route, several properties of GNRs that could only be explored on theoretical grounds, are gradually being confirmed. The production of GNRs with atomically controlled edges allowed to ascertain the presence and to measure the width of the electronic gap in AGNRs of type $3m+1$ [162, 159], as well as the narrow gap in $3m+2$ ones [125].

In contrast, direct measurements of the optical properties of GNRs are complicated, especially at the level of a single ribbon. Photoemission from GNRs embedded in carbon

nanotubes has been studied [163] as well as absorption properties in the near-infrared of low-bandgap GNRs in solution [164]. Finally, **reflectance difference spectroscopy (RDS)** on atomically precise 7-AGNRs on a metallic substrate [165] demonstrated the high impact of excitonic effects in the optical response. The role of excitonic and bi-excitonic effects have been further highlighted by pump-probe experiments on GNRs in solution [166]. Recently, Raman properties of cove-shaped GNRs have been investigated in detail [66]. These studies are supported by extensive theoretical calculations and yield consistent results, highlighting both the high level of understanding of these systems and the interest they generate. However, these are mostly *ensemble* measurements. A study of the optical properties at the single GNR level is still missing. STM-LE provides a way to study the optical properties of individual graphene nanoribbons suspended between the tip and the sample. This chapter presents a detailed study of these properties.

First, the synthesis of 7-AGNRs is described, and a distinction is made between the different types of termini that these ribbons may display. We then report on the basic transport properties of individual ribbons suspended between the tip and the sample of the STM. The results presented in this part are compared to results from the literature; this provides some important information on the electronic structure of the GNR and to the contact of the ribbon with the electrodes (STM tip and sample).

We then turn to the light emission properties of the suspended GNRs. This study reveals an intrinsic emission peak whose energy cannot be reconciled with the expected fluorescence properties of the ribbons. It however strongly suggests that the edge state, also called Tamm state, located at the ribbon termini, is directly involved in the emission process. Some possible mechanisms are discussed at the end of the chapter.

4.2 Synthesis of 7-AGNRs

We synthesized armchair graphene nanoribbons made of 7 carbon atoms (7-AGNR) on a Au(111) substrate. The synthesis, summarized in figure 4.2(a), follows the procedure described in [60]. A precursor monomer (10,10'-dibromo-9,9'-bianthryl) is sublimated on a Au(111) substrate kept at room temperature. Upon thermal annealing, dehalogenation occurs and C-C coupling results in the formation of linear polymers. Annealing to a higher temperature activates a cyclo-dehydrogenation reaction that results in the formation of fully aromatic GNRs. The two reactions were realized in a single annealing step at a temperature of 670 K.

In figure 4.2(b), (c) and (d) STM topographies of the products of the reaction are shown. As illustrated in the STM images, the produced GNRs may present different termini, a behavior that was previously reported in [43, 61] and analysed in detail in [62]. Based on a comparison with simulated STM images (figure 4.2(e), [62]), the

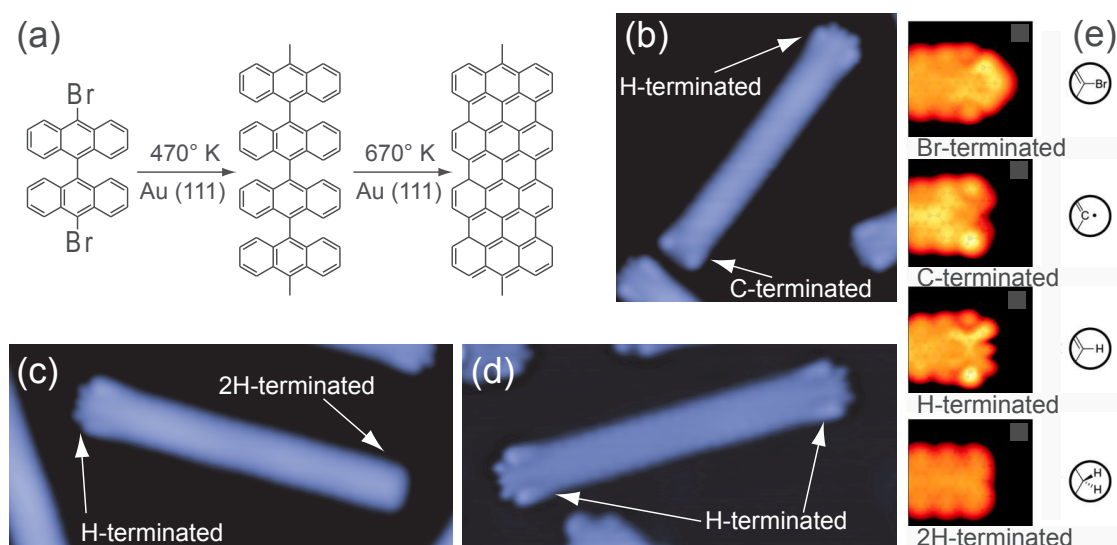


Figure 4.2 – Synthesis of 7-AGNRs. (a) Scheme of the synthesis of the GNRs (adapted from [62]). (b)(c)(d) STM topographies of GNRs ($V = 0.05$ V, $I = 0.1$ A. (b) 8.4×8.7 nm², (c) 11.8×5.5 nm², (d) 12.3×5.8 nm²) presenting different termini. (e) STM simulations, based on DFT calculations, for different types of termini (adapted from [62])

nature of the different termini has been determined. It is shown that they essentially depend on the coordination number of the central carbon atom of the 7-AGNR short edge, and on the chemical nature of the atom to which it is bound. When this C-atom is left with an unpaired electron (C-terminated) it appears darker in the central part of the edge as we see in figure 4.2(b). Most of the time the carbon is hydrogen passivated (H-terminated) resulting in a three dot structure 4.2(b), (c) and (d). A second hydrogen can bond with the same carbon (2H-terminated) resulting in a stable structure that appears featureless in the topographies 4.2(c). The first part of the chapter is dedicated to experiments performed on H-terminated ribbons.

4.3 Electronic and mechanical properties of 7-AGNRs

This section is focused on the electronic and mechanical properties of lifted 7-AGNRs. Several studies have been published on the electronic properties of narrow GNRs lying flat on Au(111) [162, 167, 168, 62, 169], and the 7-AGNRs in pulling configuration were also studied previously [43, 63]. This will allow us to compare our data with published results and to characterize the basic properties of the system under study.

4.3.1 Manipulation of GNRs

As a first step we lifted a nanoribbon following the procedure described in chapter 3.2. In figure 4.3, the normalized conductance G/G_0 is presented as a function of the tip sample separation. The formation of a contact between the tip and the GNR terminus is characterized by an inflexion (arrow in figure 4.3) in the $G(z)$ curve registered during the approach (red curve). This position is used as the origin for the x-coordinate. The black curve represents the retreat with the GNR attached to the tip. The milder slope of the conductance curve with respect to the approach confirms that a GNR is connected to the tip. The light blue curve shows the conductance decrease for a retraction of the tip up to a distance of 5 nm at a bias voltage of 0.1 V. An exponential decrease of the conductance is observed until a value $z = 4$ nm. The plateau observed above 4 nm is due to limits of the I/V converter. There, the current becomes too low to be measured.

Analysis and comparison with other systems. For a tip-sample distance z comprised between 1-3.5 nm, $G/G_0 \propto e^{-\beta z}$ as can be seen from the fit in figure 4.4(a). Here, the coefficient β , also called inverse decay length, reflects the ability of the wire to transport current at a given voltage bias [42, 43, 22, 44, 41]. For $V = -0.1$ V we found a value of $\beta = 0.39 \pm 0.02 \text{ \AA}^{-1}$, in agreement with [43]. This further confirms that we are indeed lifting the GNR in the junction.

It is instructive to compare the $G(z)$ curve of suspended GNRs with the one of polyfluorene, in figure 4.4(b), or oligothiophene (c). While periodic oscillations of the conductance with z are observed for the two polymers, they are absent for the GNR.

In the case of polyfluorene the shallow oscillations were attributed to local bending of the molecular chain [42]. For oligothiophene the changes in conductance are more abrupt. Their periodicity was attributed to the detaching of thiophene monomers from the surface [41]. The abrupt component is related to a change in the conjugation of the wire. An increase of mechanical stress occurs before the detaching of a monomer from the surface, reducing the conjugation and consequently the conductance. The

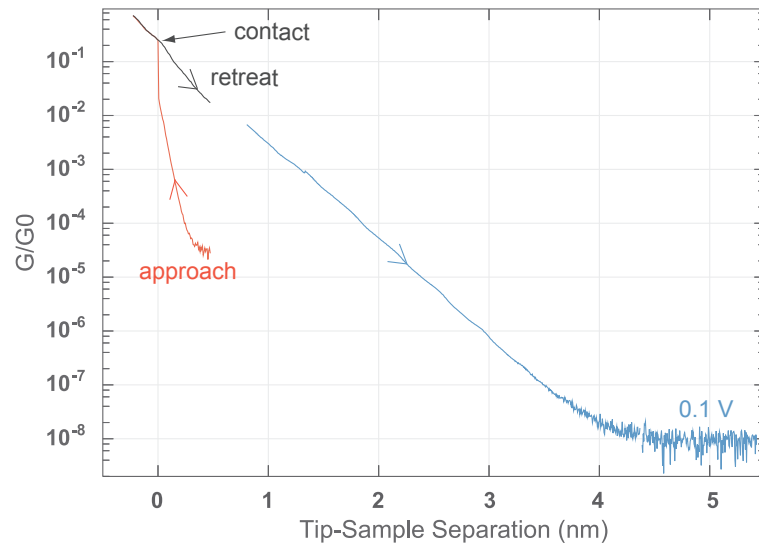


Figure 4.3 – Lifting of 7-AGNRs. Normalized conductance as a function of the tip sample separation ($V = -0.1$ V, logarithmic scale) during the lifting of the wire. The red curve represents the approach of the bare tip towards the molecule. The black curve is the retraction of the tip after contact. The light blue curve represents the retraction of the tip up to 5 nm with the molecule attached.

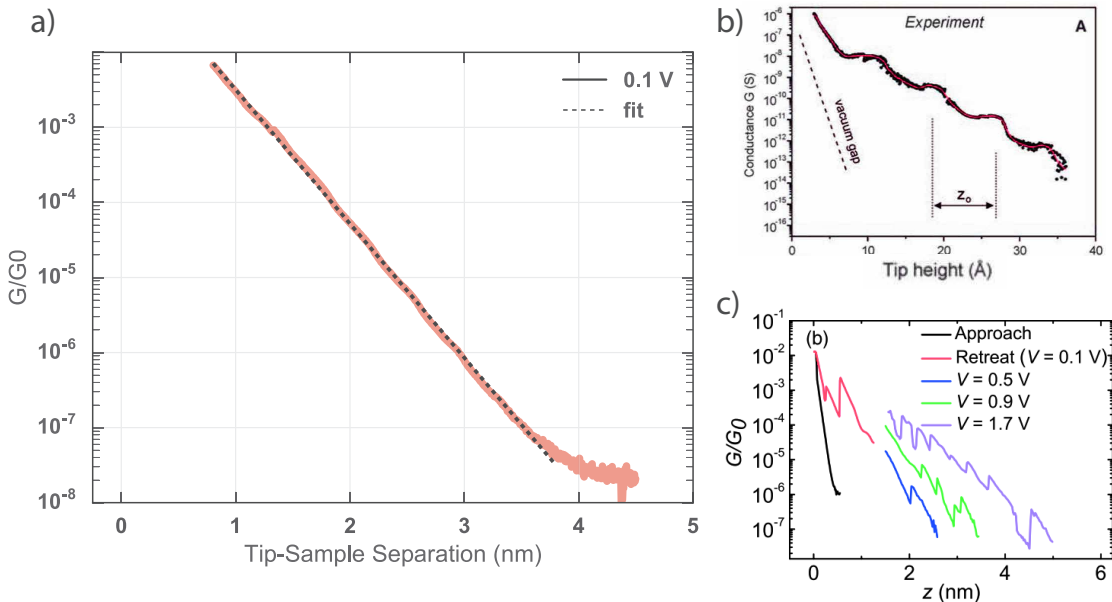


Figure 4.4 – Comparison of $G(z)$ for lifted 7-AGNRs and other molecular polymers. Normalized conductance as a function of the tip-sample separation for (a) a suspended GNR ($V = 0.1$ V), (b) a suspended polyfluorene wire ($V = 0.1$ V, adapted from [42]), (c) a suspended oligothiophene (0.1 V $\leq V \leq 1.7$ V, adapted from [22]).

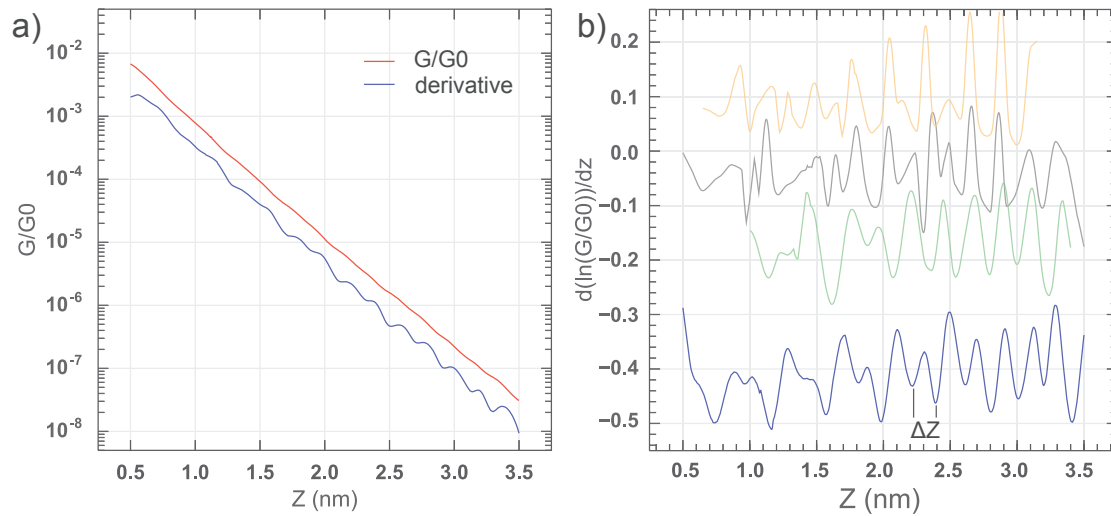


Figure 4.5 – Modulations of the conductance $G(z)$. (a) Normalized conductance (red curve) and its derivative (blue curve) as a function of the tip-sample separation. (b) Derivative of the logarithm of the conductance as a function of z for the same GNR (blue curve) and for other specimen of 7-AGNR (green, grey and yellow curve).

stress is released after the detachment of the monomer, resulting in an increased conjugation and conductance.

The absence of such features on the GNR spectrum could be sign of a lower interaction with the surface, that would result in easier sliding of GNRs on gold. Recent atomic force microscopy experiments indeed showed that GNRs move in an almost frictionless way on Au(111) [63].

Nonetheless, a closer inspection of the conductance curve shows some weak modulations of the conductance on top of the exponential decay. To highlight this effect (that was not reported in previous STM works) the $G/G_0(z)$ curve (red curve) is plotted with its derivative (blue curve) figure 4.5(a). In the derivative curve, periodic modulations of the conductance are observed. The modulations are even more clearly recognizable in the derivative of the logarithm of the conductance as a function of z , presented in the blue curve of figure 4.5(b). From this kind of plot it is possible to obtain the periodicity of the main modulation $z = 2.5 \pm 0.5 \text{ \AA}$. This value and its dispersion were obtained by averaging on nanoribbons of different lengths with lifting values lower than 5 nm, like the ones presented in the yellow, gray and green curves of figure 4.5(b). A similar value was found in [63] for the oscillation of the frequency shift, Δf , in an AFM measurement of lateral sliding GNRr on Au(111) (see figure 4.6(a)). Finally, we remark in figure 4.5 the presence of modulations of different frequencies at low tip-sample separation ($z \leq 2 \text{ nm}$).

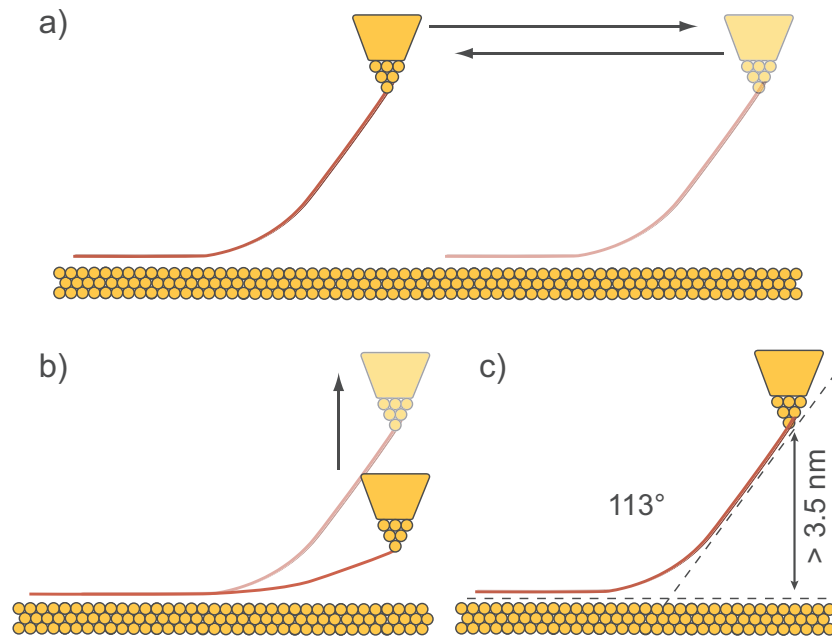


Figure 4.6 – Lateral sliding and vertical lifting. (a) Lateral sliding of a suspended GNR, as in [63]. (b) Vertical lifting of a GNR. (c) Limit of the bending angle of a suspended GNR as deduced from calculations reported in [43]

Discussion. The explanation for the modulation observed in AFM measurements is based on the position of the GNR with respect to the sample surface and the lattice mismatch between the GNR and the Au(111) lattice [63]. When lifted ($z \geq 2$ nm) the GNR has only one stable configuration on Au(111). The periodicity between two equivalent lateral positions of the GNR on Au(111) is of 2.8 Å. The modulation of the force measured with the AFM corresponds to the sliding of the GNR in and out of this stable configuration when pulled by the tip.

The frequency of the modulation observed in the conductance measurements suggests that the lattice mismatch plays a role also in the STM experiment. We suggest two hypotheses to explain the impact of the mismatch on the conductance.

- The results of Reecht *et al.* on oligothiophene, show that forces acting on the suspended molecule can impact its conductance by modifying the conjugation along the wire or the electronic characteristic of the molecule-tip bond. [41]. Even if GNRs slide with low friction on the Au(111) surface, the AFM measurements show that the force varies during the lateral sliding of the ribbon. This periodic variation of the force may translate in small variations of the conductance that we observe.
- As an alternative explanation, the lattice mismatch may influence the electronic coupling of the GNR with the metallic substrate. This would result in varia-

tions of the electron transmission of this interface. As the GNR slide on the surface between different positions, where the coupling is better or worse, the conductance would change consequently.

One general observation about the presence of different frequencies in the conductance for lifting of $z \leq 2$ nm can be made. In our experimental configuration the tip is retracted vertically, as sketched in figure 4.6(b). This implies that, during the lifting procedure, the GNR is simultaneously sliding on the surface and bending. In particular, calculations reported in [43] show that the GNR bends more and more as the tip is retracted, reaching a limiting angle of 113° for $z = 3.5$ nm, as illustrated in figure 4.6(c). For $z \leq 3.5$ nm, the effective lateral shift of the GNR on the surface does not correspond to the retraction of the tip. In this range, the relation between the lateral shift and z varies with the changing angle. This could explain the presence of variable frequencies in the modulation of the conductance for small values of z .

At this stage, the experimental results do not allow for a complete understanding of the observed modulations. A theoretical modelling, including DFT simulations, would be required to test the hypothesis we made. However, the measurements reported in this section prove that a great degree of control over the suspended GNR is possible. Moreover, they illustrate that this system is only weakly impacted by the lifting distance.

In the next section we are going to explore the impact of the tip-sample distance on the electronic properties of the wires (dI/dV spectra).

4.3.2 Differential conductance

In this section we study the dI/dV conductance spectra of GNRs. In figure 4.7(a) a typical spectrum of a GNR lying on a Au(111) surface is presented (red curve). By comparing the spectrum with the one obtained on the bare surface (black curve), it is deduced that all the broad and featureless signal between -0.35 V and +0.7 V does not originate from the GNR. In contrast, the two sharp edges at -0.7 V and 1.6 V are respectively assigned to the HOMO and to the LUMO of the ribbon. We deduce a band gap of $\Delta = 2.3$ eV for the GNR on Au(111), as supported by theoretical calculations of the bandgap, reported in [162, 165].

A typical conductance curve for a GNR suspended in a gold-gold junction is presented, in figure 4.7(b) for a tip retraction of $z = 3.9$ nm. The curve shows three narrow peaks: at -0.83 V, at +1.3 V and at +1.69 V. The central part shows a gap of zero differential conductance.

The comparison between the dI/dV curves for the lifted and planar configurations reveals strong similarities: the HOMO is at -0.8 V in both cases and closer to the Fermi level than the LUMO. The gap, however, is slightly smaller in the suspended

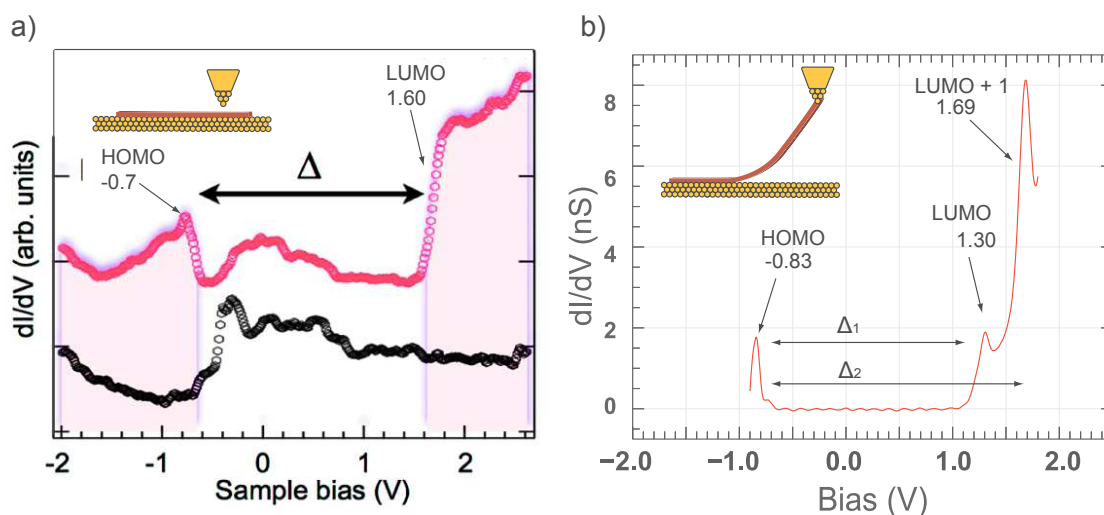


Figure 4.7 – Differential conductance as a function of the applied bias (dI/dV). (a) For of a GNR lying on the surface (red curve). The black curve is the dI/dV acquired with the tip in front of the bare surface. (adapted from [162]). (b) dI/dV spectrum of a suspended GNR ($z = 3.9$ nm). The insets illustrate the two configurations.

configuration (LUMO at 1.3 eV) than for the flat laying GNR (LUMO at 1.6 eV). Koch *et al.* [43] assigned the resonances in the pulling geometry to the same states as in planar adsorption. This conclusion implies that the voltage drops nearly exclusively at the tip-GNR interface (*i.e.* the molecular junction does not act as a voltage divider). While the energies of the peaks are essentially unaffected by the lifted configuration, their reduced widths in the dI/dV spectrum suggests that the ribbon is partially decoupled from the electrodes.

z dependency of the differential conductance

To further investigate the impact of the lifted configuration on the transport properties of the GNR, we measured how the dI/dV spectra of suspended GNRs is affected by the tip-sample separation.

In figure 4.8(a) several differential conductance spectra obtained on the same GNR for z values between 3.7 nm and 4.5 nm are presented. We observe that the overall shape of the spectrum is unchanged over all the explored z range.

A closer inspection shows that, while the HOMO has a fixed energy value, the LUMOs shift toward lower energies as z is increased. The dashed lines in the figure are aligned with the peaks at $z = 3.7$ nm (topmost curve). This is further illustrated in figure 4.8(b), where the position of the three resonances is plotted as a function of the tip sample separation and fitted with a linear regression.

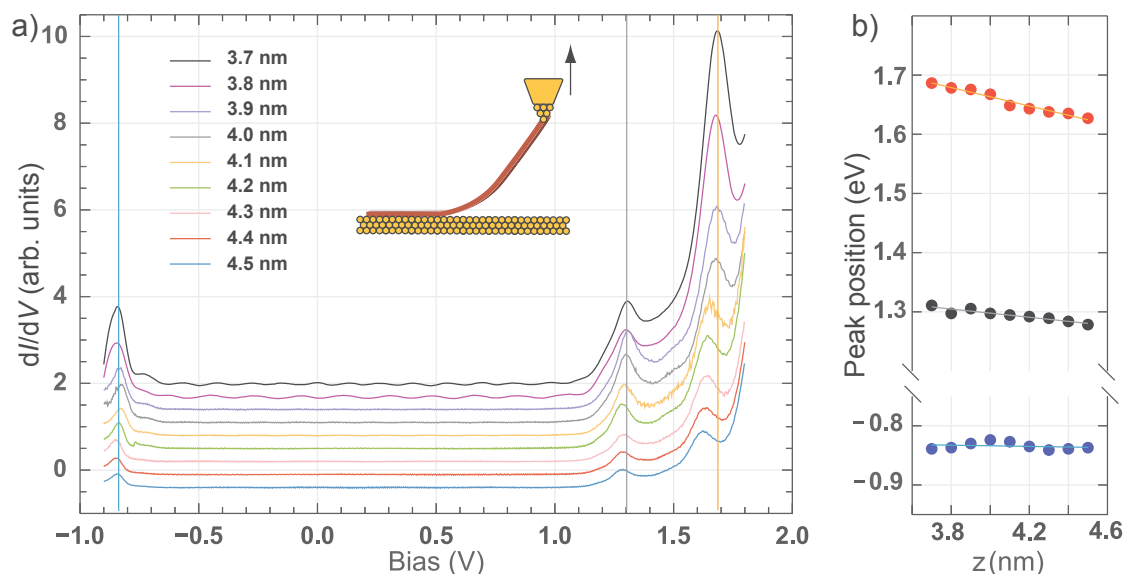


Figure 4.8 – Differential conductance as a function of the tip-sample separation. (a) dI/dV curves of the lifted GNR (configuration in inset), for different tip-sample separations. The dashed vertical lines indicate the energy of the peaks at $z = 3.7$ nm. The curves are vertically offset. (b) Position of the resonances as a function of the tip sample separation (full dots) and linear fit to the data (lines).

Discussion The plots of figure 4.8(a) further illustrate the small impact of the pulled configuration on the differential conductance of GNRs. This indirectly confirms the hypothesis of a voltage drop occurring mostly at the tip-GNR interface.

Interestingly, from the linear fits of figure 4.8(b) we can extrapolate the position of the peaks at $z = 0$ nm. We obtain 1.436 eV for the first resonance and 1.975 eV for the second one. Since the HOMO does not shift, we can deduce the gap at zero tip-sample separation, $\Delta_1 = 2.27$ eV, a value in excellent agreement with the measurements on the GNR laying flat on the surface.

Several parameters may play a role in the small shift of the unoccupied states, such as a change in the length of the suspended part of the GNR, a small variation of the voltage drop repartition, a smaller impact of the substrate on the molecular orbitals or a Stark shift induced by the strong electrostatic field in the junction.

4.3.3 Tamm state

Finite size armchair GNRs have zigzag edges on the short sides (figure 4.9(a)). The arrangement of the carbon atoms gives rise to a localized edge state with an energy close to the Fermi level for GNR/Au(111).

Also called Tamm states, these resonances were predicted [170, 43, 62] and observed

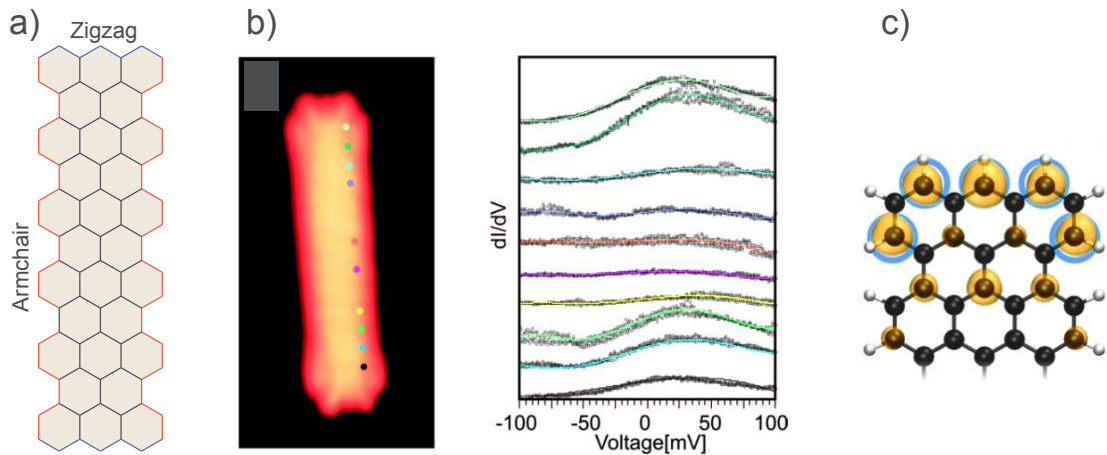


Figure 4.9 – Tamm states of C-terminated ribbons. (a) Sketch of a finite size 7-AGNR. The short edges are of the zigzag type. (b) STM topography of GNR on Au(111) and corresponding dI/dV spectra on the positions indicated by the colored dots. Adapted from [43]. (c) Constant-density isosurface based on a DFT calculation of the 7-AGNR illustrating the localization of a Tamm state at a GNR terminus. The carbons with the highest weight of the Tamm state are circled in blue. Adapted from [62].

for GNRs laying flat on surfaces [171, 43, 168]. An example of dI/dV measurements demonstrating the presence of Tamm states, and their localization close the ribbon termini, is presented in figure 4.9(b). A constant density isosurface based on DFT calculations of the 7-AGNR in vacuum, is presented in figure 4.9(c). It shows that the Tamm state is mostly localized on five carbon atoms of the GNR terminus.

In figure 4.10(a) a series of dI/dV spectra acquired with a suspended GNR for different tip-sample separations is presented. The figure illustrates the presence of a Tamm state in the lifted configuration close to the Fermi level. The intensity of the signal decreases as the separation increases, because of the reduction of the current. In figure 4.10(b) the same spectra are presented in logarithmic scale. From this figure we observe that the Tamm state is not affected by the tip-surface distance. However, due to the reduction of the current intensity, for separations above 2.7 nm the signal becomes too weak to be measured.

Discussion We note that the Tamm state was not reported on previous experiments with lifted ribbons [43]. We remark a small difference (≤ 50 meV) in the energy of the Tamm state, as compared to measurements for GNRs laying on the Au(111) surface [43, 62, 168]. This small discrepancy might be related to the tip-GNR contact. The presence of the Tamm state in the lifted configuration is especially relevant for us since, as we will discuss later in this chapter, it may play a key role in the generation of luminescence from GNRs.

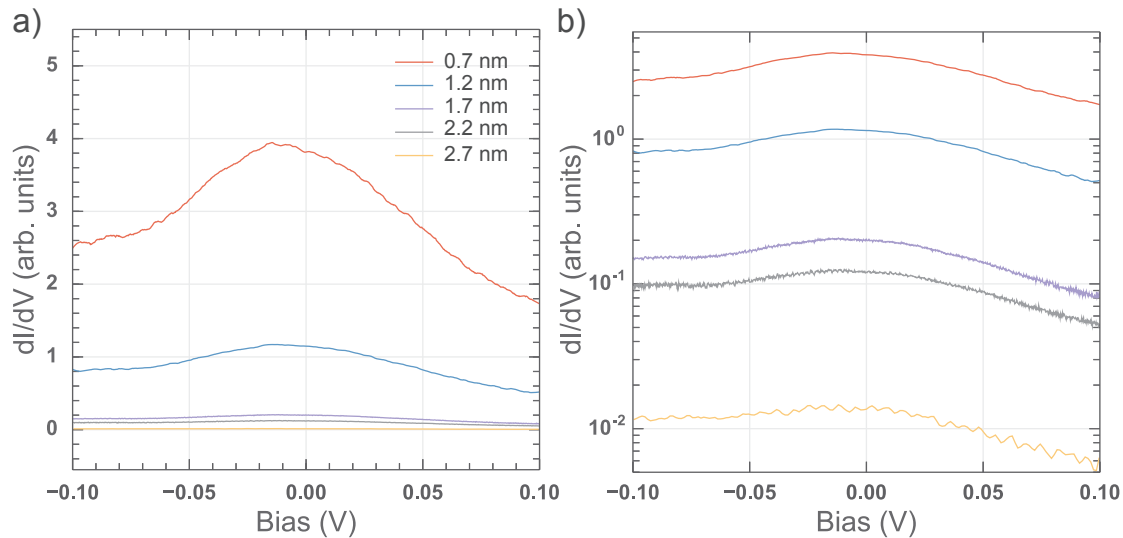


Figure 4.10 – Tamm states C-terminated ribbons in the lifted configuration. (a) dI/dV curves for different tip sample separations. (b) Same curves as in (a), logarithmic scale. Because of the weak signal, the curves acquired at z of 2.2 nm and of 2.7 nm were smoothed.

4.3.4 Conclusion

In the first part of this chapter, we reported on transport measurements through individual, H terminated, 7-AGNRs lifted in an STM junction.

Our data confirmed the quasi-frictionless sliding of the ribbons on the Au(111) surface that was observed in [63], a behavior that contrasts with similar experiments performed on other molecular wires [42, 41]. This is likely due to the low chemical interaction between the GNR and the Au(111).

The dI/dV spectrum in lifted geometry closely resembles the one of 7-AGNRs laying flat on the sample. This observation is explained by the voltage dropping mostly at the tip-GNR interface. This is further supported by the small impact of the tip-sample separation in the lifted configuration on the energy of the states.

The main effect of the tip-GNR contact is observed in the width of the resonances, that is reduced ($\text{FWHM} \approx 50$ meV) with respect to the flat lying configuration. This suggests that the lifted GNRs are partially decoupled from the electrodes. All the other characteristics of the ribbons are preserved in this configuration, including the size of the gap and the presence of the Tamm state.

We have now the essential information required for the study of the optical properties of the GNR junctions.

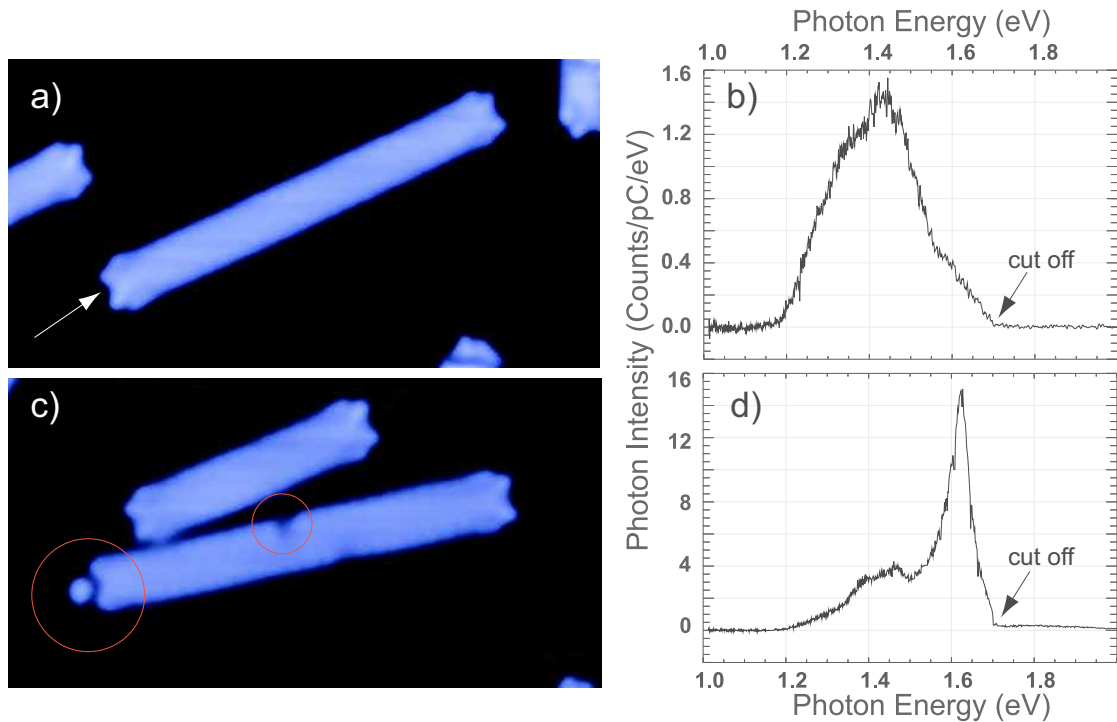


Figure 4.11 – First evidence of STM-LE from GNRs. STM topography of a GNR before a lifting experiment (a) ($15.2 \times 7.4 \text{ nm}^2$; $V = 0.05 \text{ V}$, $I = 0.1 \text{ nA}$). The lifting position is marked by a white arrow in (a). Electroluminescence of the suspended GNR right after lifting (b) and after a switch in the current (d). ($V = 1.7 \text{ V}$, $z = 3.2 \text{ nm}$, $I = 23 \text{ nA}$ for (b) and $I = 21 \text{ nA}$ for (d)). The STM image in (c) was acquired on the same wire after the acquisition of the optical spectra and the release from the STM tip. The changes in the topography are marked by red circles in (c).

4.4 Light emission from 7-AGNR

This section is dedicated to STM-induced light emission measurements of suspended 7-AGNRs.

In figure 4.11(a) the STM topography of a GNR with two H-terminated termini is shown. The GNR was lifted from the terminus indicated by a white arrow. In figure 4.11(b) the light emission obtained from the lifted GNR is presented. The spectrum appears broad and mainly featureless. It is peaked around 1.4 eV.

While performing the measurement, a small sudden switch in the tunneling current occurred. In figure 4.11(d) we show the light emission measured right after the switch. There is now a sharper peak at 1.6 eV followed by a lower energy feature. Moreover, the intensity of the spectrum is one order of magnitude higher than before the switch. Figure 4.11(c) is a topography of the GNR once it is released on the surface. The

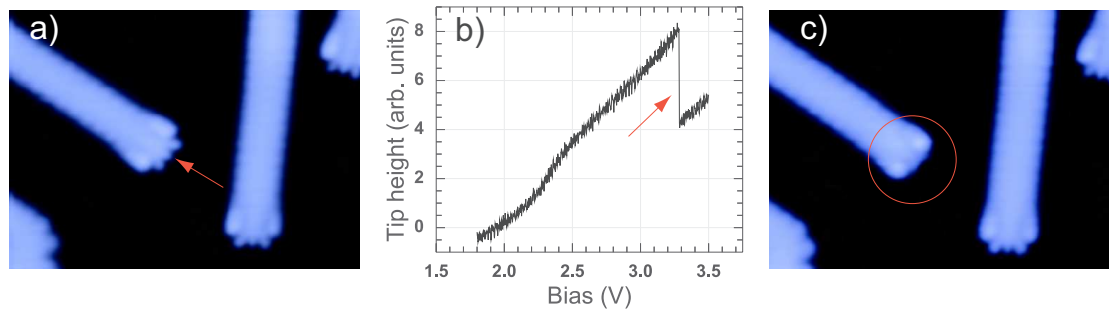


Figure 4.12 – Controlled generation of C-terminated ribbons. (a) STM topography of H-terminated GNRs ($10.0 \times 7.4 \text{ nm}^2$; $V = 0.05 \text{ V}$, $I = 0.1 \text{ nA}$). The position of the tip for hydrogen removal is marked with an arrow. (b) Tip-sample separation as a function of the voltage bias in constant current mode ($I = 0.1 \text{ nA}$). The arrow indicates a discontinuity. (c) a) STM topography of the same GNRs of (a). The red circle highlights the change in the terminus of a ribbon.

image reveals the presence of defects in the ribbon structure, that are highlighted with a red circle. The image shows a dark spot approximately in the middle of one of the long edges of the GNR. It also shows a modification of the extremity used to lift the ribbon: the “finger” structure characterizing the H-terminated ribbons is replaced by a bright circular spot. We remark that the circular spot appears disconnected from the GNR. Also, the GNR appears in a different position with respect to other objects on the surface than before the lifting.

The behavior reported here has been reproduced several times. The abrupt current changes are generally rather small in intensity (1% to 10% of the total current), but occasionally can be up to one order of magnitude. The energy of the intense feature in the optical spectra is of $(1.61 \pm 0.04) \text{ eV}$ at $V = 1.7 \text{ V}$, and its width varies from 30 meV to 100 meV.

We point out that, in some cases yielding the sharp peak, the position and number of side defects could vary; in some situations no defects on the armchair edge were detected after releasing the GNR, but the defect at the ribbon end was always present. Concerning the defect at the terminus, a close inspection reveals a similarity with a C-terminated GNR (figure 4.2) with a bright spot close to it. The spot may possibly be a gold atom detached from the tip when GNR was released.

We will now try to verify if the modification of the emission is linked to the defects.

4.4.1 Generation of C-terminated ribbons

In order to understand the origin of the peak presented in figure 4.11(d) and to distinguish the relative influence of the edge and termini defects, we tried to *controllably*

generate the defects on the GNR (figure 4.11(c)). Since we remarked that after releasing the ribbon, its terminus resembled a C-terminus we artificially created them. To do this, we positioned the tip on top of the central carbon of the H-terminus, the position indicated by an arrow in figure 4.12(a), and we performed a voltage ramp at constant current. By monitoring the tip-sample separation during the ramp (figure 4.12(b)) we can detect a discontinuity in the process. The STM topography after the ramp, presented in figure 4.12(c), confirms the transformation of the edge, which now resembles the one of a C-terminated ribbon described in figure 4.2.

We demonstrated here that it is possible to dehydrogenate the central carbon atom of the zigzag edge of a 7-AGNR. It is then possible to transform H-terminated ribbons in C-terminated ones. The same result was obtained in [168] by the application of localized voltage pulses. The method we used presents a high rate of success. We tried this procedure on other places of the ribbon, like the long edge, but the rate of defects was extremely low. The average bias needed to transform the terminus, as determined by the position of the discontinuity in tip-sample separation during the voltage ramp, is 3.4 V.

4.4.2 Effect of the terminus on the light emission properties

In the previous section we established a method to obtain C-terminated GNRs from H-terminated ones. We now turn to the comparison of the electroluminescence spectra of the two types of ribbons.

In figure 4.13(a) the topography of an H-terminated GNR is presented. We lifted the ribbon and measured its electroluminescence spectrum, which is presented in figure 4.13(b). We observe once again a broad, featureless emission centered around 1.4 eV. We then released the undefected GNR on the surface and on this same ribbon we removed the central hydrogen from the zigzag edge to obtain a C-terminated ribbon (figure 4.13(c)) as described before. We then grab the ribbon from this extremity, lift it and measure its electroluminescence spectrum for the same voltage bias and same tip-sample separation used previously for the H-terminated ribbon ($V = 1.8\text{V}$, $z = 3.2\text{ nm}$). The spectrum is presented in figure 4.13(d). We observe a drastic change of the spectrum shape, which now resembles the spectrum presented in figure 4.11(d), with a peak at 1.6 eV and some lower energy features. Comparing the photon intensities (normalized by the current) in (b) and (d), the emission efficiency is approximately one order of magnitude higher for the C-terminated ribbon. Lastly, we released the GNR on the surface. The topography of figure 4.13e shows the C-terminated ribbon with a the circular spot close to it.

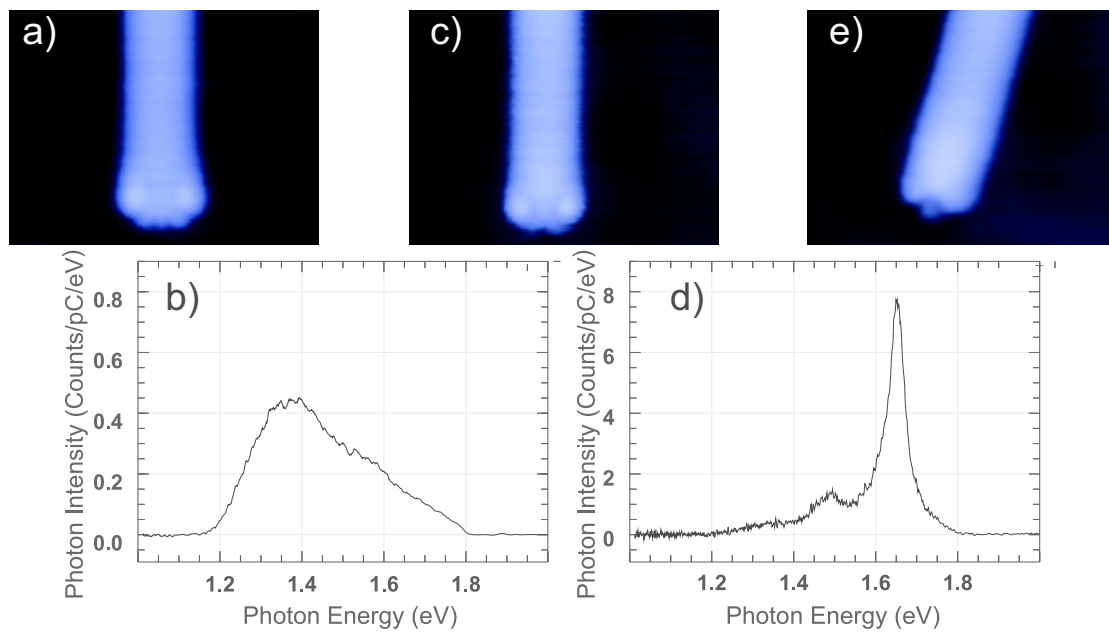


Figure 4.13 – Controlled transformation of a ribbon terminus and impact on its optical spectrum. (a) STM topography of a H-terminated ribbon. (b) Light emission spectra of the suspended H-terminated GNR ($z = 3.2$ nm, $I = 14.8$ nA, $V = 1.8$ V). (c) STM topography of the GNR after releasing and changing its terminus on the surface. (d) Light emission spectra of the suspended C-terminated GNR ($z = 3.2$ nm, $I = 1.7$ nA, $V = 1.8$ V). (e) STM topography after releasing the C-terminated GNR. Parameters of the topographies: 6.2×4.7 nm²; $V = 0.05$ V, $I = 0.1$ nA

Discussion From the data of figure 4.13 it is clear that the narrow light emission from the suspended GNR is linked to the nature of the terminus. At this stage it is unclear if the presence of the hydrogen on the central carbon changes the optical properties of the GNR or if it simply has an effect on the tip-ribbon bond. It was previously pointed out that the central carbon of the edge in a C-terminated ribbons bends towards the gold substrate [62] and can even form a bond with it [168]. It was also observed that C-terminated ribbons obtained by dehydrogenation cannot be moved laterally [168], as a further indication of a strong interaction with the substrate of these ribbons. In performing the experiment we found that picking up C-terminated GNRs with the STM tip was easier than with the H-terminated ribbons. This possibly indicates an stronger bonding with the gold atoms of the tip. The presence of the bright spot next to the lifting point once the GNR is released (figure 4.11(c) and 4.13(e)) supports this interpretation: a gold atom (or several ones) from the tip is released together with the ribbon.

We also generated side defects on H-terminated GNRs to evaluate their influence on the optical properties of GNRs. However, when we pulled them from the surface it was impossible to lift the GNR high enough to suspend the defect in the junction, making it impossible to study their effect. This suggests that the bond between the side defect and the surface is too strong to be broken while lifting the GNR.

It is anyhow clear, from the measurements reported in this section, that side defects are not necessary to switch from a broad luminescence peak to a narrow one.

4.4.3 STM-LE from C-terminated GNRs

In figure 4.14(a) is presented a well resolved electroluminescence spectrum of a suspended C-terminated GNR. The spectrum shows an intense peak and two weaker resonances. The spectrum is fitted with three Lorentzian curves.

Based on the ensemble of spectra acquired for similar bias and z conditions ($V = 1.7$ V, $3 \leq z \leq 3.5$ nm) the energy of the most intense peak is $E = 1.61 \pm 0.04$ eV. Its full width at half maximum is 40 meV. In figure 4.14(b) the values of Δ_1 and Δ_2 , that represent the energy shifts of the weak peaks with respect to the main one, are plotted for all available measurements. This plot illustrates that the energy shifts are extremely constant for Δ_1 . The number of data points for Δ_2 is however smaller because it was not always possible to resolve the third peak given its low intensity. From the data in the figure we can infer the value of $\Delta_1 = 0.162 \pm 0.015$ eV and $\Delta_2 = 0.31 \pm 0.03$ eV.

Discussion We found a main resonance at an energy of 1.61 eV in the light emission spectrum of C-terminated graphene nanoribbons. We remarked with surprise, that the

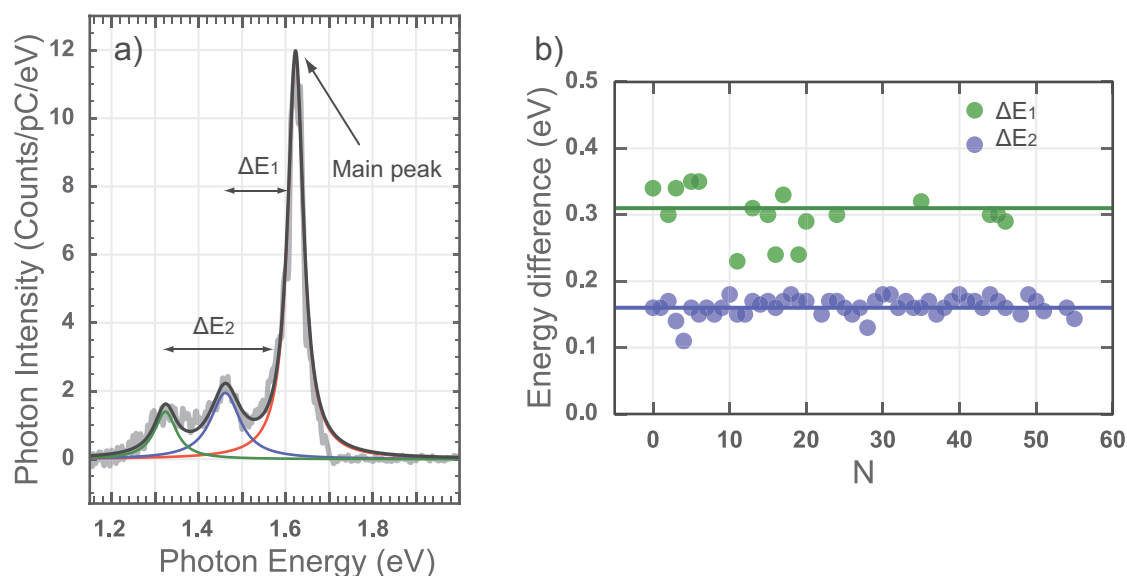


Figure 4.14 – Optical spectra of lifted C-terminated GNRs. (a) Electroluminescence spectrum of a C-terminated GNR ($V = 1.7$ V, $z = 3.2$ nm, $I = 0.4$ nA). (b) Energy gap between the first peak and the vibronic replicas at lower energy.

width of the main peak is almost one order of magnitude smaller than in the case of H-terminated ribbons. It is indeed unexpected to measure a light emission feature as sharp as 40 meV with a system in direct contact with the electrodes [22]. The narrow width of the peak and the reproducibility of its energy point towards an intra-ribbon origin of the emission.

Nevertheless, the width of the main peak is one order of magnitude larger than the one observed in chapter 3 for the fused-porphyrins. This suggests that the system is not so well decoupled.

Assuming the GNR origin of the emission, we need now to understand to which transition it is related to. A previous experimental work, investigating the optical properties of 7-AGNRs through reflectance difference spectroscopy (RDS), indicates the presence of three spectroscopic features at ≈ 1.9 , 2.3 and 4.1 eV [165]. Their result, supported by *ab initio* calculations, indicate that the two low-energy contributions at ≈ 2.0 eV originate from transitions between valence bands and conduction bands of the ribbon, with a large contribution from the excitonic binding energy.

The peak we find is at a lower energy, which suggests another origin for the emission. These aspects will be discussed further in section 4.5.

Two low energy features were also detected, which reveal a close to linear energy dispersion. Due to their low intensity and to the fact that they do not appear if the main emission line is not excited (more on this in section 4.4.5) we tentatively assign them to the vibronic progression of a single mode. Their energy shift is in

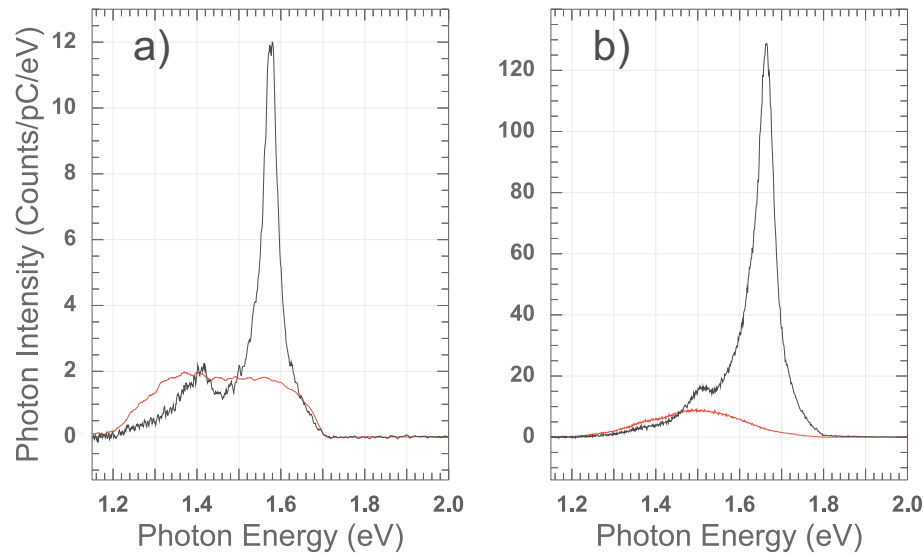


Figure 4.15 – Optical spectra from lifted GNRs and from bare metallic surface. (a) Light emission spectra of a suspended GNR (black curve, $z = 3.4$ nm) and of the plasmon measured with the same tip (red curve). The two spectra were measured in similar conditions ($V = 1.7$ V, $I = 1.1$ nA, $t = 60$ s). (b) Light emission spectra of a suspended GNR (black curve, $z = 3.6$ nm) and of the plasmon measured with the same tip (red curve). The two spectra were measured in similar conditions ($V = 1.8$ V, $I = 13$ nA, $t = 5$ s)

good agreement with the Raman D-peak of graphene ($1340\text{ cm}^{-1} \approx 0.166\text{ eV}$)^[64] and carbon sp^2 materials in general, which is associated to the breathing modes of six-atom rings. It is interesting to note, that to be observable, these modes require some disorder or the presence of defects ^[65]. The D-peak was previously measured and calculated for Raman measurements on GNRs in different configurations ^[60, 66]. Another possible explanation is that the peaks belong to two different modes. In this case, the second peak could be related to the 2D-peak that appears in Raman measurements of graphene and GNRs ($2600\text{ cm}^{-1} \approx 0.32\text{ eV}$). We have no elements to discriminate between the two hypotheses at this stage. In the following we will refer to the two low intensity features as the vibronic resonances.

4.4.4 Quantum yield of the emission

We observed in section 4.4.2 that the light emission from C-terminated ribbons is more intense than in the case of H-terminated ribbons. A way to quantify the light emission intensity is to compare their spectra to the one of the plasmon as measured with the same tip on the pristine junction. In figure 4.15(a) the spectrum of a suspended C-terminated ribbon (black curve) is compared to the plasmon measured on the pristine

junction with the same tip (red curve). The two spectra were measured using identical bias ($V = 1.7$ V), current ($I = 1.1$ nA) and acquisition time ($t = 60$ s) conditions, but with different tip-sample distances. We observe that the spectrum acquired on the ribbon is way more intense at the energy of the main peak than the plasmon. If we compare the intensity of the emitted light for the two spectra over the whole energy range we obtain a ratio of ≈ 1.4 more photons for the GNR. Since the current and bias parameters are the same for the two, this ratio is equivalent to the ratio of the quantum yields in terms of photons per electrons. An estimate for the quantum yield of the GNR is $(1 \pm 0.5) \times 10^{-5}$ photons per electron when corrected for the efficiency of the detection system.

In figure 4.15(b) the data from a similar experiment are reported. We observe that the intensity of the light from the GNR is more intense than in (a). The current passing through the ribbon was of 13 nA, a factor ten more intense compared to the spectrum of (a). In this case, the GNR was severely damaged after the observation of the light emission. In this example, the number of photons emitted by the GNR is 5 times higher than the ones emitted by the pristine junction. The overall efficiency remains the same.

Discussion The two examples presented in figure 4.15 illustrate some remarkable aspects of STM-LE from GNRs:

- First they show that, at identical current and voltage bias conditions, the emission from the ribbons has a higher yield than the plasmonic emission, despite a larger tip-sample distance. We point out that in this experiment the quantum yield is far from optimal for the pristine junction (10^{-3} photons per electron [86, 79]). However, such high photon yield is only detected for $V \geq 3$ V for a gold-gold junction [75], (here $V \leq 2$ V).
- For a similar quantum efficiency, the emission from GNRs occurs at a well defined energy and with a linewidth of 40 meV, as opposed to the plasmonic emission, whose energy is dependent on the local structure of the tip and whose linewidth is in the hundreds of meV range.
- On the lifted GNR we set the tip-sample separation z and the bias V , and measure the current. To measure the plasmon we set the current I and the bias V , and the feedback system regulates the height of the tip. If we try to measure the light emission from the pristine junction at $z \approx 3$ nm, at low bias no signal is detected. This is due to the lack of tunneling electrons at these distances. Moreover, at increased tip-sample distances, the plasmonic amplification of the emission is decreased due to a reduced strength of the LSP modes [13]. The presence of the GNR allow then to measure light at tip-sample separations that are not accessible in usual STM-LE experiments.

- The extreme cases where the emission from GNR is much more intense than the plasmonic one (e.g. figure 4.15(b)), are often associated with high current passing through the GNR ($I \geq 10$ nA). On the one hand, this proves that GNRs can be used with an elevated current. On the other hand, such wires were often heavily damaged once back on the surface. This leaves an open question on the role of side defects in increasing the quantum yield, as the presence of sp^3 defects do in the photoluminescence of carbon nanotubes [172]. A discussion of this topic is beyond the scope of this chapter.

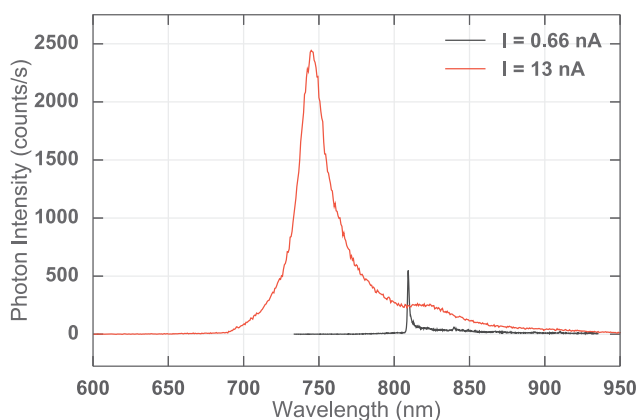


Figure 4.16 – Comparison of the emission intensity for C-terminated GNRs and fused-DPP. Light emission spectra of a suspended GNR (red curve, $t = 10$ s, $I = 13$ nA) and of a fused-DPP (black curve, $t = 60$ s, $I = 0.66$ nA). The two spectra are normalized by the duration of the respective acquisition. The two spectra present a similar photon yield ($\approx 10^{-5}$ photon/electron).

Overall, these aspects of the emission from GNRs show that they are more efficient than pristine gold junctions at generating an emission of light at low voltage bias, and that the emission has well defined and reproducible properties. Similar yields were found in the case of emission from fused-porphyrins that we presented in chapter 3. However, GNRs offer the possibility to use much larger currents, resulting in an larger absolute intensity of the emission (an example is provided in figure 4.16).

4.4.5 Shift of the spectral features with voltage

This section is dedicated to the study of the emission as a function of the applied voltage.

In figure 4.17(a) the light emission spectrum of a pulled C-terminated GNR is presented. The main peak and the first vibronic one appear at 1.65 eV and at 1.49 eV respectively. The spectrum belongs to a series of spectra acquired on the same ribbon at a given

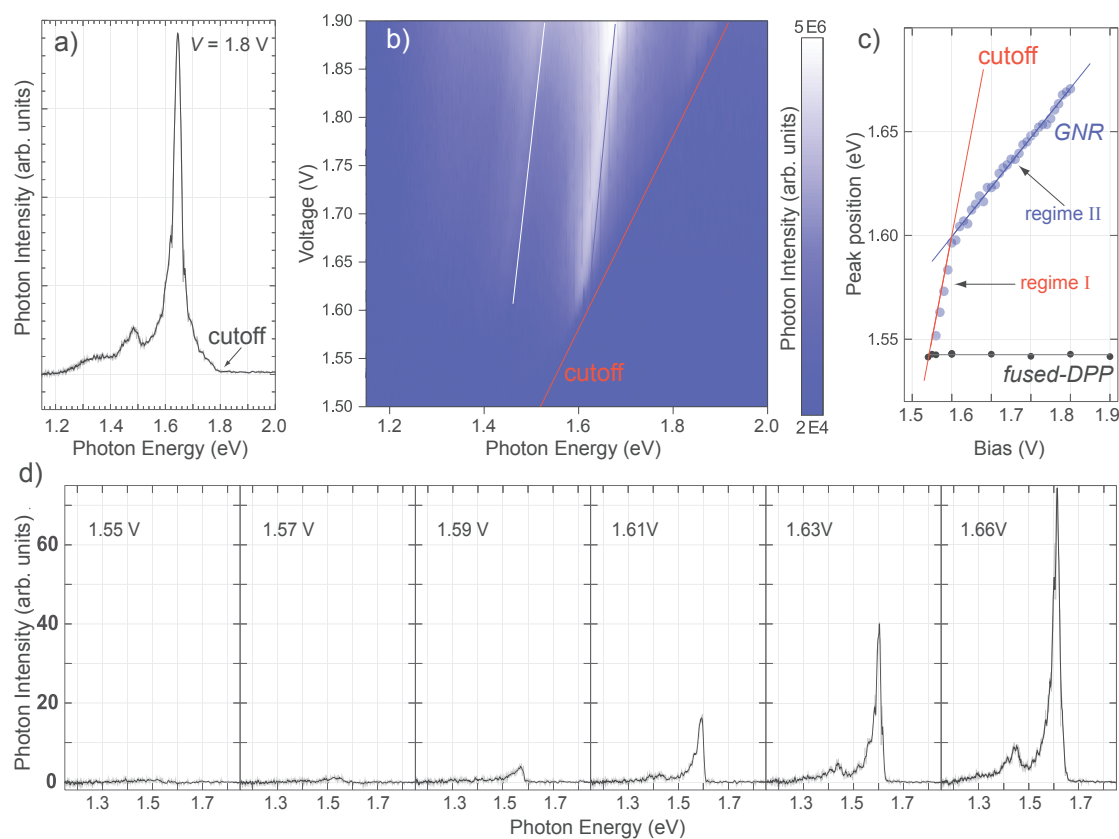


Figure 4.17 – Dependency of the light emission with the voltage bias. (a) Electroluminescence spectrum of a suspended C-terminated GNR ($z = 3.2$ nm, $V = 1.8$ V, $I = 3.7$ nA, $t = 18$ s). (b) Map of the photon intensity (logarithmic scale) as a function of the photon energy and of the applied bias for a suspended GNR ($z = 3.2$ nm, $t = 18$ s each spectrum.). The spectrum in (a) corresponds to the slice at $V = 1.8$ V. The cutoff line ($h\nu = eV$) is marked in red. Two pale dashed lines are used as guides for the position of the main peak and the first vibronic resonances. (c) Position of the main peak as a function of the bias (blue dots). The pale blue line is a linear fit. The red dashed line is the cutoff. The behavior of fused-DPP is shown for comparison (black dots). (d) Spectra belonging to the series of (b). They correspond to biases close to the onset of the main emission line.

tip-sample separation ($z = 3.2$ nm). The whole set of spectra is presented in figure 4.17(b) in the form of a heatmap, where the photon intensity (in logarithmic color scale) is mapped as a function of the photon energy (abscissa) and of the applied bias (ordinate). The spectrum of (a) corresponds to an horizontal slice of the heat map. In figure 4.17(c), the position of the main peak maximum is plotted as a function of the bias (blue dots). Finally, in (d), a set of spectra belonging to the series in (b) are presented ($V = 1.55$ V to 1.66 V).

Onset of the emission. From figure 4.17(b) we notice that, as expected, no light is observed above the quantum cutoff ($h\nu = eV$, indicated with a red line). Interestingly, due to the width of the main emission line (≈ 40 meV), it is possible to observe the impact of the cutoff on the onset of the peak. This is apparent in figure 4.17(d). Here, we observe that below $V = 1.57$ V, no light is detected. Then, the bias is progressively increased, the main peak appears. Its shape is affected by the quantum cutoff, resulting in an asymmetric lineshape, with a sharp edge on the high energy side. Eventually, when the bias is increased more, the main peak is fully observable and appears nearly symmetric (e.g. spectrum at $V = 1.66$ V). This behavior defines a regime (I) where the apparent maximum of the peak follows the cutoff line, as can be seen in (c).

We remark that the onset of the emission occurs at a voltage bias corresponding to the emission energy. As we discussed in chapter 2.2.5, and as we observed for fused-porphyrins in chapter 3.3.6, this is an indication of a plasmon mediated excitation. A more detailed discussion of the mechanism will be given in a later section of this chapter.

Shift at higher voltage bias From figure 4.17(b) and (c), we remark that above $V = 1.6$ V (regime II), the maximum of the main peak shifts, but not as fast as in regime I.

We stress that no STM-LE experiment on a single molecule ever reported such a large shift of the fluorescence with the bias V . An ideal two level system is expected to emit at the energy of its gap, which is independent of the applied bias. Fused-DPP (c.f. chapter 3) represents an example of this behavior, as it is illustrated in figure 4.17(c) (black circles). There, we observe that the energy of the light emission peak does not shift as the bias is increased.

We propose two possible explanations for the large shift in the case of GNRs:

1. The energy of the two molecular states involved in the optical transition are affected differently by the applied voltage. We speculate that this might be the case if the spatial localisation/extension of the two states is different.

2. In an alternative interpretation, the strong electric field generated by the bias ($E \approx 10^4$ keV/m) may affect the emission energy *via* Stark effect. For small variations of the applied voltage, the variation of the electric field is linear with V ($\Delta E \propto \Delta V$).

The linear shift of the emission peak with V suggests that high order components of the Stark effect are absent or of extremely low intensity. A linear Stark shift implies the presence of an effective dipole in the molecular junction [173, 174, 175]. This can be either an intrinsic molecular dipole, or a dipole induced by the environment [173, 176].

In this picture, the intensity of the linear Stark shift would be ≈ 60 GHz/MV/m. This value is one order of magnitude larger than the one found in experiments on dye molecules embedded in polymeric matrices *e.g.* in [173]. However, similarly large linear Stark shifts were observed in photoluminescence experiments on conjugated polymers [176]. In this last example mechanical strain on the polymer was proposed as possible origin of the effective dipole. In our experiment the dipole may be due to charge reorganisation at the tip-GNR and substrate-GNR interfaces, a frequently observed behavior for carbon materials on noble metals [177].

Optical transition of the unperturbed system. We remark that, in our setup, the voltage bias has two simultaneous effects.

First, it is the source of the light emission (either through a plasmon mediated mechanism or through hot electron injection). Second, it is at the origin of the energy shift. This is strikingly different from photoluminescence experiments, where the source of the excitation (typically a laser) and the source of the shift (a controllable electric field) are separated and can act independently.

As a consequence, in our setup, we do not have a direct access to the emission of the unperturbed system (without shift). However, from the linear fit of the position of the peak (blue line in figure 4.17(c)), we can extrapolate the energy of the maximum at zero applied bias²: $E(V = 0) = (1.16 \pm 0.08)$ eV.

We stress that this energy value is extremely low compared to both the STS gap (≈ 2.3 eV) and the optical resonances measured in by reflectance difference spectroscopy [165], that we discussed previously (≈ 1.9 and 2.3 eV). Since no interband transition is known at such a low energy for 7-AGNRs, it is tempting to consider the influence of the Tamm state that is measured by STS “in” the electronic gap.

Remark on the vibronic peak. From figure 4.17(b) we observe that the maximum of the vibronic peak shifts in parallel with the main peak (*i.e.* ΔE is constant). Finally, an attentive observation of (b) and (d), shows that the vibronic resonance only appears

²The experiment reported in figure 4.17 was reproduced on several GNRs and the result of the extrapolations was averaged.

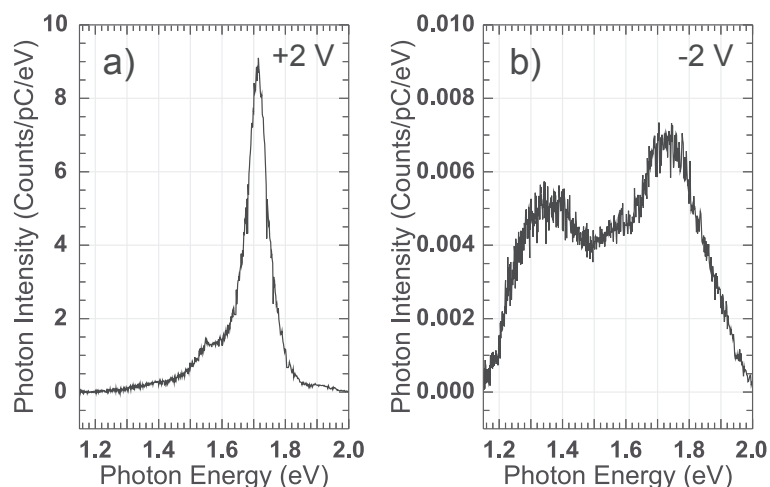


Figure 4.18 – Optical spectra from GNR at positive and negative polarities. (a) STM-LE on C-terminated GNR in pulled configuration at positive bias ($V = 2$ V, $z = 3.2$ nm, $t = 10$ s, $I = 30$ nA). (b) STM-LE on the same GNR at negative bias ($V = -2$ V, $z = 3.2$ nm, $t = 180$ s, $I = 270$ nA).

once the voltage is high enough to excite the main peak. These two observations indicate that this peak is not related to an independent electronic transition, thus confirming its vibronic nature.

The presence of vibronic replicas is another important evidence of the intra-ribbon origin of the emission.

4.4.6 Negative bias

In figure 4.18 the spectra obtained on a GNR at positive (a) and negative (b) bias with otherwise same conditions, are presented. We observe that the spectrum at negative bias does not present the structure that appears at positive bias. We observe also that the intensity is roughly 1000 times lower. The faint emission was obtained over a three minute acquisition with a current of 270 nA passing through the GNR. This behavior is different from the one of fused porphyrins that we studied in 3. In that case the peak was detectable also at negative bias, although with an extremely reduced intensity.

This data can be understood in the scheme of the voltage-induced peak shift. If we extrapolate the position of the main peak at a negative bias of $V = -2$ V, we obtain a value of ≈ 0.6 eV. Such a value is outside of the range of sensibility of the CCD camera, making the peak undetectable.

In the frame of an electron-hole injection model (*c.f.* chapter 2.2.5), the absence of the peak at negative voltage may also be explained by a bad alignment of the electronic levels with respect to the Fermi level of the electrodes [22, 67].

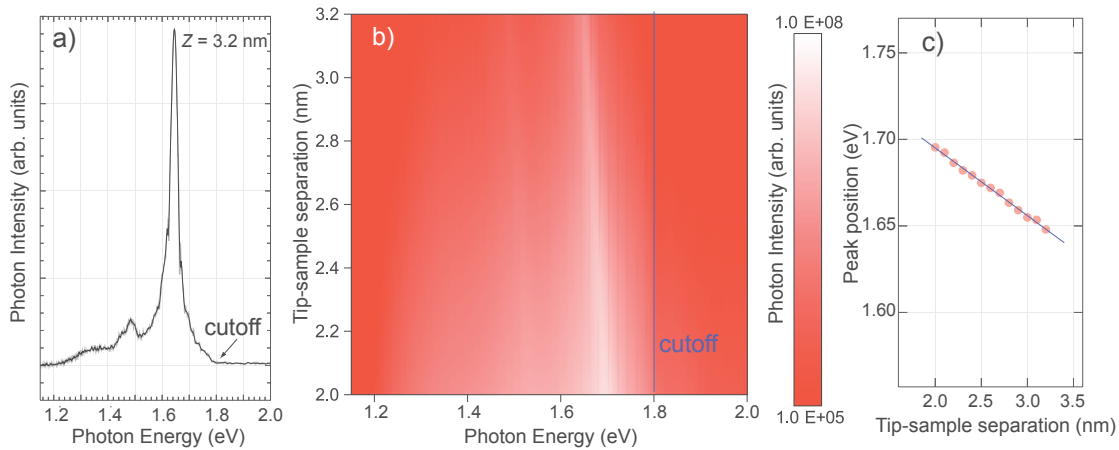


Figure 4.19 – Dependency of the light emission with the tip-sample separation. (a) Electroluminescence spectra of a suspended C-terminated GNR ($z = 3.2$ nm, $V = 1.8$ V, $I = 3.7$ nA, $t = 18$ s). (b) Map of the photon intensity (logarithmic scale) as a function of photon energy and the tip-sample separation for a suspended GNR ($V = 1.8$ V, $t = 18$ s each spectrum.). The spectrum in (a) corresponds to the slice at $z = 3.2$ nm. The cutoff line ($h\nu = 1.8$ eV) is marked in blue. (c) Position of the main peak as a function of the tip-sample separation (red dots). The blue line is a linear fit.

4.4.7 Dependency of the emission energy with z

We turn now to the study of the light emission as a function of the tip-sample separation. The experiment is performed at constant bias ($V = 1.8$ V), on the same GNR used for the study of the bias dependency (section 4.4.5). Alike measurements were performed on other specimens with similar results.

In figure 4.19 (a) we observe a light emission spectrum obtained at $z = 3.2$ nm. The main emission line as well as the first vibronic resonance are observed. The spectrum belongs to a series in which the tip was gradually approached to the surface while measuring the light emission. The ensemble of spectra is presented in (b) in the form of a heatmap, where the photon intensity (in logarithmic color scale) is mapped as a function of the photon energy (abscissa) and of the tip-sample separation (ordinate). The spectrum presented in (a) thus corresponds to an horizontal slice of the map. In the heatmap the quantum cutoff ($h\nu = eV$) is marked by a blue vertical line.

We remark that, for low tip-sample separations (bottom of the heat map) a larger emission intensity is observed, which is due to an increase of the current at lower z values. Normalizing the map by the current would remove this effect but would also add noise to the map, making it more difficult to read. The increase in current explains also why the data stop at $z = 2$ nm: when the tip is approached more to the surface at

high bias, the elevated current results in the detachment of the GNR from the tip.

Shift of the peaks with z . In the heat map two white linear regions may be distinguished, which correspond to the main peak and the first vibronic resonance. The two shift towards higher energies when the distance is decreased (bottom of the heat map). The shift with z is the same for the two peaks (*i.e.* ΔE is constant with z). In the explored range of z , the shift is linear, as can be seen in (c) where the position of the maximum of the peak is plotted as a function of the distance (red dots). In this z range, the shift of the position of the peak is of ≈ 44 meV/nm.

When analysing the shift with the voltage bias (section 4.4.5) we proposed two interpretations, a relative shift of the states involved in the transition or a Stark shift. In the following we discuss how the two hypothesis compare with the data of figure 4.19.

- We start with the Stark shift interpretation. We note that an increase in the tip-sample separation reduces the electrostatic field in the junction. According to the voltage dependency of the emission energy, such a reduction of the electrostatic field results in a shift of the main emission line towards lower energies. This is exactly what is observed in figure 4.19(b).

In a crude approximation of the junction as a two parallel plates (tip and sample) we would expect a $F \propto 1/z$ dependency. This should result in an hyperbolic shift of the maximum with z , which disagrees with the data of figure 4.19(c). However, the relation between electrostatic field and distance, in an STM, is not simply inversely proportional as was previously pointed out [178]. Moreover, the presence of the molecule in contact with the electrodes makes the situation more complex³. Consequently, a precise dependency of the electrostatic field with z cannot be calculated in a simple way in our situation.

The fact that the direction of the shift is in agreement with a reduction of the field with the distance seems to confirm the Stark effect.

We point out that here, an extrapolation of the peak position is meaningless: for $z \rightarrow 0$, the GNR is no more lifted and the calculation of the electric field is even less accurate. We can extrapolate the peak position for increasing values of z and reach a peak position of 0 eV at $z \approx 40$ nm. Not only we have no way to test this, but we are unable to give any physical meaning of this extrapolation. However, since an increased value of z reduces the electrostatic field, we can consider the expected value of the resonance at zero bias (1.16 eV).

From the analysis of this two extreme cases we can infer that even if we observe a linear shift for $2 \leq z \leq 3.2$ nm, the behavior on a larger z range must be

³One might wonder what is the effective electric field repartition, or how does the charge transfer and image charge at the GNR-electrode interface affect the optoelectronic properties of the junction.

non linear. However, observing this experimentally is challenging. For small z values, the increase in current results in detachment of the GNR from the tip or in damages to the ribbon. For high z values, we are limited either by the length of the GNRs or by a too low current that results in an undetectable light emission.

- Let us now turn to the interpretation involving a relative shift of two electronic levels involved in the optical transition, caused by the voltage bias. We suggested that one state may experience a different shift with respect to the Fermi level of the tip, than the other. In this hypothesis, also the increased lifting might affect the two states in a different manner. This may be due to a variation of the voltage drop repartition caused by a larger part of the GNR being suspended in the junction.

Overall, this experiment shows that the tip-sample separation z , impacts the optical emission, by shifting its energy. The induced shift is linear in the range we could explore. However, considerations on the limits for $z \rightarrow 0$ and for $z \rightarrow \infty$, indicate that a non linear behavior should be expected for larger variations of the distance. The shift of the peaks with z is compatible with the observed shift as a function of the voltage bias that was discussed in section 4.4.5, and with both interpretations on its nature.

4.4.8 STS on C-terminated GNRs

In section 4.3 we studied the electronic properties of H-terminated GNRs and we concluded that the dI/dV spectra in pulling configuration strongly resemble those for GNRs laying flat on the surface, in agreement with results found in the literature. A very weak shift of the states at positive bias was observed. We also observed the presence of a Tamm state, related to the zigzag termini of the ribbon, in the pulled configuration. Overall, that study confirmed that the voltage drops mostly at the tip-GNR interface.

By studying the light emission properties of the ribbons, in section 4.4.2, we observed a strong difference in the optical spectra of H-terminated and C-terminated ribbons. As a consequence of this observed difference, we now turn to the comparison of their differential conductance spectra.

In figure 4.20(a), the dI/dV spectrum of a suspended C-terminated GNR (black curve) is presented. As a reference the spectrum of an H-terminated one acquired in similar conditions is presented in red. We observe that the overall shape is similar. The main difference is in the energy of the first resonance at positive bias. It appears at a slightly higher energy (1.43 eV) in the case of C-terminated ribbons. The resonance at negative bias appears at $V = -0.83$ V for both C and H-terminated GNRs.

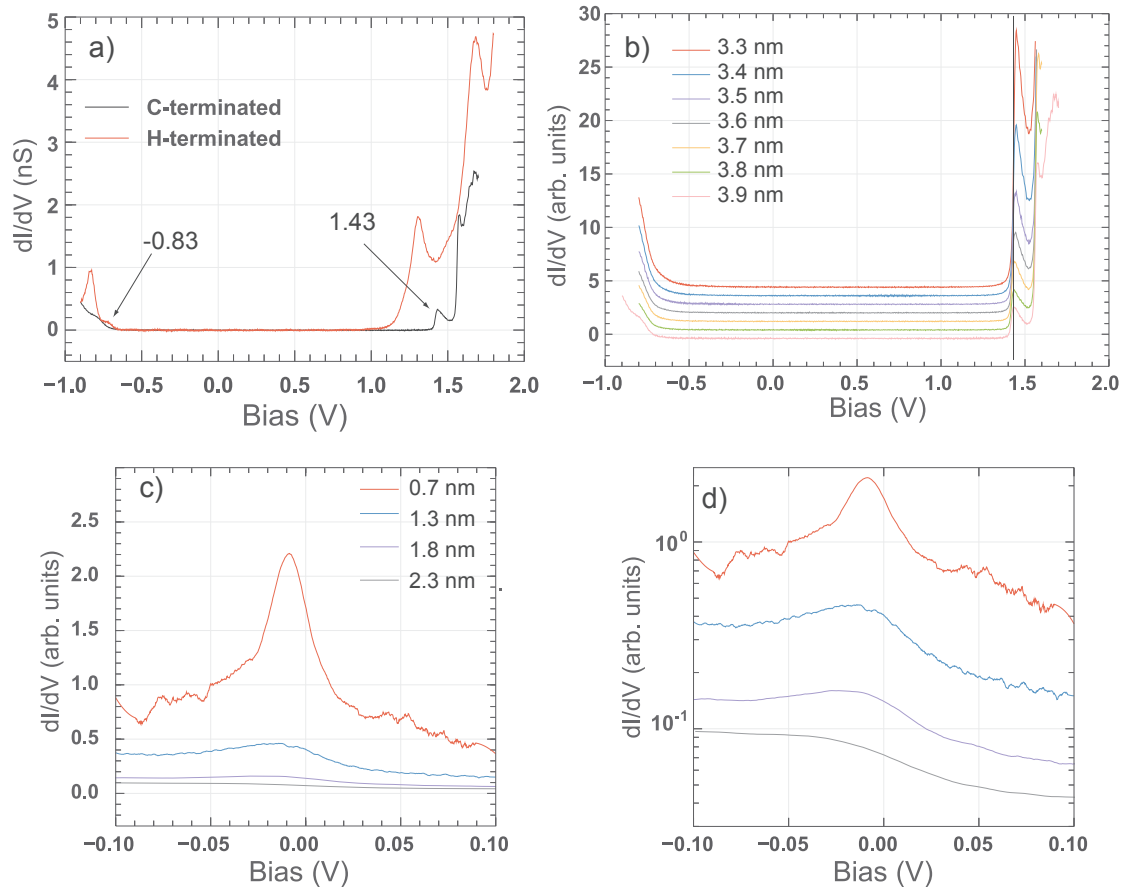


Figure 4.20 – dI/dV spectra of C-terminated GNRs. (a) dI/dV spectra of C-terminated (black curve) and H-terminated (red curve) GNR in lifted configuration ($z = 3.9$ nm). (b) dI/dV spectra of C-terminated ribbons as a function of the tip-sample separation. (c), (d) Tamm state of C-terminated ribbons. (c) dI/dV curves for different tip-sample separations close to the Fermi energy. (d) Same curves as in (c), logarithmic scale. All curves were smoothed.

In figure 4.20(b), a series of STS spectra obtained on the same GNR at different tip-sample separations is presented. In the observed z range the resonance at negative bias appears to have a constant onset. The one at positive bias presents a small linear shift towards smaller energies when increasing z (≈ 20 meV/nm). We remark that the shift is less intense than in the case of H-terminated ribbons. If we extrapolate the shift to $z = 0$ nm we obtain a gap of 2.36 eV (compared to 2.27 eV for C-terminated GNRs).

In figure 4.20(c) a series of spectra recorded on the same ribbon for voltages close to the Fermi level show the presence of the Tamm state. As the intensity of the signal decreases strongly with increasing z , the same spectra are presented in (d) in logarithmic scale. We observe that the Tamm state appears as a sharp peak (≈ 20 meV of FWHM) that broadens as we increase the tip-sample separation.

Discussion The comparison of the dI/dV spectra suggests that only minor differences exist between the electronic transport properties of the two types of ribbons, except for the gap that opens slightly in the C-terminated ones.

The difference between the two types of GNRs lies in the presence of one hydrogen atom passivating the central carbon of the zigzag edge. On the Au(111) surface, C- and H-terminated ribbons are nearly equivalent, with only a modification of the shape of the Tamm state of the terminus [168]. This seems to be the case as well in the pulled geometry.

The strong similarity between the dI/dV spectra indicates that the voltage drops at the tip-GNR interface for the C-terminated ribbon as well. It also shows that the electronic structure is only slightly affected by the difference in the structure of the ribbons. Eventually, we remark that, albeit they go in the same direction (reduction of the gap with increased tip-sample separation), the shift of the LUMO with z (figure 4.20(b)) is a factor two smaller than the shift of the light emission peak (figure 4.19). Thus, we cannot explain the difference in the optical spectra by a change of the electronic structure.

4.5 Origin of the light emission

In this section we discuss the nature and the origin of the electroluminescence observed with the suspended C-terminated 7-AGNR.

The narrow width of the peak (FWHM ≈ 40 meV) and the fact that it occurs always at the same energy, indicates that the emission is intrinsic to the GNR. This is further supported by the observation of vibronic peaks, with energy compatible to vibrations in carbon sp^2 materials [64, 65].

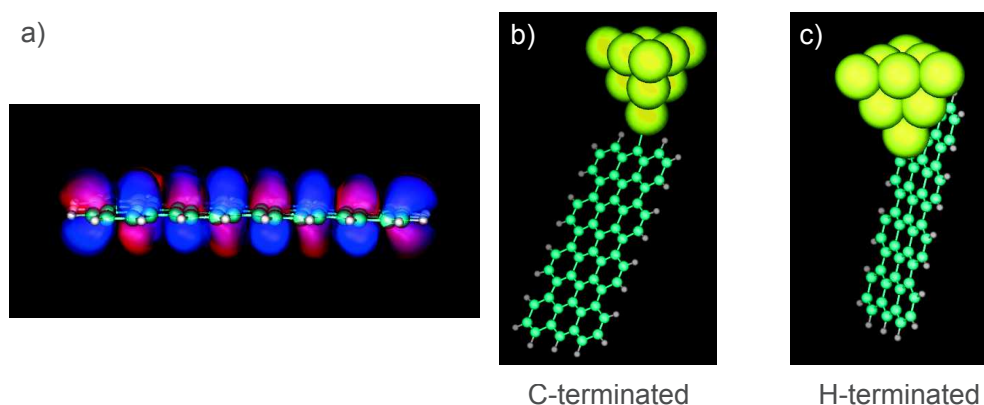


Figure 4.21 – Tip-GNR interaction. (a) Isosurface of the density of state of the LUMO, showing its delocalized nature. Calculated in the DFT approximation. (b) Sketch of possible link between the STM tip and C-terminated GNR, or (c) H-terminated ones.

The need of a state in the gap. The nature of the optical transition responsible for the light emission is however unclear. Indeed, for this type of ribbons, both the calculated optical band gap⁴, and the gap measured via reflectance difference spectroscopy, are in the range of 1.9 – 2.3 eV [165]. In contrast, the experimental value that we observe for the light emission is of $h\nu \approx 1.6$ eV, for a bias $V = 1.6$ V, and can be extrapolated to be of 1.15 eV when no voltage is applied (*c.f.* section 4.4.5). This small value is incompatible with an interband transition of this type of ribbons.

Interestingly, there is a state in the electronic gap of 7-AGNRs: the Tamm states [179, 62]. These states are spatially localized at the zigzag edge of the ribbons. We know that the terminus of the ribbons play a crucial role in the luminescence process. Moreover, despite the contact between the tip and the ribbon extremity, STS measurements show that this state persists in the lifted configuration.

This suggests that the Tamm state may be directly involved in the light emission process. In this hypothesis a radiative transition would occur between this localized edge state and one that is delocalized over the ribbon.

We already pointed out that theoretical calculations⁵ will be required for a definitive interpretation.

⁴The calculations find “optical transitions between the last valence and first conduction bands (E_{11}), and the next to last valence and second conduction bands (E_{22}), respectively” [165].

⁵DFT calculations including GW approximation are ongoing. Ab initio simulations of the configuration of the GNR with respect to the tip might be needed as well.

Coupling with the tip. Because of the direct contact with the electrodes, one would expect to observe a broad emission linewidth, as in the case of oligothiophene wires suspended between the tip and sample of the STM[22]. This is probably what happens for H-terminated ribbons. However, the linewidth of the emission from C-terminated GNRs suggests a better decoupling from the electrodes. This difference between H- and C-terminated ribbons may find its origin in the nature of the link between the tip and the ribbon.

For C-terminated ribbons we have two important evidences that suggest the formation of a C-Au covalent bond:

- For ribbons on the surface it has been shown that, once the hydrogen has been removed, the central carbon atom bends towards the gold atoms of the surface [168, 62]. This indicates a strong attraction of the dehydrogenated ribbon to the gold atoms.
- C-terminated GNR released on the surface after a lifting experiment show a bright protrusion at the wire extremity (*c.f.* section 4.4.2). This corresponds to one (or several) gold atom(s) that is strongly bound to the ribbon. This implies that the GNR-Au bond is stronger than the Au-Au bond, a strong indication of the formation of a covalent bond between the tip and the C-terminated GNR.

For junctions with H-terminated ribbons, the GNR probably lies partially on the side of the tip (figure 4.21(c)). In this case, the tip-molecule “bond” is more likely to be of a van der Waals nature.

A counterintuitive conclusion is that the very strong covalent bond between the tip and the molecule seems to allow a higher degree of decoupling to the GNR than the weaker bond for the H-terminated ribbons. This can be understood if we consider that the optical properties of the GNRs mostly depend on π orbitals, that are perpendicular to the molecular axis, as it can be observed for the example of the LUMO from DFT calculations (figure 4.21(a)). On the basis of geometrical considerations, it appears that the configuration in figure 4.21(b) provides a lower overlap between the tip orbitals and the molecular orbital (π) involved in the luminescence process than in configuration (c). DFT calculations are now required to confirm this interpretation.

Origin of the shift with the bias. The hypothesis of an optical transition between the Tamm state and a delocalized state is compatible with the observed shift of the main emission line with voltage (*c.f.* section 4.4.5).

- In the “Stark effect interpretation”, the linearity of the shift indicates the presence of an effective dipole [173, 176]. The latter could be induced by a partial charge transfer from the tip to the part of the ribbon localized at the interface, similarly

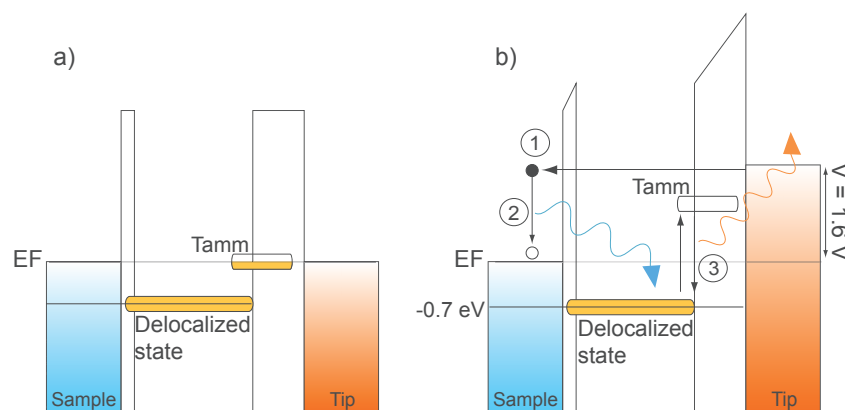


Figure 4.22 – Example of light emission mechanisms involving relative shift of GNR states. (a) Energy diagram of the unbiased junction. A delocalized molecular state is pinned to the sample while the Tamm state is partially pinned to the tip. (b) Energy diagram with $V = 1.6$ V. The plasmon mediated excitation is illustrated (1)(2) and followed by a radiative transition (3) (*c.f.* chapter 2.2.5).

to what happens for C60 on Au(111) [177]. The fact that the energy of the Tamm state is close to the Fermi level of the electrodes may favour this effect. Moreover, being close to the tip, we can naively say that the local electric field is strong independently of the actual geometry of the junction.

- In the other hypothesis, the electronic levels involved in the transition must experience a different shift with V . We know from the HOMO and LUMO positions in the STS data (*c.f.* section 4.4.8), that the voltage drops essentially at the tip-GNR interface. However, the picture might be slightly different for the Tamm state which is localised at the tip-GNR interface. The notion of voltage drop occurring at the interface is indeed a simplified one, and in reality it does not occur punctually, but rather over a small spatial extension near the interface. This implies that the Tamm state might be considered “partially pinned” to the Fermi level of the tip. This would lead to a relative shift of the states with an increased bias. An example of such a shift, leading to a radiative transition between the Tamm state and a delocalized molecular state, is presented in figure 4.22. In this figure, the excitation mechanism is the plasmon mediated one (*c.f.* chapter 2.2.5).

It is important to stress that the conclusions we have drawn in this chapter are still at the stage of a set of hypothesis. Several parts will need to be clarified or confirmed by theoretical simulations:

1. the implication of the Tamm state in the optical transition;

2. the nature of the other level(s) involved in the radiative process;
3. the nature of the bond between the tip and the GNR for the two types of ribbons;
4. the existence of a charge transfer between the tip and molecule, that would support the Stark shift scenario.

4.6 Summary and conclusions

In this chapter we presented a study of the optoelectronic properties of atomically precise 7-AGNR in a lifted configuration. We performed the on-surface synthesis of the ribbons, and showed how to lift them in the STM junction. Then, we measured the electron transport properties of the “GNR junctions”, and observed similar dI/dV spectra as the ones obtained in the tunneling regime for GNRs laying flat on the sample surface.

Here, we found two different luminescence spectra, depending on the chemical nature of the GNR termination used to grab the ribbon with the STM tip. H-terminated ribbons show a broad and featureless spectrum, while C-terminated ones show a narrow (FWHM ≈ 40 meV) emission peak at the energy $h\nu \approx 1.6$ eV, and two vibronic resonances at lower energies. The threshold bias for the emission corresponds to the energy of the light emission itself ($eV = h\nu$), implying a plasmon mediated excitation. Remarkably, the light intensity can be extremely high. This is due to a combination of a good yield (comparable to the plasmonic one in similar, low bias, conditions) and the capacity of the ribbons to sustain elevated currents.

Moreover, the optical transition shows a linear energy shift with the applied bias, as well as with the tip-sample separation. This is possibly due to a Stark effect induced by the electrostatic field in the STM junction, or to a relative shift of the molecular levels involved in the optical transition, induced by the voltage bias. By extrapolating the energy of the main peak at zero applied bias, we deduced that the optical transition, in the unperturbed system, has a value of 1.15 eV. This value is incompatible with the expected optical gap of 7-AGNR (1.9 - 2.3 eV).

These observations motivated the hypothesis that the light emission originates from a transition between a Tamm state of the ribbons and a delocalized state.

The study reported in this chapter was motivated by both fundamental and applicative reasons.

From a fundamental point of view, we aimed to use STM-LE to study the optical properties of individual GNRs. We did not observe a light emission related to the main optical gap of 7-AGNRs. However, we observed an emission of light that is intrinsic to the wire. This will hopefully provide an insight into the existence of radiative transitions that were not considered before. We suggest here an alternative way to study the

optical properties of 7-AGNRs. Recent results show that individual 7-AGNRs can be moved with the tip from a Au(111) sample to a small NaCl island on the Au(111) substrate [155]. The efficient decoupling provided by this substrate [67, 109, 68], may allow measuring the fluorescence of individual GNRs.

Graphene nanoribbons may also appear as appealing candidates for optoelectronic applications based on active nanoscale elements. Our objective here was to combine the impressive mechanical and chemical stability of graphene and its excellent conductance properties with the presence of an optical gap in the ribbons form.

In this framework, we proved that it is possible to obtain a light emitting device based on a single GNR-circuit. This molecular scale optoelectronic component is particularly interesting because (I), it shows an intense light emission and (II) the emission color can be tuned (albeit in a limited range) by changing the length of the suspended ribbon or the voltage applied at its boundaries.

These observations prove the interest in studying GNRs for the realization of future optoelectronic devices.

CHAPTER 5

Conclusion and perspectives

In this manuscript we reported on the study of the optoelectronic properties of molecular junctions performed with a scanning tunneling microscope (STM). The thesis is based on two experimental chapters. Chapter 3 is dedicated to the synthesis and optoelectronic characterization of molecular co-polymer composed of an emitter molecule embedded in a molecular wire. Chapter 4 is a study of the transport and light emission properties of graphene nanoribbons (GNRs).

The common aspects of these two studies are in the synthesis method and in the experimental configuration used to perform the light emission studies. The synthesis of the co-polymers and of the GNRs is done using an on-surface polymerization technique followed by a cyclo-dehydrogenation reaction. In both cases the molecular system is lifted between the tip and the sample of the STM to provide a decoupling from the metallic electrodes.

Aside from these methods in common, the two chapters explore different systems. In the study on GNRs of chapter 4 we make use STM-LE to probe the optical properties of individual ribbons of well defined width and edge topology: 7-AGNRs. We observed this way an intrinsic luminescence from this type of ribbons. This was possible however only when the terminus from which we lift the GNR is de-hydrogenated. Through this observation, and thanks to the energy of the emitted light ((1.61 ± 0.04) eV for a bias $V \leq 1.7$ V), we concluded that: (1) the transition responsible for the light emission involves a Tamm state, which is localised at the terminus of the ribbon, and a delocalized ribbon state. (2) That the link between the tip and the ribbon has a major impact on the emission properties, possibly through a “pinning” of the Tamm state and allowing a charge transfer from the tip to the molecule. These conclusions will need to be validated by a thorough theoretical modelling, which is currently ongoing.

The experimental concept of chapter 3 is a more innovative one. We suspended an emitter between the tip and sample of the STM using organic linkers. These linkers

provide an efficient decoupling of the emitter from the electrodes and allow electronic transport across the junction even for tip-sample separations up to several nanometers. Using this type of molecular junctions we observed the narrowest light emission line ever reported in STM-LE. Besides the main emission line (0-0), we observed two low intensity vibronic sidebands: the R-band and the B-band. The R-band, which appears at the low energy side of the 0-0 line, provides a chemical fingerprint of the emitter. The B-band, which appears on the high energy side of the 0-0 peak, is associated with the emission from nonthermalized molecular excitons. The discussion related to these sidebands led us to considerations on the light emission mechanism and on the complex interaction between the emitter and the localised surface plasmons. In this chapter we also demonstrated a high level of control on the emission properties. This includes the emission energy, which can be adapted by carefully designing the chemical nature of the emitter, and the width of the main emission line, which can be tuned by adjusting the coupling of the emitter with the surface through the position of the STM tip.

A better understanding of the excitation mechanisms. We demonstrated in chapter 3 that the excitation mechanism of the fused-porphyrins is due to an energy transfer mediated by the localised surface plasmons. It is the first time that this mechanism is proposed at the level of a single molecule emitter. One might wonder if the unusual lifted configuration that we use is responsible for this difference with respect to previous experiments, in which an electron injection mechanism was always considered [7, 14, 8].

Very recent works by Imada *et al.* help answering this question: by exciting the STM-LE of phtalocyanines lying flat on a NaCl/Ag(111) with the tip not directly above the molecules, they proved the validity of the plasmon mediated mechanism [109, 68]. This shows the generality of this mechanism, independently of the lifted/lying flat configuration.

It is therefore natural to ask whether such mechanism plays a role in *all* the experiments on single molecules. In particular it would be useful to analyse the original paper of Qiu *et al.* of 2003 (ZnEtiol on alumina/NiAl [7]) and all the works based on the same experimental strategy [14, 8, 15, 67], under the hypothesis of a pure plasmonic excitation of the emitters, a mechanism that was not considered at the time. Unluckily, a proper analysis is currently impossible based only on the published data, and one should consider reproducing the experiment in order to test this hypothesis.

Limits of the lifted configuration. From a fundamental point of view the main limit of the lifted configuration is the loss of imaging capability of the STM. Moreover, once a wire is suspended in the junction, we can no longer measure the variation of the light emission with the tip position, nor do we have the possibility to displace nearby objects or molecules.

Some recent experiments of STM-LE from interacting phthalocyanines on NaCl/Ag [67, 68] highlight the interest of using a configuration where the molecules are lying flat on a surface. In these experiments, thanks to the spatially resolved excitation, the interaction between neighboring molecules can be observed in the optical spectra, showing “real-space” variations.

An interesting extension of our work that would exploit the potential of the lying flat configuration, would be a study of the vibrational peaks of the R-band (section 3.3.5). Here, one could explore the impact of the precise localisation of the tip on the energy or the intensity of the vibronic peaks. This kind of measurement would be compared to recent tip-enhanced Raman scattering measurements at the single molecule level [88, 137].

Finally, as we mentioned in the conclusions of chapter 4, the use of insulating layers might also allow the measurement of interband radiative transitions of GNRs that we did not observe in the lifted configuration.

Towards molecular optoelectronic devices? STM-LE experiments in the lifted configuration remain of great importance to study future molecular devices. From this perspective we already discussed the great control that can be obtained by embedding an emitter in a suspended molecular wire (chapter 3). However, this system revealed also some limits in terms of stability, reproducibility, and brightness. These issues were partially solved using GNRs as light emitting sources. Moreover, thanks to the high currents that can be used with the ribbons, and thanks to a quantum efficiency that is comparable with the plasmonic one at similar voltages (10^{-5} photon/electrons), the GNR proved to be interesting for the absolute intensity of their light emission.

Two perspectives can be foreseen for this kind of molecular junctions. (1) The combination of the two systems we explored in this thesis, for instance by embedding a chromophore inside a GNR. This way one could hope to keep the stability of the ribbons and introduce the flexibility of a dedicated emitter. (2) The combination of molecular junctions with plasmonic guides for surface plasmon polaritons (SPP). Our device would then work as a source for monochromatic SPPs. In this way one would effectively combine an electronic and a photonic circuit, with the molecular junction acting as a transducer.

Appendices

APPENDIX **A**

Voltage threshold in the electron injection luminescence mechanism

For an electron injection excitation mechanism, the voltage bias necessary to allow for an intramolecular radiative recombination is higher than the energy of the emission:

$$eV > E_G = h\nu. \quad (\text{A.1})$$

This is illustrated through an example in figure [A.1](#).

In (a) an unbiased double barrier tunneling junction is presented. The Fermi levels of the tip and the sample are aligned, and two molecular levels, HOMO and LUMO, have an energy of E_H and E_L respectively. Their energy is defined with respect to the Fermi level of the sample.

In figure [A.1\(b\)](#) the evolution of energy of sample, tip, HOMO and LUMO as a function of the applied bias is plotted. The plot is presented for an arbitrary set of values of initial energy of the HOMO and LUMO, and for a repartition of the voltage drop of $\alpha = 1/3$ on the sample side and $(1 - \alpha) = 2/3$ on the tip side.

One notices that: (1) the Fermi level of the sample is used as reference, therefore it does not shift; (2) the Fermi level of the tip shifts with the applied bias; (3) the molecular levels shift with the applied bias but with a smaller slope than the tip level. (3) is a consequence of the repartition of the voltage drop at the two barriers.

The energy diagram of the unbiased junction corresponds to the position marked as (a) in the plot of figure [A.1\(b\)](#). The situation corresponding to a voltage bias equal to the molecular gap, $eV = E_G$, is represented in (c). We observe that the HOMO is in the energy window between the Fermi levels of tip and sample, therefore electrons can tunnel through it. However, it is still impossible to have a radiative recombination inside the molecule since the LUMO is now at a higher energy. By increasing the bias the configuration of (d) is reached. Here, both molecular levels are in the energy

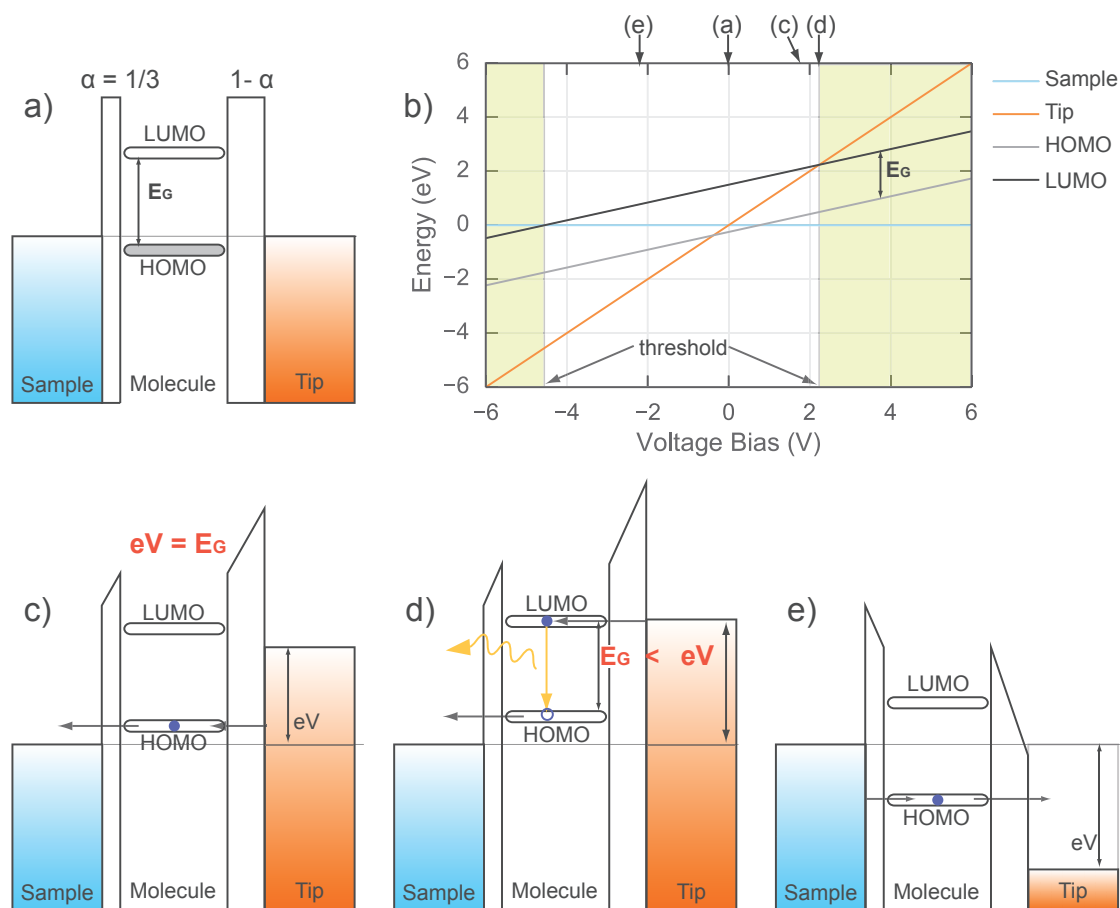


Figure A.1 – Impact of the voltage drop in the electron injection mechanism. (a) Energy diagram of the unbiased double barrier tunneling junction. (b) Evolution of the position of the energy levels as a function of the applied bias for an asymmetric junction. (c)-(e) Energy diagram of the junction at different voltage bias.

window between the Fermi levels of the electrodes. This configuration is available after a certain bias threshold is reached (pale green regions in figure A.1(b)). In this situation both molecular levels are available for transport, and electrons can be injected in the LUMO as well as holes in the HOMO, making radiative intramolecular transitions possible.

From this example and from the plot of figure A.1(b), it should be clear that with this excitation mechanism the threshold for molecular luminescence is higher than the energy of the photons emitted by this process.

In an asymmetric situation like the one we are discussing, there is another consequence: *the threshold for the intrinsic luminescence is asymmetric in the two polarities*. This is illustrated in the scheme in A.1(e) that corresponds to a situation where the same voltage of (d) is applied, but for the negative polarity. We observe that only one state, the HOMO, is available for transport thus making intramolecular luminescence impossible.

APPENDIX B

Cyclo-dehydrogenation of porphyrins

In this appendix, the possible cyclo-dehydrogenation reactions of the main porphyrins that we studied in chapter 3 are presented. Figure B.1(a) represents the only possible cyclo-dehydrogenation that can occur on MPPH₂. We refer to the resulting molecular species as to fused-MPP. A topography is presented in (b).

In figure B.1(c) we see that the reaction on DPPH₂ can result two new molecular species, type A fused-DPP and type B fused-DPP. The difference between the two lies in the respective side of dehydrogenation for the two phenyl rings resulting in a *cis* or in a *trans* isomer, similarly to what we find in the STM topographies (d). It is worth noticing that the molecule is symmetric before cyclodehydrogenation. There is no preferential side for the cyclo-dehydrogenation, therefore no prevalence of one product compared to the other is expected. Experimentally we observe a 50:50 ratio of the two fused-DPP, both isolated on the surface and inside of the co-polymers with oligothiophene. No experimental difference between the two isomers is observed in terms of light emission.

The case of DNPH₂ is the richest as we can see from figure B.1(e). For this molecule even before annealing there are two possible configurations since the naphthalene groups are free to turn: when confined on a 2D plane they can be in *cis* or in *trans* configuration. Starting from a *trans* configuration there are three possible outcomes : fused-DNP of type A,B or C. Starting from the *cis* it is possible to obtain fused-DNP of type D, E or F. The reason for the different types of fused-DNP lies in the two non-equivalent ways in which the cyclo-dehydrogenation can occur for every naphthalene unit. One results in the fused naphthalene group forming a straight continuation of the macro-cycle (green bond in figure B.1(e)), the other results in the naphthalene group turned outwards with respect to the macro-cycle (red bond). Consequently, for each of the two starting configurations the fusion of the two groups can occur in three

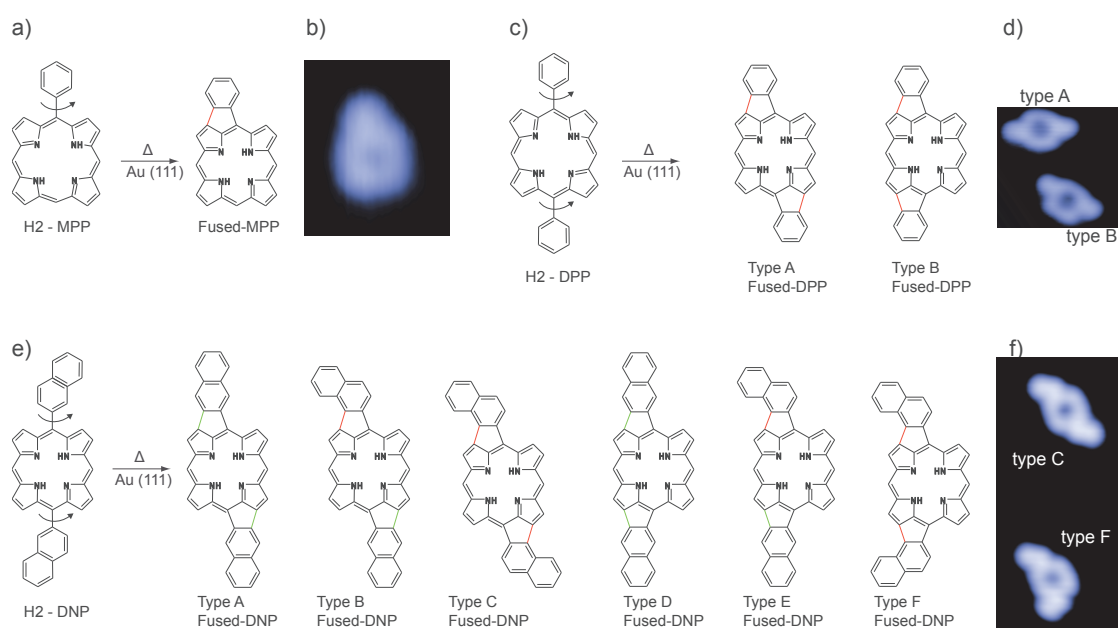


Figure B.1 – Porphyrins and their fused counterparts after dehydrogenation. (a) Sketch of the cyclo-dehydrogenation reaction on H₂-MPP. (b) STM topography of fused-MPP $V = -0.1$ V, $i = 0.1$ nA, 2×2.4 nm². (c) Sketch of the cyclo-dehydrogenation reaction on H₂-DPP. (d) STM topography of fused-DPP $V = -0.1$ V, $i = 0.1$ nA, 3.5×2.9 nm². (e) Sketch of the cyclo-dehydrogenation reaction on H₂-DNP. (f) STM topography of fused-DNP $V = -0.1$ V, $i = 0.1$ nA, 2.9×6.5 nm².

possible combinations:

- both in a sort of continuation of the macrocycle (type A and type D);
- both in the other configuration, with the naphthalene units twisted outwards (type C and type F);
- alternating a “straight” and a “twisted” units (type B and type E).

Experimentally we observe only fused-DNP of type C and of type F, as presented in figure B.1(f). The observed ratio is 95:5.

Interestingly, DFT calculations of the isolated fused-DNP species show that the most stable conformers are type A and type D, that are not observed experimentally. Conversely, type C and F are the least favorable from a purely energetic point of view. This indicates that the products of the reaction are not determined by their energy. One explanation is that the kinetics of the reaction plays a major role. Another possibility is that the Au(111) substrate plays a major role, and therefore should be included in future calculations.

APPENDIX C

Interaction between thiophene and fused-DPP

In chapter 3.3.3, we concluded that the presence of oligothiophene chains allows the transport of electrons while simultaneously decoupling the fused-porphyrin from the electrodes. Moreover in section 3.3.4 we reported the TD-DFT calculations of the optical gap of fused-DPP, showing little changes when the presence of oligothiophene chains was considered.

The calculations of the structure of the fused-porphyrins with terthiophene units on the side provide a possible explanation for these effects (figure C.1). Here, a dihedral angle of 45° between the porphyrin and the oligothiophene wire is found. This confirms a reduced coupling between the fused-porphyrin and the oligothiophene compared to a case where the molecules would be on the same plane.

An alternative fused-DPP.

Here, an experiment on a co-polymer of oligothiophene and a different fused-DPP is described.

The synthesis was performed using DBrTT in combination with a functionalized DPPH₂ species, where the bromine units are originally on the phenyl rings: 5,15-(dibromo - diphenyl)-porphyrin. The sketch of the reaction is presented in figure C.2(a). During the annealing the porphyrin undergoes a cyclo-dehydrogenation and becomes fused-DPP. The resulting co-polymer is presented in the STM topography of figure C.2(b). We observe that the link between oligothiophene and fused-DPP occurs on the part of the macrocycle derived from the phenyl rings.

DFT calculations of the structure of the resulting co-polymer, presented in figure

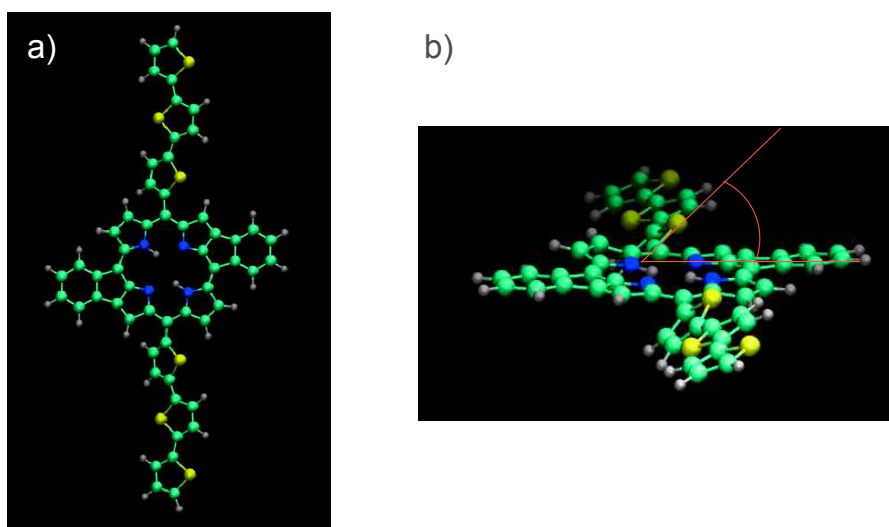


Figure C.1 – DFT calculation of the relaxed structure of a co-polymer of fused-DPP and oligothiophene. (a) Top view of co-polymer. (b) Frontal view. The dihedral angle between the fused-DPP and the oligothiophene is indicated.

C.2(c), show that, in this case, the dihedral angle between oligothiophene and fused-DPP is close to zero. Moreover, the molecular gap of the fused-DPP is reduced, when considering the presence of two terthiophene units connected in this way, with respect to the gap of the isolated fused-DPP.

These two elements indicate a stronger coupling between the fused-DPP and the oligothiophene for this molecule, as compared to the case discussed in the main manuscript (and illustrated in figure C.1).

An optical spectrum obtained on the lifted co-polymer of figure C.2(b) is presented in figure C.2(d) (black curve) and compared to the spectrum measured on the bare surface with the same tip (red curve). The spectrum of the molecule is essentially featureless. This may be understood by the lack of decoupling of this co-polymer. The fused-porphyrin is not an isolated emitter in this configuration.

We remark, however, that a negative experimental result is difficult to use as evidence in our case. We know that for the other fused-porphyrins there is a huge variability of the quantum yield and not all the co-polymer resulted in a measurable emission. The absence of a measurable peak might be due to undersampling. If further theoretical calculations (for instance of the DOS of the system) or extensive experimental sampling were to confirm this hypothesis, we would have an important indication for the design of decoupled systems inside of a molecular wire. This indeed suggests that an efficient optical decoupling can be obtained only in presence of a large dihedral angle between the molecular wire and the emitter.

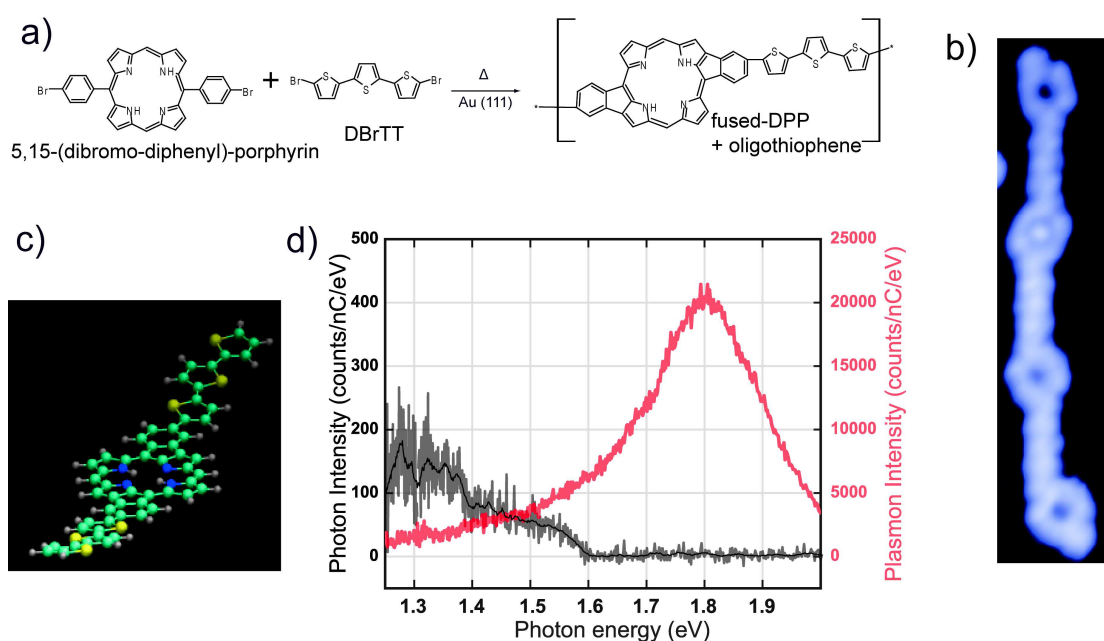


Figure C.2 – Synthesis and characterization of co-polymers based on 5,15- (dibromo - diphenyl)-porphyrin. and DBrTT. (a) Sketch of the reaction. (b) Topography of the co-polymer; $V = -0.1$ V, $i = 0.1$ nA, 2.5×11 nm². (c) TD-DFT calculation of the structure fused-DPP connected with the terthiophene units as in the co-polymer of (a) and (b). (d) Electroluminescence spectrum of the co-polymer obtained in (a) (black curve; $V = -1.6$ V, $i = 9$ nA, $t = 60$ s, $z = 2$ nm). The red curve corresponds to the plasmon measured on on the bare surface with the same tip.

APPENDIX D

Scanning tunneling spectroscopy of suspended fused-DPP

Scanning tunneling spectroscopy can provide important information on the energy of the molecular levels. In an electron injection excitation mechanism the positions of the molecular levels are of major importance, since electrons (and holes) need to tunnel from the electrodes to the molecule before recombining.

For a plasmon mediated excitation, however, the exact position of the molecular orbitals is less useful, as we discussed in chapter 2.2.5.

We acquired dI/dV spectra on lifted co-polymers, at tip-sample separations z in the same range used for light emission measurements. An example of such spectrum is provided in figure D.1(a) for a co-polymer of fused-DPP and oligothiophene. The spectrum presents some resonances at positive and negative bias separated by a zero conductance gap.

The assignment of these resonances to molecular orbitals is not straightforward here. Both orbitals from fused-DPP and from the oligothiophene chains may contribute to this spectrum. Moreover, there are several interfaces in the system where the potential can drop: the contact point between the anchoring porphyrin and the tip, the connection between fused-porphyrins and oligothiophene, and a part of the co-polymer is still on the surface. Eventually, these different aspects may evolve substantially depending on the detailed geometry of the suspended wire in the junction. We are thus observing a signal generated by several interacting entities, where the voltage drop is not well known.

With these considerations in mind, it is not surprising to see that *on the same wire* the dI/dV signal can change drastically by retracting the STM tip by some ångströms from the surface (figure D.1(b),(c)). In (b) we observe conductance peaks that are reminiscent of charge events (e.g. [180, 181]), while in (c) the gap appears much larger than in (a), and the dI/dV resonances are broader.

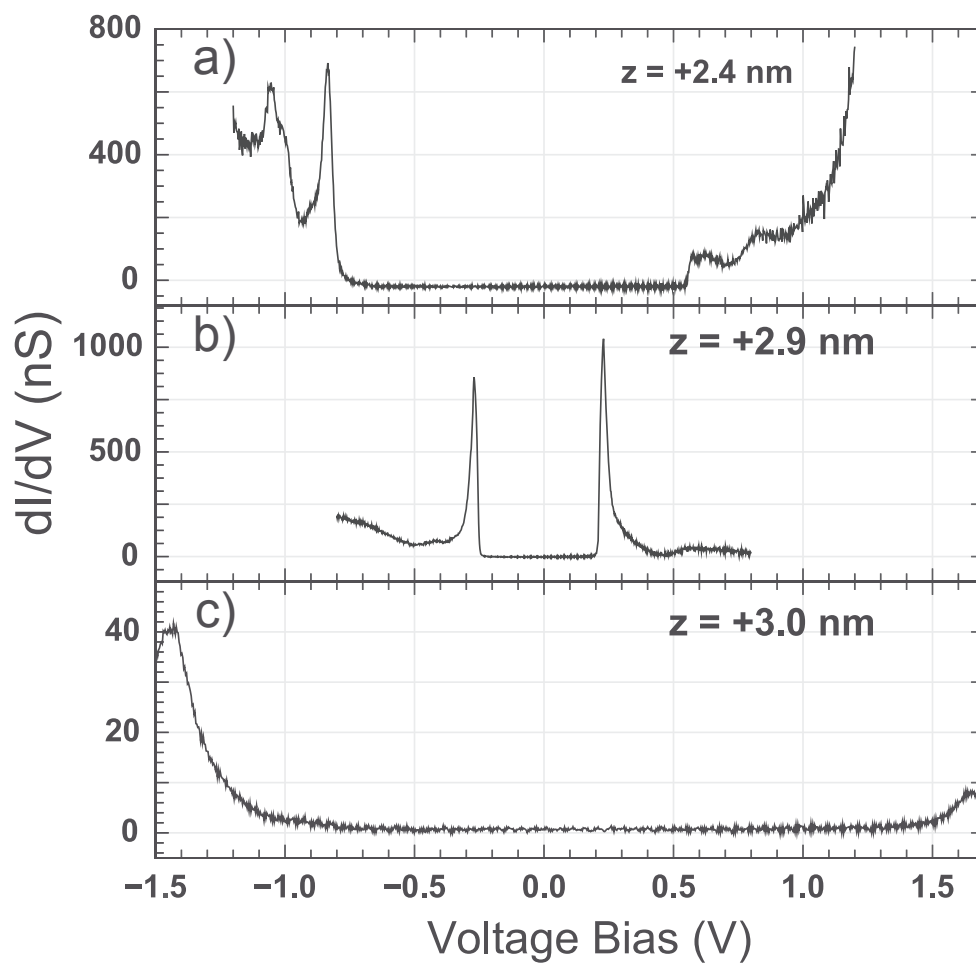


Figure D.1 – Extreme variability of the STS spectra for a single suspended co-polymer of oligothiophene and fused-DPP. The spectra were acquired at tip-sample separation of $z = 2.4$ nm (a), $z = 2.9$ nm (b) and $z = 3.0$ nm (c).

We stress that similar variations were observed upon lifting different co-polymers. Finally, we note that the sharp peaks (as in (b)), are not always observed, and that there is no clear relation between the width of the gap and the tip-sample separation.

Bibliography

- [1] W. E. Moerner and L. Kador, "Optical detection and spectroscopy of single molecules in a solid", *Phys. Rev. Lett.*, **62**, 2535–2538, (1989).
- [2] M. Orrit and J. Bernard, "Single pentacene molecules detected by fluorescence excitation in a p-terphenyl crystal", *Phys. Rev. Lett.*, **65**, 2716, (1990).
- [3] W. E. Moerner and M. Orrit, "Illuminating single molecules in condensed matter", *Science*, **283**, 1670–6, (1999).
- [4] W. P. Ambrose, T. Basche, and W. E. Moerner, "Detection and spectroscopy of single pentacene molecules in a p-terphenyl crystal by means of fluorescence excitation", *J. Chem. Phys.*, **95**, 7150, (1991).
- [5] J. Bernard, L. Fleury, H. Talon, and M. Orrit, "Photon bunching in the fluorescence from single molecules: A probe for intersystem crossing", *J. Chem. Phys.*, **98**, 850, (1993).
- [6] P. Tchénio, A. B. Myers, and W. Moerner, "Vibrational analysis of the dispersed fluorescence from single molecules of terylene in polyethylene", *Chem. Phys. Lett.*, **213**, 325–332, (1993).
- [7] X. H. Qiu, G. V. Nazin, and W. Ho, "Vibrationally resolved fluorescence excited with submolecular precision.", *Science*, **299**, 542, (2003).
- [8] C. Chen, P. Chu, C. A. Bobisch, D. L. Mills, and W. Ho, "Viewing the Interior of a Single Molecule: Vibronically Resolved Photon Imaging at Submolecular Resolution", *Phys. Rev. Lett.*, **105**, 217402, (2010).
- [9] J. S. Foster, J. E. Frommer, and P. C. Arnett, "Molecular manipulation using a tunnelling microscope", *Nature*, **331**, 324–6, (1988).
- [10] E. K. Eigler and D. K. Schweizer, "Positioning single atoms with a scanning tunneling microscope", *Nature*, **344**, 524–525, (1990).
- [11] J. a. Stroscio and D. M. Eigler, "Atomic and Molecular Manipulation with the Scanning Tunneling Microscope", *Science*, **254**, 1319–1326, (1991).

- [12] P. Avouris and B. N. J. Persson, "Excited States at Metal Surfaces and Their Nonradiative Relaxation", *J. Phys. Chem.*, **88**, 837–848, (1984).
- [13] R. Berndt, R. Gaisch, J. K. Gimzewski, B. Reihl, R. R. Schlittler, W. D. Schneider, and M. Tschudy, "Photon emission at molecular resolution induced by a scanning tunneling microscope.", *Science*, **262**, 1425, (1993).
- [14] S. W. Wu, G. V. Nazin, and W. Ho, "Intramolecular photon emission from a single molecule in a scanning tunneling microscope", *Phys. Rev. B*, **77**, (2008).
- [15] J. Lee, S. M. Perdue, A. Rodriguez Perez, and V. A. Apkarian, "Vibronic motion with joint angstrom-femtosecond resolution observed through Fano progressions recorded within one molecule.", *ACS Nano*, **8**, 54, (2014).
- [16] M. a. Reed, C. Zhou, C. J. Muller, T. P. Burgin, and J. M. Tour, "Conductance of a molecular junction", *Science*, **278**, 252–254, (1997).
- [17] R. H. M. Smit, Y. Noat, C. Untiedt, N. D. Lang, M. C. van Hemert, and J. M. van Ruitenbeek, "Measurement of the conductance of a hydrogen molecule", *Nature*, **419**, 906–909, (2002).
- [18] D. Miller, "Optical interconnects to electronic chips.", *Appl. Opt.*, **49**, F59, (2010).
- [19] R. J. Walters, R. V. A. Van Loon, I. Brunets, J. Schmitz, and A. Polman, "A silicon-based electrical source for surface plasmon polaritons", *Nat. Mater.*, **9**, 21, (2010).
- [20] D. Y. Fedyanin, A. V. Krasavin, A. V. Arsenin, and A. V. Zayats, "Surface plasmon polariton amplification upon electrical injection in highly integrated plasmonic circuits", *Nano Lett.*, **12**, 2459, (2012).
- [21] T. Wang and C. a. Nijhuis, "Molecular electronic plasmonics", *Applied Materials Today*, **3**, 73, (2016).
- [22] G. Reecht, F. Scheurer, V. Speisser, Y. J. Dappe, F. Mathevet, and G. Schull, "Electroluminescence of a Polythiophene Molecular Wire Suspended between a Metallic Surface and the Tip of a Scanning Tunneling Microscope", *Phys. Rev. Lett.*, **112**, 047403, (2014).
- [23] G. Binnig, H. Rohrer, C. Gerber, and E. Weibel, "Tunneling through a controllable vacuum gap", *Appl. Phys. Lett.*, **40**, 178, (1982).
- [24] G. Binnig, H. Rohrer, C. Gerber, and E. Weibel, "Surface studies by scanning tunneling microscopy", *Phys. Rev. Lett.*, **49**, 57, (1982).
- [25] G. Binnig, H. Rohrer, C. Gerber, and E. Weibel, " 7×7 reconstruction on si(111) resolved in real space", *Phys. Rev. Lett.*, **50**, 120, (1983).

- [26] R. Young, J. Ward, and F. Scire, "Observation of metal-vacuum-metal tunneling, field emission, and the transition region", *Phys. Rev. Lett.*, **27**, 922–924, (Oct 1971).
- [27] R. Young, J. Ward, and F. Scire, "The topografiner: An instrument for measuring surface microtopography", *Rev. Sci. Instrum.*, **43**, 999–1011, (1972).
- [28] G. Binnig, C. F. Quate, and C. Gerber, "Atomic force microscope", *Phys. Rev. Lett.*, **56**, 930–933, (Mar 1986).
- [29] U. Hartmann, "Magnetic force microscopy: Some remarks from the micromagnetic point of view", *J. Appl. Phys.*, **64**, 1561–1564, (1988).
- [30] M. Nonnenmacher, M. P. OBoyle, and H. K. Wickramasinghe, "Kelvin probe force microscopy", *Appl. Phys. Lett.*, **58**, 2921–2923, (1991).
- [31] J. K. Gimzewski, B. Reihl, J. H. Coombs, and R. R. Schlittler, "Photon emission with the scanning tunneling microscope", *Zeitschrift fur Physik B Condensed Matter*, **72**, 497–501, (1988).
- [32] J. H. Coombs, J. K. Gimzewski, B. Reihl, J. K. Sass, and R. R. Schlittler, "Photon emission experiments with the scanning tunnelling microscope", *J. Microsc.*, **152**, 325–336, (1988).
- [33] J. K. Gimzewski, J. K. Sass, R. R. Schlitter, and J. Schott, "Enhanced photon emission in scanning tunneling microscopy", *Eur. Lett.*, **8**, 435–440, (1989).
- [34] L. Douillard and F. Charra, "High-resolution mapping of plasmonic modes: photoemission and scanning tunnelling luminescence microscopies", *J. Phys. D: Appl. Phys.*, **44**, 464002, (2011).
- [35] P. Merino, C. Große, a. Rosawska, K. Kuhnke, and K. Kern, "Exciton dynamics of C60-based single-photon emitters explored by Hanbury Brown-Twiss scanning tunnelling microscopy.", *Nat. Commun.*, **6**, 1, (2015).
- [36] Z. Dong, X. L. Zhang, H. Y. Gao, Y. Luo, C. Zhang, L. G. Chen, R. Zhang, X. Tao, Y. Zhang, J. L. Yang, and J. G. Hou, "Generation of molecular hot electroluminescence by resonant nanocavity plasmons", *Nat. Photonics*, **4**, 50–54, (2009).
- [37] N. L. Schneider and R. Berndt, "Plasmonic excitation of light emission and absorption by porphyrine molecules in a scanning tunneling microscope", *Phys. Rev. B*, **86**, 035445, (2012).
- [38] M. Heiss, Y. Fontana, a. Gustafsson, G. Wüst, C. Magen, D. D. O'Regan, J. W. Luo, B. Ketterer, S. Conesa-Boj, a. V. Kuhlmann, J. Houel, E. Russo-Averchi, J. R. Morante, M. Cantoni, N. Marzari, J. Arbiol, a. Zunger, R. J. Warburton, and a. Fontcu-

- berta i Morral, "Self-assembled quantum dots in a nanowire system for quantum photonics.", *Nat. Mater.*, **12**, 439, (2013).
- [39] L. Grill, M. Dyer, L. Lafferentz, M. Persson, M. V. Peters, and S. Hecht, "Nano-architectures by covalent assembly of molecular building blocks.", *Nat. Nanotechnol.*, **2**, 687, (2007).
- [40] G. Reecht, H. Bulou, F. Scheurer, V. Speisser, B. Carriere, F. Mathevet, and G. Schull, "Oligothiophene nanorings as electron resonators for whispering gallery modes", *Phys. Rev. Lett.*, **110**, 056802, (2013).
- [41] G. Reecht, H. Bulou, F. Scheurer, V. Speisser, F. Mathevet, C. González, Y. J. Dappe, and G. Schull, "Pulling and Stretching a Molecular Wire to Tune its Conductance", *J. Phys. Chem. Lett.*, **6**, 2987, (2015).
- [42] L. Lafferentz, F. Ample, H. Yu, S. Hecht, C. Joachim, and L. Grill, "Conductance of a single conjugated polymer as a function of its length.", *Science*, **323**, 1193, (2009).
- [43] M. Koch, F. Ample, C. Joachim, and L. Grill, "Voltage-dependent conductance of a single graphene nanoribbon", *Nat. Nanotechnol.*, **7**, 713, (2012).
- [44] C. Nacci, F. Ample, D. Blegler, S. Hecht, C. Joachim, and L. Grill, "Conductance of a single flexible molecular wire composed of alternating donor and acceptor units", *Nat. Commun.*, **6**, 7397, (2015).
- [45] G. Kuang, S.-Z. Chen, W. Wang, T. Lin, K. Chen, X. Shang, P. N. Liu, and N. Lin, "Resonant charge transport in conjugated molecular wires beyond 10 nm range", *J. Am. Chem. Soc.*, **138**, 11140–11143, (2016).
- [46] K. Takeuchi, Y. Uehara, S. Ushioda, and S. Morita, "Prism-coupled light emission from a scanning tunneling microscope", *J. Vac. Sci. Technol. B Microelectron. Nanom. Struct.*, **9**, 557, (1991).
- [47] Y. Uehara, Y. Kimura, S. Ushioda, and K. Takeuchi, "Theory of Visible Light Emission from Scanning Tunneling Microscope", *Jpn. J. Appl. Phys.*, **31**, 2465–2469, (1992).
- [48] T. Wang, E. Boer-Duchemin, Y. Zhang, G. Comtet, and G. Dujardin, "Excitation of propagating surface plasmons with a scanning tunnelling microscope.", *Nanotechnology*, **22**, 175201, (2011).
- [49] P. Bharadwaj, A. Bouhelier, and L. Novotny, "Electrical excitation of surface plasmons", *Phys. Rev. Lett.*, **106**, 226802, (2011).
- [50] P. Rai, N. Hartmann, J. Berthelot, J. Arocas, G. Colas des Francs, A. Hartschuh, and A. Bouhelier, "Electrical excitation of surface plasmons by an individual carbon nanotube transistor", *Phys. Rev. Lett.*, **111**, 026804, (2013).

- [51] P. M. Ajayan and S. Iijima, "Smallest carbon nanotube", *Nature*, **358**, 23–23, (1992).
- [52] T. W. Ebbesen and P. M. Ajayan, "Large-scale synthesis of carbon nanotubes", *Nature*, **358**, 220–222, (1992).
- [53] B. Obradovic, R. Kotlyar, F. Heinz, P. Matagne, T. Rakshit, M. D. Giles, M. A. Stettler, and D. E. Nikonov, "Analysis of graphene nanoribbons as a channel material for field-effect transistors", *Appl. Phys. Lett.*, **88**, 142102, (2006).
- [54] Y. W. Son, M. L. Cohen, and S. G. Louie, "Energy gaps in graphene nanoribbons", *Phys. Rev. Lett.*, **97**, 216803, (2006).
- [55] M. Y. Han, B. Ozyilmaz, Y. Zhang, and P. Kim, "Energy band-gap engineering of graphene nanoribbons", *Phys. Rev. Lett.*, **98**, 206805, (2007).
- [56] P. Avouris, "Graphene: Electronic and photonic properties and devices", *Nano Lett.*, **10**, 4285–4294, (2010).
- [57] L. Brey and H. A. Fertig, "Electronic states of graphene nanoribbons studied with the Dirac equation", *Phys. Rev. B*, **73**, 235411, (2006).
- [58] Y.-W. Son, M. L. Cohen, and S. G. Louie, "Half-Metallic Graphene Nanoribbons", *Nature*, **444**, 347–349, (2006).
- [59] W. Han, R. K. Kawakami, M. Gmitra, and J. Fabian, "Graphene spintronics", *Nature*, **9**, 794–807, (2014).
- [60] J. Cai, P. Ruffieux, R. Jaafar, M. Bieri, T. Braun, S. Blankenburg, M. Muoth, A. P. Seitsonen, M. Saleh, X. Feng, K. Müllen, and R. Fasel, "Atomically precise bottom-up fabrication of graphene nanoribbons.", *Nature*, **466**, 470–473, (2010).
- [61] S. Linden, D. Zhong, A. Timmer, N. Aghdassi, J. H. Franke, H. Zhang, X. Feng, K. Müllen, H. Fuchs, L. Chi, and H. Zacharias, "Electronic structure of spatially aligned graphene nanoribbons on Au(788)", *Phys. Rev. Lett.*, **108**, 216801, (2012).
- [62] L. Talirz, H. Söde, J. Cai, P. Ruffieux, S. Blankenburg, R. Jafaar, R. Berger, X. Feng, K. Müllen, D. Passerone, R. Fasel, and C. a. Pignedoli, "Termini of bottom-up fabricated graphene nanoribbons", *J. Am. Chem. Soc.*, **135**, 2060–2063, (2013).
- [63] S. Kawai, A. Benassi, E. Gnecco, H. Söde, R. Pawlak, X. Feng, K. Müllen, D. Passerone, C. a. Pignedoli, P. Ruffieux, R. Fasel, and E. Meyer, "Superlubricity of graphene nanoribbons on gold surfaces", *Science*, **351**, 957–962, (2016).
- [64] A. C. Ferrari, J. C. Meyer, V. Scardaci, C. Casiraghi, M. Lazzeri, F. Mauri, S. Piscanec, D. Jiang, K. S. Novoselov, S. Roth, and A. K. Geim, "Raman spectrum of graphene and graphene layers", *Phys. Rev. Lett.*, **97**, 187401, (2006).

- [65] A. C. Ferrari and D. M. Basko, "Raman spectroscopy as a versatile tool for studying the properties of graphene", *Nat. Nanotechnol.*, **8**, 235–46, (2013).
- [66] I. Verzhbitskiy, M. De Corato, A. Ruini, E. Molinari, A. Narita, Y. Hu, M. G. Schwab, M. Bruna, D. Yoon, S. Milana, X. Feng, K. Müllen, A. C. Ferrari, C. Casiraghi, and D. Prezzi, "Raman fingerprints of atomically precise graphene nanoribbons", *Nano Lett.*, **16**, 3442–3447, (2016).
- [67] Y. Zhang, Y. Luo, Y. Zhang, Y. Yu, Y. Kuang, L. Zhang, Q. Meng, Y. Luo, J. Yang, Z. Dong, and J. G. Hou, "Visualizing coherent intermolecular dipole-dipole coupling in real space", *Nature*, **531**, 623, (2016).
- [68] H. Imada, K. Miwa, M. Imai-Imada, S. Kawahara, K. Kimura, and Y. Kim, "Real-space investigation of energy transfer in heterogeneous molecular dimers", *Nature*, **538**, 364–367, (2016).
- [69] M. C. Chong, G. Reecht, H. Bulou, A. Boeglin, F. Scheurer, F. Mathevet, and G. Schull, "Narrow-Line Single-Molecule Transducer between Electronic Circuits and Surface Plasmons", *Phys. Rev. Lett.*, **116**, 036802, (2016).
- [70] M. C. Chong, L. Sosa-vargas, H. Bulou, A. Boeglin, F. Scheurer, F. Mathevet, and G. Schull, "Ordinary and Hot Electroluminescence from Single-Molecule Devices: Controlling the Emission Color by Chemical Engineering", *Nano Lett.*, **16**, 6480–6484, (2016).
- [71] J. Tersoff and D. R. Hamann, "Theory and application for the scanning tunneling microscope", *Phys. Rev. Lett.*, **50**, 1998–2001, (1983).
- [72] J. Tersoff and D. R. Hamann, "Theory of the scanning tunneling microscope", *Phys. Rev. B*, **31**, 805–813, (1985).
- [73] J. Li, W.-D. Schneider, and R. Berndt, "Local density of states from spectroscopic scanning-tunneling-microscope images: Ag(111)", *Phys. Rev. B*, **56**, 7656–7659, (1997).
- [74] I. Ekvall, E. Wahlström, D. Claesson, H. Olin, and E. Olsson, "Preparation and characterization of electrochemically etched w tips for stm", *Measurement Science and Technology*, **10**, 11, (1999).
- [75] R. Berndt, J. K. Gimzewski, and P. Johansson, "Inelastic tunneling excitation of tip-induced plasmon modes on noble-metal surfaces", *Phys. Rev. Lett.*, **67**, 3796, (1991).
- [76] J. Aizpurua, S. P. Apell, and R. Berndt, "Role of tip shape in light emission from the scanning tunneling microscope", *Phys. Rev. B*, **62**, 2065–2073, (2000).
- [77] K. Meguro, K. Sakamoto, R. Arafune, M. Satoh, and S. Ushioda, "Origin of multiple

- peaks in the light emission spectra of a $\text{Au}(111)$ surface induced by the scanning tunneling microscope”, *Phys. Rev. B*, **65**, 165405, (2002).
- [78] J. G. Keizer, J. K. Garleff, and P. M. Koenraad, “Simple and efficient scanning tunneling luminescence detection at low-temperature”, *Rev. Sci. Instrum.*, **80**, 123704, (2009).
- [79] R. Berndt, *Photon Emission From the Scanning Tunneling Microscope*. PhD thesis, Basel University, (1992).
- [80] G. Reecht, *Propriétés optoélectroniques de fils moléculaires uniques*. PhD thesis, Université de Strasbourg, (2014).
- [81] I. Horcas, R. Fernández, J. M. Gómez-Rodríguez, J. Colchero, J. Gómez-Herrero, and a. M. Baro, “WSXM: A software for scanning probe microscopy and a tool for nanotechnology”, *Rev. Sci. Instrum.*, **78**, 013705, (2007).
- [82] W. L. Barnes, A. Dereux, and T. W. Ebbesen, “Surface plasmon subwavelength optics”, *Nature*, **424**, 824–830, (2003).
- [83] R. W. Rendell, D. J. Scalapino, and B. Mühlischlegel, “Role of local plasmon modes in light emission from small-particle tunnel junctions”, *Phys. Rev. Lett.*, **41**, 1746–1750, (1978).
- [84] P. Johansson, R. Monreal, and P. Apell, “Theory for light emission from a scanning tunneling microscope”, *Phys. Rev. B*, **42**, (1990).
- [85] F. Rossel, M. Pivetta, and W. D. Schneider, “Luminescence experiments on supported molecules with the scanning tunneling microscope”, *Surf. Sci. Reports*, **65**, 129–144, (2010).
- [86] B. N. J. Persson and A. Baratoff, “Theory of photon emission in electron tunneling to metallic particles”, *Phys. Rev. Lett.*, **68**, 3224, (1992).
- [87] R. M. Stockle, Y. D. Suh, V. Deckert, and R. Zenobi, “Nanoscale chemical analysis by tip-enhanced raman spectroscopy”, *Chem. Phys. Lett.*, **318**, 131 – 136, (2000).
- [88] R. Zhang, Y. Zhang, Z. Dong, S. Jiang, C. Zhang, L. G. Chen, L. Zhang, Y. Liao, J. Aizpurua, Y. Luo, J. L. Yang, and J. G. Hou, “Chemical mapping of a single molecule by plasmon-enhanced Raman scattering.”, *Nature*, **498**, 82, (2013).
- [89] R. Berndt and J. K. Gimzewski, “The role of proximity plasmon modes on noble metal surfaces in scanning tunneling microscopy”, *Surf. Sci*, **269**, 556 – 559, (1992).
- [90] K. Sakamoto, K. Meguro, R. Arafune, M. Satoh, Y. Uehara, and S. Ushioda, “Light

- emission spectra of the monolayer-island of C60 molecules on Au(1 1 1) induced by scanning tunneling microscope", *Surf. Sci.*, **502-503**, 149–155, (2002).
- [91] F. Geng, Y. Zhang, Y. Yu, Y. Kuang, Y. Liao, Z. Dong, and J. Hou, "Modulation of nanocavity plasmonic emission by local molecular states of C60 on Au(111).", *Opt. Express*, **20**, 26725–35, (2012).
- [92] W. Deng, D. Fujita, T. Ohgi, S. Yokoyama, K. Kamikado, and S. Mashiko, "STM-induced photon emission from self-assembled porphyrin molecules on a Cu(100) surface", *J. Chem. Phys.*, **117**, 4995–5000, (2002).
- [93] Z. C. Dong, a. S. Trifonov, X. L. Guo, K. Amemiya, S. Yokoyama, T. Kamikado, T. Yamada, S. Mashiko, and T. Okamoto, "Tunneling electron induced photon emission from monolayered H2TBP porphyrin molecules on Cu(100)", *Surf. Sci.*, **532-535**, 237–243, (2003).
- [94] I. Smolyaninov, "Photon emission from a layer of copper phthalocyanine molecules on a gold (111) film surface induced by stm", *Surf. Sci.*, **364**, 79 – 88, (1996).
- [95] D. Ino, T. Yamada, and M. Kawai, "Luminescence from 3,4,9,10-perylenetetracarboxylic dianhydride on ag(111) surface excited by tunneling electrons in scanning tunneling microscopy", *The Journal of Chemical Physics*, **129**, (2008).
- [96] X.-L. Guo, Z.-C. Dong, A. S. Trifonov, S. Yokoyama, S. Mashiko, and T. Okamoto, "Light emission from organic molecules on metal substrates induced by tunneling currents", *Jpn. J. Appl. Phys.*, **42**, 6937, (2003).
- [97] G. Hoffmann, T. Maroutian, and R. Berndt, "Color View of Atomic Highs and Lows in Tunneling Induced Light Emission", *Phys. Rev. Lett.*, **93**, 076102, (2004).
- [98] N. L. Schneider, F. Matino, G. Schull, S. Gabutti, M. Mayor, and R. Berndt, "Light emission from a double-decker molecule on a metal surface", *Phys. Rev. B*, **84**, 153403, (2011).
- [99] C. Grosse, A. Kabakchiev, T. Lutz, R. Froidevaux, F. Schramm, M. Ruben, M. Etzkorn, U. Schlickum, K. Kuhnke, and K. Kern, "Dynamic Control of Plasmon Generation by an Individual Quantum System.", *Nano Lett.*, 5693, (2014).
- [100] G. V. Nazin, X. H. Qiu, and W. Ho, "Atomic engineering of photon emission with a scanning tunneling microscope", *Phys. Rev. Lett.*, **90**, 216110, (2003).
- [101] C. Chen, C. A. Bobisch, and W. Ho, "Visualization of Fermi's golden rule through imaging of light emission from atomic silver chains.", *Science*, **325**, 981–5, (2009).

- [102] G. Schull, M. Becker, and R. Berndt, "Imaging confined electrons with plasmonic light", *Phys. Rev. Lett.*, **101**, 136801, (2008).
- [103] D. L. Dexter, "A theory of sensitized luminescence in solids", *The Journal of Chemical Physics*, **21**, 836–850, (1953).
- [104] D. Andrews, "A unified theory of radiative and radiationless molecular energy transfer", *Chem. Phys.*, **135**, 195 – 201, (1989).
- [105] A. Campion, A. Gallo, C. Harris, H. Robota, and P. Whitmore, "Electronic energy transfer to metal surfaces: a test of classical image dipole theory at short distances", *Chem. Phys. Lett.*, **73**, 447 – 450, (1980).
- [106] M. Daffertshofer, H. Port, and H. C. Wolf, "Fluorescence quenching of ultrathin anthracene films by dielectric and metallic substrates", *Chem. Phys.*, **200**, 225, (1995).
- [107] Z. Dong, X.-L. Guo, A. Trifonov, P. Dorozhkin, K. Miki, K. Kimura, S. Yokoyama, and S. Mashiko, "Vibrationally Resolved Fluorescence from Organic Molecules near Metal Surfaces in a Scanning Tunneling Microscope", *Phys. Rev. Lett.*, **92**, 086801, (2004).
- [108] X. Guo, Z. Dong, a.S. Trifonov, K. Miki, K. Kimura, and S. Mashiko, "STM-induced molecular fluorescence from porphyrin molecules on metal substrates", *Applied Physics A*, **81**, 367–370, (2004).
- [109] H. Imada, K. Miwa, M. Imai-imada, S. Kawahara, K. Kimura, and K. Yousoo, "Orbital-selective single molecule excitation and spectroscopy based on plasmon-exciton coupling", *Arxiv*, (2016).
- [110] S.-E. Zhu, Y.-M. Kuang, F. Geng, J.-Z. Zhu, C.-Z. Wang, Y.-J. Yu, Y. Luo, Y. Xiao, K.-Q. Liu, Q.-S. Meng, L. Zhang, S. Jiang, Y. Zhang, G.-W. Wang, Z. Dong, and J. G. Hou, "Self-decoupled porphyrin with a tripodal anchor for molecular-scale electroluminescence.", *J. Am. Chem. Soc.*, **135**, 15794–800, (2013).
- [111] E. Čavar, M.-C. Blüm, M. Pivetta, F. Patthey, M. Chergui, and W.-D. Schneider, "Fluorescence and Phosphorescence from Individual C60 Molecules Excited by Local Electron Tunneling", *Phys. Rev. Lett.*, **95**, 196102, (2005).
- [112] F. Rossel, M. Pivetta, F. Patthey, and W. D. Schneider, "Plasmon enhanced luminescence from fullerene molecules excited by local electron tunneling", *Optics express*, **17**, 2714, (2009).
- [113] A. Kabakchiev, *Scanning Tunneling Luminescence of Pentacene Nanocrystals*. PhD thesis, Ecole Polytechnique Fédérale de Lausanne, (2010).
- [114] N. L. Schneider, J. T. Lü, M. Brandbyge, and R. Berndt, "Light emission probing

- quantum shot noise and charge fluctuations at a biased molecular junction”, *Phys. Rev. Lett.*, **109**, 186601, (2012).
- [115] N. L. Schneider, G. Schull, and R. Berndt, “Optical probe of quantum shot-noise reduction at a single-atom contact”, *Phys. Rev. Lett.*, **105**, 026601, (2010).
- [116] E. M. Purcell, H. C. Torrey, and R. V. Pound, “Resonance absorption by nuclear magnetic moments in a solid”, *Phys. Rev.*, **69**, 37–38, (1946).
- [117] G. Tian, J.-C. Liu, and Y. Luo, “Density-Matrix Approach for the Electroluminescence of Molecules in a Scanning Tunneling Microscope”, *Phys. Rev. Lett.*, **106**, 177401, (2011).
- [118] G. Tian and Y. Luo, “Electroluminescence of molecules in a scanning tunneling microscope: Role of tunneling electrons and surface plasmons”, *Phys. Rev. B*, **84**, 205419, (2011).
- [119] R. Carminati, J.-J. Greffet, C. Henkel, and J. Vigoureux, “Radiative and non-radiative decay of a single molecule close to a metallic nanoparticle”, *Optics Communications*, **261**, 368, (2006).
- [120] P. Anger, P. Bharadwaj, and L. Novotny, “Enhancement and quenching of single-molecule fluorescence”, *Phys. Rev. Lett.*, **96**, 113002, (2006).
- [121] C. W. Marquardt, S. Grunder, A. Baszczyk, S. Dehm, F. Henrich, H. V. Löhneysen, M. Mayor, and R. Krupke, “Electroluminescence from a single nanotube-molecule-nanotube junction.”, *Nat. Nanotechnol.*, **5**, 863–7, (2010).
- [122] L. Lafferentz, V. Eberhardt, C. Dri, C. Africh, G. Comelli, F. Esch, S. Hecht, and L. Grill, “Controlling on-surface polymerization by hierarchical and substrate-directed growth”, *Nat. Chem.*, **4**, 215, (2012).
- [123] R. Gutzler, H. Walch, G. Eder, S. Kloft, W. M. Heckl, and M. Lackinger, “Surface mediated synthesis of 2d covalent organic frameworks: 1,3,5-tris(4-bromophenyl)benzene on graphite(001), cu(111), and ag(110)”, *Chem. Commun.*, 4456–4458, (2009).
- [124] A. Basagni, F. Sedona, C. a. Pignedoli, M. Cattelan, L. Nicolas, M. Casarin, and M. Sambri, “MoleculesOligomersNanowiresGraphene Nanoribbons: A Bottom-Up Stepwise On-Surface Covalent Synthesis Preserving Long-Range Order”, *J. Am. Chem. Soc.*, **137**, 1802–1808, (2015).
- [125] A. Kimouche, M. M. Ervasti, R. Drost, S. Halonen, A. Harju, P. M. Joensuu, J. Sainio, and P. Liljeroth, “Ultra-narrow metallic armchair graphene nanoribbons”, *Nat. Commun.*, **6**, 10177, (2015).
- [126] “Focus on: 2D polymers”, *Nat. Chem.*, **6**, (2014).

- [127] H. Marbach, "Surface-mediated in situ metalation of porphyrins at the solidvacuum interface", *Acc. Chem. Res.*, **48**, 2649–2658, (2015).
- [128] A. C. Papageorgiou, S. Fischer, S. C. Oh, Z. Saglam, J. Reichert, A. Wiengarten, K. Seufert, S. Vijayaraghavan, D. Ecija, W. Auwärter, F. Allegretti, R. G. Acres, K. C. Prince, K. Diller, F. Klappenberger, and J. V. Barth, "Self-terminating protocol for an interfacial complexation reaction in vacuo by metal-organic chemical vapor deposition", *ACS Nano*, **7**, 4520, (2013).
- [129] A. Wiengarten, J. a. Lloyd, K. Seufert, J. Reichert, W. Auwärter, R. Han, D. a. Duncan, F. Allegretti, S. Fischer, S. C. Oh, O. Salam, L. Jiang, S. Vijayaraghavan, D. Ecija, A. C. Papageorgiou, and J. V. Barth, "Surface-Assisted Cyclodehydrogenation; Break the Symmetry, Enhance the Selectivity", *Chem. - A Eur. J.*, **21**, 12285, (2015).
- [130] W. Auwärter, D. Ecija, F. Klappenberger, and J. V. Barth, "Porphyrins at interfaces.", *Nat. Chem.*, **7**, 105, (2015).
- [131] M. Treier, C. A. Pignedoli, T. Laino, R. Rieger, K. Müllen, D. Passerone, and R. Fasel, "Surface-assisted cyclodehydrogenation provides a synthetic route towards easily processable and chemically tailored nanographenes.", *Nat. Chem.*, **3**, 61–67, (2011).
- [132] U. Fano, "Effects of configuration interaction on intensities and phase shifts", *Phys. Rev.*, **124**, 1866, (1961).
- [133] M. Born and E. Wolf, *Principles of optics: Electromagnetic Theory of Propagation, Interference and Diffraction of Light*. Cambridge University Press, 7th ed., (1999).
- [134] V. Heisig, A. Jeffrey, M. McGlade, and G. Small, "Fluorescence-line-narrowed spectra of polycyclic aromatic carcinogen-dna adducts", *Science*, **223**, 289–291, (1984).
- [135] M. Orrit, J. Bernard, and R. I. Personov, "High-resolution spectroscopy of organic molecules in solids: from fluorescence line narrowing and hole burning to single molecule spectroscopy", *The Journal of Physical Chemistry*, **97**, 10256–10268, (1993).
- [136] L. Fleury, P. Taramat, B. Lounis, J. Bernard, and M. Orrit, "Fluorescence spectra of single pentacene molecules in p-terphenyl at 1.7 K", *Chem. Phys. Lett.*, **236**, 87, (1995).
- [137] S. Jiang, Y. Zhang, R. Zhang, C. Hu, M. Liao, Y. Luo, J. Yang, Z. Dong, and J. G. Hou, "Distinguishing adjacent molecules on a surface using plasmon-enhanced Raman scattering", *Nat. Nanotechnol.*, **10**, 865, (2015).
- [138] C. Galland, A. Högele, H. E. Türeci, and A. m. c. Imamoğlu, "Non-markovian decoherence of localized nanotube excitons by acoustic phonons", *Phys. Rev. Lett.*, **101**, 067402, (2008).

- [139] A. E. Miroschnichenko, S. Flach, and Y. S. Kivshar, "Fano resonances in nanoscale structures", *Rev. Mod. Phys.*, **82**, 2257–2298, (2010).
- [140] B. Luk'yanchuk, N. I. Zheludev, S. A. Maier, N. J. Halas, P. Nordlander, H. Giessen, and C. T. Chong, "The Fano resonance in plasmonic nanostructures and metamaterials.", *Nat. Mater.*, **9**, 707–15, (2010).
- [141] S. Dey, M. Banik, E. Hulkko, K. Rodriguez, V. a. Apkarian, M. Galperin, and a. Nitzan, "Observation and analysis of Fano-like lineshapes in the Raman spectra of molecules adsorbed at metal interfaces", *Phys. Rev. B*, **93**, 035411, (2016).
- [142] K. Miwa, M. Sakaue, and H. Kasai, "Vibration-assisted upconversion of molecular luminescence induced by scanning tunneling microscopy", *Nanoscale Res. Lett.*, 2–7, (2013).
- [143] K. Miwa, M. Sakaue, B. Gumhalter, and H. Kasai, "Effects of plasmon energetics on light emission induced by scanning tunneling microscopy.", *J. Phys.: Condens. Matter*, **26**, 222001, (2014).
- [144] B. Y. M. Kasha, "Characterization of electronic transitions in complex molecules", *Discuss. Faraday Soc.*, **9**, 14, (1950).
- [145] J. S. Baskin, H.-Z. Yu, and A. H. Zewail, "Ultrafast dynamics of porphyrins in the condensed phase: I. free base tetraphenylporphyrin", *The J. Phys. Chem. A*, **106**, 9837–9844, (2002).
- [146] P. H. Kumar, Y. Venkatesh, D. Siva, B. Ramakrishna, and P. R. Bangal, "Ultrafast relaxation dynamics of 5,10,15,20-meso-tetrakis pentafluorophenyl porphyrin studied by fluorescence up-conversion and transient absorption spectroscopy", *The J. Phys. Chem. A*, **119**, 1267–1278, (2015).
- [147] K. Rebane and P. Saari, "Hot luminescence and relaxation processes in resonant secondary emission of solid matter", *Journal of Luminescence*, **16**, 223 – 243, (1978).
- [148] U. Even, J. Magen, J. Jortner, J. Friedman, and H. Levanon, "Isolated ultracold porphyrins in supersonic expansions. i. freebase tetraphenylporphyrin and zntetraphenylporphyrin", *The Journal of Chemical Physics*, **77**, 4374–4383, (1982).
- [149] K. S. Novoselov, A. K. Geim, S. V. Morozov, D. Jiang, Y. Zhang, S. V. Dubonos, I. V. Grigorieva, and A. A. Firsov, "Electric Field Effect in Atomically Thin Carbon Films", *Science*, **306**, 666–669, (2004).
- [150] S. Stankovich, D. a. Dikin, G. H. B. Dommett, K. M. Kohlhaas, E. J. Zimney, E. a. Stach, R. D. Piner, S. T. Nguyen, and R. S. Ruoff, "Graphene-based composite materials", *Nature*, **442**, 282–286, (2006).

- [151] A. K. Geim and K. S. Novoselov, "The rise of graphene.", *Nat. Mater.*, **6**, 183–91, (2007).
- [152] F. Schedin, a.K. Geim, S. Morozov, E. W. Hill, P. Blake, M. Katsnelson, and K. Novoselov, "Detection of individual gas molecules adsorbed on graphene.", *Nat. Mater.*, **6**, 652–5, (2007).
- [153] A. K. Geim, "Graphene : Status and Prospects", *Science*, **324**, 1530–1534, (2009).
- [154] A. H. Castro Neto, F. Guinea, N. M. R. Peres, K. S. Novoselov, and A. K. Geim, "The electronic properties of graphene", *Rev. Mod. Phys.*, **81**, 109–162, (2009).
- [155] S. Wang, L. Talirz, C. a. Pignedoli, X. Feng, K. Muellen, R. Fasel, and P. Ruffieux, "Giant edge state splitting at atomically precise zigzag edges", *Nat. Commun.*, **7**, 11507, (2016).
- [156] Z. Chen, Y.-M. Lin, M. J. Rooks, and P. Avouris, "Graphene nano-ribbon electronics", *Physics E*, **40**, 228 – 232, (2007).
- [157] X. Li, X. Wang, L. Zhang, S. Lee, and H. Dai, "Chemically derived, ultrasmooth graphene nanoribbon semiconductors", *Science*, **319**, 1229–1232, (2008).
- [158] L. Jiao, L. Zhang, X. Wang, G. Diankov, and H. Dai, "Narrow graphene nanoribbons from carbon nanotubes", *Nature*, **458**, 877–880, (2009).
- [159] Y. C. Chen, D. G. De Oteyza, Z. Pedramrazi, C. Chen, F. R. Fischer, and M. F. Crommie, "Tuning the band gap of graphene nanoribbons synthesized from molecular precursors", *ACS Nano*, **7**, 6123–6128, (2013).
- [160] P. Ruffieux, S. Wang, B. Yang, C. Sanchez-Sanchez, J. Liu, T. Dienel, L. Talirz, P. Shinde, C. A. Pignedoli, D. Passerone, T. Dumslaff, X. Feng, K. Muellen, and R. Fasel, "On-surface synthesis of graphene nanoribbons with zigzag edge topology", *Nature*, **531**, 489–493, (2016).
- [161] J. Liu, B.-W. Li, Y. Tan, A. Giannakopoulos, C. Sanchez-Sanchez, D. Beljonne, P. Ruffieux, R. Fasel, X. Feng, and K. Müllen, "Towards Cove-Edged Low Band Gap Graphene Nanoribbons.", *J. Am. Chem. Soc.*, **137**, 6097–6103, (2015).
- [162] P. Ruffieux, J. Cai, N. C. Plumb, L. Patthey, D. Prezzi, A. Ferretti, E. Molinari, X. Feng, K. Müllen, C. a. Pignedoli, and R. Fasel, "Electronic structure of atomically precise graphene nanoribbons", *ACS Nano*, **6**, 6930–6935, (2012).
- [163] A. I. Chernov, P. V. Fedotov, A. V. Talyzin, I. S. Lopez, I. V. Anoshkin, A. G. Nasibulin, E. I. Kauppinen, and E. D. Obraztsova, "Optical Properties of Graphene Nanoribbons Encapsulated in Single-Walled Carbon Nanotubes", *ACS Nano*, **7**, 6346–6353, (2013).

- [164] A. Narita, I. a. Verzhbitskiy, W. Frederickx, K. S. Mali, S. A. Jensen, M. R. Hansen, M. Bonn, S. De Feyter, C. Casiraghi, X. Feng, and K. Müllen, "Bottom-up synthesis of liquid-phase-processable graphene nanoribbons with near-infrared absorption", *ACS Nano*, **8**, 11622–11630, (2014).
- [165] R. Denk, M. Hohage, P. Zeppenfeld, J. Cai, C. a. Pignedoli, H. Söde, R. Fasel, X. Feng, K. Müllen, S. Wang, D. Prezzi, A. Ferretti, A. Ruini, E. Molinari, and P. Ruffieux, "Exciton-dominated optical response of ultra-narrow graphene nanoribbons.", *Nat. Commun.*, **5**, 4253, (2014).
- [166] G. Soavi, S. Dal Conte, C. Manzoni, D. Viola, A. Narita, Y. Hu, X. Feng, U. Hohenester, E. Molinari, D. Prezzi, K. Müllen, and G. Cerullo, "Exciton-exciton annihilation and biexciton stimulated emission in graphene nanoribbons.", *Nat. Commun.*, **7**, 11010, (2016).
- [167] C. Bronner, F. Leyssner, S. Stremlau, M. Utecht, P. Saalfrank, T. Klamroth, and P. Tegeder, "Electronic structure of a subnanometer wide bottom-up fabricated graphene nanoribbon: End states, band gap, and dispersion", *Phys. Rev. B*, **86**, 085444, (2012).
- [168] J. van der Lit, M. P. Boneschanscher, D. Vanmaekelbergh, M. Ijäs, A. Uppstu, M. Ervasti, A. Harju, P. Liljeroth, and I. Swart, "Suppression of electronvibron coupling in graphene nanoribbons contacted via a single atom", *Nat. Commun.*, **4**, 2023, (2013).
- [169] H. Söde, L. Talirz, O. Gröning, C. A. Pignedoli, R. Berger, X. Feng, K. Müllen, R. Fasel, and P. Ruffieux, "Electronic band dispersion of graphene nanoribbons via fourier-transformed scanning tunneling spectroscopy", *Phys. Rev. B*, **91**, 045429, (2015).
- [170] K. Nakada, M. Fujita, G. Dresselhaus, and M. S. Dresselhaus, "Edge state in graphene ribbons: Nanometer size effect and edge shape dependence", *Phys. Rev. B*, **54**, 17954–17961, (1996).
- [171] C. Tao, L. Jiao, O. V. Yazyev, Y.-C. Chen, J. Feng, X. Zhang, R. B. Capaz, J. M. Tour, A. Zettl, S. G. Louie, H. Dai, and M. F. Crommie, "Spatially Resolving Spin-split Edge States of Chiral Graphene Nanoribbons", *Nat. Phys.*, **7**, 616–620, (2011).
- [172] Y. Piao, B. Meany, L. Powell, N. Valley, H. Kwon, G. Schatz, and Y. Wang, "Brightening of carbon nanotube photoluminescence through the incorporation of sp³ defects.", *Nat. Chem.*, **5**, 840, (2013).
- [173] M. Orrit, J. Bernard, A. Zumbusch, and R. I. Personov, "Stark effect on single molecules in a polymer matrix", *Chem. Phys. Lett.*, **196**, 595–600, (1992).
- [174] U. P. Wild, F. Guttler, M. Pirotta, and A. Renn, "Single molecule spectroscopy: Stark effect of pentacene in p-terphenyl", *Chem. Phys. Lett.*, **193**, 451–455, (1992).

- [175] C. Brunel, P. Tamarat, B. Lounis, J. C. Woehl, and M. Orrit, "Stark effect on single molecules of dibenzanthanthrene in a naphthalene crystal and in a n-hexadecane Shpol'skii matrix", *J. Phys. Chem. A*, **103**, 2429–2434, (1999).
- [176] F. Schindler, J. M. Lupton, J. Müller, J. Feldmann, and U. Scherf, "How single conjugated polymer molecules respond to electric fields.", *Nat. Mater.*, **5**, 141–6, (2006).
- [177] G. Schull, N. Néel, M. Becker, J. Kröger, and R. Berndt, "Spatially resolved conductance of oriented C 60", *New J. Phys.*, **10**, 065012, (2008).
- [178] C. Girard, C. Joachim, C. Chavy, and P. Sautet, "The electric field under a STM tip apex: implications for adsorbate manipulation", *Surf. Sci.*, **282**, 400–410, (1993).
- [179] A. V. Savin and Y. S. Kivshar, "Vibrational Tamm states at the edges of graphene nanoribbons", *Phys. Rev. B*, **81**, 165418, (2010).
- [180] D. Porath, Y. Levi, M. Tarabiah, and O. Millo, "Tunneling spectroscopy of isolated C₆₀ molecules in the presence of charging effects", *Phys. Rev. B*, **56**, 9829–9833, (1997).
- [181] G. Mikaelian, N. Ogawa, X. W. Tu, and W. Ho, "Atomic scale control of single molecule charging", *J. Chem. Phys.*, **124**, (2006).

List of publications

Narrow-Line Single-Molecule Transducer between Electronic Circuits and Surface Plasmons. **M.C. Chong**, G. Reecht, H. Bulou, A. Boeglin, F. Scheurer, F. Mathevet, G. Schull. *Physical Review Letters*, **116**, 036802, January 2016

Ordinary and Hot Electroluminescence from Single-Molecule Devices: Controlling the Emission Color by Chemical Engineering. **M.C. Chong**, L. Sosa-Vargas, H. Bulou, A. Boeglin, F. Scheurer, F. Mathevet, G. Schull. *Nano Letters*, **16**, 6480-6484, September 2016

Electrically-driven vibronic spectroscopy with sub-molecular resolution.
B. Doppagne, **M.C. Chong**, E. Lorchat, S. Berciaud, M. Romeo, H. Bulou, A. Boeglin, F. Scheurer, G. Schull. *In preparation*

Electrically driven fluorescence of single molecule junctions

Résumé

Les propriétés optoélectroniques de jonctions moléculaires sont étudiées par microscopie à effet tunnel (STM). Premièrement, les structures moléculaires sont synthétisées sur une surface Au(111). Puis, par manipulation, nous soulevons et suspendons une molécule entre la pointe du STM et la surface d'or pour obtenir une jonction moléculaire. En appliquant une tension entre la pointe et l'échantillon, un courant est généré, ce qui conduit à l'excitation de la molécule. Ce processus est médié par des modes de plasmons de surface localisé de la pointe. Finalement, la molécule se désexcite de manière radiative et génère un signal de fluorescence.

On utilise cette technique pour étudier deux systèmes moléculaires différents.

Dans le premier, un émetteur (fused-porphyrin) est suspendu dans la jonction grâce à des fils organiques (oligothiophène). Ce type de jonction génère une émission de lumière étroite dont la couleur est contrôlée en sélectionnant la structure chimique de l'unité émettrice. Le contrôle de la largeur du pic d'émission est obtenu en détachant progressivement l'unité émettrice de la surface. On observe aussi des pics vibroniques décalés vers le rouge qui fournissent une empreinte chimique de l'émetteur, et des pics décalés vers le bleu, signe d'une désexcitation d'un exciton non-thermalisé.

Le deuxième type de jonction est composé de nano-rubans de graphène (GNRs) dont la largeur et la structure de l'arrête sont définies avec une précision atomique. Une fois suspendu dans la jonction, les GNRs qui présentent une terminaison spécifique (terminaison C) montrent un spectre d'émission de lumière avec un pic principal et deux pics vibroniques décalés vers le rouge. Le pic principale est associé à une transition intra-ruban entre un état Tamm localisé et un état delocalisé

Mots-clés : STM, STS, électronique moléculaire, optoélectronique, émission de lumière induite par STM, molécules uniques, fluorescence, porphyrines, désexcitation d'un exciton non-thermalisé, rubans de graphène, spectroscopie vibrationnelle.

Résumé en anglais

This thesis presents a study of the optoelectronic properties of molecular junctions performed by scanning tunneling microscopy (STM). First, the molecular structures are synthesized on a Au(111) surface. Then, by manipulation we lift and suspend a molecule between the tip of the STM and the gold surface, creating a single molecule junction. By applying a voltage bias between the tip and the sample, a current is generated, which leads to the excitation of the molecule. This process is mediated by the localized surface plasmon modes of the tip. Eventually, the molecule de-excites in a radiative way, generating a fluorescence signal.

We use this technique to study two different molecular junctions.

First, an emitting unit (fused-porphyrin) is suspended in the junction by means of organic linkers (oligothiophene). This type of junction generates a narrow-line emission of light whose color is controlled by selecting the chemical structure of the emitting unit. Moreover, control over the linewidth is obtained by progressively detaching the emitting unit from the surface. Also, we observe red-shifted vibronic features that provide a chemical fingerprint of the emitter, and blue-shifted vibronic features that are a sign of hot-luminescence.

For the second type of junctions we use graphene nanoribbons (GNRs) of atomically precise width and edge structure. When lifted in the junction, GNRs with a specific type of termination (C-terminated) exhibit a light emission spectrum with a main peak and two red-shifted vibrational features. The main peak is associated to an intra-ribbon transition between a localized state (Tamm) and a delocalized state.

Key words : STM, STS, molecular electronics, optoelectronics, STM-induced luminescence, single molecules, fluorescence, porphyrins, hot-luminescence, graphene nanoribbons, vibronic spectroscopy.